Neutron Diffraction and Reflection Studies of Superconductors

John M. Reynolds

Oxford University

1998

Neutron Diffraction and Reflection

Studies of Superconductors

by John M. Reynolds,

Corpus Christi College, Oxford,

submitted for the degree of Doctor of Philosophy

in September 1998

Abstract

I have studied two magnetic properties of superconductors using different neutron scattering techniques. Due to their magnetic moment and lack of electrical charge, neutrons can provide an extremely sensitive probe into magnetism on a small scale.

Unusual magnetic structures have previously been observed in the non-superconducting $PrBa_2Cu_3O_{6+\delta}$, in particular showing a coupling between the rare-earth and the Cu-O_2 planes. For comparison, I have used elastic neutron scattering to measure the temperature dependent magnetic structure of the high-T_c superconductor $NdBa_2Cu_3O_7$, and its non-superconducting reduced form $NdBa_2Cu_3O_6$. The magnetic structures of both the Nd and Cu sub-lattices are presented. Measurements are shown for single crystals of both the oxygenated and reduced form, and also for a non-stoichiometric single crystal with Nd substituted on the Ba sites. I present a quantitative analysis of the magnetic moments, with account taken of the instrumental resolution including sample mosaicity and intrinsic peak shapes. No evidence was found for any coupling of the type seen in $PrBa_2Cu_3O_{6+\delta}$.

Many of the underlying properties of superconductors are evidenced in the way magnetic fields are excluded in the different states. I have used polarized neutron reflectometry to measure the magnetic field profile in thin film superconductors. I present measurements for pure niobium and preliminary measurements for $YBa_2Cu_3O_7$. The samples studied are much thicker than those previously measured, to provide a closer match to the bulk superconductor properties and allow meaningful measurements of the higher field states. For niobium, the applied field dependence is measured for fields covering the Meissner and mixed states, and models are compared for these states and the surface superconductivity state.

Acknowledgements

I would firstly like to thank my supervisor, Andrew Boothroyd. He has been continually supportive, which was particularly valuable during the times we were suffering from instrumental difficulties.

Thanks also for the help from the post-docs of our group, Valerie Nunez and Robert Georgi. Valerie's work on the CRISP reflectometer was essential to understanding the problems.

I would also like to thank the other members (past and present) of Andrew Boothroyd's and Roger Cowley's groups who have made the Clarendon laboratory a pleasant place to work; all the best to Alan, Anders, Andrew S, Andrew W, Bella, Bernard, Bobby, Caelia, Chess, Jon, Julian, Martin, Radu, Roberto, Roger, Sasha and Steve.

Thanks to Eric Brecht who worked on the Risø experiments with us, making an invaluable contribution. The neutron experiments were made much easier by the assistance of the local contacts for the experiments. In particular thanks go to Niels Anderson at Risø and Jeff Penfold, David Bucknall and Sean Langridge at RAL.

Good samples are vital for the experimentation. Thomas Wolf, Rob Somekh and Torsten Freltoft's abilities in producing samples with specific characteristics made the experiments possible.

This work was funded by the Engineering and Physical Sciences Research Council of Great Britain, and the elastic neutron scattering experiments were supported by the EC TMR Access to Large Scale Facilities Programme at Risø National Laboratory.

Finally, a huge thank you to my parents who have been supportive thoughout, and all my other friends who have put up with me during times of stress.

Contents

List of Figures

List of Tables

Chapter 1

Introduction

1.1 Aims

Superconductors have been an active and interesting field of research in the recent history of condensed matter physics.

The electrical conduction properties of superconductors give them their name, but the magnetic properties of superconductor are also unusual and interesting and can provide insights into the underlying physical processes.

In this thesis, I investigate two different magnetic properties of superconductors. In both cases, I have used a technique of neutron scattering that has not been extensively applied to the property in question. Because of this I have endeavoured in this thesis to provide a description of the techniques used and our findings with regard to the practicalities of them.

1.2 Superconductivity

1.2.1 Conventional superconductivity

The phenomenon of superconductivity was discovered in 1911 by H. Kamerlingh Onnes in Leiden (only three years after he first liquefied helium). He discovered that below a (very low) critical temperature T_c, the electrical resistance of several metals such as lead and tin vanished completely. In 1914 he showed that a magnetic field above a critical field H_c

would destroy the superconducting effect. This field could be produced by the current in the superconductor, so there was an upper limit on the current that could be carried.

In 1933, W. Meissner and R. Ochsenfeld discovered another property of superconductors. They found that below the critical field H_c, bulk superconductors acted as perfect diamagnets: an applied magnetic field was completely excluded. This is a separate effect to 'perfect' conduction; a perfect conductor would simply hold flux lines in place rather than expelling them.

The brothers F. and H. London proposed a set of equations (the London equations) in 1935 to describe the microscopic electromagnetic fields inside a superconductor (See Section 6.3.1 for more details). These gave a reasonable model for many of the properties, but said little about the underlying physical processes.

In 1953 A.B. Pippard introduced a non-local generalization of these equations by introducing the concept of the coherence length

$$\xi_0 = a\frac{\hbar v_F}{kT_c}, \tag{1.1}$$

where a is a constant of order unity and v_F is the Fermi velocity. This improved the model considerably, and covered some of the differences between the types of superconductor. Though in good agreement with many measurements, it still did not give a microscopic understanding of the processes.

The real breakthrough in theoretical understanding of conventional superconductors did not come until 1956 with the concept of Cooper pairs [1]. A Cooper pair is two electrons with opposite spin and opposite but equal crystal momentum. The initial concept was expanded in 1957 by J. Bardeen, L.N. Cooper and J.R. Schrieffer into the well known BCS theory [2], which gives a microscopic description of superconductivity.

The BCS theory showed that a weak attractive interaction between electrons (such as caused by an electron-phonon interaction) would cause an instability in the ground state Fermi-sea of electrons, leading to the formation of Cooper pairs. One of the key predictions of the theory was the existence of a (temperature dependent) minimum energy E_g required

to break a pair. The theory predicted that this energy was

$$E_g(0) = 2\Delta(0) = 3.528kT_c. \tag{1.2}$$

Thus, there was a bound state of lower energy than the usual Fermi energy. This energy gap at the Fermi energy meant that the electrons in this bound state could not be scattered as there are no energy states for them to be scattered into.

The predictions of BCS theory for the energy gap and other physical properties agreed well with experiment, and the BCS theory remains a good description of conventional superconductors.

The other significant early theory of superconductors is the Ginzburg-Landau (GL) theory (see Chapter 7 for more details). This was proposed in 1950 by V.L. Ginzburg and L.D. Landau and gives a more macroscopic description of superconductivity. GL theory introduces a wavefunction like parameter ψ to describe the superconducting electrons where the density of superconducting electrons is given by $n_s = |\psi(x)|^2$. Like the London theory this proved very useful in describing the physical properties of superconductors. In particular it was used to predict the existence and properties of Type-II superconductors.

In 1959 L.P. Gor'kov showed that Ginzburg-Landau theory was a limiting case of BCS theory when the temperature is near T_c and ψ and the magnetic potential do not vary rapidly. This placed GL theory on a sound physical basis.

During the 1960s the BCS and GL theories combined to give a remarkably complete theoretical understanding of superconductivity.

1.2.2 High T_c superconductivity

In 1986, the field of superconductivity was drastically changed by the discovery of a new class of superconductors with much higher critical temperatures [3, 4].

These materials all have a feature in common: they all contain planes of Cu-O_2, and are thus commonly known as the cuprate superconductors.

These materials are notable not only in their high T_c which opens up many practical applications, but also in that the BCS theory is not sufficient to describe their physical

properties accurately.

The high temperature superconductors have a number of different properties to those of the conventional superconductors:

- They (obviously) have a much higher T_c. This can lead to thermal fluctuations having a more significant effect.
- The cuprate superconductors are strongly two-dimensional, whereas conventional superconductors are usually isotropic.
- The cuprate superconductors have magnetically ordered phases (as studied in Part I of this thesis). Conventional superconductors are usually non-magnetic, as in conventional superconductors magnetic moments damage superconductivity by destroying the Cooper pairs.
- The cuprate superconductors have very short coherence lengths, generally in the tens of angstroms at most, compared with up to thousands of angstroms for the conventional superconductors.
- The normal state properties of the cuprate superconductors also show unusual behaviour, for example the linear variation of the resistivity with temperature.

Theoretical models of cuprate superconductors are still controversial. Many current models are extensions of the BCS theory, with modifications to the source of the coupling. Other theories more radically change the conventional understanding.

Many of the most commonly used and studied of these materials are the $RBa_2Cu_3O_7$ superconductors (where R is a rare earth or Y). These are described in more detail in Chapter 2.

1.3 Magnetic structure

In Part I of this thesis, I investigate the magnetic structure of the cuprate superconductor $NdBa_2Cu_3O_7$, as well as its reduced, non-superconducting form $NdBa_2Cu_3O_6$, using elastic neutron scattering.

For this I have used a triple axis spectrometer. This has not commonly been used for fully quantitative measurements of magnetic ordering due to the difficulties in the experiment and analysis.

However, it does have the advantage of being a relatively direct measurement of the magnetic structure, and has a good signal-to-noise ratio which is essential to measure the weak magnetic signals.

$NdBa_2Cu_3O_{6+\delta}$ was chosen for study for comparison with $PrBa_2Cu_3O_{6+\delta}$, which in most cases is a non-superconductor, and for which unusual magnetic structures have been observed.

The measurements on $NdBa_2Cu_3O_{6+\delta}$ presented here use single crystal samples. This enables considerably more detail of the structure to be obtained than with polycrystalline samples.

1.4 Magnetic penetration in thin films

In Part II of this thesis, I have studied the the penetration of magnetic fields into thin film superconductors. I have studied the conventional type-II superconductor niobium, and the high temperature cuprate superconductor $YBa_2Cu_3O_7$.

For this I have used the technique of polarized neutron reflectometry. This is a technique that has only relatively recently been used for measurement of flux penetration, and the experimental techniques are still in development.

There are several reasons for using this technique. It gives a much more direct measurement of the behaviour of the magnetic field than many of the other techniques for measuring penetration, and opens the possibility of measuring how the field behaves in higher field states than the Meissner state.

The measurements presented here are innovative in covering the mixed state of niobium, and in using much thicker samples than have been used previously. Using thicker samples means they match the behaviour of the bulk superconductor more closely, and enables the investigation of the states above the Meissner state.

1.5 References

[1] L.N. Cooper, *Bound electron pairs in a degenerate Fermi gas*, Phys. Rev. **104** 1189–1190 (1956).

[2] J. Bardeen, L.N. Cooper and J.R. Schrieffer, *Theory of superconductivity*, Phys. Rev. **108** 1175–1204 (1957).

[3] G. Bednorz and K.A. Müller, *Possible high T_c superconductivity in the Ba-La-Cu-O system*, Z. Phys. **B64** 189–193 (1986).

[4] M.K. Wu, J.R. Ashburn, C.J. Torng, P.H. Hor, R.L. Mena, L. Gao, Z.J. Huang, Y.Q. Wang and C.W. Chu, *Superconductivity at 93K in a new mixed-phase Y-Ba-Cu-O compound system at ambient pressure*, Phys. Rev. Lett. **58** 908–910 (1987).

Part I

Elastic Neutron Scattering Studies of the Magnetic Structure of $NdBa_2CuO_{6+\delta}$

Chapter 2

Magnetic Structure

Introduction

In Part I of this thesis, I study the magnetic structure of single crystals of $NdBa_2Cu_3O_{6+\delta}$.

This chapter outlines the properties of the ceramic cuprate high temperature superconductors of the $RBa_2Cu_3O_7$ type and the magnetic structures that they form.

2.1 The $RBa_2Cu_3O_{6+\delta}$ series of superconductors

$NdBa_2Cu_3O_7$ is one of the series of $RBa_2Cu_3O_7$ ceramic superconductors, where R is one of a number of ions, usually a rare earth (members of the lanthanide series).

These superconductors have a characteristic structure, shown in Figure 2.1. Figure 2.2 shows the structure of the $RBa_2Cu_3O_6$ reduced form.

Most of the rare earth ions and a few others form this structure and superconduct with a critical temperature, T_c, around 90 K.

Current theories suggest that below the critical temperature, superconductivity occurs in the copper–oxygen planes above and below the rare earth ion.

Particularly interesting superconductors of this type include:

- $YBa_2Cu_3O_7$ is probably the best known of this type of superconductor. Discovered in 1987 (see Chapter 1 Ref. [4]), it has a T_c of around 93 K. Notably yttrium is not a

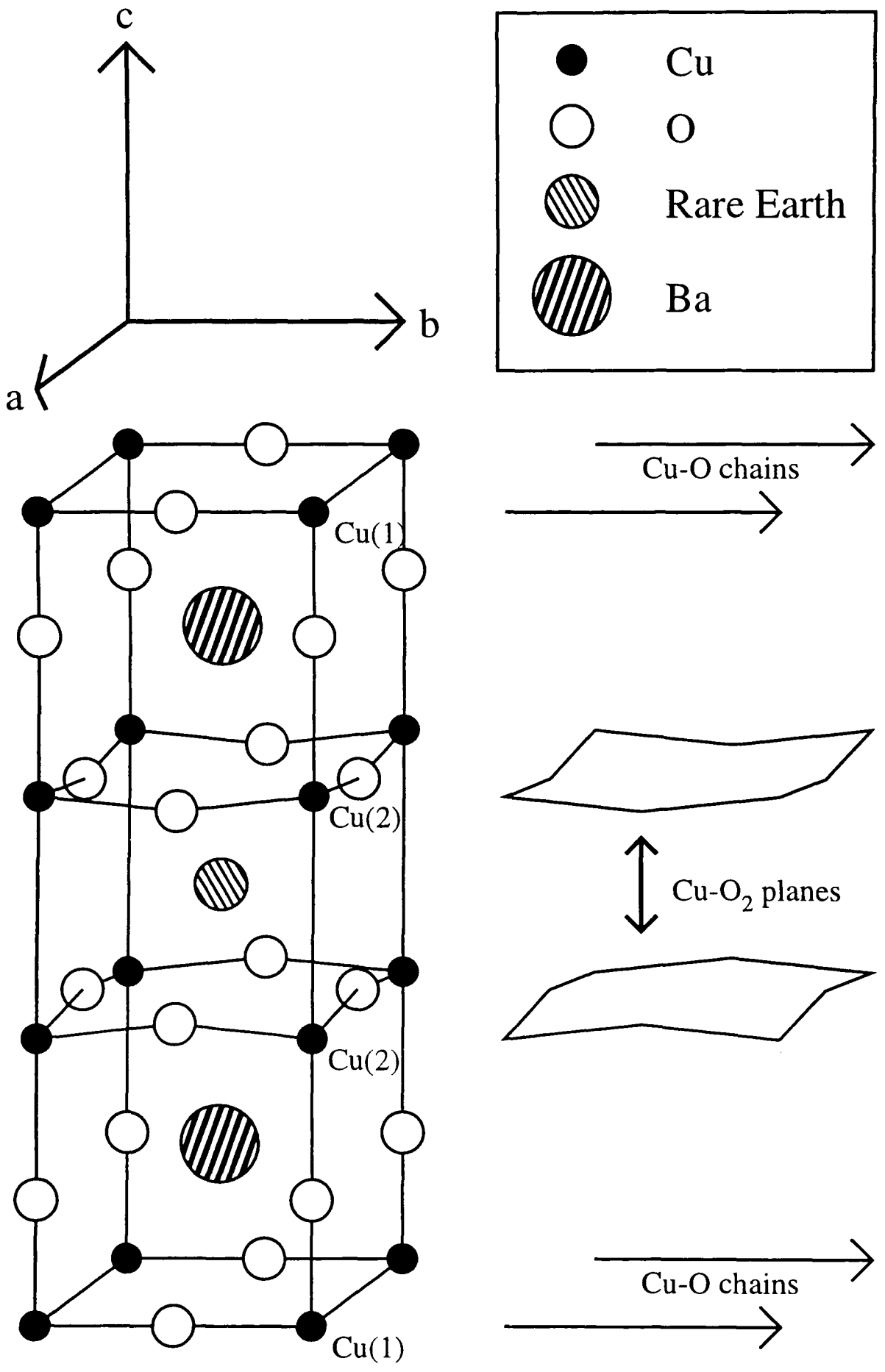

Figure 2.1: The orthorhombic structure of the oxidized form

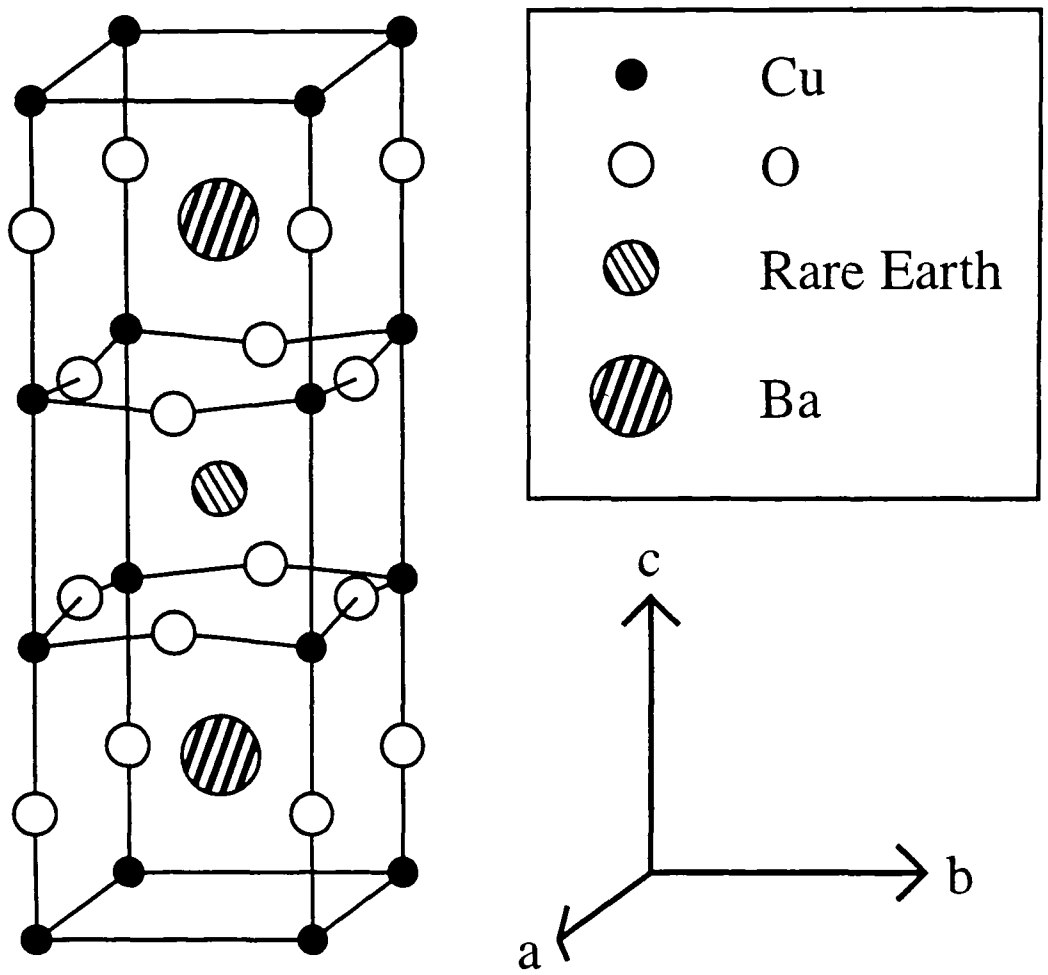

Figure 2.2: The tetragonal structure of the reduced form

member of the lanthanide series, but resides directly above lanthanum in the periodic table. $YBa_2Cu_3O_7$ has been extensively studied, and has been used in many practical applications. It is also easy and cheap to make. Samples exhibiting the Meissner effect can be produced by secondary-school students.

- $CeBa_2Cu_3O_7$ and $TbBa_2Cu_3O_7$ are notable in that they do not form the structure in Figure 2.1 at all.

- $PrBa_2Cu_3O_7$ is particularly interesting in that it does form the same structure, but does not superconduct. However, recent studies [1, 2] suggest that samples produced with a particular growth method can superconduct.

$PrBa_2Cu_3O_7$ (the smallest of the Lanthanide series that forms the structure in Figure 2.1) has gathered much interest. This is because understanding why it does not superconduct may give clues to the processes in the compounds that do. $PrBa_2Cu_3O_{6+\delta}$ has been shown to have a number of unusual magnetic features:

- It displays Cu antiferromagnetism up to and above room temperature, even when fully oxidized to $PrBa_2Cu_3O_7$ [3, 4, 5, 6, 7, 8, 9].

- The Pr sub-lattice orders at the unusually high temperature of 11–17 K for $x = 0$–1 [3, 4, 5, 10, 11, 12].

- Recent measurements have indicated a coupling between the Pr and Cu ordering [13, 14, 15]. This ordering is described in Section 2.2.3.

From a physical point of view $NdBa_2Cu_3O_{6+\delta}$, which I have measured, is not in itself particularly interesting (though there are technological applications), with the exception of it having a high critical current. Like most of the others it forms the structure in Figure 2.1, and superconducts below $T_c \approx 95$ K. However, Nd is the nearest to Pr in the periodic table to have these properties, and it has a similar ionic radius.

It was also chosen because like $PrBa_2Cu_3O_{6+\delta}$ it has a high rare earth ordering temperature compared to the other rare earth members in the series [16, 17] ($T \approx 0.6$ K at $\delta \approx 1$, $T \approx 1.7$ K at $\delta \approx 0$), which varies with oxygen concentration [18, 19]. This indicates that the neodymium ordering is affected by the surrounding ions which opens the possibility of a coupling like that seen with praseodymium.

Previous studies [16, 17, 18, 19] have established the broad features of the magnetic ordering in $NdBa_2Cu_3O_{6+\delta}$ polycrystalline samples. These have shown that the Nd moment orders antiferromagnetically along all three axes. In the oxygenated superconducting samples the Nd moment has been reported to have a magnitude $\approx 1\ \mu_B$ aligned in the c direction. In the reduced samples the ordered moment is slightly smaller and is tilted away from the c axis. For samples with oxygen concentrations between these extremes, the ordering is poorly correlated in the c direction leading to broadening of the diffraction peaks. The copper moments order antiferromagnetically at high temperatures and some studies have found AF2 (see later) ordering at low temperature.

In this thesis, I present a study of the magnetic structure of single crystal samples of $NdBa_2Cu_3O_{6+\delta}$ for comparison with $PrBa_2Cu_3O_{6+\delta}$.

So far measurements of any kind on magnetism in single crystals of $NdBa_2Cu_3O_{6+\delta}$ have been rare [20]. A previous single crystal neutron diffraction study [21] on reduced samples

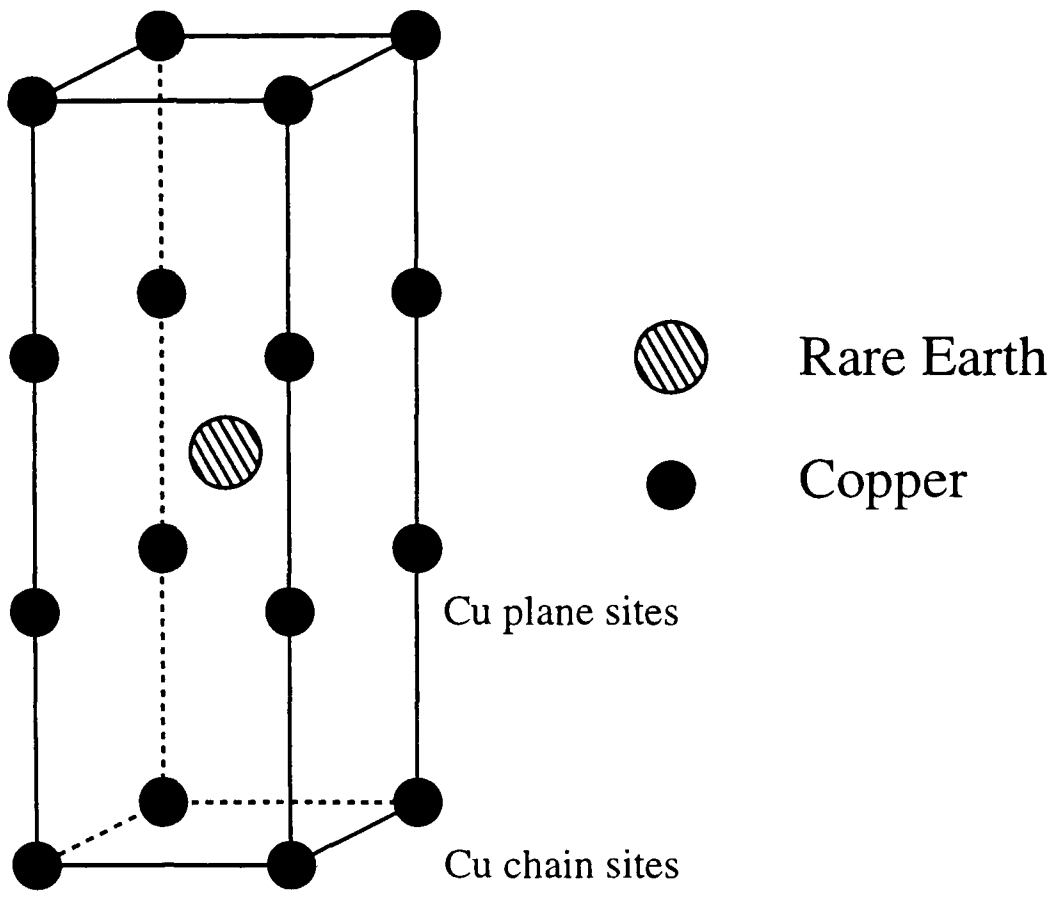

Figure 2.3: The magnetic ions

has measured the copper ordering, finding an AF2 (see later) structure.

2.2 Magnetic structure

The only magnetic ions present in the $RBa_2Cu_3O_{6+\delta}$ series are the central rare earth ion and the copper ions. See Figure 2.3 for their positions.

As shown in previous studies and presented here, copper magnetic ordering usually occurs mainly on the copper–oxygen plane sites, though an ordered moment on the chain sites has been observed.

In most cases, the magnetic ordering of the rare earth ion and the copper ions have been shown to be independent. However, there is evidence for coupling between Pr and the Cu ions [13].

There are several structures allowed by symmetry for the copper and rare earth ions, and many of these have been observed.

In this section I outline the types of ordering observed in the series.

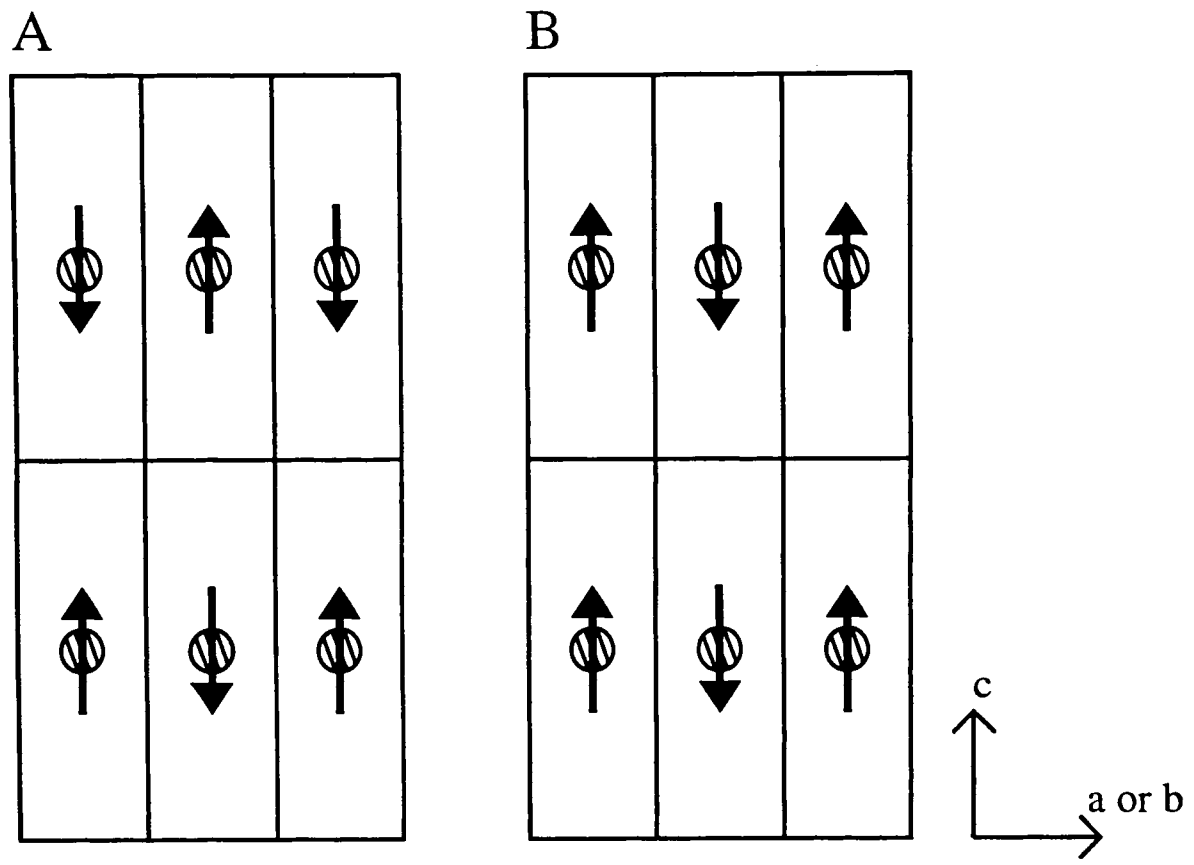

Figure 2.4: Rare earth magnetic ordering: Diagram A shows the antiferromagnetic ordering of the rare earth ions. Diagram B shows rare earth ordering that is antiferromagnetic in the *ab* plane and ferromagnetic in the *c* direction.

2.2.1 Rare earth ordering

The ordering of the central rare earth ion is relatively simple.

Previous studies have shown Pr ordering to be antiferromagnetic in all three directions as shown in part A of Figure 2.4 (for example see Ref. [10]). This produces magnetic scattering at the $(h+\frac{1}{2}, k+\frac{1}{2}, l+\frac{1}{2})$ positions, where h, k and l are integers. This is the structure that is also displayed by Nd in previous measurements.

Another possibility is for the central ion to order antiferromagnetically in the a and b directions, but ferromagnetically in the c direction as shown in part B of Figure 2.4. This produces magnetic scattering at the $(h+\frac{1}{2}, k+\frac{1}{2}, l)$ positions. This has also been observed for Pr [3].

Note that in both cases, the magnetic unit cell is larger than the chemical unit cell.

It is also possible for the moments to be poorly correlated in the c direction. This will either lead to Lorentzian broadening in this direction, or the formation of Bragg rods indicating a fully two-dimensional ordering.

Due to twinning, different parts of the crystal may have different alignments of the rare earth moments. The effect of this is described in Chapter 3 Section 3.11.

2.2.2 Copper ordering

Due to the copper ions being in different positions in the unit cell, the copper magnetic ordering is more complex.

As with the rare earth ordering, twinning can make certain details of the structure difficult to determine.

The simplest copper ordering, which generally occurs at relatively high temperature is a phase I will label AF1. In this ordering, the copper ions in the copper–oxygen plane are ordered purely antiferromagnetically along all three axes.

This structure is shown in Figure 2.5. Note that as there are two copper–oxygen planes in the chemical unit cell, then this ordering is periodic every two cells in the a and b directions, but every cell in the c direction. Thus this ordering produces peaks at the $(h+\frac{1}{2}, k+\frac{1}{2}, l)$ positions (where again h, k, l are integers).

The copper moments lie in the ab plane, but the exact direction within the plane has not been well defined by experiment (see Section 3.11 for one reason). This is why Figure 2.5 does not show a direction for the spins, but just their relative orientation.

At lower temperatures there is the possibility of a further ordering. As the temperature decreases, there can be a ferromagnetic coupling in the c direction between the copper ions in the copper–oxygen planes of adjacent unit cells. This can be accompanied by the appearance of an ordered moment on the copper chain sites.

The effect of this is to cause the copper moments in the plane to rotate, with the copper ions in one chemical unit cell rotating in the same direction, but ions in adjacent cells in the c direction rotating in the opposite direction. As different copper moments rotate in different directions, this rotation is detectable and changes the ordering, despite the original direction being uncertain.

In the ordering this eventually leads to, which I will label AF2, the copper ions remain antiferromagnetically ordered in the a and b directions and between the planes either side of the rare earth ion, but ferromagnetically ordered between planes across the copper chain

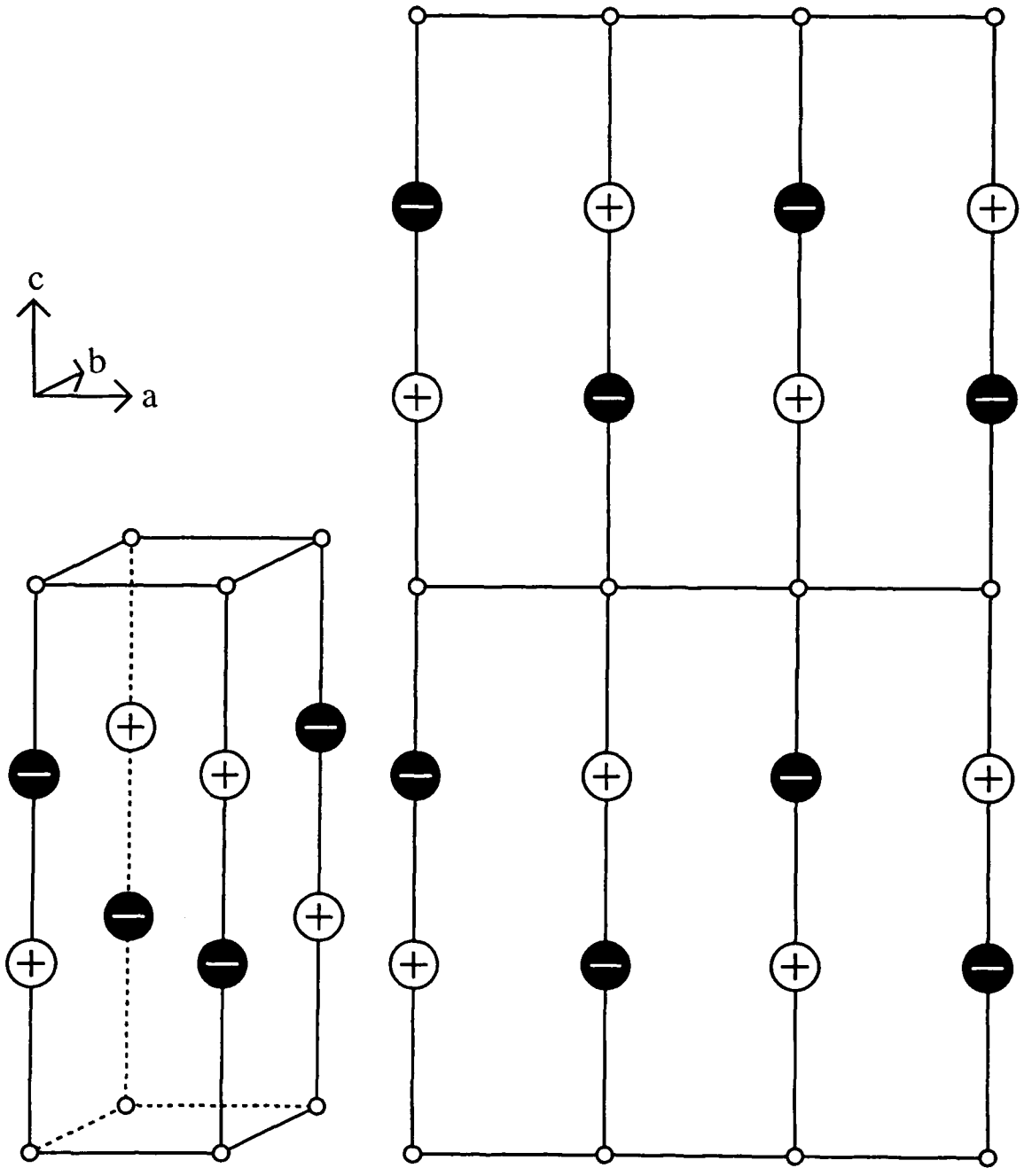

Figure 2.5: Cu antiferromagnetic ordering: this is the simplest form of Cu ordering (AF1); the ions order antiferromagnetically in all three directions. The Cu moments lie in the *ab* plane.

sites.

This process and the resulting ordering is illustrated in Figure 2.6.

This final ordering is periodic every two cells in each direction, and so leads to magnetic peaks at the $(h+\frac{1}{2}, k+\frac{1}{2}, l+\frac{1}{2})$ positions. In the intermediate state, intensity may be observed at both sets of positions.

2.2.3 Mixed ordering

Another type of ordering, which I will label AF3, has been observed with praseodymium as the central ion [13], which suggests a coupling between the central ion and the copper–oxygen plane [22]. Other studies [14, 15] have also indicated some form of coupling.

In this structure, the copper plane moments rotate in the *ab* plane in opposite directions either side of the central ion.

This structure indicates a coupling between the moments, as without an external influence, the copper ions have no energetic reason to rotate.

Similar structures should be possible whether the central ion is antiferromagnetic or ferromagnetic in the *c* direction. In the former case, the sense of rotation will alternate every chemical unit cell in the *c* direction; in latter case it will be the same.

Figure 2.7 illustrates the rotation in a single unit cell.

2.3 References

[1] Z. Zou, K. Oka, T. Ito and Y. Nishihara, *Bulk Superconductivity in Single Crystals of* $PrBa_2Cu_3O_x$, Jpn. J. Appl. Phys. **36** L18–L20 (1997).

[2] Z. Zou, J. Ye, K. Oka and Y. Nishihara, *Superconducting* $PrBa_2Cu_3O_x$, Phys. Rev. Lett. **80** 5 1074–1077 (1998).

[3] A. Longmore, *Neutron Scattering and Praseodymium Suppression of Superconductivity*, Thesis, Oxford University (1995).

[4] A. Longmore, A.T. Boothroyd, Chen Changkang, Hu Yongle, M.P. Nutley, N.H. Andersen, H. Casalta, P. Schleger and A.N. Christensen, *Magnetic ordering in* $PrBa_2Cu_{3-y}Al_yO_{6+x}$, Phys. Rev. B **53** 14 9382–9395 (1996).

[5] A. Longmore, M.P. Nutley, A.T. Boothroyd, N.H. Andersen, H. Casalta, P. Schleger, Chen Changkang, Hu Yongle and A.N. Christensen, *Magnetic order in* $PrBa_2Cu_3O_{6+x}$, Physica C **235** 3 1581–1582 (1994).

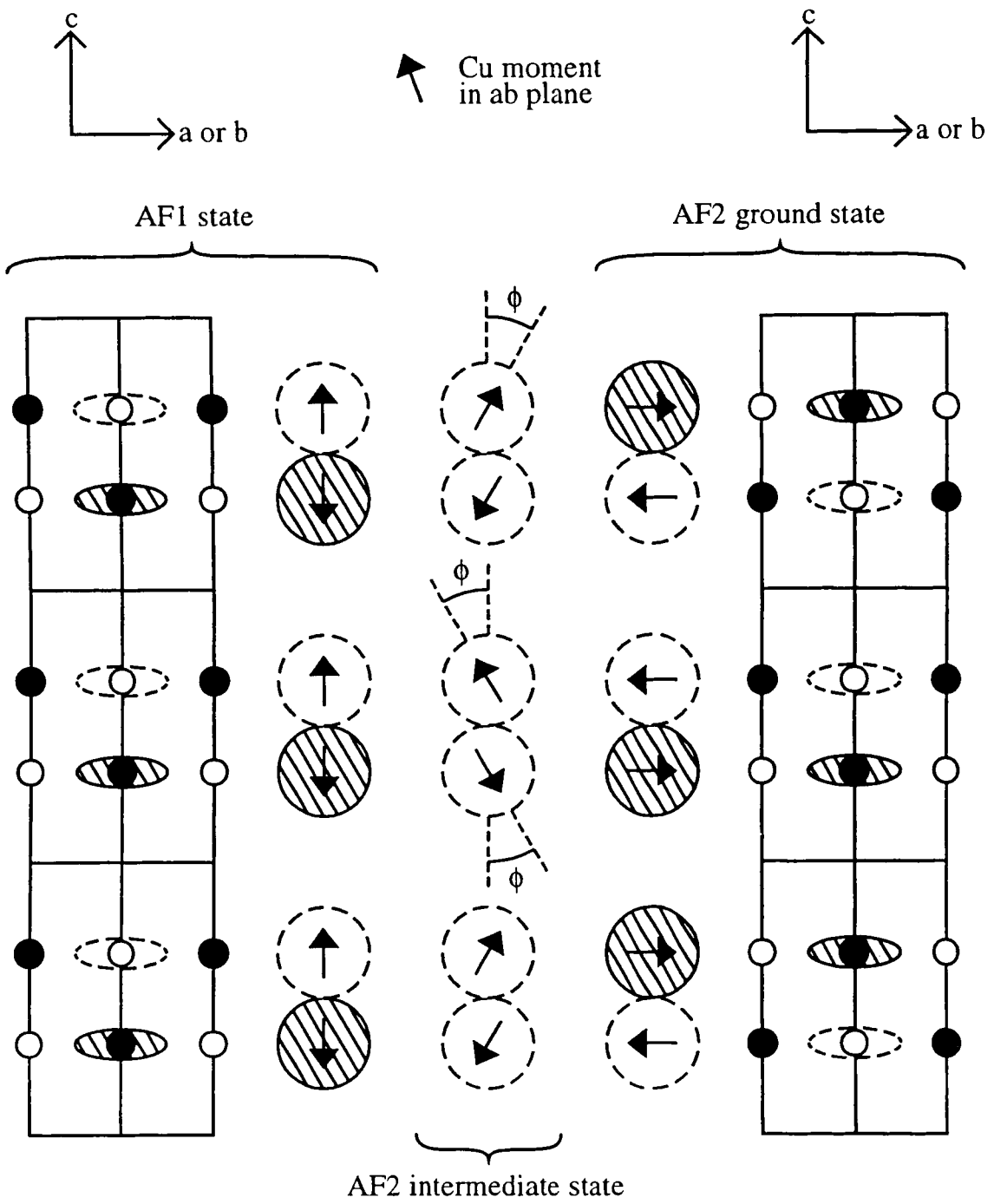

Figure 2.6: Cu AF2 ordering: The moments rotate in the *ab* plane, remaining antiferromagnetic within a unit cell, but ferromagnetic between cells. The copper chain sites may also magnetically order.

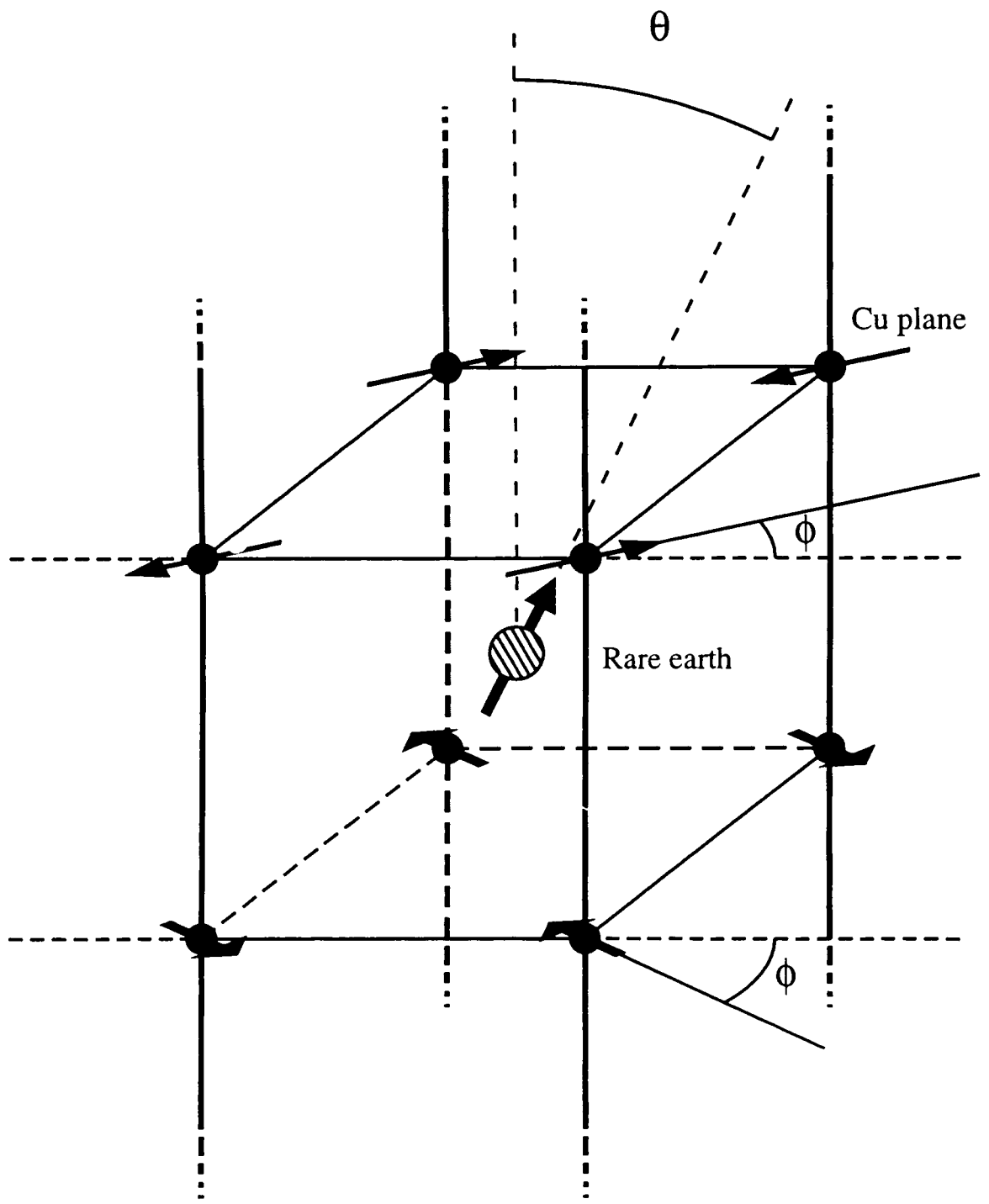

Figure 2.7: AF3 mixed ordering: The Cu plane moments rotate in the *ab* plane, in opposite directions around the rare earth ion. The Cu moments have the same magnitude.

[6] D.W. Cooke, R.S. Kwok, M.S. Jahan, R.L. Lichti, T.R. Adams C. Boekema, W.K. Dawson, A. Kebede, J. Schwegler, J.E. Crow and T. Mihalisin, *Magnetic ordering in* $(Y_{1-x}Pr_x)Ba_2Cu_3O_7$ *as evidenced by muon spin relaxation*, J. Appl. Phys. **67** 9 5061–5063 (1990).

[7] I. Felner, U. Yaron, I. Nowik, E.R. Bauminger, Y. Wolfus, E.R. Yacoby, G. Hilscher and N. Pillmayer, *Magnetic order and superconductivity in* $Y_{1-x}Pr_xBa_2Cu_3O_7$, Phys. Rev. B **40** 10 6739–6744 (1989).

[8] A.P. Reyes, D.E. MacLaughlin, M. Takigawa, P.C. Hammel, R.H. Heffner, J.D. Thompson, J.E. Crow, A. Kebede, T. Mihalisin and J. Schwegler, *Observation of NMR in antiferromagnetic* $PrBa_2Cu_3O_7$ *— evidence for hole band filling*, Phys. Rev. B **42** 4 2688–2691 (1990).

[9] N. Rosov, J.W. Lynn, G. Cao, J.W. O'Reilly, P. Pernambuco-Wise and J.E. Crow, *Magnetic ordering of the* Cu *spins in* $PrBa_2Cu_3O_{6+x}$, Physica C **204** 1–2 171–178 (1992).

[10] W.-H. Li, J.W. Lynn, S. Skanthakumar, T.W. Clinton, A. Kebede, C.-S. Jee, J.E. Crow and T. Mihalisin, *Magnetic order of* Pr *in* $PrBa_2Cu_3O_7$, Phys. Rev. B **40** 7 5300–5303 (1989).

[11] G. Wortmann and I. Felner, *Magnetic order of the* Pr *sublattice in tetragonal and orthorhombic* $Pr_{1-x}Gd_xBa_2Cu3O_{7-\delta}$ *observed by* ^{155}Gd-*Mössbauer spectroscopy*, Solid State Communications **75** 12 981–985 (1990).

[12] A. Kebede, C.-S. Jee, J. Schwegler, J.E. Crow, T. Mihalisin, G.H. Myer, R.E. Saloman, P. Schlottmann, M.V. Kuric, S.H. Bloom and R.P. Guertin, *Magnetic-ordering and superconductivity in* $Y_{1-x}Pr_xBa_2Cu_3O_{7-y}$, Phys. Rev. B **40** 7 4453–4462 (1989).

[13] A.T. Boothroyd, A. Longmore, N.H. Andersen, E. Brecht and T. Wolf, *Novel* Pr-Cu *magnetic phase at low temperature in* $PrBa_2Cu_3O_{6+x}$ *observed by neutron diffraction*, Phys. Rev. Lett. **78** 1 130–133 (1997).

[14] S. Uma, W. Schnelle, E. Gmelin, G. Rangarajan, S. Skanthakumar, J.W. Lynn, R. Walter, T. Lorenz, B. Büchner, E. Walker and A. Erb, *Magnetic ordering in single crystals of* $PrBa_2Cu_3O_{7-\delta}$, J. Phys.: Condens. Matter **10** 2 L33–L39 (1998).

[15] S. Skanthakumar, J.W. Lynn, N. Rosov, G. Cao and J.E. Crow, *Observation of* Pr *magnetic order in* $PrBa_2Cu_3O_7$, Phys. Rev. B **55** 6 R3406–R3409 (1997).

[16] T.W. Clinton, J.W. Lynn, J.Z. Liu, Y.X. Jia, T.J. Goodwin, R.N. Shelton, B.W. Lee, M. Buchgeister, M.B. Maple and J.L. Peng, *Effects of oxygen of the magnetic order of the rare-earth ions in* $RBa_2Cu_3O_{6+\delta}$ $(R = Dy, Er, Nd)$, Phys. Rev. B **51** 21 15429–15447 (1995).

[17] T.W. Clinton, J.W. Lynn, B.W. Lee, M. Buchgeister and M.B. Maple, *Oxygen dependence of the magnetic order of* Nd *in* $NdBa_2Cu_3O_{6+x}$, J. Appl. Phys. **73** 10 6320–6322 (1993).

[18] P. Fischer, B. Schmid, P. Brüesch, F. Stucki and P. Uternährer, *3-dimensional antiferromagnetic ordering in the light rare-earth high-*T_c *superconductor* $NdBa_2Cu_3O_{6.86}$, Z. Phys. B **74** 2 183–189 (1989).

[19] K.N. Yang, J.M. Ferreira, B.W. Lee, M.B. Maple, W.-H. Li, J.W. Lynn and R.W. Erwin, *Antiferromagnetic ordering in superconducting and oxygen deficient nonsuperconducting* $RBa_2Cu_3O_{7-\delta}$ *compounds* (R = Nd *and* Sm), Phys. Rev. B **40** 16 10963–10972 (1989).

[20] N. Senthilkumaran, T. Sarkar, G. Rangarajan, Chen Changkang, J.W. Hodby, M. Spears and B.M. Wanklyn, *Magnetic susceptibilities and crystalline electric field effects in single crystals of* $NdBa_2Cu_3O_{7-\delta}$, Physica B **224** 1–4 565–567 (1996).

[21] J.W. Lynn, W.-H Li, H.A. Mook, B.C. Sales and Z. Fisk, *Nature of the magnetic order of* Cu *in oxygen-deficient* $NdBa_2Cu_3O_{6+x}$, Phys. Rev. Lett. **60** 3 2781–2784 (1988).

[22] A.T. Boothroyd, R–Cu *magnetic coupling in* $RBa_2Cu_3O_{6+x}$ *with particular reference to* $PrBa_2Cu_3O_{6+x}$, Physica B **241–243** 792–794 (1998).

Chapter 3

Elastic Neutron Scattering Theory

3.1 Introduction

To measure the magnetic structure of $NdBa_2Cu_3O_{6+\delta}$, I have used elastic neutron scattering with a triple axis spectrometer.

Elastic neutron scattering means that neutrons are Bragg scattered from the sample with no change in energy. Neutrons interact with nuclei via the strong nuclear force and (more weakly) with magnetic fields from unpaired electrons.

A triple axis spectrometer can give information about the nuclear and magnetic structure of the sample, though the normalization for the magnetic case is not straightforward.

This chapter will outline the theory of magnetic elastic neutron scattering and the use of a triple axis spectrometer. In particular the corrections necessary for the analysis of data due to instrumental effects will be detailed.

3.2 The triple axis spectrometer

Figure 3.1 shows a schematic diagram of a triple axis spectrometer. Neutrons enter from the reactor and strike the monochromator crystal, which selects a single wavelength. The

mosaicity of this crystal affects the resolution of the instrument.

The neutron beam impinges on the sample which can be rotated by an angle ω, which controls the angular position of the scattering vector in reciprocal space. The parameter $2\theta_s$ is controlled by the position of the analyzer, which gives the radial position of the scattering vector in reciprocal space.

The analyzer again selects a particular wavelength, and the neutrons are picked up at the detector. Like the monochromator, the mosaicity of this crystal will affect the spectrometer resolution. The analyzer also helps to reduce the background.

At various points in the instrument collimators select the neutrons to define the resolution and cut down on background noise.

3.3 Intensities of nuclear Bragg peaks

Although this thesis is concerned with the magnetic scattering, the nuclear scattering is also important for a number of reasons, even though a triple axis spectrometer is not an ideal way of measuring nuclear scattering.

Firstly, as the magnetic scattering is much weaker than the nuclear scattering, the nuclear scattering is used to align the crystal and check the functioning of the instrument.

Secondly, the most straightforward way of normalizing the magnetic scattering to give absolute magnetic moments is to compare the intensities of the magnetic scattering peaks with the nuclear peaks. Theoretically, the absolute magnetic scattering could be calculated from first principles assuming that the intensity of the beam and the size of the crystals are known. However, with difficulties in aligning the crystal and calibrating the instrument, this would introduce another large error. It is easier and more accurate to compare the intensities. Section 3.7 details the relationship between the intensities.

This comparison of course requires the theoretical intensities of the nuclear peaks to be known.

The absolute intensity of a Bragg peak from nuclear scattering is given in terms of a sum over all the nuclei in the unit cell (see Chapter 2 Ref. [3]):

$$I_{\mathrm{nuc}}(\boldsymbol{\kappa}) \quad = \quad k_{\mathrm{nuc}} \left\langle |F_N(\boldsymbol{\kappa})|^2 \right\rangle , \tag{3.1}$$

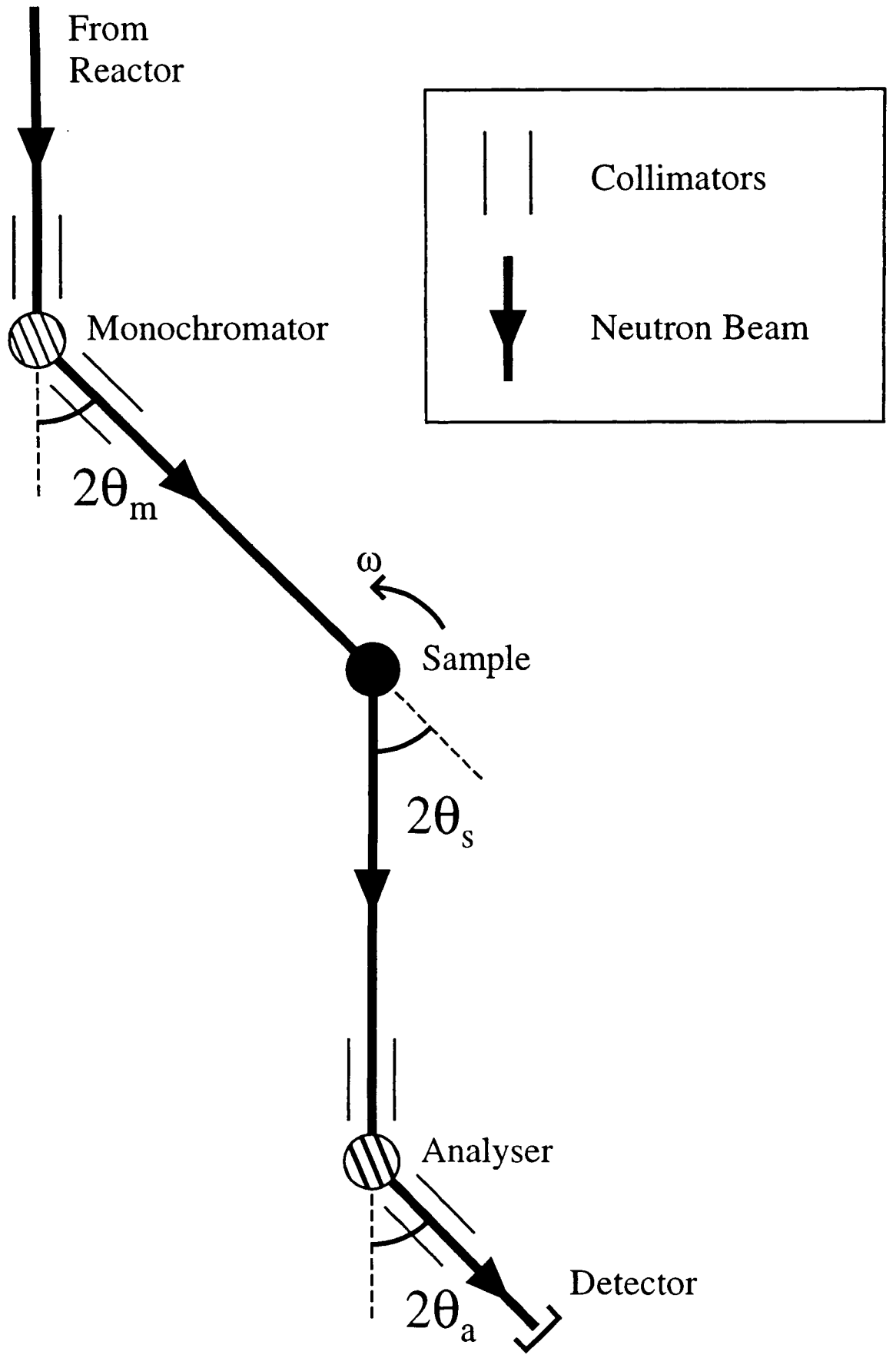

Figure 3.1: A schematic diagram of a triple axis spectrometer.

$$F_N(\boldsymbol{\kappa}) = \sum_{j=1}^{n} b_j e^{\mathrm{i}\boldsymbol{\kappa}\cdot\mathbf{r}_j} e^{-W_j(\boldsymbol{\kappa})}, \tag{3.2}$$

where j indexes the n nuclei in the nuclear unit cell,

$\boldsymbol{\kappa}$ is the scattering vector,

k_{nuc} is a constant,

b_j is the scattering length for nuclei j,

$\mathbf{r}_j$ is the position in the unit cell of nuclei j and

$W_j(\boldsymbol{\kappa})$ is the Debye-Waller factor.

The normalization of this to the measured intensity is explained in Section 3.7.

3.4 Magnetic scattering

The magnetic interaction is more complex, and it can be shown [1] that the scattering formula becomes

$$I_{\mathrm{mag}}(\boldsymbol{\kappa}) = k_{\mathrm{mag}} \sum_{\alpha,\beta} \left\langle (\delta_{\alpha\beta} - \hat{\kappa}_\alpha \hat{\kappa}_\beta) F^\alpha(\boldsymbol{\kappa}) F^{\beta^*}(\boldsymbol{\kappa}) \right\rangle, \tag{3.3}$$

where $\boldsymbol{\kappa}$ is the scattering vector,

k_{mag} is a constant,

α, β index the axes x, y, z,

$\langle\rangle$ represent a domain average,

$\delta_{\alpha\beta}$ is the Kronecker delta,

$\hat{\kappa}_\alpha$ is the α component of the unit vector $\hat{\boldsymbol{\kappa}}$

and $F^\alpha(\boldsymbol{\kappa})$, the structure factor, becomes

$$F^\alpha(\boldsymbol{\kappa}) = \sum_j \mu_j^\alpha f_j(\boldsymbol{\kappa}) \exp(\mathrm{i}\boldsymbol{\kappa}.\mathbf{r}_j), \tag{3.4}$$

where j indexes the magnetic moments in the magnetic unit cell,

μ_j^α is the α component of moment j,

$f_j(\kappa)$ is the magnetic form factor of moment j and

$\mathbf{r}_j$ is the position of moment j.

3.5 Cu form factor

The magnetic form factor for the copper ions, depends on the details of the electron orbital.

I assume a form for the copper ions that has been used previously (see Chapter 2 Ref. [3]). This assumes that the copper ions are Cu^{2+} with a $3d^9$ electronic configuration.

To be able to calculate the matrix elements of the form factor for the Cu ion I expand them to:

$$f_{mm'}(\kappa) = \sqrt{4\pi} \sum_{n=0,2,4\ldots}^{\infty} \sqrt{2n+1}\, \mathrm{i}^n C^n(lm, lm') \langle j_n(\kappa) \rangle \Phi_{m-m'}(\gamma) \Theta_n^{m-m'}(\cos\beta). \quad (3.5)$$

For the pure $(x^2 - y^2)$ orbital the full form factor becomes [2]

$$f(\kappa) = \langle j_0(\kappa) \rangle - \frac{5}{7}(1 - 3\cos^2\beta)\langle j_2(\kappa) \rangle + \frac{9}{56}\left(1 - 10\cos^2\beta + \frac{35}{3}\cos^4\beta\right)\langle j_4(\kappa) \rangle. \quad (3.6)$$

The expectation values of the Bessel functions $\langle j_n \rangle$ can be approximated as

$$\langle j_0(s) \rangle = A\exp(-as^2) + B\exp(-bs^2) + C\exp(-cs^2) + D, \quad (3.7)$$

$$\langle j_{n>0}(s) \rangle = (A\exp(-as^2) + B\exp(-bs^2) + C\exp(-cs^2) + D)s^2, \quad (3.8)$$

where $s = \kappa/4\pi$ and the coefficients for copper [3] are given in Table 3.1.

n	A	a	B	b	C	c	D
0	0.0232	34.969	0.4023	11.564	0.5882	3.843	-0.0137
2	1.5189	10.478	1.1512	3.813	0.2918	1.398	0.0017
4	-0.3914	14.740	0.1275	3.384	0.2548	1.255	0.0103

Table 3.1: Coefficients for the Cu form factor

An empirical adjustment can be made to the form factor to represent an expansion

or contraction of the wavefunction due to the surrounding ions. If the wavefunction has expanded by a factor of $(1+\alpha)$ it can be shown (see Chapter 2 Ref. [3]) that the resulting form faction $f'(\kappa)$ is given by

$$f'(\kappa) = f\left(\kappa(1+\alpha)\right). \tag{3.9}$$

3.6 Nd form factor

Similarly, I also approximate the Nd form factor. I assume a Nd^{3+} state with a $4f^3$ electronic configuration.

Using the dipole approximation [4], for a spherically symmetric form factor we get

$$f(\kappa) = \langle j_0(\kappa)\rangle + \frac{g_L}{g_J}\langle j_2(\kappa)\rangle, \tag{3.10}$$

$$= \langle j_0(\kappa)\rangle + \frac{2-g_J}{g_J}\langle j_2(\kappa)\rangle, \tag{3.11}$$

where

$$g_L = \frac{J(J+1)-S(S+1)+L(L+1)}{2J(J+1)}, \tag{3.12}$$

$$g_J = \frac{3J(J+1)+S(S+1)-L(L+1)}{2J(J+1)}. \tag{3.13}$$

For the Nd^{3+} ion, $g_J = 8/11$.

As with the Cu form factor, the expectation values of the Bessel functions can be approximated by Equations 3.7 and 3.8, with the coefficients given in Table 3.2.

n	A	a	B	b	C	c	D
0	0.0540	25.029	0.3101	12.102	0.6576	4.722	-0.0216
2	0.6751	18.342	1.6272	7.260	0.9644	3.602	0.0150

Table 3.2: Coefficients for the Nd form factor

3.7 Normalization of magnetic peak intensities

To be able to normalize the magnetic scattering to absolute magnetic moments, the ratio of the magnetic scattering to the nuclear scattering needs to be known.

The differential cross-section at a direction given by θ, ϕ is defined as

$$\frac{\mathrm{d}\sigma}{\mathrm{d}\Omega} = \frac{\mathrm{d}R}{\Phi \mathrm{d}\Omega}, \tag{3.14}$$

where $\mathrm{d}R$ is the number of neutrons scattered into $\mathrm{d}\Omega$ in unit time,

Φ is the number of neutrons incident on the sample per unit time per unit area perpendicular to the beam, and

$\mathrm{d}\Omega$ is the solid angle element in the direction θ, ϕ.

The elastic differential cross sections can be written as (see Chapter 2 Ref. [3]):

$$\left(\frac{\mathrm{d}\sigma}{\mathrm{d}\Omega}\right)_{\mathrm{nuc}} = N\frac{(2\pi)^3}{\nu_0}\left\langle |F_N(\boldsymbol{\kappa})|^2 \right\rangle, \tag{3.15}$$

$$F_N(\boldsymbol{\kappa}) = \sum_{j=1}^{n} b_j e^{\mathrm{i}\boldsymbol{\kappa}\cdot\mathbf{r}_j} e^{-W_j(\boldsymbol{\kappa})}, \tag{3.16}$$

$$\left(\frac{\mathrm{d}\sigma}{\mathrm{d}\Omega}\right)_{\mathrm{mag}} = \frac{N}{8}\frac{(2\pi)^3}{8\nu_0}\left(\frac{\gamma r_0}{2}\right)^2 \sum_{\alpha,\beta}\left\langle (\delta_{\alpha\beta} - \hat{\kappa}_\alpha\hat{\kappa}_\beta) F^\alpha(\boldsymbol{\kappa}) F^{\beta^*}(\boldsymbol{\kappa}) \right\rangle, \tag{3.17}$$

$$F^\alpha(\boldsymbol{\kappa}) = \sum_j \mu_j^\alpha f_j(\boldsymbol{\kappa}) \exp(\mathrm{i}\boldsymbol{\kappa}.\mathbf{r}_j), \tag{3.18}$$

where γ is the gyromagnetic ratio ($= 1.913$),

r_0 is the classical electron radius ($= 2.818$ fm)

N is the number of unit cells in the sample and

ν_0 is the volume of each of the crystallographic unit cells.

The observed intensities are proportional to the differential cross section, so the ratio of the nuclear and magnetic cross sections should be equal to the ratio of the nuclear and magnetic intensities.

Many of the magnetic structures considered in this thesis are antiferromagnetic and have a periodicity of two cells in two or three of the orthogonal axes. Thus, I have expressed Equation 3.17 for the case of a magnetic unit cell which is $2 \times 2 \times 2$ crystallographic unit cells. This is why N is divided by 8 and ν_0 is multiplied by 8.

By taking the ratio of the cross sections and the intensities and simplifying, the relationship between the constants of proportionality, k_{nuc} and k_{mag} is

$$\frac{k_{\text{mag}}}{k_{\text{nuc}}} = \left(\frac{\gamma r_o}{16}\right)^2 = 0.1135. \tag{3.19}$$

3.8 The Lorentz factor and spectrometer resolution

This thesis is concerned with the absolute values of the ordered moments in the samples. To be able to normalize the intensities, the resolution of the spectrometer must be modelled.

Most of the measurements in this thesis were performed by scanning across the Bragg peaks to obtain the area of the peaks, as this helps to avoid systematic errors due to misalignment of the sample. Thus the way the widths of the peaks are affected by the instrument is crucial if the intensities are to be normalized.

Most of the following sections describing the corrections for resolution effects summarize the approach described in more detail in Chapter 2 Ref. [3].

3.8.1 Terminology

For reference, the notation used in this section is described in Table 3.3.

3.8.2 The geometric Lorentz factor

Firstly, the measured area of a peaks is affected by an intrinsic property of the way a triple-axis spectrometer functions: the angle at which the Ewald sphere cuts the Bragg peak.

The Ewald sphere is defined by the locus of points $\boldsymbol{\kappa} = \boldsymbol{k}_f - \boldsymbol{k}_i$, where $\boldsymbol{k}_i$ and $\boldsymbol{k}_f$ are the initial and final neutron wavevectors respectively. Figure 3.2 illustrates this in the k-space of the spectrometer.

The technique used for most of the measurements in this thesis consists of scanning $\boldsymbol{\kappa}$ (the wavevector transfer) across a Bragg peak at position $\boldsymbol{\tau}$. This is illustrated in Figure 3.3. The angle α, the angle of the scan relative to the nominal position, is measured from the nominal position, and so is negative in this diagram, with the x and y axes as shown.

As the crystal is rotated (ω is changed) and the analyzer is moved to change θ_s, then $\boldsymbol{k}_i$

Symbol	Meaning
$\mathbf{k}_i$	The incident wavevector
$\mathbf{k}_i$	The scattered wavevector
α_j	The horizontal collimation angle, where
	$j = 0$ In-pile region
	$j = 1$ Monochromator to sample
	$j = 2$ Sample to analyzer
	$j = 3$ Analyzer to detector
η_m	Horizontal mosaic spread of monochromator
η_a	Horizontal mosaic spread of analyzer
η_s	Mosaic spread of sample
$\boldsymbol{\kappa}$	$\mathbf{k}_f - \mathbf{k}_i$ (wavevector transfer)
$\boldsymbol{\tau}$	Bragg peak position
$2\theta_m$	Monochromator angle
$2\theta_s$	Sample angle
$2\theta_a$	Analyzer angle
$\boldsymbol{\kappa}_0$	Nominal spectrometer position in reciprocal space
L	Lorentz factor
α	Angle between scan direction and $\boldsymbol{\kappa}_0$

Table 3.3: Elastic neutron scattering theory terminology

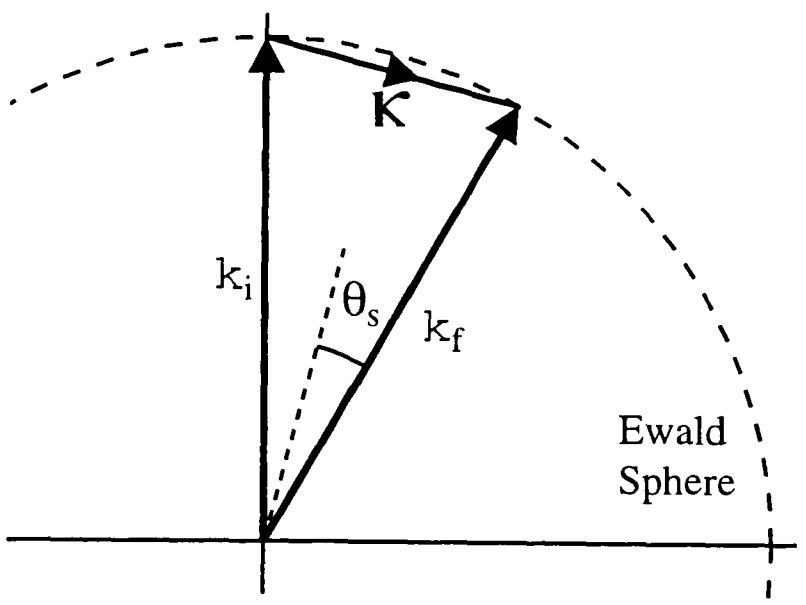

Figure 3.2: The Ewald sphere

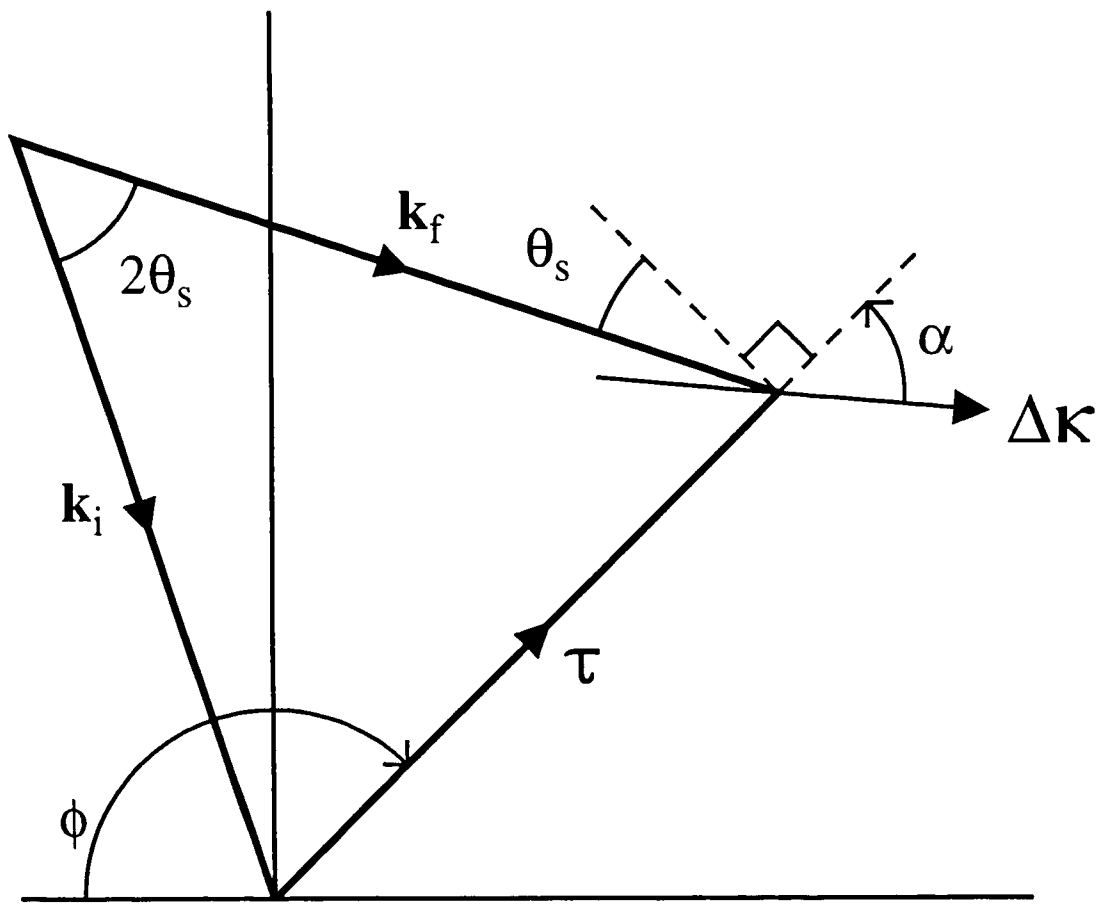

Figure 3.3: The geometry of a Bragg scan in reciprocal space

and $\boldsymbol{k}_f$ rotate in the reciprocal space of the crystal. For elastic scattering $|\boldsymbol{k}_i| = |\boldsymbol{k}_f| = k$ where k is usually constant.

As $\boldsymbol{k}_i$ is fixed in the k-space of the spectrometer, then (in the reciprocal space of the crystal) the direction of $\boldsymbol{k}_i$ is given by ω, the rotation of the crystal (with a suitable zero point). As shown in Figure 3.3, the angle between $\boldsymbol{\tau}$ and $\boldsymbol{k}_i$ is $\pi + \theta_s$. Thus, we have

$$\omega = \phi \pm \theta_s + C, \tag{3.20}$$

where C is a constant dependent on the geometry and where the zero point of ω is defined and the plus or minus is dependent on the direction that θ_s is measured in.

As the scan is performed, the Ewald sphere passes over the Bragg point $\boldsymbol{\tau}$. Figure 3.4 illustrates this.

The wavevector transfer $\boldsymbol{\kappa}$ follows the path $\Delta\boldsymbol{\kappa}$. The normal to the Ewald sphere at the point $\boldsymbol{\kappa}$ is parallel to $\boldsymbol{k}_f$. During the scan, more neutrons in total will be scattered if the Ewald sphere passes over $\boldsymbol{\tau}$ obliquely.

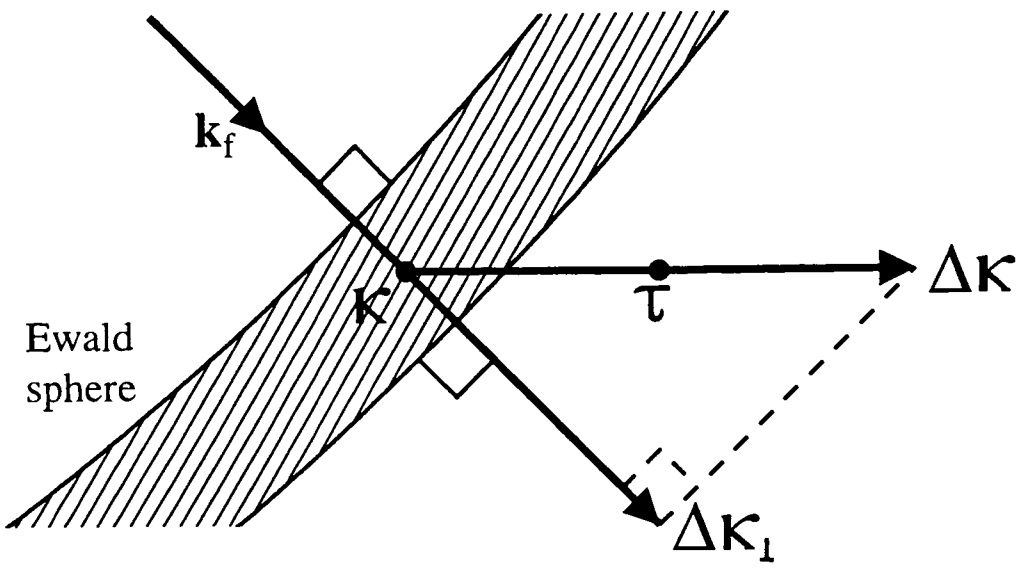

Figure 3.4: The geometric Lorentz factor: the number of neutrons scattered depends on the direction in which the Ewald sphere (illustrated as a shell) crosses the Bragg point

To correct for this, we define the Lorentz factor L which is the ratio of the measured area of the peak A (i.e. the area of the scattering intensity plotted against the position of the scan in reciprocal space) to the peak's intrinsic intensity I. The intrinsic intensity is given in Sections 3.3–3.6. In this thesis A is usually measured in the units *count rate*.Å^{-1}.

The way that the sphere cuts the peak will not affect the peak height, but the width will be inversely proportional to the projection of $\Delta\boldsymbol{\kappa}$ in the direction of $\boldsymbol{k}_f$ (i.e. perpendicular to the Ewald sphere surface).

For ease, working with L^{-1},

$$L^{-1} = \frac{I}{A}, \tag{3.21}$$

and defining α as the angle between $\Delta\boldsymbol{\kappa}$ and $\boldsymbol{\tau}$,

$$\begin{aligned} L^{-1} &= \Delta\hat{\boldsymbol{\kappa}}_\perp \\ &= \Delta\hat{\boldsymbol{\kappa}} \cdot \hat{\boldsymbol{k}}_f \\ &= \left|\cos(\pi - (\theta_s + \frac{\pi}{2} + \alpha))\right| \qquad (3.22) \\ &= \left|\sin(\theta_s + \alpha)\right|. \qquad (3.23) \end{aligned}$$

This is referred to as the geometric Lorentz factor, and forms the basis for the following corrections to the Lorentz factor.

As a special case, for an ω scan in which the sample is rotated, but the spectrometer is fixed, the geometric Lorentz factor can be simplified further. $\Delta\boldsymbol{\kappa}$ for this scan is perpendicular to $\boldsymbol{\tau}$ so $\alpha = \pi/2$. For this type of scan, the width of the peak is commonly measured in terms of the angular rotation (as is the case in this thesis). Thus A has the units of *count rate.degrees.*

Thus, as $\Delta\boldsymbol{\kappa} = \kappa\Delta\omega = 2k\Delta\omega\sin\theta_s$ the geometric Lorentz factor becomes

$$L_\omega^{-1} = \cos\theta_s 2k\sin\theta_s, \tag{3.24}$$

$$= k\sin 2\theta_s. \tag{3.25}$$

3.8.3 Spectrometer resolution

As well as the geometric Lorentz factor, the measured area of the peak is affected by the resolution of the spectrometer.

We approximate the resolution of the spectrometer by an ellipsoid in reciprocal space.

The full derivation of the effect of the resolution was made by M.J. Cooper and R. Nathans [5], with corrections by N.J. Chesser and J.D. Axe [6].

I define $\mathbf{q}$ as the displacement in reciprocal space from the nominal spectrometer position $\boldsymbol{\kappa}_0$. The q_x axis is defined to be parallel to $\boldsymbol{\kappa}_0$ for convenience.

The resolution ellipsoid is the locus of points in reciprocal space where the transmission of the spectrometer has fallen to half of the value at the nominal spectrometer position. Figure 3.5 illustrates the resolution ellipsoid.

The resolution function can be represented as:

$$R(\mathbf{q}) = N\exp\left[-\frac{1}{2}M_{11}q_x^2 - M_{12}q_xq_y - \frac{1}{2}M_{22}q_y^2\right], \tag{3.26}$$

which is simply a two-dimensional Gaussian ellipsoid, with N as a normalization.

Thus the M_{ij} define the shape of the ellipsoid.

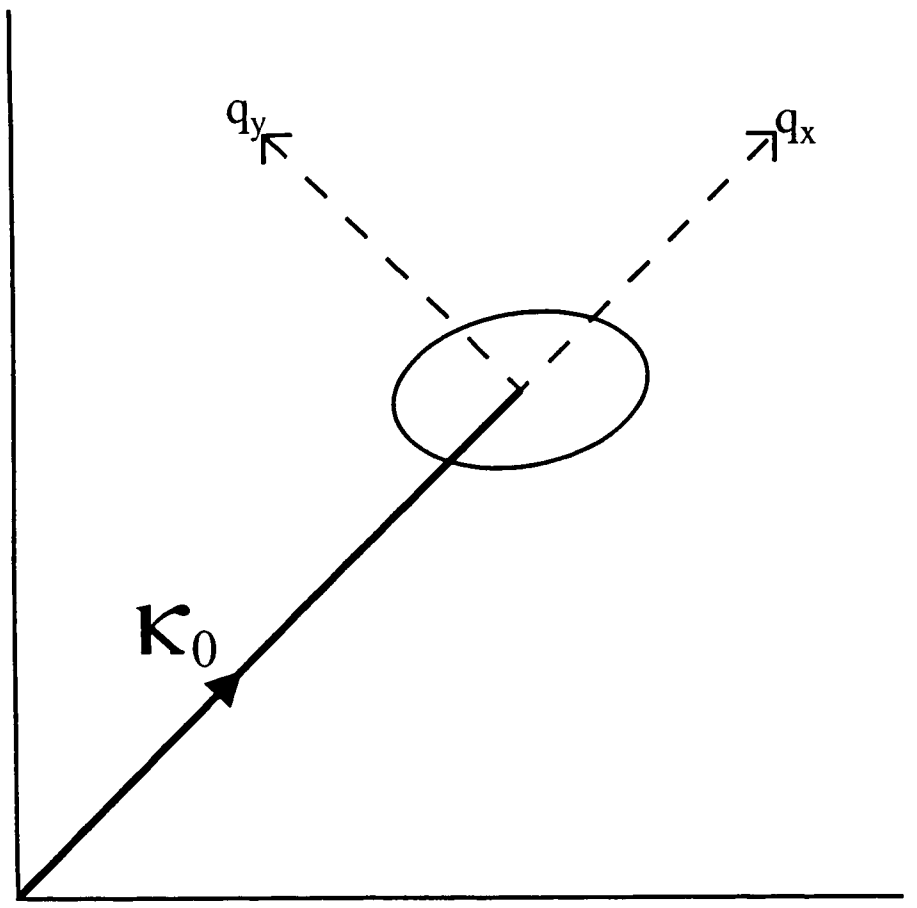

Figure 3.5: The resolution ellipsoid

To calculate the ellipsoid, Cooper and Nathans [5] define a_j parameters as:

$$\begin{aligned}
a_1 &= \frac{\tan\theta_m}{\eta_m k_i} & a_2 &= \frac{1}{\eta_m k_i} & a_3 &= \frac{1}{\alpha_1 k_i} \\
a_4 &= \frac{1}{\alpha_2 k_f} & a_5 &= \frac{\tan\theta_a}{\eta_a k_f} & a_6 &= \frac{-1}{\eta_a k_f} \\
a_7 &= \frac{2\tan\theta_m}{\alpha_0 k_i} & a_8 &= \frac{1}{\alpha_0 k_i} & a_9 &= \frac{2\tan\theta_a}{\alpha_3 k_f} \\
& & a_{10} &= \frac{-1}{\alpha_3 k_f}
\end{aligned} \tag{3.27}$$

and b_j parameters as:

$$\begin{aligned}
b_0 &= a_1 a_2 + a_7 a_8 \\
b_1 &= {a_2}^2 + {a_3}^2 + {a_8}^2 \\
b_2 &= {a_4}^2 + {a_6}^2 + {a_{10}}^2 \\
b_3 &= {a_5}^2 + {a_9}^2 \\
b_4 &= a_5 a_6 + a_9 a_{10} \\
b_5 &= {a_1}^2 + {a_7}^2 .
\end{aligned} \tag{3.28}$$

For elastic scattering, the matrix elements of the resolution function can be written as:

$$M_{11} = \frac{B_{11}}{4A' \cos^2 \theta_s}, \tag{3.29}$$

$$M_{12} = \frac{B_{12}}{4A' \cos \theta_s \sin \theta_s}, \tag{3.30}$$

$$M_{22} = \frac{B_{22}}{4A' \sin^2 \theta_s}, \tag{3.31}$$

where

$$\begin{aligned} A' &= (b_1 + b_2) \tan^2 \theta_s + 2(b_4 - b_0) \tan \theta_s + b_3 + b_5, \\ B_{11} &= (b_1 + b_2)(b_3 + b_5) - (b_4 - b_0)^2, \\ B_{12} &= 2(b_1 b_4 + b_0 b_2) \tan \theta_s + b_4^2 - b_0^2 + (b_1 - b_2)(b_3 + b_5), \\ B_{22} &= 4 b_1 b_2 \tan^2 \theta_s + 4(b_1 b_4 - b_0 b_2) \tan \theta_s + \\ &\quad (b_1 + b_2)(b_3 + b_5) - (b_4 + b_0)^2. \end{aligned} \tag{3.32}$$

The normalization N can be written as

$$N = \frac{C}{\sqrt{A'} \sin 2\theta_s}. \tag{3.33}$$

In the case of an open detector (i.e. all scattered neutrons are measured) we have $\alpha_2 = \alpha_3 = \eta_a = \infty$, thus $b_2 = b_3 = b_4 = 0$ and $B_{11} = B_{12} = B_{22} = B_0$ where

$$B_0 = b_1 b_5 - b_0^2. \tag{3.34}$$

This B_0 term is used in the normalization of the Lorentz factor including the spectrometer resolution.

For elastic scattering, $k_i = k_f$ and thus, as all the a_j values are proportional to k_i^{-1}, all the b_j values are proportional to ${k_i}^2$, the B_{ij} are proportional to ${k_i}^4$ and A' is proportional to ${k_i}^2$. Thus k_i can be removed from the calculation until the end.

Another value z may be defined as the ratio of the measured peak height to the intrinsic intensity and is given by

$$z = \frac{1}{N} \sqrt{\frac{2\pi}{B_0}}. \tag{3.35}$$

The value z is useful for correcting the measured intensity for the cases where a full scan

across the peak is not available. In this thesis this is often the case for temperature scans, where taking a full scan for each temperature would be prohibitively time consuming. The ratio of the Lorentz factor to z also immediately gives the width of a scan.

3.8.4 Lorentz factor including spectrometer resolution

As shown in equation 3.26, the resolution can be represented as an ellipsoid in reciprocal space. The matrix elements specify the shape of this ellipsoid.

The Lorentz factor (as defined by Equation 3.21 in Section 3.8.2) can be modified to include the effects of the spectrometer resolution. The Lorentz factor needs to be modified by the width of the ellipsoid in the direction of the scan, and the overall normalization factor N.

The corrected Lorentz factor becomes:

$$L^{-1} = \frac{1}{N'\sqrt{B_0}} \left(M_{11}\cos^2\alpha + 2M_{12}\cos\alpha\sin\alpha + M_{22}\sin^2\alpha\right)^{\frac{1}{2}}, \tag{3.36}$$

$$= \frac{\sin\theta_s\cos\theta_s}{\sqrt{B_0}} \left(\frac{\cos^2\alpha}{\cos^2\theta_s}B_{11} + \frac{2\cos\alpha\sin\alpha}{\cos\theta_s\sin\theta_s}B_{12} + \frac{\sin^2\alpha}{\sin^2\theta_s}B_{22}\right)^{\frac{1}{2}}. \tag{3.37}$$

3.8.5 Including sample mosaicity

Although not truly a resolution effect, sample mosaicity can also be included in the Lorentz factor, as it will broaden the peaks in a similar way.

To a good approximation, the mosaicity can be regarded as a spread in the sample angle, ω. This will appear as another error in the angle, and can be treated as a resolution limiting effect.

Thus, the mosaicity will cause the peaks to be spread tangentially to τ. For most samples, the sample mosaicity η_s is sufficiently small that the broadening at any peak can be considered to be linear in reciprocal space, rather than an arc.

The distance of this spread in reciprocal space is simply $\eta_s\tau$, assuming that the mosaicity is sufficiently small that the curvature is not significant.

As a measure of the mosaic broadening at a peak I define m as

$$m = \frac{1}{(\eta_s \tau)^2}. \tag{3.38}$$

In the transverse direction, where the broadening occurs, the peak height is decreased, but the total area of the peak will be unchanged; the intensity has simply been spread out.

For a longitudinal scan however, as the peak height has decreased without a corresponding increase in the width, so the area will be smaller.

It can be shown (see Chapter 2 Ref. [3]) that the matrix elements and the overall normalization are thus modified:

$$N \rightarrow \frac{N}{(1 + M_{22}/m)^{\frac{1}{2}}}, \tag{3.39}$$

$$M_{11} \rightarrow M_{11} - \frac{{M_{12}}^2}{M_{22} + m}, \tag{3.40}$$

$$M_{12} \rightarrow \frac{M_{12}}{1 + M_{22}/m}, \tag{3.41}$$

$$M_{22} \rightarrow \frac{M_{22}}{1 + M_{22}/m}. \tag{3.42}$$

Thus by applying these transformations and simplifying by removing the common factor $\sqrt{1 + M_{22}/m}$, L^{-1} transforms to

$$L^{-1} = \frac{1}{N'\sqrt{B_0}} \left(\left(M_{11} + \frac{M_{11}M_{22} - M_{12}^2}{m} \right) \cos^2 \alpha + 2M_{12} \cos \alpha \sin \alpha + M_{22} \sin^2 \alpha \right)^{\frac{1}{2}}. \tag{3.43}$$

Similarly, due to the decrease of the peak height, the value of z (the peak height to measured intensity ratio) must be modified to:

$$z = \frac{1}{N} \sqrt{\frac{2\pi(1 + M_{22}/m)}{B_0}}. \tag{3.44}$$

As well as the mosaicity, the crystal can be broken into multiple parts. This can lead to a more complex spread of the peak. For instance, the Bragg peak may appear as a double peak. For the crystals measured in this thesis, I assume that this is sufficiently small that the spread can be modelled adequately by a Gaussian.

3.8.6 Widths of the peaks

To compare with the observed widths, it is useful to calculate the widths of the peaks from the resolution effects.

For a linear scan in reciprocal space at an angle α from q_x, we can substitute $q_x = q' \cos\alpha$ and $q_y = q' \sin\alpha$ into the definition of the resolution ellipsoid in equation 3.26 to get

$$R = N \exp\left[-\frac{1}{2}\left(M_{11}\cos^2\alpha + 2M_{12}\cos\alpha\sin\alpha + M_{22}\sin^2\alpha\right) q'\right]. \tag{3.45}$$

Thus, the full width at half maximum for this scan is:

$$\text{FWHM} = 2\sqrt{2\ln 2}\left(M_{11}\cos^2\alpha + 2M_{12}\cos\alpha\sin\alpha + M_{22}\sin^2\alpha\right)^{-\frac{1}{2}}. \tag{3.46}$$

As an alternative, the width can also be obtained by taking the ratio of the Lorentz factor to z.

3.9 The Bragg rod

If magnetic ordering occurs in two directions but not in the third, then instead of Bragg peaks, Bragg rods occur. These are ridges of scattering, forming a line in reciprocal space.

In the types of crystals studied here, two-dimensional ordering has been observed with the rare earth ion ordering in the a and b directions, but not in the c direction.

For the Bragg rod, the peak intensity is spread over a distance equal to the separation of the Bragg peaks in reciprocal space.

For the case of ordering in the ab plane, this distance is given by

$$c^* = \frac{2\pi}{c}. \tag{3.47}$$

The intensity is calculated in the same way (though possibly with a different size of magnetic unit cell), but intensity is seen in a line rather than just at the peaks, and the normalization is modified by a factor of $c/(2\pi)$.

Again, we use the definition of the resolution ellipsoid in Equation 3.26.

The Lorentz factor becomes clear if the axes q_x and q_y are rotated as shown in Figure 3.6.

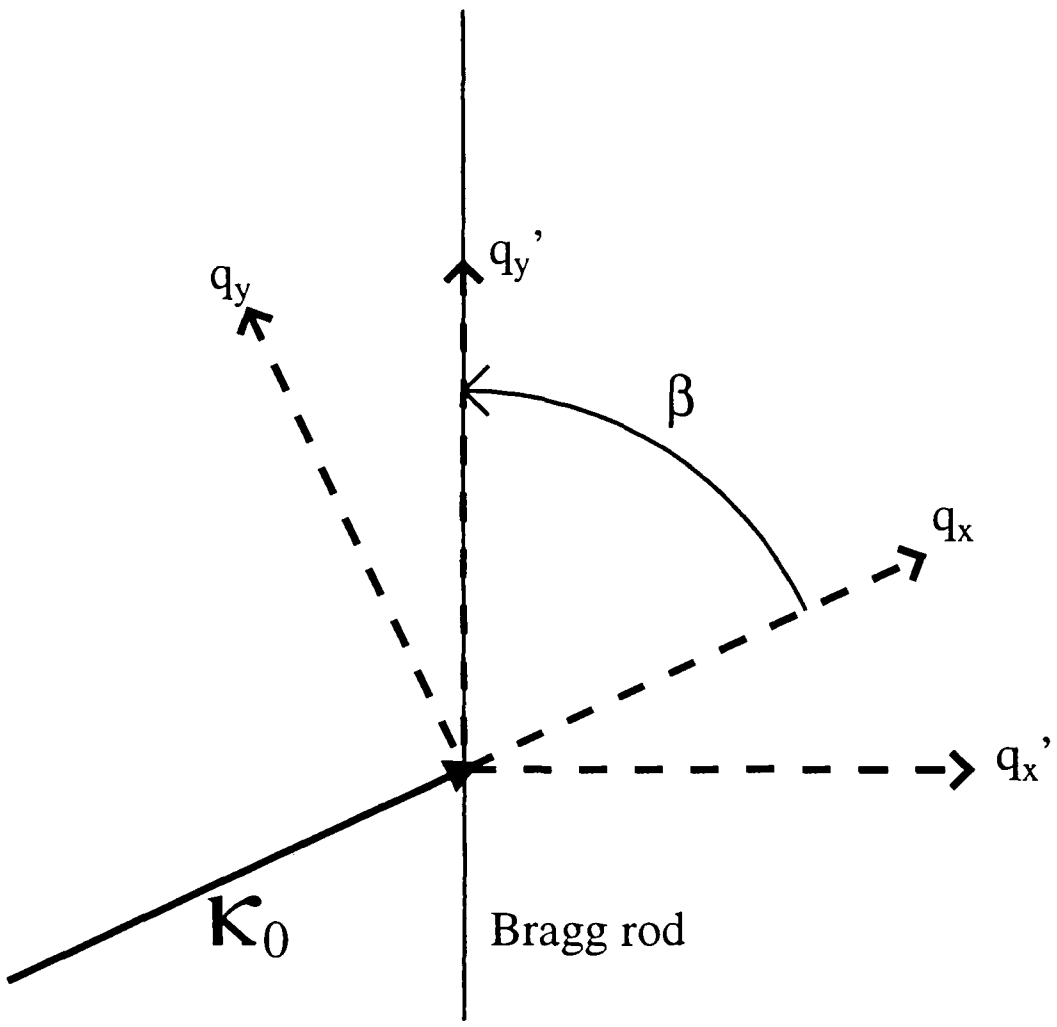

Figure 3.6: The rotation of coordinates for the Bragg rod

Thus the matrix elements are transformed as:

$$M'_{11} = M_{11}\sin^2\beta + M_{22}\cos^2\beta - 2M_{12}\sin\beta\cos\beta \tag{3.48}$$

$$M'_{12} = M'_{21} = (M_{11} - M_{22})\cos\beta\sin\beta + M_{12}(\sin^2\beta - \cos^2\beta) \tag{3.49}$$

$$M'_{22} = M_{11}\cos^2\beta + M_{22}\sin^2\beta + 2M_{12}\sin\beta\cos\beta. \tag{3.50}$$

Rotating α so that

$$\alpha' = \left(\frac{\pi}{2} - \beta\right) + \alpha, \tag{3.51}$$

we end up with a Lorentz factor of

$$L^{-1} = \frac{c^*\cos\alpha'}{N}\sqrt{\frac{M_{11}M_{22} - {M_{12}}^2}{2\pi B_0}}, \tag{3.52}$$

and the intensity at the top of the ridge is normalized by

$$z = \frac{c^*}{N}\sqrt{\frac{{M_{22}}'}{B_0}}. \tag{3.53}$$

Note that as expected when $\alpha' = \pi/2$ then $L^{-1} = 0$ which corresponds to measuring along the rod. In this case the measured area becomes infinite.

To include the effects of sample mosaicity, the mosaicity can be again considered to be a spectrometer effect, so applying the transformations in Equations 3.39–3.42 we get:

$$\begin{aligned} L^{-1} &= \frac{c^* \cos\alpha'}{\sqrt{2\pi B_0}} \frac{(1 + M_{22}/m)^{\frac{1}{2}}}{N} \\ &\quad \times \left[\left(M_{11} - \frac{{M_{12}}^2}{M_{22} + m} \right) \left(\frac{M_{22}}{1 + M_{22}/m} \right) \right. \\ &\quad \left. - \left(\frac{M_{12}}{1 + M_{22}/m} \right)^2 \right]^{\frac{1}{2}}, \end{aligned} \tag{3.54}$$

and

$$\begin{aligned} z &= \frac{c^*}{\sqrt{B_0}} \frac{(1 + M_{22}/m)^{\frac{1}{2}}}{N} \\ &\quad \times \left[\left(M_{11} - \frac{{M_{12}}^2}{M_{22} + m} \right) \cos^2\beta + \left(\frac{M_{22}}{1 + M_{22}/m} \right) \sin^2\beta \right. \\ &\quad \left. + 2 \left(\frac{M_{12}}{1 + M_{22}/m} \right) \sin\beta\cos\beta \right]^{\frac{1}{2}}. \end{aligned} \tag{3.55}$$

Note that due to the complexity of these expressions, it is simpler to actually perform the transformations and use Equations 3.52 and 3.53.

3.10 The Lorentzian

If the coherence between planes in one direction decays exponentially, the intrinsic peak shape will be broadened by a Lorentzian in one direction.

If the Lorentzian lies at an angle β to the nominal spectrometer position κ_0 then it can

be shown (see Chapter 2 Ref. [4]) that:

$$L^{-1} = \frac{\pi}{N'}\sqrt{\frac{a(\alpha)}{B_0}}\frac{1}{U(\alpha)}, \tag{3.56}$$

$$z = \frac{\pi}{N'}\sqrt{\frac{2\pi}{B_0}}\frac{1}{u(\mathbf{0})}. \tag{3.57}$$

where

$$U(\alpha) = \int \frac{\Gamma}{\Gamma^2 + {q_y'}^2} \exp\left\{-\frac{M_{11}M_{22} - {M_1}^2}{2a(\alpha)}\sin^2(\beta-\alpha){q_y'}^2\right\} \mathrm{d}q_y', \tag{3.58}$$

$$a(\alpha) = M_{11}\cos^2\alpha + 2M_{12}\cos\alpha\sin\alpha + M_{22}\sin^2\alpha. \tag{3.59}$$

This does not have a simple algebraic solution and will in general need to be solved numerically.

3.11 Twinning

Although the samples measured in this thesis are single crystals, they do show significant mosaicity. The samples thus are likely to be made up of a number of crystals in very similar alignment.

However, the crystal structure of the $RBa_2Cu_3O_{6+\delta}$ series of crystals is such that the a and b directions are very similar.

Thus (as is assumed in this thesis), the small crystals may have random alignment within the constraint that the long axis must be in the same direction (but either way around) and that the other two axis are aligned between the small crystals, but may be in any order.

Note that there may also be magnetic domains where the a and b directions are swapped, and this will have a similar effect.

These effects can be modelled simply by calculating the intensity for the equivalent crystallographic directions and averaging them.

Thus, the intensities are calculated for the $(h, k, \pm l)$, $(h, -k, \pm l)$, $(k, h, \pm l)$ and $(k, -h, \pm l)$ directions.

This has no effect on the calculation of the nuclear intensities. However, this averaging

over domains is very significant for the magnetic structure. This twinning effect means that even though this is a single crystal experiment, certain orientations of the moments cannot be derived from the data. For instance, the angle θ of the rare earth moment away from the c direction can be found, but the angle ϕ at which it lies in the ab plane cannot.

3.12 Two dimensional measurement corrections

Due to difficulties in aligning the sample and spectrometer, in some cases it can be considerably more accurate to measure the intensity at points in a two dimensional area around the peak, rather than in a line scan across the peak. See Section 4.5.7 for measurements that use this technique.

This reduces the risk of the line scan missing the center of the peak, and does not rely on all of the approximations of the Lorentz factor correction.

The corrections to obtain an absolute intensity from such a measurement are much simpler than in the one-dimensional case.

We can calculate what a two-dimensional Lorentz factor would be from the previous results in this chapter.

- The z factor (see for instance Equations 3.35 and 3.44) gives the ratio between the intrinsic intensity of the Bragg peak and the measured peak height. This gives the overall normalization of the peak.

- The transformed matrix elements M_{11}, M_{12} and M_{22} give the shape of the resolution ellipsoid as defined in Equation 3.26.

Now, the integrated volume of the two dimensional Gaussian ellipsoid given by:

$$R(\boldsymbol{q}) = \exp\left[-\frac{1}{2}M_{11}q_x^2 - M_{12}q_xq_y - \frac{1}{2}M_{22}q_y^2\right], \tag{3.60}$$

is

$$\int R(\boldsymbol{q})\mathrm{d}\boldsymbol{q} = \frac{\pi}{\sqrt{M_{11}M_{22} - {M_{12}}^2}}. \tag{3.61}$$

Thus, defining L_2 to be the ratio of the measured volume of the peak to the intrinsic

intensity of the peak we have

$$L_2^{-1} = \frac{z}{\pi}\sqrt{M_{11}M_{22} - {M_{12}}^2}. \tag{3.62}$$

Crucially, this value is found to be independent of both ω and θ_s (demonstrating this by algebraic methods is lengthy and tedious). Thus, as long as the measured intensity of the magnetic peaks are normalized against nuclear peaks measured in the same way, the Lorentz factor correction can be entirely neglected.

It can be seen that this must be the case, as by performing the grid scan all of the scattering in the plane is measured. This is reflected in the Lorentz factor; as the area of the ellipsoid changes, the z factor changes to compensate.

A simple way to measure a peak in a two dimensional grid is to measure a series of linear scans across the peak with different offsets. By completing the square, the intensity around a peak can be rewritten as

$$I = I_0 \exp\left\{-\left[\frac{1}{2}M_{11}x'^2 + M_{12}x'y' + \frac{1}{2}M_{22}y'^2\right]\right\} \tag{3.63}$$

$$= I_0 \exp\left\{-\frac{M_{11}}{2}\left[\left(x' - \frac{M_{12}y'}{M_{11}}\right)^2 - y'^2\left(\frac{{M_{12}}^2 - M_{11}M_{22}}{{M_{11}}^2}\right)\right]\right\}, \tag{3.64}$$

where $x' = x - x_0$ and $y' = y - y_0$ and x_0 and y_0 give the position of the peak.

Thus a scan at $y' = y'_s$ in the x direction will have a maximum at $x' = (M_{12}/M_{11})y'$, have a width equal to $1/\sqrt{M_{11}}$ and a maximum value of

$$I_{\max} = I_0 \exp\left[-\frac{1}{2}\left(\frac{M_{11}M_{22} - {M_{12}}^2}{{M_{11}}^2}\right)y'^2_s\right]. \tag{3.65}$$

The coordinate system can be rotated so that x lies in the scan direction. Thus, each of the scans in a particular direction will have the same Gaussian width. Furthermore, their centres will be offset in a line with a slope given by the ratio of the transformed M_{12} and M_{11} matrix elements and have an amplitude given by Equation 3.65 using the transformed matrix elements.

The only complexity to account for in the grid scans is to convert the units of the scans into an area of Å^{-1}.

In all the measurements presented here, we have taken the (110) and (001) vectors as a basis.

Many of the grid scans are measured in the (110) and (001) directions with units of h and l respectively. In this case the conversion is easy. The conversion factor for the h direction is $C_h = 2\sqrt{2}\,\pi/a$ (assuming $a = b$) and for the l direction $C_l = 2\pi/c$. Thus the area conversion factor is

$$C = \sqrt{32}\,\pi^2 \frac{hl}{ac}. \tag{3.66}$$

However, scanning in the ω direction (i.e. simply rotating the crystal) is much faster as the detector does not have to be moved. Thus, many of our measurements have one of the scan directions being ω rather than one of the axes.

Due to the scans being short compared to the distance from the origin, we ignore the curvature of the scan for simplicity.

With ω in degrees, the conversion factor is $C_\omega = r\pi/180$ where r is the distance from the origin in Å^{-1}.

If the other axis is (110) or (001) then the correction factor is as above, but with an additional factor as the two scan directions are no longer perpendicular.

For a (110) scan, the projection of the scan onto the perpendicular to the ω direction gives a correction of the ratio of the measured distance to the radial distance, i.e. $2\sqrt{2}\,\pi h/(ar)$.

Thus, the overall correction is

$$C = 8\pi^3 \frac{h}{180a^2}. \tag{3.67}$$

Similarly, the correction for an ω–(001) scan is

$$C = 4\pi^3 \frac{l}{180c^2}. \tag{3.68}$$

It should be noted that this procedure relies on all of the area of the peak being covered within the grid. Thus, it is not suitable for measuring two-dimensional ordering, or any other form of scattering where the peak is not highly localized.

3.13 References

[1] G.L. Squires, *Introduction to the theory of thermal neutron scattering*, (Cambridge University Press, 1978, ISBN 0-486-69447-X).

[2] S. Shamoto, M. Sato, J.M. Tranquada, B.J. Sternlieb and G. Shirane, *Neutron-scattering of antiferromagnetism in* $YBa_2Cu_3O_6.15$, Phys. Rev. B **48** 13817–13825 (1993).

[3] P.J. Brown, *International tables of crystallography, vol. C*, (Dordecht, 1993).

[4] S.W. Lovesey, *Theory of neutron scattering from condensed matter*, (Oxford Science Publications, 1986).

[5] M.J. Cooper and R. Nathans, *The resolution function in neutron diffractometry I. The resolution function of a neutron diffractometer and its application to phonon measurements*, Acta. Cryst. **23**, 357–367, (1967).

[6] N.J. Chesser and J.D. Axe, *Derivation and experimental verification of the normalized resolution function for inelastic neutron scattering*, Acta. Cryst. A **29** 160–169, (1973).

Chapter 4

Magnetic Structure Measurements

4.1 Introduction

In this chapter I will describe the measurements on $NdBa_2Cu_3O_{6+\delta}$, the analysis of the magnetic ordering and compare the results with previous measurements on $PrBa_2Cu_3O_{6+\delta}$. Three samples were measured:

- A relatively pure sample of the oxidized form, $NdBa_2Cu_3O_7$ which was superconducting and showed ordering of only the neodymium moments.
- A sample of the reduced form, $NdBa_2Cu_3O_6$ which is believed to have Nd substitution on the Ba sites giving a composition of $NdBa_{2-y}Nd_yCu_3O_6$. This showed ordering of the copper moments (which rotated at low temperatures), and a two-dimensional ordering of the neodymium moments. As it was of the reduced form, it did not superconduct.
- A relatively stoichiometric sample of $NdBa_2Cu_3O_6$. This showed a simple copper ordering at high temperatures and a more complex (but independent) ordering of both the neodymium and copper at low temperatures. As with the second sample, this was not a superconductor.

This chapter will describe the experimental techniques used, the results obtained and include a discussion of the results.

4.2 Experimental technique

The measurements were carried out on the TAS1 triple axis spectrometer on reactor DR3 at Risø National Laboratory in Denmark. This section outlines the experimental procedures and equipment used.

4.2.1 Equipment

The TAS1 spectrometer is a triple axis spectrometer on the liquid H_2 moderated 'cold source' reactor DR3.

TAS1 in the configuration we used is similar in overall design to the general triple axis spectrometer described in Section 3.2 and illustrated in Figure 3.1.

TAS1 has a selectable incident energy for the neutrons. For most of the measurements, we used a nominal fixed incident energy of 13.7 meV, which gives a neutron wavelength of 2.47 Å. This matched the peak in the reactor flux, and gives a convenient scale for the measurements of the sample.

The exact incident energy is slightly uncertain, which leads to a systematic error on our results. A calibration made during the later measurements put the incident energy at closer to 14.1 meV than the nominal value.

The neutron detector was a proportional ^{3}He gas detector.

4.2.2 Sample environment

These measurements have been made over a wide range of temperatures. Various different sample environments provided this range.

- A small furnace provided temperatures above room temperature. This was the simplest environment used and the sample could be mounted directly on the goniometer of the spectrometer.

- For some initial measurements at low temperatures a standard Orange cryostat provided cooling.

- To obtain temperatures down to 313 mK, a Heliox insert from Oxford Instruments was used with a special cryostat. The Heliox is a ^{3}He sorption pump. Once the ^{3}He was fully condensed, the sorption pump would maintain base temperature for greater than a day, which was a vital property for some of the long measurements.

- For some of the wide range temperature dependent measurements, a displex was used to obtain easy control of the temperature.

In the measurements with either of the cryostats, the sample had to be mounted in the cryostat, and the entire cryostat placed on the goniometer. This meant that the sample was inverted compared to the other measurements, and the sample alignment relative to the goniometer was not obvious.

To obtain absolute measurements, each of the sample environments needed separate calibration. For instance, the Heliox has a considerable amount of helium in the beam, which adds to the background and attenuates the beam. As the majority of the final measurements were made using the Heliox (which covers the temperature range over which the neodymium orders), this is only significant for measuring the copper ordering at high temperatures.

4.2.3 Crystal alignment

For each of the measurements made on the crystals, we aligned the crystal such that the c axis of the crystal was in the plane of the spectrometer, and the crystal was rotated by 45° around the c axis. Thus the axes for the scattering were the (1,1,0) and (0,0,1) directions.

To align the crystal, the (0,0,4) and (1,1,0) peaks were used. These peaks are sufficiently intense that they can be found easily by rotating the crystal while continuously monitoring the count rate.

One difficulty in using a triple axis spectrometer to measure absolute intensities is that the alignment must be very precise, or not all of the intensity will be measured. The alignment is complicated by the resolution ellipsoid changing in orientation as the position

in reciprocal space varies. This means that generally the axes of the ellipsoid will not match the direction of an alignment scan. Thus, it is not necessarily sufficient for accurate alignment to scan in perpendicular directions looking for the maximum intensity, as this can lead to alignment on a point that is on a principal axis of the ellipsoid.

The sizes of the samples used in these experiments were small compared to the sizes of samples usually measured on similar triple axis spectrometers, which leads to further difficulties in obtaining a perfect alignment.

In particular, as well as the orientation of the sample, the position is critical. Otherwise the rotation of the sample will cause it to precess, and move away from the beam. For the measurements outside the cryostat this is not a real problem, as the position of the sample can be modified directly as the sample can be seen. However, for measurements using the Heliox insert, the sample is mounted in the sample chamber of the insert and so the position cannot be checked directly. Also, there is a long connection between the sample and the cryostat, so any misalignment in angle will give a significant positional error.

With a small sample and a narrow beam, a precession of the sample will give a significant change in the measured intensity. The change will be different depending on the position of the spectrometer, and so can skew results for different Bragg peaks. A precession may also give a variation in the width of a peak, as the sample changes position as it is rotated to perform the scan. On a truly open detector, these effects would be small, but to reduce the background we used fairly narrow collimators at the detector. This means that neutrons scattered from the sample when it is off center may be stopped by the collimators.

To obtain alignment in the cryostats, the crystals were aligned at room temperature outside the cryostat. The mounts were then modified so that the crystal was almost aligned at the zero position of the goniometer. This enabled the alignment of the crystal in the cryostat without excessive tilting of the cryostat which would cause instability.

4.2.4 Sample mounting

To mount the sample, we first wrapped it in a small piece of foil with a stem to keep it fixed and to provide a flexible mounting point so that its position could be adjusted. This provided a coarse adjustment.

Normally, high purity aluminium foil would be used for this (and it was used for some test measurements). This has the advantages that it is easy to work with and matches the material of the cryostat and mountings and so does not add as much to the powder scattering background.

Unfortunately, we wished to take measurements at very low temperatures where aluminium superconducts. This would lead to very poor thermal contact between the sample and the environment, making temperature changes and measurement difficult, particularly when measuring across a temperature range.

Thus, for mounting the samples at low temperature we used various thicknesses of high purity copper foil to produce suitable mounts.

These were then mounted on copper stem mounts, which were wrapped in cadmium foil to reduce any background scattering from them.

4.2.5 Analysis of data

To measure the absolute magnetic moments, the intensities of the Bragg peaks must be normalized to correct for the resolution of the spectrometer, the mosaicity of the sample, intrinsic broadening, and the strength of the scattering by the crystals. Chapter 3 describes the mathematical techniques used for this.

For each crystal, the nuclear peaks were measured at low temperature to align the crystal and to check and refine the parameters of the resolution correction. The intensities of these peaks are then used to normalize the magnetic peaks to absolute magnetic moments.

Figure 4.1 illustrates the types of scans through reciprocal space performed for each Bragg peak. The scans in the hk and l directions produce data that is simple to analyse. However, they have the disadvantage that to perform such a scan, θ_s needs to be changed for each point. On TAS1 this is a slow process, as the entire analyzer and detector assembly must move and stabilize at the new position. Thus, for the typical count times used in these measurements, such a scan is relatively slow. Conversely, an ω scan simply involves rotating the sample and is relatively quick to perform.

To obtain the intensities of the peaks, the scans across the peaks in reciprocal space were then fitted to a Gaussian with a sloping background. In most cases sufficient points could

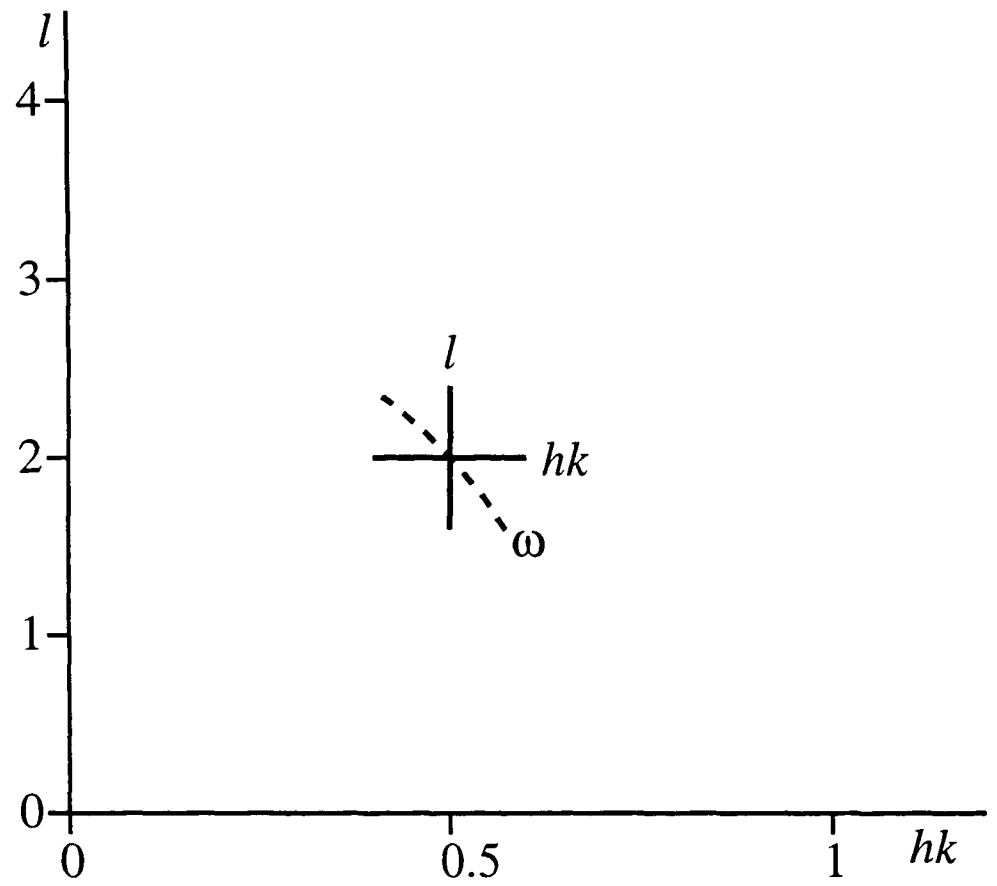

Figure 4.1: An illustration of the types of scan: Shown here are the directions of the scans through the $(\frac{1}{2}, \frac{1}{2}, 2)$ magnetic Bragg peak. The hk and l scans are along the axes and the ω scan is a rotation about the origin.

be measured for an accurate determination of the background. In some cases this was not possible due to contamination by the powder scattering from the mounting. In these cases estimates of the intensity from the uncontaminated points were made as appropriate.

In the cases where the absolute value of the background was important (for instance, Section 4.4.7), the scans were fitted to a Gaussian with a flat background, the value of which was used for the corrections.

Using Gaussian fits to the peaks enables the background to be removed, and also allows meaningful results to be obtained from scans which are contaminated with powder scattering. This technique does have a disadvantage: some of the peaks (particularly those with Lorentzian broadening) are significantly non-Gaussian. This can lead to the area of the best-fit Gaussian missing some of the intensity.

4.2.6 Systematic errors

In this chapter I quote the results with errors given by the random errors calculated from the scatter of points.

In this section I attempt to quantify the systematic errors inherent in this technique.

- The exact incident energy of the neutrons provided by the monochromator is slightly uncertain. Calibration measurements put the difference between the measured and nominal values at up to 3%. The exact effect of this is dependent on the measurement being performed. We do not rely on the measurements to obtain the nuclear structure of the crystal, so the exact value of the incident energy is not critical. The energy only affects the Lorentz factor correction for the resolution of the instrument. Calculations using different values for the incident energy put the error on a peak intensity at less than 2% due to this effect. The later grid measurements are independent of the incident energy.

- For simplicity, the Debye-Waller factor has been neglected. This is justified as almost all of the measurements are made at low temperatures, and with only small temperature differences between measurements. Also, the nuclear measurements used for calibration were also made at low temperature. This will only cause a significant error for the higher temperature measurements. In particular the high temperature copper ordering may be slightly distorted, however the absolute intensity of this measurement is only of minor importance.

- Again, for simplicity, a simple model has been used for the nuclear structure. This leads to a not ideal match between theory and experiment for the nuclear structure. However, the intensities of large numbers of peaks are combined to produce the normalization factor, so the overall normalization error on absolute magnetic moments caused by this should be less than 5%.

- As described in the previous section, the use of Gaussian fits for the data, though generally improving the quality of the data, can lead to a systematic error on the intensity. This will be most noticeable for the second reduced crystal, which showed Lorentzian broadening, and the oxygenated crystal, which had significant mosaicity.

Calculations using the integrated intensity put the error in these cases at less than 10%.

- Many of the scans have been corrected using a Lorentz factor. Due to the uncertainties in the instrumental parameters and the approximations in the correction, this by itself will lead to a systematic error. The version used here is more detailed than has been commonly used previously (as it includes corrections for sample mosaicity and intrinsic broadening), but even so there were noticeable differences between the predicted and measured resolutions. This is why most peaks have been measured at least three times in different directions. Calculations using different values for the Lorentz correction put the systematic error on a peak intensity from this at around 10%. The later grid scans are unaffected by this as they do not need the correction.

Overall, we believe the systematic error on the measurements of absolute magnetic moments to be around 10%, and slightly less for the grid measurements. Note that the error on the moment is a factor of two lower than the error on the intensity as the moment is proportional to the square root of the intensity.

The temperature sensors are believed to be accurate. Measurements were made of the magnetic transitions when the temperature was changed to quantify the thermal contact between the sample and the environment. For the temperature scan measurements, the step time was chosen such that the sample temperature could equilibrate. Thus we believe that systematic errors in the measurement of temperature for measurement of the temperature dependence of the magnetic ordering to be less than 0.02 K.

4.2.7 Samples

All three samples were produced by Th. Wolf at Forschungszentrum Karlsruhe.

The oxygenated crystal had a mass of 42 mg and the non-stoichiometric and stoichiometric reduced samples had masses of 23 mg and 19 mg respectively.

The oxygenated crystal, the non-stoichiometric and the stoichiometric crystal are those referred to as S, NS(B) and NS(A) in Ref. [1].

The growth method used was similar to that described in Ref. [2]. High purity Nd_2O_3,

$BaCO_3$ and CuO powders were used (except where described below). The crystals were grown in 60–70 mbar air while the temperature was decreased from 1010 °C to 964 °C at 0.4 °C per hour. The furnace was then evacuated to 30 mbar and cooled to room temperature at around 50 °C per hour.

In the case of crystal NS(B), the oxygen partial pressure was higher during the cooling to room temperature, which was also slower. These conditions lead to a small excess of Nd, which is likely to be substituted onto the Ba site.

Crystal S and NS(B) were grown in yttria stabilized zirconia crucibles, while NS(A) was grown in a SnO2 crucible. Thus, small quantities of Y or Sn may contaminate the crystals. NS(A) was also formed from slightly impure CuO, which may lead to Zn, Sn and Fe impurities at around 1% per site.

To obtain the desired oxygen contents, the crystals were annealed after growth.

Crystal NS(A) was reduced using a gas volumetric system [3]. The sample was reduced at 700 °C with 5 g of YBCO powder acting as a buffer. Degassing oxygen was removed from the system for two days, and then the system was allowed to equilibrate at 0.5 mbar and cooled to 200 °C over 10 hours.

Crystal NS(B) was reduced in a 0.02 mbar oxygen atmosphere 695 °C for 138 hours.

Crystal S was annealed in 1 bar oxygen between temperatures of 601 °C and 379 °C for 790 hours.

The compositions of the samples (quoted in Tables 4.3, 4.7 and 4.14), were measured by Shamimo Chowdhury by EPMA in the Clarendon Laboratory, Oxford.

4.3 $NdBa_2Cu_3O_7$

4.3.1 Introduction

$NdBa_2Cu_3O_7$ was relatively easy to measure and analyse, as it was clear from preliminary measurements on some $(\frac{1}{2}, \frac{1}{2}, l)$ peaks that the Cu atoms do not magnetically order. This is expected as the crystal has a high oxygen content and is a superconductor. Thus, only the low temperature Nd ordering needed to be measured.

The low temperature ordering of the neodymium moments was measured using the Heliox

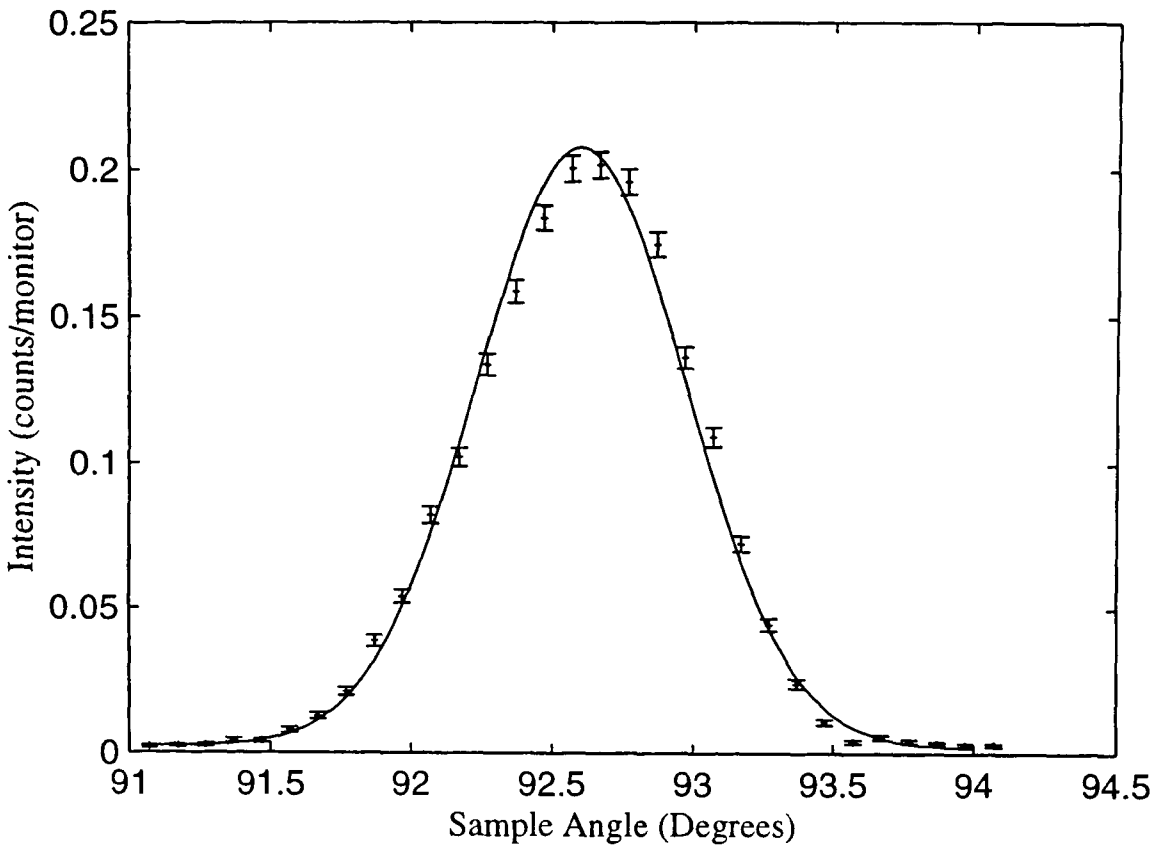

Figure 4.2: Oxygenated crystal ω scan across $(1, 1, 3)$

insert.

4.3.2 Sample mosaicity

Figure 4.2 shows a typical ω scan across the $(1, 1, 3)$ nuclear peak to give an indication of the sample mosaicity. The line is the best-fit Gaussian.

The width (standard deviation) of the peak shown is $0.371 \pm 0.007°$. With the mosaicity as in Table 4.3 the theoretical width is $0.372°$. Without the correction for the sample mosaicity, the theoretical width would be $0.114°$.

Despite the relatively large mosaicity, it does not distort the peak significantly from a Gaussian, as can be seen from the graph.

Due to the significant mosaicity, the sample is assumed to be twinned (see Section 3.11 for details). The later crystals are also assumed to show twinning.

4.3.3 Nuclear structure

From the measured T_c of 95.5 ± 0.5 K (see Section 8.1.2) and comparison to similar samples, we believe the oxygen content of the crystal to be 6.93 ± 0.02. As the exact crystal structure

was not measured, I have used nominal parameters [4] with the occupancy set for this oxygen content.

The peak intensities and widths correspond reasonably with the expected values based on the known structure. Tables 4.1 and 4.2 show the relation between the measured and theoretical values for the intensities and widths. The differences that are visible are expected, as most of the parameters used are the nominal ones, and the model used is simple, neglecting extinction and other effects. A more complex model is not justified considering the inaccuracy of this method for measuring nuclear structure.

The values for the resolution correction used in the above tables are shown in Table 4.3 as well as the nominal values of the resolution parameters.

The definitions of the parameters are given in Section 3.8 and summarized in Table 3.3.

4.3.4 Magnetic peaks at 0.313 K

Table 4.4 shows the magnetic peaks measured at 0.313 K. The intensities have been normalized to the nuclear peaks to obtain the intensities in units of $\mu_B{}^2$. Note that this does not include the magnetic form factor, so the magnetic moment is not simply the square root of this. Comparisons to theoretical values must be made to obtain the actual moments.

The theoretical values are a fit to the data assuming a structure for the Nd moment that is antiferromagnetic in all three directions as shown in part A of Figure 2.4.

Note that this is a different ordering to an ordering that has been observed for Pr in $PrBa_2Cu_3O_7$ (see Chapter 2 Ref. [4]). This ordering actually makes the analysis much easier for the later crystals: the neodymium and copper peaks do not usually coincide, so the added complication of separating the intensities does not occur.

The only parameters varied in the fit were the magnitude and direction of the Nd moment. The definition of χ^2 used in the results given (and the rest of the results in this thesis) is

$$\chi^2 = \frac{1}{N}\sum_{i=1}^{N}\left[\frac{x_{mi} - x_{ti}}{\sigma_i}\right]^2, \tag{4.1}$$

$(h\ k\ l)$	Scan	Intensity	Theory	Ratio
(001)	ω	8.96E-04 ± 3.1E-05	9.30E-09	9.6E+04
	l	1.29E-03 ± 3.0E-05		1.4E+05
(002)	ω	2.54E-04 ± 1.3E-05	6.19E-10	4.1E+05
	l	3.33E-04 ± 1.0E-05		5.4E+05
(003)	ω	4.29E-03 ± 1.2E-04	3.01E-08	1.4E+05
	l	4.88E-03 ± 1.1E-04		1.6E+05
(004)	ω	8.45E-03 ± 2.4E-04	4.50E-08	1.9E+05
	l	9.13E-03 ± 1.9E-04		2.0E+05
(005)	ω	1.35E-02 ± 3.3E-04	1.02E-07	1.3E+05
	l	1.48E-02 ± 5.0E-04		1.5E+05
(006)	ω	3.24E-02 ± 8.9E-04	2.88E-07	1.1E+05
	l	3.64E-02 ± 1.8E-03		1.3E+05
(007)	ω	7.01E-03 ± 2.1E-04	6.10E-08	1.1E+05
	l	7.63E-03 ± 5.8E-04		1.3E+05
(110)	ω	8.93E-03 ± 2.7E-04	5.76E-08	1.6E+05
	hk	9.73E-03 ± 2.0E-04		1.7E+05
	l	8.97E-03 ± 3.5E-04		1.6E+05
(111)	ω	2.57E-03 ± 9.4E-05	1.33E-08	1.9E+05
	hk	2.51E-03 ± 7.4E-05		1.9E+05
	l	2.66E-03 ± 1.0E-04		2.0E+05
(112)	ω	5.32E-04 ± 2.7E-05	3.50E-09	1.5E+05
	hk	5.21E-04 ± 2.4E-05		1.5E+05
	l	5.69E-04 ± 4.7E-05		1.6E+05
(113)	ω	1.27E-02 ± 4.1E-04	8.21E-08	1.5E+05
	hk	1.14E-02 ± 3.5E-04		1.4E+05
	l	1.48E-02 ± 4.8E-04		1.8E+05
(114)	ω	2.37E-03 ± 9.8E-05	1.98E-08	1.2E+05
	hk	2.27E-03 ± 9.5E-05		1.1E+05
	l	2.93E-03 ± 9.6E-05		1.5E+05
(115)	ω	1.46E-03 ± 1.0E-04	5.09E-09	2.9E+05
	hk	1.45E-03 ± 1.1E-04		2.9E+05
	l	1.94E-03 ± 1.2E-04		3.8E+05
(116)	ω	1.81E-02 ± 4.7E-04	1.28E-07	1.4E+05
	hk	1.97E-02 ± 7.0E-04		1.5E+05

Table 4.1: Oxygenated crystal nuclear peak intensities: The intensity of the peak is given in arbitrary units after correction for resolution effects by the use of a Lorentz factor.

$(h\ k\ l)$	Scan	Width	Theory	Ratio
(001)	ω	3.83E-01 ± 8.0E-03	3.87E-01	0.99
	l	3.06E-02 ± 3.7E-04	2.18E-02	1.41
(002)	ω	3.79E-01 ± 1.2E-02	3.79E-01	1.00
	l	3.25E-02 ± 5.4E-04	2.61E-02	1.25
(003)	ω	3.83E-01 ± 6.1E-03	3.75E-01	1.02
	l	3.58E-02 ± 4.0E-04	3.16E-02	1.13
(004)	ω	3.90E-01 ± 6.7E-03	3.73E-01	1.05
	l	4.09E-02 ± 4.5E-04	3.79E-02	1.08
(005)	ω	3.87E-01 ± 5.8E-03	3.72E-01	1.04
	l	4.71E-02 ± 9.4E-04	4.46E-02	1.06
(006)	ω	3.94E-01 ± 6.5E-03	3.72E-01	1.06
	l	5.52E-02 ± 1.9E-03	5.15E-02	1.07
(007)	ω	3.73E-01 ± 6.3E-03	3.72E-01	1.00
	l	5.71E-02 ± 2.3E-03	5.86E-02	0.98
(110)	ω	3.72E-01 ± 6.6E-03	3.73E-01	1.00
	hk	9.78E-03 ± 1.3E-04	9.30E-03	1.05
	l	2.80E-02 ± 5.9E-04	2.78E-02	1.01
(111)	ω	3.61E-01 ± 7.5E-03	3.73E-01	0.97
	hk	9.52E-03 ± 1.7E-04	1.04E-02	0.91
	l	2.82E-02 ± 5.9E-04	2.73E-02	1.03
(112)	ω	3.55E-01 ± 1.0E-02	3.72E-01	0.95
	hk	1.04E-02 ± 3.2E-04	1.13E-02	0.92
	l	3.12E-02 ± 1.5E-03	2.90E-02	1.07
(113)	ω	3.72E-01 ± 7.0E-03	3.72E-01	1.00
	hk	1.04E-02 ± 2.0E-04	1.20E-02	0.87
	l	3.81E-02 ± 6.8E-04	3.23E-02	1.18
(114)	ω	3.77E-01 ± 9.5E-03	3.72E-01	1.01
	hk	1.17E-02 ± 3.7E-04	1.26E-02	0.93
	l	4.48E-02 ± 9.1E-04	3.67E-02	1.22
(115)	ω	3.78E-01 ± 1.8E-02	3.72E-01	1.02
	hk	1.28E-02 ± 8.1E-04	1.35E-02	0.95
	l	5.34E-02 ± 2.5E-03	4.18E-02	1.28
(116)	ω	3.71E-01 ± 5.6E-03	3.72E-01	1.00
	hk	1.49E-02 ± 4.4E-04	1.45E-02	1.03

Table 4.2: Oxygenated crystal nuclear peak widths: The units of the widths are dependent on the scan type, with ω scans expressed in degrees, and the linear scans in fractions of Miller indices.

Parameter	Nominal Value	Derived Value
η_m	30	30
η_a	30	30
α_0	60	60
α_1	30	30
α_2	60	60
α_3	open	200
Geometry	r,r,l	r,r,l
Crystal a	3.856	
Crystal b	3.912	
Crystal c	11.719	
η_s	Unknown	50
Oxygen content	6.93 ± 0.02	
Ba z	0.1809	
Cu2 z	0.3494	
O1 z	0.1577	
O2 z	0.3681	
O3 z	0.3737	
Nd content	0.97 ± 0.01	
Ba content	2.00 ± 0.01	
Y content	0.007 ± 0.004	

Table 4.3: Oxygenated crystal resolution and structure parameters

$(h\ k\ l)$	Intensity / μ_B^2	Theory
$(\frac{1}{2}\ \frac{1}{2}\ \frac{1}{2})$	97.6 ± 2.0	101.1
$(\frac{1}{2}\ \frac{1}{2}\ \frac{3}{2})$	78.3 ± 1.8	72.6
$(\frac{1}{2}\ \frac{1}{2}\ \frac{5}{2})$	45.5 ± 1.4	47.2
$(\frac{1}{2}\ \frac{1}{2}\ \frac{7}{2})$	30.4 ± 1.3	31.5
$(\frac{1}{2}\ \frac{1}{2}\ \frac{9}{2})$	27.1 ± 2.3	22.1
$(\frac{1}{2}\ \frac{1}{2}\ \frac{11}{2})$	15.5 ± 2.9	16.3
$(\frac{1}{2}\ \frac{1}{2}\ \frac{13}{2})$	11.0 ± 1.7	12.3
$(\frac{3}{2}\ \frac{3}{2}\ \frac{1}{2})$	75.8 ± 8.2	75.2
$(\frac{3}{2}\ \frac{3}{2}\ \frac{3}{2})$	68.3 ± 7.8	70.7
$(\frac{3}{2}\ \frac{3}{2}\ \frac{5}{2})$	61.8 ± 3.0	62.8
$(\frac{3}{2}\ \frac{3}{2}\ \frac{7}{2})$	55.2 ± 3.3	53.4
χ^2	1.94	
Nd moment / μ_B	**1.344** ± 0.014	
Nd angle °	**16.3** ± 2.3	

Table 4.4: Oxygenated crystal magnetic peak intensities

where i indexes the measurement points,

N is the number of measurement points,

x_{mi} is the value of point i,

x_{ti} is the theoretical value of point i, and

σ_i is the standard error of point i.

The relatively low χ^2 value for the fit (and low random error) indicates that this model matches the results well.

Without a tilt on the neodymium moment, the match with the theoretical value is considerably worse, with a χ^2 of 5.40.

The widths of the peaks match the theoretical predictions quite well, and the intrinsic width of the peaks is small compared to the resolution width, indicating a long range order. The intrinsic width (HWHM) in the c direction is estimated to be less than 0.002 Å^{-1}, giving a correlation length of greater than 500 Å. This is estimated from the smallest change that may be observed considering the resolution width. Thus, no attempt has been made to correct the values for Lorentzian broadening.

The value of the moment is slightly larger than has been reported previously (see Chapter 2 Refs. [16, 18, 19]), and we find a slight tilt away from the c axis, whereas the previous results have shown alignment with the c axis.

4.3.5 Temperature scan

To show the development of Nd ordering, we measured the intensity of the $(\frac{1}{2}, \frac{1}{2}, \frac{1}{2})$ peak as a function of temperature from 0.313 K to 0.68 K.

Figure 4.3 shows the normalized moment of the peak, using the structure derived in Table 4.4. The points shown have been corrected for the background, so the negative points just show statistical fluctuation.

This shows that the Nd begins to order magnetically at 0.65 ± 0.01 K.

The line is a fit based on the power law equation that describes critical phenomena near a phase transition,

$$\mu = \mu_i \left[1 - \frac{T}{T_c}\right]^{\beta}, \tag{4.2}$$

where β is the order parameter critical exponent.

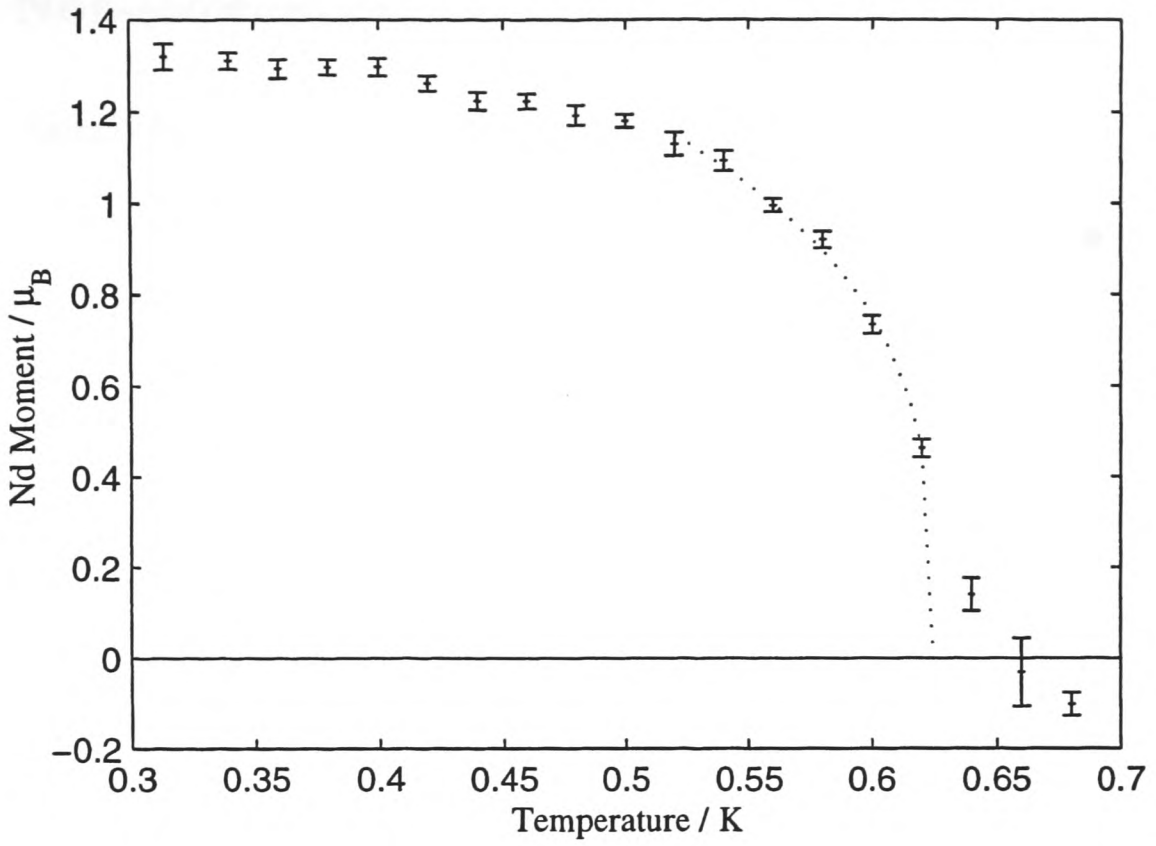

Figure 4.3: Oxygenated crystal magnetic peak temperature scan: The variation of the magnetic moment with temperature.

This power law form does not give a particularly good fit in this case, and gives an ordering temperature of $T_c = 0.624 \pm 0.004$ K, but this is clearly slightly out from the measurement.

The fit gives a value of 0.28 ± 0.09 for β.

4.3.6 Discussion

In this superconductor, the Cu moments did not magnetically order at any temperature that was measured. This is consistent with other measurements of $RBa_2Cu_3O_7$ compounds that superconduct (not $PrBa_2Cu_3O_7$).

The Nd moments ordered at a relatively low temperature, forming a different coupling to that seen in Chapter 2 Ref. [4] in $PrBa_2Cu_3O_7$. This ordering is a very simple antiferromagnetic structure in all three directions, with the moments aligned close to the c direction, but with a slight but significant tilt away.

4.4 Non-stoichiometric $NdBa_{2-y}Nd_yCu_3O_6$

4.4.1 Introduction

From the measurements on this sample and others [5], we believe that the sample had Nd substitution on the Ba sites.

In particular, two-dimensional ordering of the neodymium was seen, which is characteristic of this.

Unlike the oxygenated crystal, ordering was seen of both the copper and neodymium peaks. The copper peaks showed a rotation towards the AF2 phase at low temperature.

4.4.2 Sample mosaicity

For comparison with the previous crystal, Figure 4.4 shows a typical ω scan across the $(1,1,3)$ nuclear peak. Again the line is the best-fit Gaussian.

The width of the peak shown is $0.175 \pm 0.003°$. With the mosaicity as in Table 4.7 the theoretical width is 0.143°. Without the correction for the sample mosaicity, the theoretical width would be 0.114°. The corrected width is significantly different to the measured width; the reasons for this are discussed in the next section.

4.4.3 Nuclear peaks

From the preparation technique and similar samples, we believe the oxygen content to be 6.20 ± 0.02.

As with the previous sample, the exact parameters for the crystal structure are not available, so I have again used the nominal structure, corrected for the oxygen content. As the exact degree of substitution is unknown, the standard $NdBa_2Cu_3O_6$ structure has been used.

The measurements of the nuclear peaks for normalization are shown in Tables 4.5 and 4.6, along with the theoretical widths and intensities. As with the oxygenated crystal, the measured values show some discrepancy with the theoretical values. The match with the theoretical values is slightly worse, which may indicate a slight misalignment, or be symptomatic of the slightly non-stoichiometric composition.

$(h\ k\ l)$	Scan	Intensity	Theory	Ratio
(001)	ω	5.92E-04 ± 2.3E-05	1.86E-08	3.2E+04
	l	8.68E-04 ± 9.5E-05		4.7E+04
(002)	ω	7.54E-06 ± 2.2E-06	2.45E-11	3.1E+05
	l	6.92E-06 ± 2.0E-06		2.8E+05
(003)	ω	7.06E-04 ± 2.5E-05	1.70E-08	4.2E+04
	l	8.89E-04 ± 7.9E-05		5.2E+04
(004)	ω	2.94E-03 ± 1.3E-04	7.51E-08	3.9E+04
	l	3.31E-03 ± 3.7E-04		4.4E+04
(005)	ω	3.32E-03 ± 1.2E-04	7.10E-08	4.7E+04
	l	3.53E-03 ± 4.4E-04		5.0E+04
(006)	ω	5.54E-03 ± 2.1E-04	2.33E-07	2.4E+04
	l	5.49E-03 ± 5.6E-04		2.4E+04
(007)	ω	2.20E-03 ± 9.4E-05	7.45E-08	3.0E+04
	l	2.10E-03 ± 2.4E-04		2.8E+04
(110)	ω	4.80E-03 ± 2.0E-04	7.97E-08	6.0E+04
	hk	5.03E-03 ± 1.8E-04		6.3E+04
	l	4.92E-03 ± 3.0E-04		6.2E+04
(111)	ω	2.32E-03 ± 6.1E-05	2.58E-08	9.0E+04
	hk	1.45E-03 ± 7.7E-05		5.6E+04
	l	2.41E-03 ± 9.0E-05		9.3E+04
(112)	ω	9.02E-06 ± 7.2E-06	2.94E-11	3.1E+05
	hk	3.41E-06 ± 1.9E-06		1.2E+05
	l	7.60E-06 ± 4.3E-06		2.6E+05
(113)	ω	3.06E-03 ± 1.1E-04	5.98E-08	5.1E+04
	hk	2.04E-03 ± 1.6E-04		3.4E+04
	l	3.41E-03 ± 1.5E-04		5.7E+04
(114)	ω	1.12E-03 ± 6.1E-05	2.71E-08	4.1E+04
	hk	8.42E-04 ± 3.2E-05		3.1E+04
	l	1.36E-03 ± 5.1E-05		5.0E+04
(115)	ω	5.00E-05 ± 4.6E-05	1.80E-09	2.8E+04
	hk	5.59E-03 ± 8.6E-02		3.1E+06
	l	1.27E-03 ± 1.0E-03		7.1E+05
(116)	ω	4.09E-04 ± 3.8E-05	1.53E-07	2.7E+03
	hk	3.51E-04 ± 3.5E-05		2.3E+03

Table 4.5: Non-stoichiometric reduced crystal nuclear peak intensities

$(h\ k\ l)$	Scan	Width	Theory	Ratio
(001)	ω	1.40E-01 ± 2.9E-03	1.78E-01	0.79
	l	2.16E-02 ± 1.2E-03	1.99E-02	1.09
(002)	ω	2.96E-01 ± 6.8E-02	1.61E-01	1.84
	l	2.85E-02 ± 5.6E-03	2.19E-02	1.31
(003)	ω	1.45E-01 ± 2.7E-03	1.51E-01	0.96
	l	2.98E-02 ± 1.4E-03	2.51E-02	1.19
(004)	ω	1.47E-01 ± 3.3E-03	1.46E-01	1.01
	l	3.32E-02 ± 1.9E-03	2.91E-02	1.14
(005)	ω	1.62E-01 ± 3.0E-03	1.43E-01	1.13
	l	3.84E-02 ± 2.4E-03	3.37E-02	1.14
(006)	ω	1.62E-01 ± 3.2E-03	1.42E-01	1.14
	l	4.32E-02 ± 2.4E-03	3.86E-02	1.12
(007)	ω	1.61E-01 ± 3.5E-03	1.41E-01	1.14
	l	4.61E-02 ± 2.8E-03	4.38E-02	1.05
(110)	ω	1.71E-01 ± 3.5E-03	1.45E-01	1.19
	hk	9.39E-03 ± 2.0E-04	7.08E-03	1.33
	l	1.29E-02 ± 3.7E-04	1.08E-02	1.19
(111)	ω	1.73E-01 ± 2.4E-03	1.44E-01	1.20
	hk	7.58E-03 ± 2.1E-04	1.04E-02	0.73
	l	1.36E-02 ± 2.6E-04	1.08E-02	1.26
(112)	ω	2.32E-01 ± 1.4E-01	1.43E-01	1.62
	hk	7.58E-03 *	9.22E-03	0.82
	l	9.22E-03 ± 3.7E-03	1.16E-02	0.79
(113)	ω	1.75E-01 ± 3.3E-03	1.42E-01	1.23
	hk	6.28E-03 ± 3.2E-04	7.33E-03	0.86
	l	1.82E-02 ± 4.6E-04	1.32E-02	1.38
(114)	ω	1.70E-01 ± 5.5E-03	1.42E-01	1.20
	hk	5.72E-03 ± 1.3E-04	6.52E-03	0.88
	l	2.24E-02 ± 5.0E-04	1.55E-02	1.44
(115)	ω	2.72E-01 ± 2.0E-01	1.41E-01	1.92
	hk	4.51E-02 ± 2.4E-01	6.29E-03	7.18
	l	9.20E-02 ± 3.5E-02	1.83E-02	5.02
(116)	ω	1.47E-01 ± 7.9E-03	1.42E-01	1.04
	hk	6.23E-03 ± 3.4E-04	6.36E-03	0.98

Table 4.6: Non-stoichiometric reduced crystal nuclear peak widths: Asterisks denote widths that could not be determined accurately by measurement. Units are appropriate for the scan type.

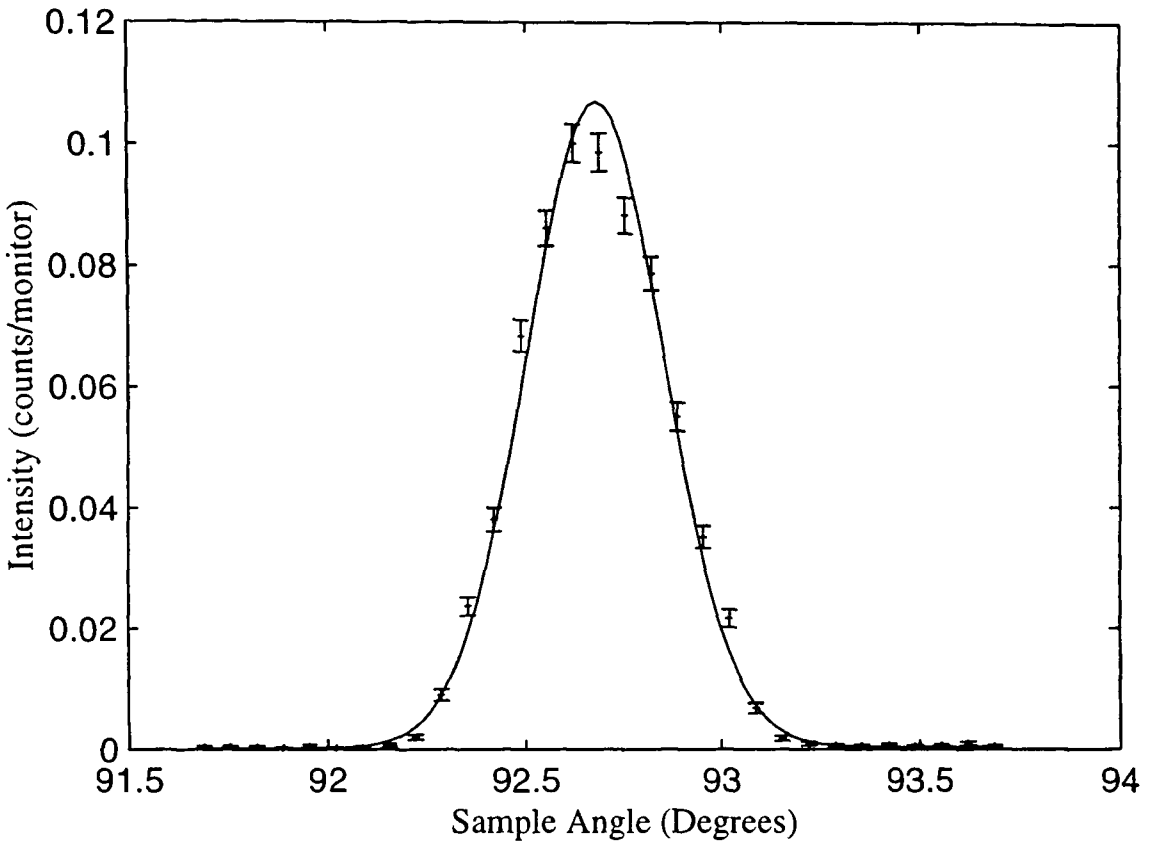

Figure 4.4: Non-stoichiometric reduced crystal ω scan across $(1, 1, 3)$.

The values for the resolution correction used in the above tables are shown in Table 4.7 as well as the nominal values of the resolution parameters.

4.4.4 Magnetic peaks at 50 K

Unlike the oxygenated crystal, this crystal showed high temperature ordering of the copper moments in the copper–oxygen plane.

Table 4.8 shows the intensities of the $(\frac{1}{2}, \frac{1}{2}, l)$ peaks at 50 K, after normalization to the nuclear peaks.

The theoretical values are a fit assuming an AF1 structure (see Figure 2.5). The only adjustable parameter for the fit was the magnitude of the Cu moment. An additional parameter describing the expansion of the Cu wave function (see Equation 3.9) was initially used, but this did not give a significantly better fit to the data, and the derived value was within error of zero. Similarly, there was no sign of significant ordering of the Cu(1) moments.

The χ^2 is somewhat large, but does indicate a reasonable match. Considering the slight discrepancies in the nuclear measurements, a significantly better fit cannot be expected.

Parameter	Nominal Value	Derived Value
η_m	30	30
η_a	30	30
α_0	60	60
α_1	30	30
α_2	60	60
α_3	open	200
Geometry	r,r,l	r,r,l
Crystal a	3.893	
Crystal b	3.893	
Crystal c	11.83	
η_s	Unknown	12
Oxygen content	6.2 ± 0.05	
Ba z	0.1908	
Cu2 z	0.3512	
O1 z	0.1524	
O2 z	0.3711	
Nd content	0.98 ± 0.02	
Ba content	2.03 ± 0.02	
Y content	0.010 ± 0.006	

Table 4.7: Non-stoichiometric reduced crystal resolution parameters

$(h\ k\ l)$	Intensity / μ_B^2	Theory
$(\frac{1}{2}\ \frac{1}{2}\ 1)$	30.9 ± 1.2	31.6
$(\frac{1}{2}\ \frac{1}{2}\ 2)$	61.3 ± 2.1	53.5
$(\frac{1}{2}\ \frac{1}{2}\ 3)$	9.8 ± 1.6	6.9
$(\frac{1}{2}\ \frac{1}{2}\ 4)$	16.3 ± 1.9	19.9
$(\frac{1}{2}\ \frac{1}{2}\ 5)$	45.3 ± 3.7	59.5
$(\frac{1}{2}\ \frac{1}{2}\ 6)$	14.1 ± 5.9	21.4
$(\frac{3}{2}\ \frac{3}{2}\ 2)$	6.7 ± 3.9	12.2
χ^2	5.68	
Cu moment / μ_B	**0.620** ± 0.021	

Table 4.8: Non-stoichiometric reduced crystal magnetic peak intensities at 50 K

$(h\ k\ l)$	Intensity / μ_B^2	Theory
$(\frac{1}{2}\ \frac{1}{2}\ \frac{1}{2})$	5.9 ± 0.7	6.9
$(\frac{1}{2}\ \frac{1}{2}\ 1)$	8.9 ± 0.9	8.5
$(\frac{1}{2}\ \frac{1}{2}\ \frac{3}{2})$	39.5 ± 2.0	40.6
$(\frac{1}{2}\ \frac{1}{2}\ 2)$	15.5 ± 1.4	14.4
$(\frac{1}{2}\ \frac{1}{2}\ \frac{5}{2})$	31.0 ± 1.7	24.6
$(\frac{1}{2}\ \frac{1}{2}\ 3)$	2.7 ± 1.2	1.9
$(\frac{1}{2}\ \frac{1}{2}\ \frac{7}{2})$	2.8 ± 1.3	0.8
$(\frac{1}{2}\ \frac{1}{2}\ 4)$	4.0 ± 1.5	5.4
$(\frac{1}{2}\ \frac{1}{2}\ \frac{9}{2})$	26.0 ± 3.5	36.2
$(\frac{1}{2}\ \frac{1}{2}\ 5)$	12.6 ± 3.6	16.0
$(\frac{1}{2}\ \frac{1}{2}\ \frac{11}{2})$	28.3 ± 8.3	36.5
$(\frac{1}{2}\ \frac{1}{2}\ 6)$	0.5 ± 2.5	5.8
$(\frac{1}{2}\ \frac{1}{2}\ \frac{13}{2})$	-0.6 ± 2.2	1.7
χ^2	2.86	
Cu moment / μ_B	**0.632** ± 0.020	
Cu rotation °	**59.4** ± 1.9	

Table 4.9: Non-stoichiometric reduced crystal magnetic peak intensities at 4 K

The lack of peaks at the $(\frac{1}{2}, \frac{1}{2}, l+\frac{1}{2})$ positions rules out the formation of an AF2 structure (see Figure 2.6).

4.4.5 Magnetic peaks at 4 K

As the temperature decreases, there is evidence of an AF2 intermediate structure, as peaks appear at the $(\frac{1}{2}, \frac{1}{2}, l+\frac{1}{2})$ positions.

Table 4.9 shows the intensities of the peaks at 4 K normalized to the nuclear peaks.

The theoretical values are a fit assuming an AF2 intermediate structure. The only free parameters were the copper moment and the copper moment rotation towards the AF2 ground state away from the AF1 state. The χ^2 indicates that this is a reasonable model for the structure, and the moment is consistent with that at 50 K, showing that the ordered moment has not significantly changed, but has simply rotated. As both temperatures are well below the ordering temperature, the magnitude of the moment would not be expected to change. There is no evidence for significant ordering of the copper chain sites, but the relatively large error does not rule this out.

The magnitude of the moment is also consistent with that reported for $PrBa_2Cu_3O_6$ (see Chapter 2 Ref. [4]).

4.4.6 Temperature scan 0.313 K to 5 K

At the temperature decreases further, there is evidence for a two-dimensional ordering of the Nd. Ridges of magnetic scattering along the $(\frac{1}{2}, \frac{1}{2}, l)$ and $(\frac{3}{2}, \frac{3}{2}, l)$ where l is continuously varying, indicate a two-dimensional structure.

The ridge shows up as additional signal in the scans across the Bragg peaks. For scans in the l direction this is not a problem, as the Bragg rod simply adds a constant background. However, for scans that are across the Bragg rod, the rod will appear as a peak, and this needs to be corrected for if the copper ordering is to be found.

We measured the intensities of three positions as a function of temperature to show the development of the two-dimensional ordering:

- $(\frac{1}{2}, \frac{1}{2}, 1.3)$ to show the formation of the magnetic ridge, and
- $(\frac{1}{2}, \frac{1}{2}, \frac{3}{2})$ and $(\frac{1}{2}, \frac{1}{2}, 2)$ to show the copper ordering and the variation of the AF2 state.

Figure 4.5 shows the intensities of the $(\frac{1}{2}, \frac{1}{2}, \frac{3}{2})$ positions normalized to the nuclear peaks to give them in units of ${\mu_B}^2$. These measurements have not been corrected for the ridge of scattering. The $(\frac{1}{2}, \frac{1}{2}, 2)$ peak shows a slight rise as the temperature decreases, but this is due to the addition of the ridge.

Figure 4.6 shows the intensities of the $(\frac{1}{2}, \frac{1}{2}, 1.3)$ position, showing the formation of the magnetic ridge. The background has not been removed. The higher temperature measurements put the background at $321.0 \pm 3.7 {\mu_B}^2$.

As in Section 4.3.5 the line is based on Equation 4.2. From this, the ordering temperature is 1.501 ± 0.003 K, with a value of 2β of 0.35 ± 0.09. The value is given for 2β as the intensity is proportional to the square of the moment.

4.4.7 Magnetic ridge

At low temperatures, the Nd forms a two-dimensional structure. This is indicative of a non-stoichiometric composition with Nd substitution on the Ba sites. Such an ordering could also suggest contamination, but other studies [5] indicate the former is more likely.

Figures 4.7,4.8 and 4.9 show scans in the hk direction across the ridge at three different positions. The lines show the best fit Gaussian for each peak.

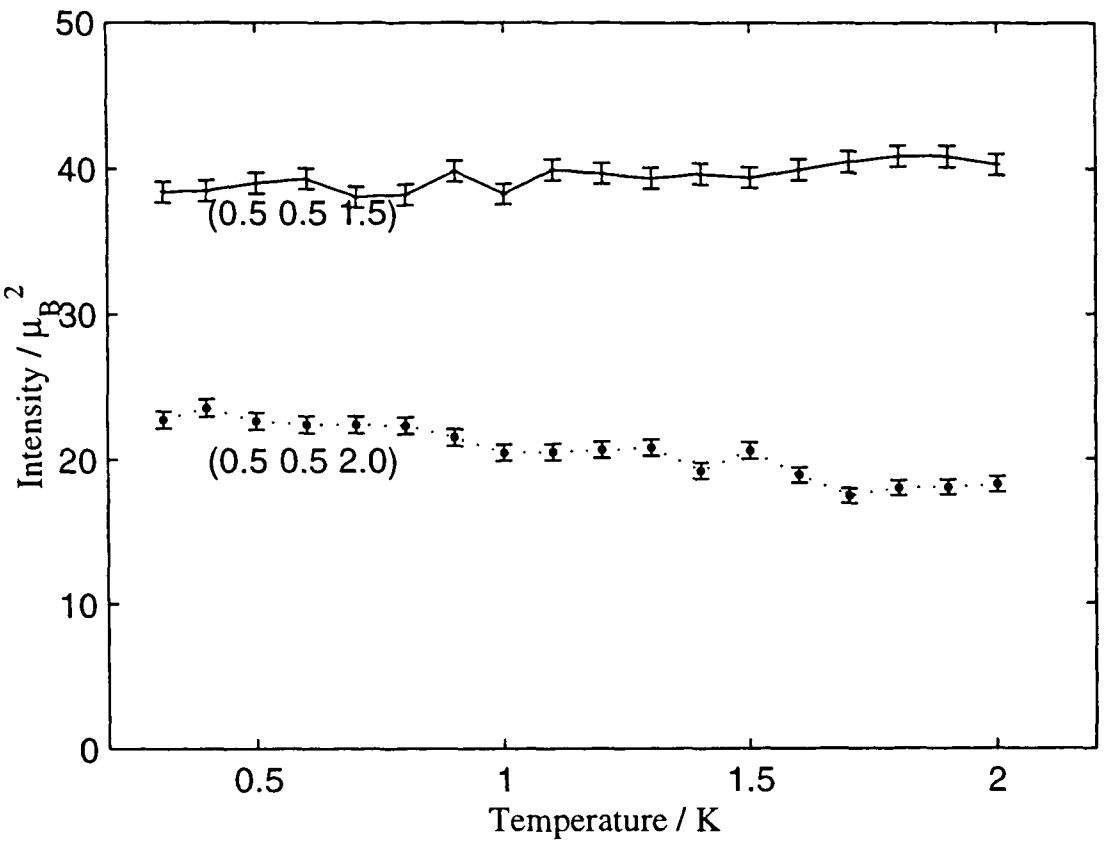

Figure 4.5: Non-stoichiometric reduced crystal magnetic peak temperature scan: The variation of the intensities with temperature.

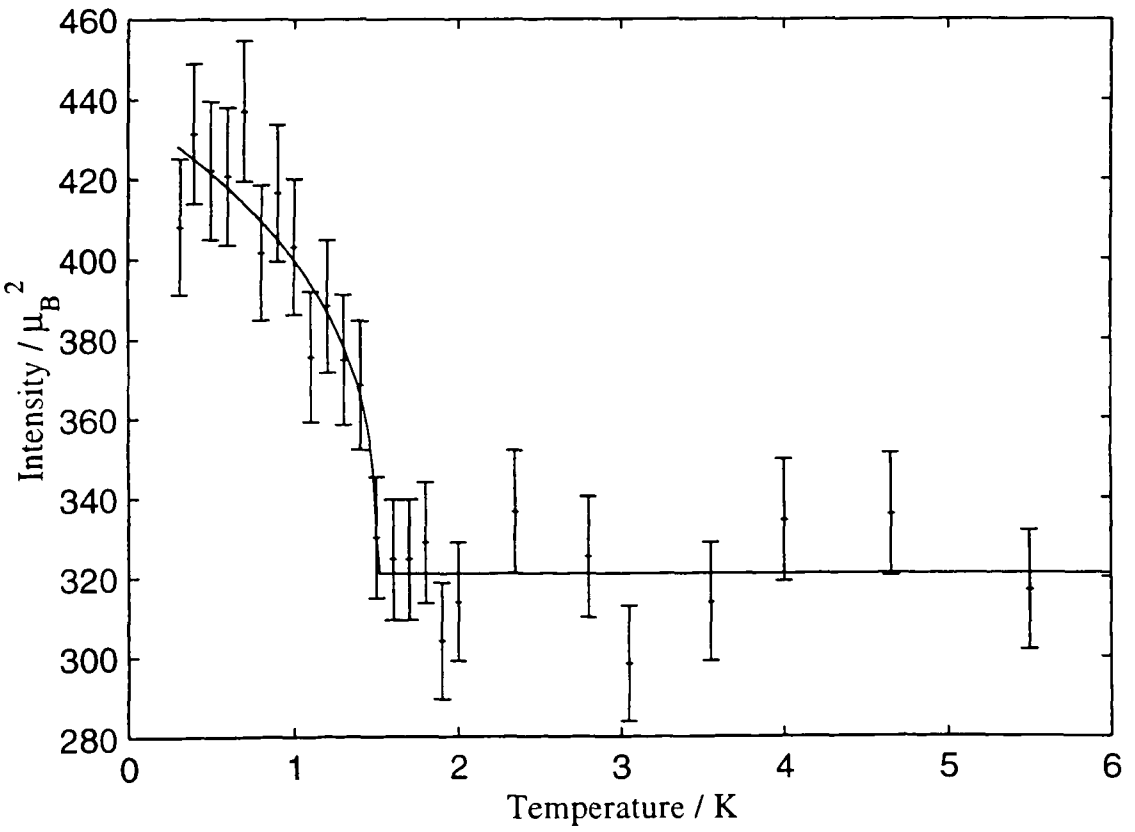

Figure 4.6: Non-stoichiometric reduced crystal magnetic ridge temperature scan: The variation of the intensity with temperature. This shows the intensity without the background removed.

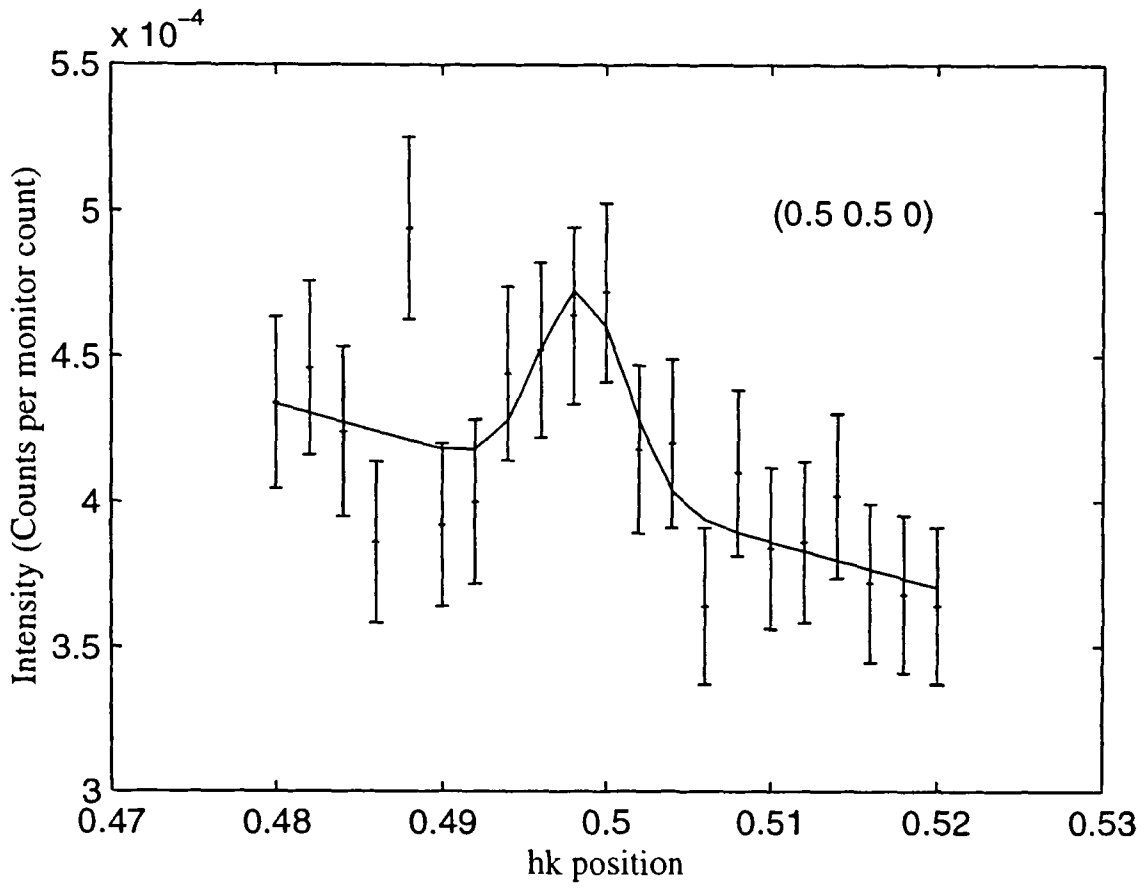

Figure 4.7: Non-stoichiometric reduced crystal magnetic ridge (0.5, 0.5, 0)

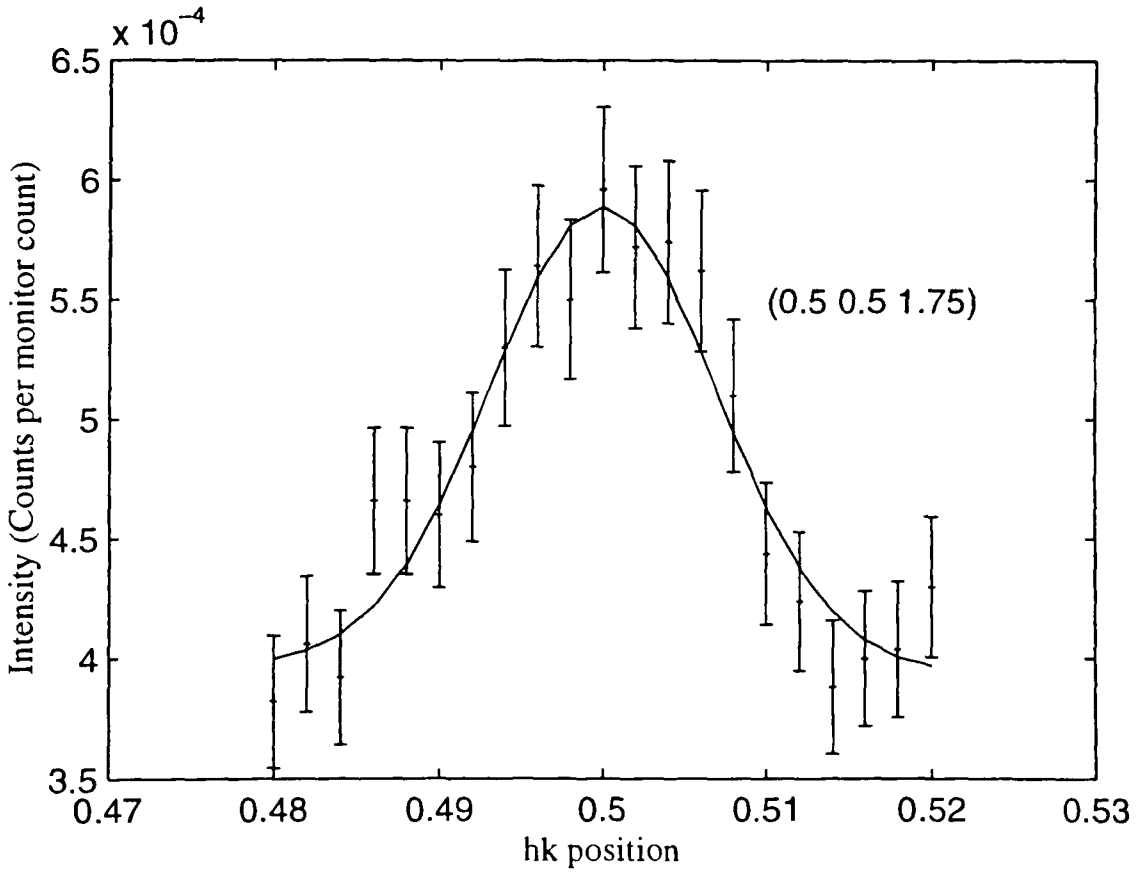

Figure 4.8: Non-stoichiometric reduced crystal magnetic ridge (0.5, 0.5, 1.75)

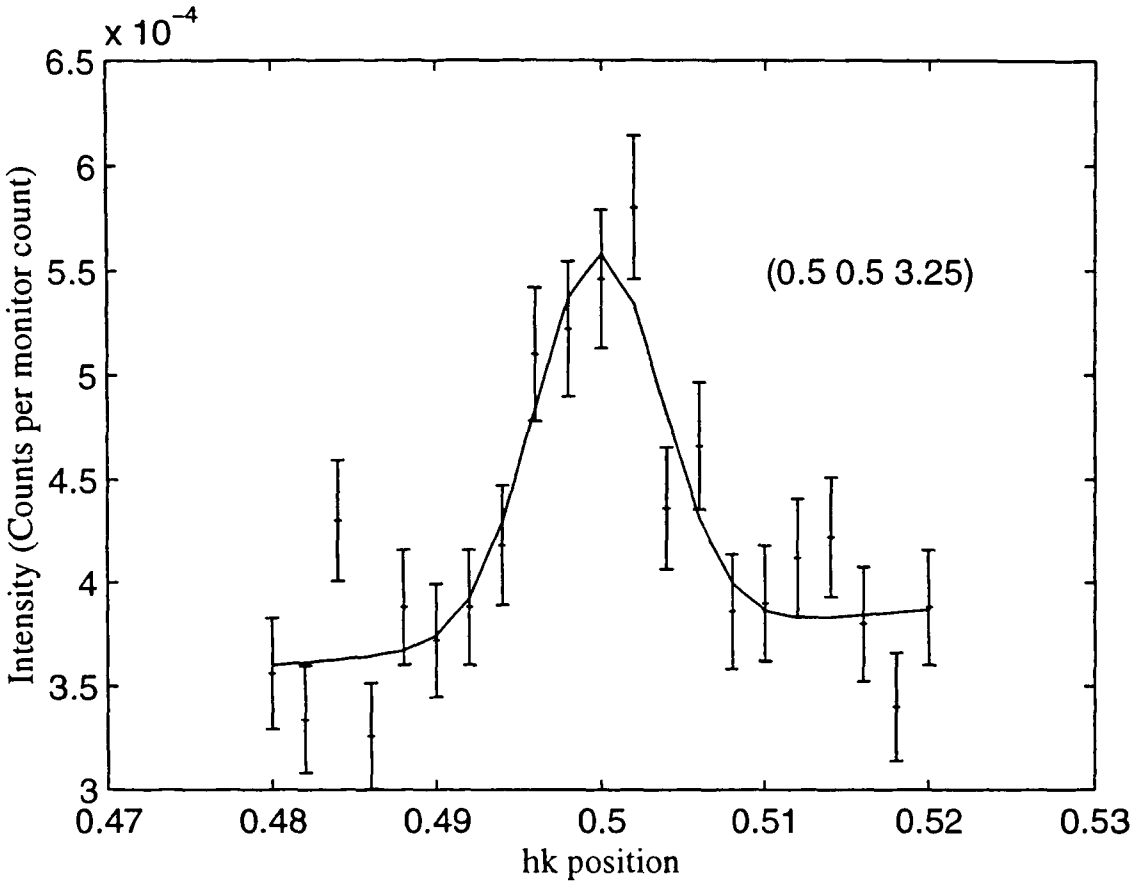

Figure 4.9: Non-stoichiometric reduced crystal magnetic ridge (0.5, 0.5, 3.25)

From this we can confirm the width of the ridge to check the resolution calculation so that the ridge contribution can be removed from the Bragg peaks.

Figure 4.10 shows a scan along the ridge in the l direction. Each point is simply a count of the scattered neutrons at the nominal position. The powder scattering lines around $l = 4.5, 5.3, 6.2$ have been removed for clarity, and the points have been chosen to avoid the Bragg peaks.

The intensity has been normalized using the z factor for a Bragg rod (See Equation 3.53). Due to the simple counting procedure, the background is not well defined, and so the background has not been subtracted. The lines show an estimated background (and the error) taken from interpolated values of the background on the peak measurements in Section 4.4.8. Note that the background estimate at large l is poor, mainly due to the presence of the powder lines.

The actual ordering of the ridge can be analysed by taking the background corrected values for the ridge (as in Section 4.4.8), and correcting them as described in Section 3.9.

In this case, as the Nd moments are not ordering in the c direction, a different magnetic unit cell was used for the calculation; the cell was $2 \times 2 \times 1$ nuclear unit cells, and the

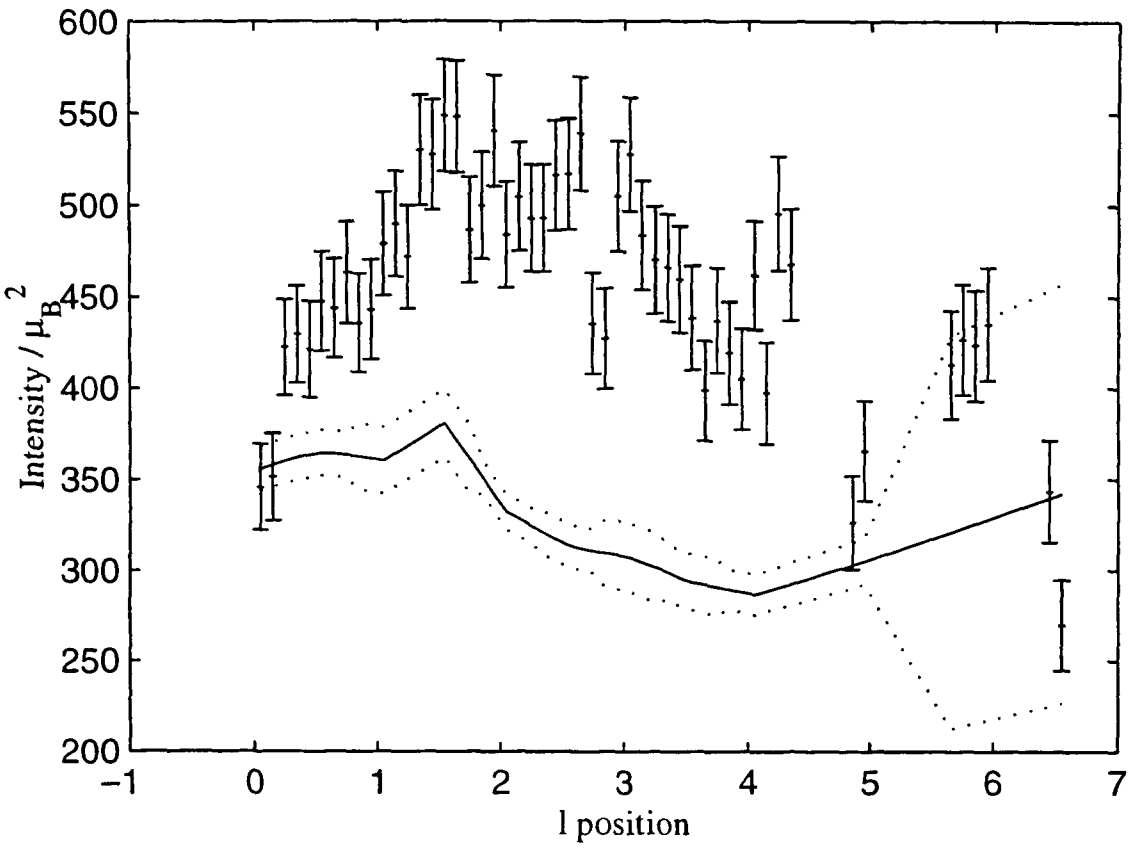

Figure 4.10: Non-stoichiometric reduced crystal magnetic ridge l scan. The values have been normalized and corrected for instrumental effects. The line shows the estimated background and the dashed lines indicate the error on this.

normalization was corrected appropriately.

Table 4.10 gives the measured and theoretical intensities. It is immediately noticeable that there are considerable differences in the measured and model intensities. These discrepancies are similar in form to those observed for the second reduced crystal, as discussed in Section 4.5.4. The main discrepancy is that the $(\frac{1}{2}, \frac{1}{2}, \frac{1}{2})$ is far lower than expected (and this skews the other values due to the theoretical intensity being a least squares fit). This may be due to a misalignment, but also may indicate a variation in the neodymium form factor. Further discussion is given in the sections describing the next crystal.

The free parameters were the neodymium moment and the angle of tilt away from the c direction. However, the angle was found to be close to parallel to the ab plane. At this angle, the intensities of the Bragg peaks are insensitive to the variation of the angle. Thus, the moment was set to being in the ab plane and the fit shown has only the neodymium moment as a free parameter. The moment is similar to the moments found for the other crystals, but the error is likely to be large due to the discrepancies with the model.

$(h\ k\ l)$	Intensity / μ_B^2	Theory
$(\frac{1}{2}\ \frac{1}{2}\ \frac{1}{2})$	59.4 ± 3.7	69.6
$(\frac{1}{2}\ \frac{1}{2}\ 1)$	84.8 ± 5.0	77.5
$(\frac{1}{2}\ \frac{1}{2}\ \frac{3}{2})$	132.0 ± 7.5	86.4
$(\frac{1}{2}\ \frac{1}{2}\ 2)$	150.5 ± 8.9	93.7
$(\frac{1}{2}\ \frac{1}{2}\ \frac{5}{2})$	168.7 ± 10.0	98.8
$(\frac{1}{2}\ \frac{1}{2}\ 3)$	173.0 ± 10.3	101.6
$(\frac{1}{2}\ \frac{1}{2}\ \frac{7}{2})$	128.9 ± 8.2	102.5
$(\frac{1}{2}\ \frac{1}{2}\ 4)$	121.3 ± 8.3	101.9
$(\frac{1}{2}\ \frac{1}{2}\ 5)$	50.2 ± 3.8	97.4
χ^2	39.8	
Nd moment / μ_B	**1.47** ± 0.12	
Nd angle °	**90** (See text)	

Table 4.10: Non-stoichiometric reduced crystal magnetic ridge intensities at 313 mK

4.4.8 Magnetic peaks at 0.313 K

Measuring the magnetic peaks of the Cu ordering is complicated by the ridge of scattering.

To correct for this, I have used the measurement of the intensity of the ridge (Figure 4.10) interpolated from the values surrounding the peak to give a value at the peak. I then removed the background from this by subtracting the background measured in scans in the hk direction. From the values for the Bragg rod z factor and Lorentz factor (Equations 3.53 and 3.52), the theoretical width for the rod in a particular scan can be calculated. To correct the hk or ω scans, I thus performed a fit using two Gaussians, with one Gaussian constrained to the amplitude and width for the rod as described above.

The random error on the size of the rod peak calculated by this method is quite large, but for most of the peaks the correction is relatively small compared to the amplitude of the peak.

As the temperature decreases below 4 K we would expect the copper ordering to tend more towards an AF2 ground state.

Table 4.11 shows the peak intensities after the contributions from the Bragg rod have been removed.

The theoretical values assume an AF2 intermediate structure. The only free parameters are the magnitude of the Cu moment and the rotation of the moments away from the AF1 structure towards the AF2 structure.

$(h\ k\ l)$	Intensity / μ_B^2	Theory
$(\frac{1}{2}\ \frac{1}{2}\ \frac{1}{2})$	4.6 ± 0.4	6.2
$(\frac{1}{2}\ \frac{1}{2}\ 1)$	10.1 ± 0.7	9.5
$(\frac{1}{2}\ \frac{1}{2}\ \frac{3}{2})$	39.2 ± 1.5	36.9
$(\frac{1}{2}\ \frac{1}{2}\ 2)$	17.0 ± 0.9	16.1
$(\frac{1}{2}\ \frac{1}{2}\ \frac{5}{2})$	23.9 ± 1.4	22.3
$(\frac{1}{2}\ \frac{1}{2}\ 3)$	2.6 ± 0.9	2.1
$(\frac{1}{2}\ \frac{1}{2}\ \frac{7}{2})$	1.0 ± 1.6	0.8
$(\frac{1}{2}\ \frac{1}{2}\ 4)$	5.8 ± 1.5	6.0
$(\frac{1}{2}\ \frac{1}{2}\ \frac{9}{2})$	29.9 ± 4.5	32.9
$(\frac{1}{2}\ \frac{1}{2}\ 5)$	12.7 ± 2.0	17.9
$(\frac{1}{2}\ \frac{1}{2}\ \frac{11}{2})$	47.3 ± 5.7	33.2
$(\frac{1}{2}\ \frac{1}{2}\ 6)$	2.5 ± 2.2	6.4
$(\frac{1}{2}\ \frac{1}{2}\ \frac{13}{2})$	4.2 ± 5.4	1.5
$(\frac{3}{2}\ \frac{3}{2}\ \frac{7}{2})$	2.9 ± 3.4	0.2
χ^2	2.9	
Cu moment / μ_B	**0.620** ± 0.015	
Cu rotation °	**56.8** ± 1.3	

Table 4.11: Non-stoichiometric reduced crystal magnetic peak intensities at 313 mK

The moment and rotation is essentially unchanged from that as measured at 4.4 K. Thus, the copper ordering does not seem to be affected by the Nd ordering. This is also indicated in Figure 4.6, where the peaks corresponding to the copper moments do not significantly change in intensity except with the addition of the ridge scattering. There is again no evidence for a significant ordered moment on the copper chain sites.

It is notable that the measured intensity of the $(\frac{1}{2}, \frac{1}{2}, \frac{1}{2})$ is again significantly smaller than the theoretical value. This is further indication that the discrepancy in Section 4.4.7 is likely to be an alignment problem.

4.4.9 Discussion

This crystal shows two unusual magnetic structure features.

- At low temperatures the Cu moments rotate towards an AF2 structure.
- The formation of a ridge of scattering indicates that the Nd is forming a two dimensional structure, with the moments uncorrelated in the c direction. The measurements shown that the Nd moments do not significantly form any kind of three dimensional ordering, at any of the temperatures at which they were measured.

The Cu moment structure is adequately explained by an AF2 structure, and there is no evidence for an AF3 like coupling between the Nd and the Cu moments. Of course, an AF3 structure itself cannot occur as the Nd moments do not form a three dimensional structure. The AF2 structure of the Cu moments is within error of being identical above and below the temperature at which the Nd ions order.

Other studies [5] have shown that the behaviour of the Cu moments is likely to be due to the crystal being slightly non-stoichiometric. The particular difference in the structure is believed to be substitution of Nd on the Ba sites.

It seems likely that this is the reason also for the behaviour of the Nd moments, in that the substitution will have changed the crystal field sufficiently to stop the interaction across unit cells in the c direction. However, the unusual ordering of the Cu and Nd do not seem to be directly related to each other, as the AF2 structure of the Cu moments begins to form at temperatures higher than the point where the Nd moments order. Thus, again, there is no evidence from this for any coupling between the Nd and Cu moments.

There is a significant discrepancy between the measured intensity and the theoretical intensity at low temperature, particularly for the $(\frac{1}{2}, \frac{1}{2}, \frac{1}{2})$ peak. This seems to be largely an alignment effect. A similar discrepancy is seen in the next crystal, which led to further measurements.

4.5 Stoichiometric $NdBa_2Cu_3O_6$

4.5.1 Introduction

Following the evidence of a non-stoichiometric composition in the previous reduced sample, we measured another sample which we believe to be more stoichiometric.

4.5.2 Sample mosaicity

For comparison with the previous crystals, Figure 4.11 shows a typical ω scan across the $(1, 1, 3)$ nuclear peak.

The width of the peak shown is $0.161 \pm 0.005°$. With the mosaicity as in Table 4.14 the theoretical width is $0.156°$. Without the correction for the sample mosaicity, the theoretical

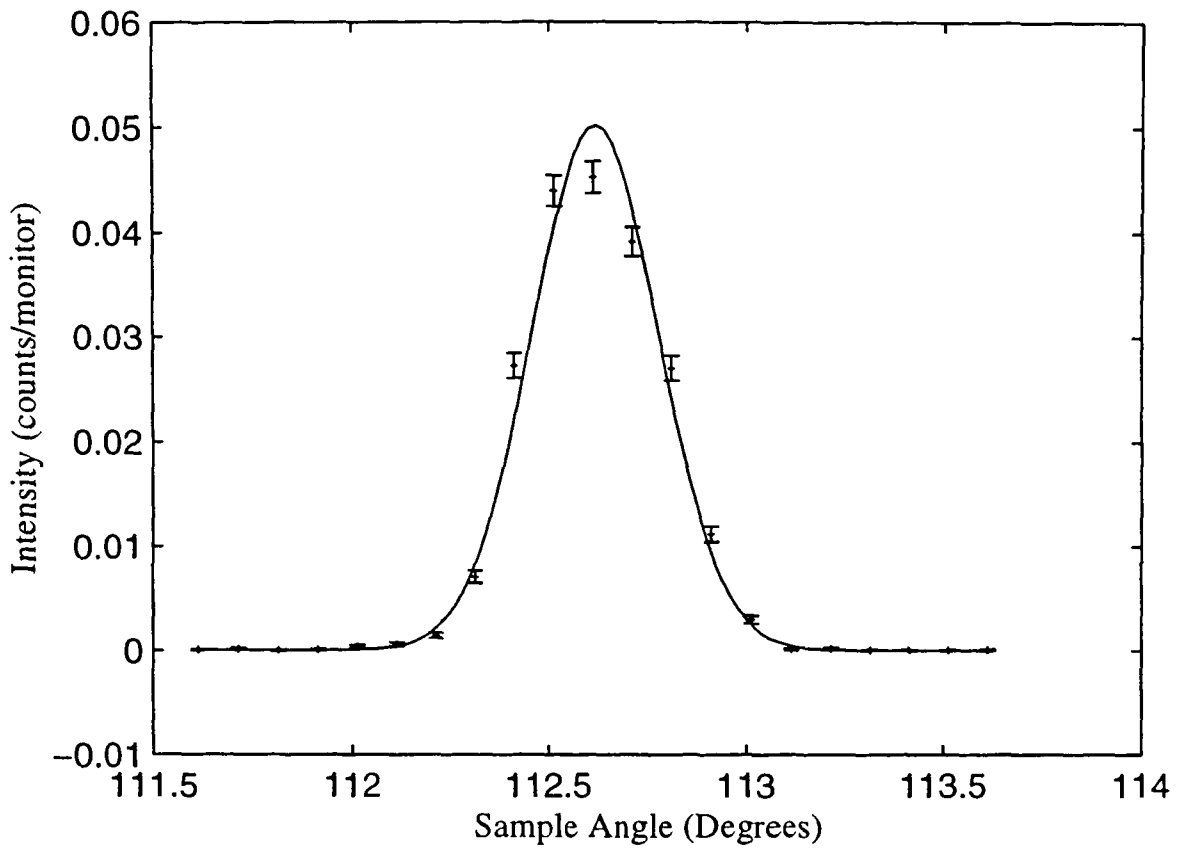

Figure 4.11: Stoichiometric reduced crystal ω scan across $(1, 1, 3)$.

width would be 0.114°.

4.5.3 Nuclear Peaks

The crystal structure was provided by four-circle neutron diffraction data [5].

The measurements of the nuclear peaks for normalization are shown in Tables 4.12 and 4.13, along with the theoretical widths and intensities.

The values for the resolution correction used in the above table are shown in Table 4.14 as well as the nominal values of the resolution parameters. The crystal structure parameters are as measured.

4.5.4 Magnetic peaks at 0.313 K

At 313 mK, two distinct sets of peaks were visible.

- At the $(\frac{1}{2}, \frac{1}{2}, l + \frac{1}{2})$ positions, peaks originating from neodymium ordering occurred. These were characterized by a small amount of Lorentzian broadening in the c direction. This gave an intrinsic width (HWHM) of approximately 0.0053 Å^{-1}, corresponding to a correlation length of $\xi_c \approx 190$ Å.

$(h\ k\ l)$	Scan	Intensity	Theory	Ratio
(001)	ω	1.40E-04 ± 3.5E-05	2.14E-08	6.55E+03
	l	2.49E-04 ± 4.7E-05		1.17E+04
(002)	ω	4.32E-06 ± 1.3E-06	3.22E-11	1.34E+05
(003)	ω	3.38E-04 ± 5.8E-05	1.46E-08	2.31E+04
	l	3.70E-04 ± 2.0E-05		2.53E+04
(004)	ω	1.42E-03 ± 2.1E-04	7.97E-08	1.79E+04
	l	1.18E-03 ± 4.4E-05		1.48E+04
(005)	ω	1.78E-03 ± 2.6E-04	7.65E-08	2.33E+04
	l	1.33E-03 ± 6.2E-05		1.75E+04
(006)	ω	4.10E-03 ± 4.5E-04	2.06E-07	1.99E+04
	l	2.49E-03 ± 7.7E-05		1.21E+04
(007)	ω	2.91E-03 ± 2.5E-04	8.09E-08	3.60E+04
	l	1.79E-03 ± 9.6E-05		2.21E+04
(110)	ω	1.80E-03 ± 2.2E-04	8.33E-08	2.16E+04
	hk	1.94E-03 ± 5.6E-05		2.33E+04
	l	1.77E-03 ± 2.1E-04		2.13E+04
(111)	ω	6.00E-04 ± 5.4E-05	2.72E-08	2.20E+04
	hk	4.88E-04 ± 3.9E-05		1.79E+04
	l	5.75E-04 ± 5.5E-05		2.11E+04
(112)	ω	-9.50E-07 ± 6.8E-07	6.46E-12	-1.47E+05
(113)	ω	1.31E-03 ± 7.7E-05	5.62E-08	2.33E+04
	hk	9.26E-04 ± 1.1E-04		1.65E+04
	l	1.36E-03 ± 9.0E-05		2.42E+04
(114)	ω	9.14E-04 ± 6.1E-05	2.89E-08	3.16E+04
	hk	6.76E-04 ± 6.0E-05		2.34E+04
	l	9.25E-04 ± 4.5E-05		3.20E+04
(115)	ω	2.28E-05 ± 1.3E-05	7.63E-10	2.99E+04
(116)	ω	3.68E-03 ± 1.7E-04	1.51E-07	2.44E+04
	hk	3.04E-03 ± 1.5E-04		2.02E+04
	l	3.96E-03 ± 1.2E-04		2.63E+04

Table 4.12: Stoichiometric reduced crystal nuclear peak intensities

$(h\ k\ l)$	Scan	Width	Theory	Ratio
(001)	ω	1.61E-01 ± 2.1E-02	1.89E-01	0.85
	l	2.10E-02 ± 2.1E-03	2.04E-02	1.03
(002)	ω	2.18E-01 ± 4.4E-02	1.73E-01	1.26
(003)	ω	1.59E-01 ± 1.5E-02	1.64E-01	0.97
	l	2.48E-02 ± 6.9E-04	2.63E-02	0.94
(004)	ω	1.51E-01 ± 1.2E-02	1.59E-01	0.95
	l	2.62E-02 ± 5.1E-04	3.07E-02	0.85
(005)	ω	1.50E-01 ± 1.1E-02	1.56E-01	0.96
	l	2.82E-02 ± 6.9E-04	3.56E-02	0.79
(006)	ω	1.64E-01 ± 9.1E-03	1.55E-01	1.05
	l	3.22E-02 ± 5.2E-04	4.09E-02	0.79
(007)	ω	1.68E-01 ± 7.0E-03	1.55E-01	1.08
	l	3.49E-02 ± 9.7E-04	4.64E-02	0.75
(110)	ω	1.53E-01 ± 9.6E-03	1.58E-01	0.97
	hk	7.35E-03 ± 1.1E-04	7.47E-03	0.98
	l	1.15E-02 ± 6.9E-04	1.19E-02	0.97
(111)	ω	1.35E-01 ± 6.6E-03	1.58E-01	0.86
	hk	8.32E-03 ± 3.7E-04	1.05E-02	0.79
	l	1.07E-02 ± 5.5E-04	1.18E-02	0.91
(112)	ω	1.61E-01 *	1.57E-01	1.02
(113)	ω	1.61E-01 ± 4.7E-03	1.56E-01	1.03
	hk	5.31E-03 ± 3.2E-04	7.82E-03	0.68
	l	1.59E-02 ± 5.1E-04	1.45E-02	1.09
(114)	ω	1.59E-01 ± 5.3E-03	1.55E-01	1.02
	hk	5.34E-03 ± 2.4E-04	7.04E-03	0.76
	l	1.86E-02 ± 4.6E-04	1.70E-02	1.10
(115)	ω	1.59E-01 ± 0.0E+00	1.55E-01	1.02
(116)	ω	1.73E-01 ± 0.0E+00	1.55E-01	1.11
	hk	6.14E-03 ± 1.5E-04	6.92E-03	0.89
	l	2.78E-02 ± 4.3E-04	2.36E-02	1.18

Table 4.13: Stoichiometric reduced crystal nuclear peak widths: Asterisks denote widths that could not be determined accurately by measurement. As with the other crystals, the units of the widths are dependent on the scan types.

Parameter	Nominal Value	Derived Value
η_m	30	30
η_a	30	30
α_0	60	60
α_1	30	30
α_2	60	60
α_3	open	200
Geometry	r,r,l	r,r,l
Crystal a	3.898	
Crystal b	3.898	
Crystal c	11.882	
η_s	Unknown	15
Oxygen content	6.09 ± 0.01	
Ba z	0.1925	
Cu2 z	0.3537	
O1 z	0.1521	
O2 z	0.3718	
Nd content	1.01 ± 0.01	
Ba content	2.01 ± 0.02	
Sn content	$\approx$0.001	
Al content	0.02 ± 0.01	
Zn content	$\approx$0.001	

Table 4.14: Stoichiometric reduced crystal resolution parameters

$(h\ k\ l)$	Intensity / μ_B^2	Theory
$(\frac{1}{2}\ \frac{1}{2}\ 0)$	0.0 ± 1.1	0.0
$(\frac{1}{2}\ \frac{1}{2}\ \frac{1}{2})$	46.7 ± 1.4	56.5
$(\frac{1}{2}\ \frac{1}{2}\ 1)$	20.4 ± 1.0	25.5
$(\frac{1}{2}\ \frac{1}{2}\ \frac{3}{2})$	45.4 ± 1.7	70.1
$(\frac{1}{2}\ \frac{1}{2}\ 2)$	39.4 ± 1.7	45.0
$(\frac{1}{2}\ \frac{1}{2}\ \frac{5}{2})$	72.0 ± 2.3	80.2
$(\frac{1}{2}\ \frac{1}{2}\ 3)$	8.6 ± 0.7	7.3
$(\frac{1}{2}\ \frac{1}{2}\ \frac{7}{2})$	93.9 ± 2.8	83.3
$(\frac{1}{2}\ \frac{1}{2}\ 4)$	17.8 ± 1.2	13.5
$(\frac{1}{2}\ \frac{1}{2}\ \frac{9}{2})$	109.3 ± 3.3	81.4
$(\frac{1}{2}\ \frac{1}{2}\ 5)$	70.3 ± 3.1	48.6
$(\frac{1}{2}\ \frac{1}{2}\ \frac{11}{2})$	122.2 ± 4.3	76.5
$(\frac{1}{2}\ \frac{1}{2}\ 6)$	34.5 ± 2.7	21.9
$(\frac{1}{2}\ \frac{1}{2}\ \frac{13}{2})$	130.2 ± 4.2	69.8
$(\frac{1}{2}\ \frac{1}{2}\ 7)$	4.8 ± 2.3	0.9
$(\frac{1}{2}\ \frac{1}{2}\ \frac{1}{2})$	43.2 ± 10.3	38.6
$(\frac{3}{2}\ \frac{3}{2}\ 1)$	0.0 ± 5.6	6.7
$(\frac{3}{2}\ \frac{3}{2}\ \frac{5}{2})$	94.1 ± 2.8	41.1
$(\frac{3}{2}\ \frac{3}{2}\ 3)$	1.3 ± 2.3	1.6
Nd χ^2	115	
Nd moment / μ_B	**1.325** ± 0.066	
Nd angle °	**90** (See text)	
Cu χ^2	13.7	
Cu moment / μ_B	**0.563** ± 0.075	

Table 4.15: Stoichiometric reduced crystal magnetic peak intensities at 313 mK

- At the $(\frac{1}{2}, \frac{1}{2}, l)$ positions peaks corresponding to AF1 ordering of the copper were visible.

Table 4.15 shows the normalized peak intensities, and the intensities from the model. Unfortunately, the peaks showed significant discrepancies between the model of the apparatus and the measured values. In particular, the widths of the peaks were significantly different, especially very near the origin of reciprocal space. The neodymium peaks shown in the table have been corrected by the use of a Lorentz factor for the intrinsic width of the peak. Due to the discrepancies, the copper peaks have been simply normalized using the z factor.

As with the previous sample, the neodymium ordering has some particular differences between theory and measurement. As before, the $(\frac{1}{2}, \frac{1}{2}, \frac{1}{2})$ peak is far lower than would be expected. This leads to the huge χ^2. As with the previous crystal, the neodymium moment

was tilted away from the c axis, and was set to be parallel to the ab for the fit. Despite the discrepancies between theory and experiments, the model used for the neodymium moment is likely to be correct, as the different possible structures for the neodymium moments give very different intensity patterns for the peaks.

The copper peaks are much closer to the intensities indicated by theory, but there is still considerable difference.

To improve the reliability of the measurements on these peaks and to see if the discrepancy in the neodymium measurements was an alignment problem, some additional measurements were later taken (see Section 4.5.7).

The theoretical values assume independent Nd and Cu ordering, so there is no indication of AF3 type ordering.

4.5.5 Temperature scan 0.31 K to 3 K

To further investigate the ordering, we measured the $(\frac{1}{2}, \frac{1}{2}, \frac{3}{2})$, $(\frac{1}{2}, \frac{1}{2}, 2)$, and $(\frac{1}{2}, \frac{1}{2}, \frac{7}{2})$ peaks as a function of temperature.

Figure 4.12 shows the intensities of these peaks. The intensities have been normalized against the nuclear peaks.

The formation of the Nd ordering is clear from the $(\frac{1}{2}, \frac{1}{2}, \frac{3}{2})$ and $(\frac{1}{2}, \frac{1}{2}, \frac{7}{2})$ peaks. As this ordering occurs, there is no visible change in the intensity of the copper peak at $(\frac{1}{2}, \frac{1}{2}, 2)$. This is again evidence of no coupling between the Nd and Cu moments.

The lines for the neodymium ordering are based on Equation 4.2. These give the ordering temperatures as 1.78 ± 0.04 K and 1.74 ± 0.01 K. These of course should be identical, but the fits agree within error. The fitted curves give values for 2β of 0.52 ± 0.07 and 0.42 ± 0.03.

4.5.6 Temperature scan 10 K to 378 K

To determine the copper ordering, we measured the $(\frac{1}{2}, \frac{1}{2}, 2)$ peak as a function of temperature from 10 K to 378 K in relatively coarse steps.

The low temperature range was obtained using a displex. The temperatures above room temperature required a furnace. Each region requires different normalization of the intensities. The normalization measurements for the furnace part were relatively inaccurate,

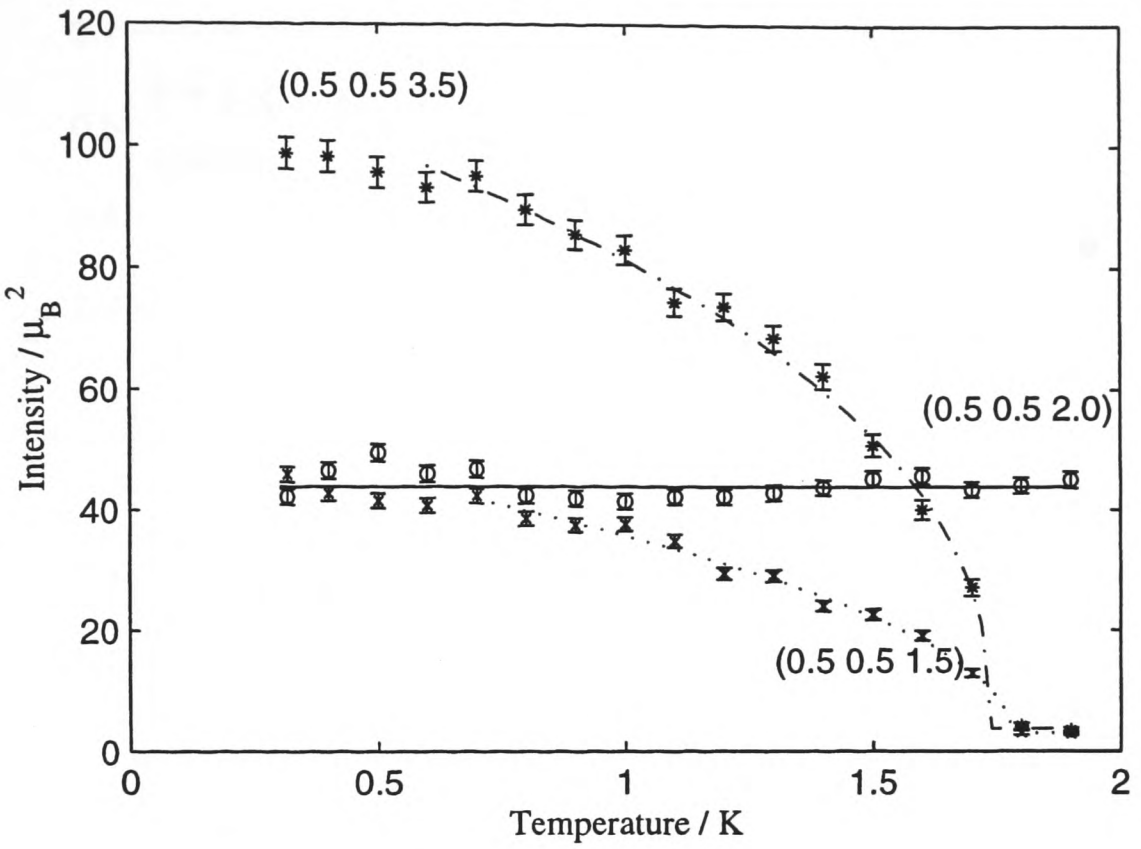

Figure 4.12: Stoichiometric reduced crystal magnetic peak temperature scan: The variation of the intensities with temperature.

so the furnace section has simply been scaled to match the displex section.

Figure 4.13 shows the derived value of the ordered Cu moment. The moment is calculated from the normalized intensities using the model from Section 4.5.5.

The line is a fit based on Equation 4.2 and gives a very good fit to the data. In fact the fitted curve indicates that the errors on the displex measurements are likely to be slightly overestimated. The fit gives an ordering temperature of $T_c = 375.9 \pm 0.1$ K which seems consistent with where the peak disappears (judging directly from the data, a slightly more realistic estimate is 378 ± 2 K). The fit gives a value of 0.237 ± 0.003 for β.

4.5.7 Grid measurements

Due to the discrepancies in the measurements of the peaks at low temperatures, further measurements were made.

To reduce the alignment systematic errors on the measurements, the procedure was changed. For these measurements, a series of scans were taken across the peak, offset by differing amounts perpendicular to the direction of the scan. This gives a two-dimensional

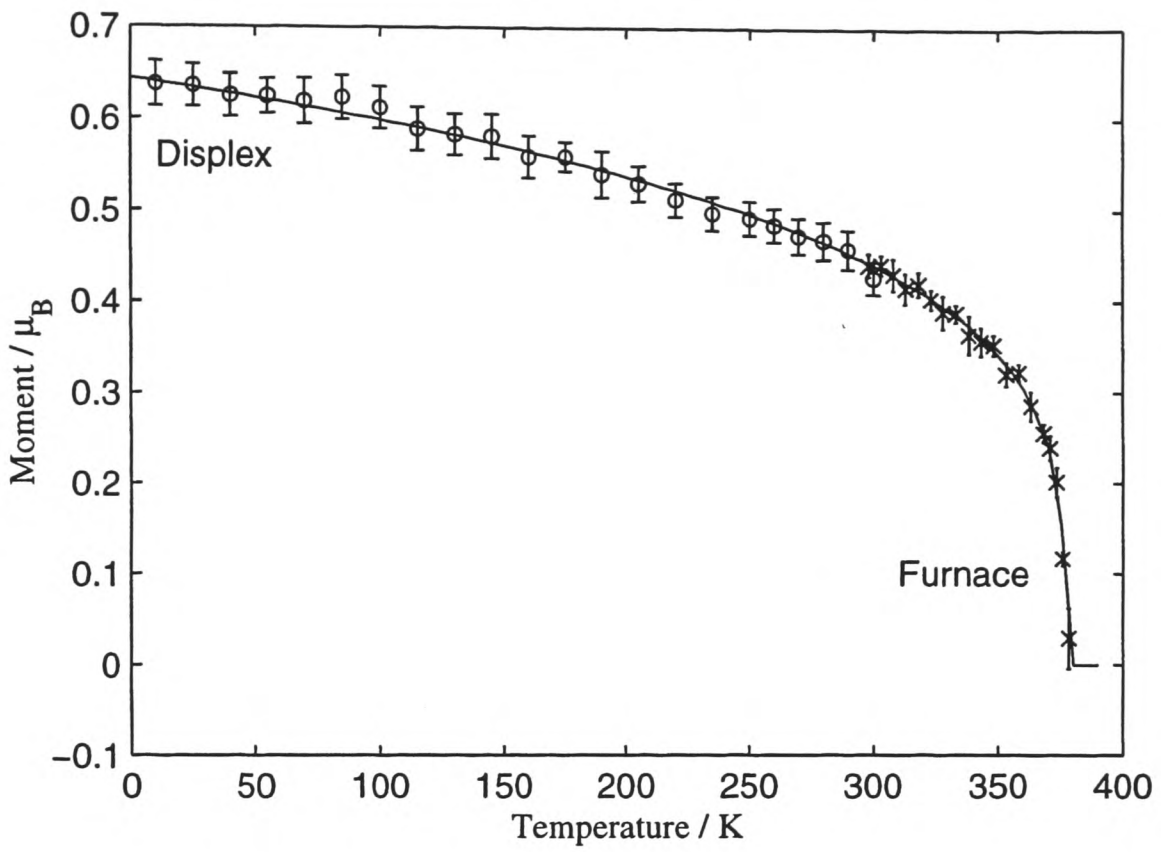

Figure 4.13: Stoichiometric reduced crystal copper ordering: The variation of the moment with temperature.

representation of the peak. This should remove virtually all rotational alignment errors, but may still be prone to errors caused by a precession of the sample.

As explained in Section 3.12 the normalization of the peaks in this case is much simpler.

To calculate the volume of the peak on a two dimensional grid, each of the scans were fitted to a Gaussian shape, with a background. The areas of these peaks were then taken and also fitted to a Gaussian shape. In all but a few cases the shape was very close to that of a Gaussian, indicating that the Gaussian ellipsoid approximation is justified. The area of this peak is proportional to the volume of the peak.

4.5.8 Nuclear peaks grid scans

To perform the normalization, the nuclear peaks were scanned in a grid fashion.

Table 4.16 shows the intensities of the peaks, and the theoretical values for the intensities. Note that there is a scaling factor between the two.

As with the other nuclear measurements, the agreement between theory and experiment is quite poor. However, this is to be expected due to the simple model used for the nuclear

$(h\ k\ l)$	Intensity	Theory	Ratio
(001)	1.52E-06 ± 2.8E-07	2.14E-08	7.12E+01
(002)	1.44E-08 ± 1.7E-09	3.22E-11	4.47E+02
(003)	2.27E-06 ± 1.1E-07	1.46E-08	1.55E+02
(004)	8.96E-06 ± 2.2E-07	7.97E-08	1.13E+02
(005)	9.10E-06 ± 3.5E-07	7.65E-08	1.19E+02
(006)	1.95E-05 ± 8.0E-07	2.06E-07	9.46E+01
(007)	1.17E-05 ± 6.8E-07	8.09E-08	1.44E+02
(110)	1.01E-05 ± 7.7E-07	8.33E-08	1.21E+02
(111)	4.43E-06 ± 2.4E-07	2.72E-08	1.63E+02
(112)	5.71E-09 ± 2.4E-09	6.46E-12	8.83E+02
(113)	7.64E-06 ± 6.3E-07	5.62E-08	1.36E+02
(114)	4.85E-06 ± 4.3E-07	2.89E-08	1.68E+02
(115)	1.65E-07 ± 8.1E-09	7.63E-10	2.16E+02
(116)	1.40E-05 ± 1.6E-06	1.51E-07	9.28E+01
		Average	1.36E+02
		Error	1.92E+00

Table 4.16: Stoichiometric reduced crystal nuclear grid scans

intensities.

4.5.9 Magnetic Peaks 4.4 K grid scans

To measure the copper ordering, the $(h+\frac{1}{2}, k+\frac{1}{2}, l)$ peaks were measured using the grid scan technique.

Initial measurements of the $(h+\frac{1}{2}, k+\frac{1}{2}, l+\frac{1}{2})$ peaks had no intensity, showing that the Nd ions do not order at this temperature. Thus, the peaks with non-integer l values were not measured fully.

Table 4.17 shows the normalized intensities of the peaks, and the theoretical values for a fit with the Cu ions forming a simple AF1 structure.

The theoretical values have only the copper moment as a free parameter. The low χ^2 indicates that this is an adequate model of the copper ordering.

4.5.10 Linear scans at 4.4 K and 0.3 K

The previous measurements had suggested that the copper ordering did not change with the onset of the Nd ordering.

$(h\ k\ l)$	Intensity / μ_B^2	Theory
$(\frac{1}{2}\ \frac{1}{2}\ 1)$	28.7 ± 1.7	30.6
$(\frac{1}{2}\ \frac{1}{2}\ 2)$	49.6 ± 2.0	54.2
$(\frac{1}{2}\ \frac{1}{2}\ 3)$	10.3 ± 1.2	8.8
$(\frac{1}{2}\ \frac{1}{2}\ 4)$	16.7 ± 1.6	16.2
$(\frac{1}{2}\ \frac{1}{2}\ 5)$	62.1 ± 3.8	58.5
$(\frac{1}{2}\ \frac{1}{2}\ 6)$	29.6 ± 1.4	26.4
$(\frac{3}{2}\ \frac{3}{2}\ 1)$	10.7 ± 3.3	8.1
$(\frac{3}{2}\ \frac{3}{2}\ 2)$	18.0 ± 2.9	12.4
χ^2	2.39	
Cu moment / μ_B	**0.618** ± 0.013	

Table 4.17: Stoichiometric reduced crystal copper ordering

To test this, $(h+\frac{1}{2}, k+\frac{1}{2}, l)$ peaks were also measured using the previous linear scan technique at both 4.4 K and 3.3 K.

As a simpler normalization technique, these scans were normalized directly against the intensity of the grid scans at 4.4 K. This assumes that the grid scan measurements are accurate, and so the random errors quoted on the moments in this section do not include the systematic error on the normalization factor.

Table 4.18 shows the unnormalized areas of the measured peaks at 0.3 K and 4.4 K for comparison. Any changes in the measured area are consistent with experimental error. The average ratio of the intensities is unity to better than 1%. The random error on the measurements puts a limit on the size of any change at 3%.

Table 4.19 shows the intensities of the copper peaks normalized to the grid scans to give a value for the copper moment.

These measurements show that the copper ordering does not significantly change between 4.4 K and 0.3 K and thus the copper ordering is not affected by the neodymium ordering.

4.5.11 Magnetic Peaks 0.3 K grid scans

To measure the Nd ordering, the $(h+\frac{1}{2}, k+\frac{1}{2}, l+\frac{1}{2})$ peaks were measured using the grid scan technique.

As shown in Section 4.5.10, the copper ordering does not change, so the copper peaks were not measured again with the grid technique at this temperature.

$(h\ k\ l)$	Scan	Scan area at 0.3 K	Scan area at 4.4 K	Difference
$(\frac{1}{2}\ \frac{1}{2}\ 1)$	ω	8.96E-05 ± 4.0E-06	8.89E-05 ± 3.3E-06	0.14
$(\frac{1}{2}\ \frac{1}{2}\ 1)$	l	3.87E-06 ± 2.2E-07	3.92E-06 ± 1.8E-07	0.17
$(\frac{1}{2}\ \frac{1}{2}\ 2)$	ω	1.13E-04 ± 5.2E-06	1.19E-04 ± 4.2E-06	0.81
$(\frac{1}{2}\ \frac{1}{2}\ 2)$	l	6.89E-06 ± 2.4E-07	7.01E-06 ± 2.7E-07	0.33
$(\frac{1}{2}\ \frac{1}{2}\ 3)$	ω	1.93E-05 ± 2.0E-06	1.71E-05 ± 1.8E-06	0.84
$(\frac{1}{2}\ \frac{1}{2}\ 3)$	l	1.56E-06 ± 8.4E-08	1.44E-06 ± 1.7E-07	0.66
$(\frac{1}{2}\ \frac{1}{2}\ 4)$	ω	2.49E-05 ± 2.1E-06	2.67E-05 ± 2.1E-06	0.58
$(\frac{1}{2}\ \frac{1}{2}\ 4)$	l	3.03E-06 ± 2.3E-07	2.92E-06 ± 2.5E-07	0.32
$(\frac{1}{2}\ \frac{1}{2}\ 5)$	ω	6.50E-05 ± 4.3E-06	6.86E-05 ± 4.3E-06	0.58
$(\frac{1}{2}\ \frac{1}{2}\ 5)$	l	9.16E-06 ± 6.6E-07	1.01E-05 ± 6.3E-07	0.93
$(\frac{1}{2}\ \frac{1}{2}\ 6)$	ω	2.57E-05 ± 2.2E-06	2.29E-05 ± 1.9E-06	1.01
$(\frac{1}{2}\ \frac{1}{2}\ 6)$	l	4.82E-06 ± 5.1E-07	5.08E-06 ± 9.3E-07	0.24

Table 4.18: Stoichiometric reduced crystal copper peaks scan area: The unnormalized areas of the measured peaks at 0.3 K and 4.4 K. The difference column is the ratio of the difference between the intensities to the error on the difference.

Temperature	$(h\ k\ l)$	Moment
0.3 K	$(\frac{1}{2}\ \frac{1}{2}\ 1)$	5.98E-01 ± 1.6E-02
	$(\frac{1}{2}\ \frac{1}{2}\ 2)$	5.74E-01 ± 1.3E-02
	$(\frac{1}{2}\ \frac{1}{2}\ 3)$	6.43E-01 ± 3.5E-02
	$(\frac{1}{2}\ \frac{1}{2}\ 4)$	6.40E-01 ± 3.3E-02
	$(\frac{1}{2}\ \frac{1}{2}\ 5)$	6.22E-01 ± 2.3E-02
	$(\frac{1}{2}\ \frac{1}{2}\ 6)$	6.28E-01 ± 1.9E-02
	Weighted average	6.04E-01 ± 7.9E-03
4.4 K	$(\frac{1}{2}\ \frac{1}{2}\ 1)$	5.83E-01 ± 1.5E-02
	$(\frac{1}{2}\ \frac{1}{2}\ 2)$	5.76E-01 ± 1.3E-02
	$(\frac{1}{2}\ \frac{1}{2}\ 3)$	6.58E-01 ± 3.8E-02
	$(\frac{1}{2}\ \frac{1}{2}\ 4)$	6.42E-01 ± 3.3E-02
	$(\frac{1}{2}\ \frac{1}{2}\ 5)$	6.43E-01 ± 2.4E-02
	$(\frac{1}{2}\ \frac{1}{2}\ 6)$	6.25E-01 ± 2.0E-02
	$(\frac{3}{2}\ \frac{3}{2}\ 1)$	6.89E-01 ± 1.1E-01
	$(\frac{3}{2}\ \frac{3}{2}\ 2)$	6.37E-01 ± 9.7E-02
	Weighted average	6.03E-01 ± 7.8E-03

Table 4.19: Stoichiometric reduced crystal copper peak moments: The copper peaks measured by linear scans normalized to the grid scans to give a value for the copper moment at each peak.

$(h\ k\ l)$	Intensity / μ_B^2	Theory
$(\frac{1}{2}\ \frac{1}{2}\ \frac{1}{2})$	51.7 ± 2.0	67.1
$(\frac{1}{2}\ \frac{1}{2}\ \frac{3}{2})$	81.2 ± 5.0	83.2
$(\frac{1}{2}\ \frac{1}{2}\ \frac{5}{2})$	97.5 ± 1.8	95.2
$(\frac{1}{2}\ \frac{1}{2}\ \frac{7}{2})$	104.9 ± 3.8	98.9
$(\frac{1}{2}\ \frac{1}{2}\ \frac{9}{2})$	105.8 ± 4.1	96.6
$(\frac{1}{2}\ \frac{1}{2}\ \frac{11}{2})$	95.8 ± 3.4	90.8
$(\frac{1}{2}\ \frac{1}{2}\ \frac{13}{2})$	91.1 ± 3.7	82.9
$(\frac{3}{2}\ \frac{3}{2}\ \frac{1}{2})$	41.6 ± 2.7	45.8
$(\frac{3}{2}\ \frac{3}{2}\ \frac{3}{2})$	49.7 ± 3.5	47.0
$(\frac{3}{2}\ \frac{3}{2}\ \frac{5}{2})$	60.7 ± 3.8	48.8
χ^2	9.15	
Nd moment / μ_B	**1.443** ± 0.028	
Nd angle °	**90** (See text)	

Table 4.20: Stoichiometric reduced crystal neodymium ordering

Table 4.20 shows the normalized intensities of the Nd peaks, and the fitted theoretical values. As before, the only fit free parameter was the moment, with the angle set to parallel to the *ab* plane.

The agreement between theory and experiment is much better than the measurement with linear scans, indicating that discrepancy is largely due to a misalignment.

However, the $(\frac{1}{2}, \frac{1}{2}, \frac{1}{2})$ peak is still significantly low. This may indicate that a problem with the neodymium form factor, or it may still be an instrumental effect.

4.5.12 Nd ordering temperature scan

To measure the ordering temperature of the Nd, linear scans of the $(\frac{1}{2}, \frac{1}{2}, \frac{1}{2})$ peak were made over a temperature range of 0.3 K to 1.9 K.

Figure 4.14 shows the intensity of this peak normalized to the Nd magnetic moment. Note that the normalization is based on the intensity of this peak alone. Compared to the other peaks the $(\frac{1}{2}, \frac{1}{2}, \frac{1}{2})$ peak is somewhat lower than expected, which is why the moments shown in the graph are lower than the moment calculated from the full fit. For the last two points (1.8 K and 1.9 K), no peak was visible. The error bars shown for these are the estimated error for detection of a peak.

The fitted line gives an ordering temperature of $T_c = 1.742 \pm 0.025$ K, and a value for β of 0.33 ± 0.05.

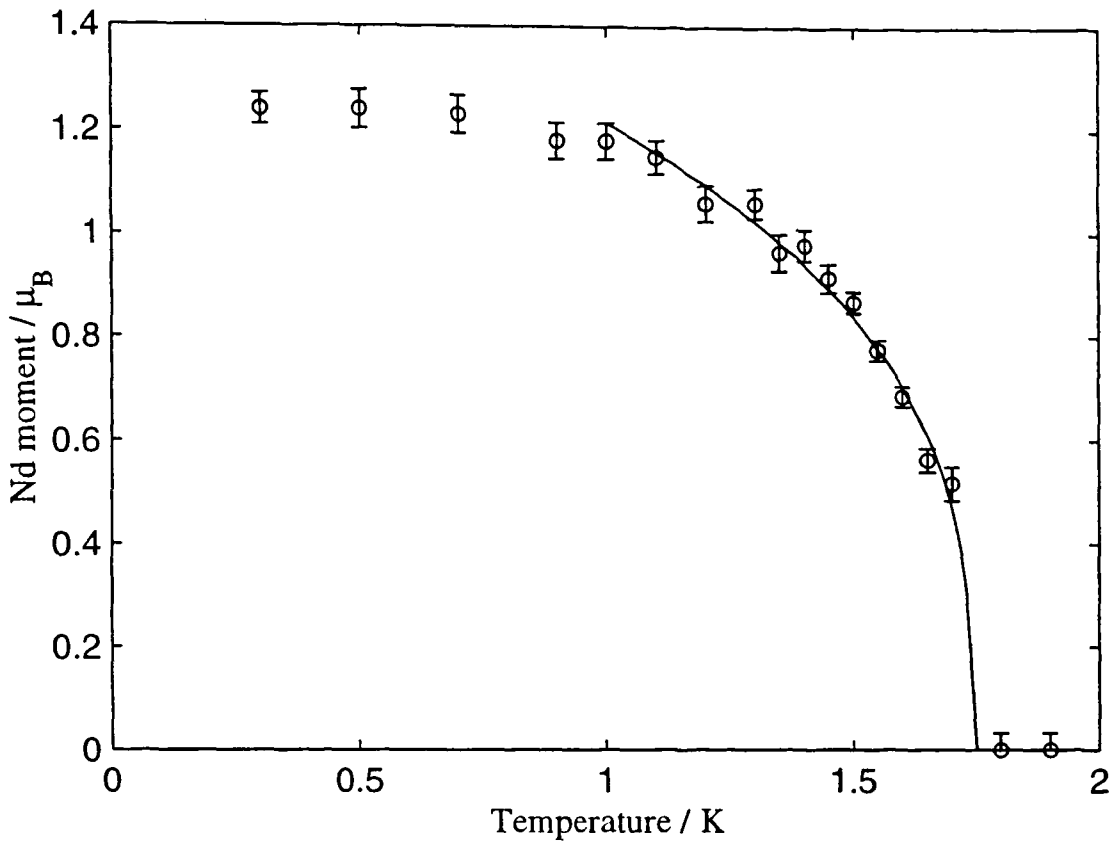

Figure 4.14: Stoichiometric reduced crystal $(\frac{1}{2}, \frac{1}{2}, \frac{1}{2})$ temperature variance

4.5.13 Discussion

The magnetic ordering in this crystal has proved to be relatively simple.

The Cu moments form an AF1 structure and remain so to the lowest temperatures measured.

The Nd moments form a simple antiferromagnetic structure in three dimensions. However, the moments do not lie in a direction close to the c direction. Unlike the oxygenated crystal, the Nd moments lie in or close to the ab plane.

Other studies [6, 7] have deduced the crystal field for the neodymium ion from inelastic neutron scattering measurements. From this they have predicted the neodymium moment direction to be dependent on the oxygen content. These results are consistent with this. Thus, the direction of the neodymium moment seems to be determined by the local crystal field.

The results presented here do not show any form of AF3 like coupling between the Nd and Cu moment as has been observed in $PrBa_2Cu_3O_6$.

4.6 References

[1] A.T. Boothroyd, J.M. Reynolds, N.H. Andersen, E. Brecht and Th. Wolf *Magnetic Ordering of* Nd^{3+} *in* $NdBa_2Cu_3O_{6+x}$, in press.

[2] Th. Wolf, A.C. Bornarel, H. Küpfer, R. Meier-Hirmer and B. Obst, *High irreversibility fields and current densities in* $NdBa_2Cu_3O_{7-\delta}$ *single crystals and melt textured samples*, Phys. Rev. B **56** 10 6308–6319 (1997).

[3] N.H. Andersen, B. Lebech and H.F. Poulsen, *The structural phase-diagram and oxygen equilibrium partial pressure of* $YBa_2Cu_3O_{6+x}$ *studied by neutron powder diffraction and gas volumetry*, Physica C **172** 1-2 31–42 (1990).

[4] M. Guillaume, P. Allenspach, W. Henggeler, J. Mesot, B. Roessli, U. Staub, P. Fischer, A. Furrer and V. Trounov, *A systematic low-temperature neutron diffraction study of the* $RBa_2Cu_3O_x$ *(R = yttrium and rare earths; x = 6 and 7) compounds*, J. Phys.: Cond. Matter **6** 39 7963–7976 (1994)

[5] E. Brecht, P. Schweiss, Th. Wolf, A.T. Boothroyd, J.M. Reynolds, N.H. Andersen, H. Lütgemeier and W.W. Schmahl, *On the antiferromagnetic states of oxygen deficient* $NdBa_2Cu_3O_{6+x}$ *and* $Nd_{1+y}Ba_{2-y}Cu_3O_{6+x}$ *single crystals*, Phys. Rev. B, in press.

[6] P. Allenspach, B.W. Lee, D.A. Gajewski, V.B. Barbeta, M.B. Maple, G. Nieva, S.-I. Yoo, M.J. Kramer, R.W. McCallum and L. Ben-Dor, *Comparison between the magnetic specific heat of* $NdBa_2Cu_3O_x$ *and* $DyBa_2Cu_3O_x$, Z. Phys. B **96** 4 455–464 (1995).

[7] P. Allenspach, J. Mesot, U. Staub, M. Guillaume, A. Furrer, S.-I. Yoo, M.J. Kramer, R.W. McCallum, H. Maletta, H. Blank, H. Mutka, R. Osborn, M. Arai, Z. Bowden and A.D. Taylor, *Magnetic properties of* Nd^{3+} *in* $Nd-Ba-Cu-O$*-compounds*, Z. Phys. B **95** 301–310 (1994).

Chapter 5

Magnetic Structure Conclusions

In this chapter, I summarize the measurements that were made and the conclusions from the results.

5.1 $NdBa_2Cu_3O_7$

The ordering of the $NdBa_2Cu_3O_7$ proved to be very simple.

There was no ordering of the copper moments and the neodymium moments ordered at 0.65 ± 0.01 K, forming a simple antiferromagnetic structure. The measured moment was $1.344 \pm 0.014\mu_B$ at $16.3 \pm 2.3°$ to the c direction.

The neodymium ordering is similar to that previously reported (see Chapter 2 Refs. [16, 18, 19]), but with a slightly higher moment, and a small tilt away from the c axis.

The neodymium showed evidence of slight Lorentzian broadening in the c direction, but this was less than 0.002 $Å^{-1}$ (HWHM), indicating a correlation length of greater than 500 Å.

5.2 Non-stoichiometric $NdBa_{2-y}Nd_yCu_3O_6$

The ordering of the non-stoichiometric $NdBa_{2-y}Nd_yCu_3O_6$ was considerably more complex.

At high temperatures, the Cu moments form an AF1 structure, with a moment of $0.620 \pm 0.021\mu_B$.

However, at low temperatures, the moments rotate towards an AF2 structure, with the rotation away from the AF2 structure being $59.4 \pm 1.9°$ at 4 K, and $56.8 \pm 1.4°$ at 0.313 K. The values of the moment at 4 K and 0.313 K are $0.632 \pm 0.020\mu_B$ and $0.620 \pm 0.015\mu_B$. Thus the moment remains essentially unchanged.

At 1.5 ± 0.1 K the Nd moments begin to form a two-dimensional structure, uncorrelated in the c direction. This causes a ridge of scattering in the l direction, the position of which shows the ordering to be antiferromagnetic. This ridge of scattering corresponds to a neodymium moment of $1.47 \pm 0.12\mu_B$. However, there are significant discrepancies between the measured intensities and the theoretical values; from the later measurements this is likely to largely be due to misalignment. Thus the actual error on the moment will be higher.

The moments are aligned well away from the c axis. Due to the discrepancies in the measurements, the exact angle is uncertain, but is likely to be greater than 60°.

Other studies (see Chapter 4 Ref. [5]) have indicated that the behaviour of the Cu moments is due to non-stoichiometric substitution of Nd on the Ba sites. It is likely that this is the cause of the Nd ordering as well, rather than an intermediate oxygenation.

The ordering does not indicate any form of coupling between the Cu and Nd moments.

5.3 Stoichiometric $NdBa_2Cu_3O_6$

The stoichiometric $NdBa_2Cu_3O_6$ showed a relatively simple ordering.

At 378 ± 2 K, the Cu moments form a AF1 structure with a low temperature moment of $0.618 \pm 0.013\mu_B$. This structure remains throughout all of the temperatures that were measured.

At 1.75 ± 0.02 K the Nd moments form a simple antiferromagnetic structure with a low temperature moment of $1.443 \pm 0.028\mu_B$.

The moments are tilted far away from the c direction. As with the previous sample, the exact angle is somewhat uncertain due to the insensitivity of the measurements to the angle when the moment is aligned far from the c direction.

The neodymium moments, while displaying a three dimensional ordering, showed signifi-

cant Lorentzian broadening. This had a width (HWHM) in the c direction of approximately 0.0053 $Å^{-1}$, giving a correlation length around 190 Å.

There is no evidence for any coupling of the copper and neodymium moments. The upper limit on the Cu spin turn angle towards an AF3 like phase is around 6° (See Chapter 4 Ref. [1]). Assuming that the antiparallel Cu spins on adjacent layers in the bilayer are coupled by an exchange energy $J_{\perp 1} \approx 10$ meV [1, 2], then the upper limit on the Nd-Cu pseudodipolar interaction energy will be ≈ 0.05 meV. Thus, the interaction energy is at least twenty times less than that observed in $PrBa_2Cu_3O_{6+\delta}$ (See Chapter 2 Ref. [13]).

5.4 Measurement techniques

For most of the measurements, the peak intensity was measured by taking linear scans across the peak centre.

This proved to be effective for many of the measurements. However, the necessary corrections to the measurements to account for the instrumental resolution are complex, and make various assumptions. In particular, a high precision in the alignment of the crystal is necessary.

For some of the measurements, this technique proved to be unreliable.

We then used the technique of making measurements of the intensity in a grid around the peak. This has the advantage of being less sensitive to the alignment of the crystal and the configuration of the instrument.

Of course, this method takes considerably more time to perform, as more scans are needed. However, the additional time need not be great if the measurements are chosen carefully. As the background can be taken from each scan individually, there is little need for background scans at the edges of the peak. Eliminating these scans means that a reasonable measurement of the shape of the peak can be obtained with around ten linear scans. Thus, around three times as many scans are required as the purely linear scan technique. However, the considerable setup time is not changed, so overall using the grid scan technique takes approximately twice as long.

This technique produces data that are far easier to analyse. In particular, the mea-

surements are independent of most of the configuration parameters of the instrument, the mosaicity and intrinsic broadening of the sample and the incident wavevector. This makes correction of the results much easier, and removes many sources of error.

The grid scan technique seems to be considerably more reliable for measurements where the absolute intensity is required. Whether this additional reliability is worth the extra time needed is dependent on the type of measurement. We have found it extremely useful to get accurate results.

5.5 References

[1] D. Reznik, P. Bourges, H.F. Fong, L.P. Regnault, J. Bossy, C. Vettier, D.L. Milius, I.A. Aksay and B. Keimer, *Direct observation of optical magnons in* $YBa_2Cu_3O_{6.2}$, Phys. Rev. B **53** 22 R14741–R14744 (1996).

[2] S.M. Hayden, G. Aeppli, T.G. Perring, H.A. Mook and F. Dogan, *High frequency spin-waves in* $YBa_2Cu_3O_{6.15}$, Phys. Rev. B **54** 10 R6905–R6908 (1996).

Part II

Neutron Reflectometry Studies of Flux Penetration in Thin Film Superconductors

Chapter 6

Flux Penetration in Superconductors Introduction

In Part II of this thesis, I study flux penetration in thin film superconductors using the technique of polarized neutron reflectometry.

This chapter will outline the flux exclusion properties of thin film superconductors, previous measurements that have been made, and the types of samples that are used.

6.1 Introduction

One of the crucial properties of superconductors is that below the critical field they are diamagnetic.

The magnetic field profile within a superconductor can be probed by the technique of polarized neutron reflectometry (PNR).

Neutron reflectometry is a technique that has been used for a long time, but it is only in the last two decades that polarization of the beam has enabled the study of magnetism [1, 2, 3, 4].

We have used PNR to investigate the field penetration in two different superconductors:

- Niobium is a model type-II superconductor. Magnetic penetration has been studied in niobium by a variety of methods [5, 6, 7, 8, 9]. The flux penetration in the Meissner

state has been studied previously using PNR [2, 10, 11], but I present here results also from the mixed state.

- $YBa_2Cu_3O_7$ is a well known ceramic superconductor. As a particularly interesting material both scientifically and for practical use, this has been extensively studied by PNR [12, 13, 14, 15] and other techniques [7, 16, 17, 18]. I present here preliminary measurements for a thicker sample than has been used previously. Unfortunately instrumental difficulties have prevented conclusive results at this stage.

6.2 Superconducting states

Below the critical temperature T_c, a type-II superconductor can demonstrate several different phases when different magnetic fields H are applied parallel to the surface.

According to Ginzburg-Landau theory (see Section 6.3.3) these states are characterized by a dimensionless parameter κ (see Equation 6.7).

6.2.1 The Meissner state

With $H < H_{c1}$ the superconductor is in the true Meissner state, and the magnetic induction vanishes everywhere except in a region of order the penetration depth λ from the surface, where the induction falls off approximately as an exponential, $e^{-x/\lambda}$.

All superconductors will show this state at low field. For type-I superconductors H_{c1} is equal to H_c, the thermodynamic critical field.

6.2.2 The mixed state

With an an applied field $H_{c1} < H < H_{c2}$ a type-II superconductor exhibits the mixed state, with flux lines penetrating the bulk superconductor.

A type-I superconductor will not exhibit this state (except under very specific conditions such as a very thin film with a perpendicular field). For a superconductor to be type-II (and show the mixed state), κ must be greater than $1/\sqrt{2}$ as H_{c2} (given by Equation 6.11) must be greater than H_c.

6.2.3 The surface superconductivity state

With $H > H_{c2}$ the bulk superconducting state is destroyed, but if $H_{c2} < H < H_{c3}$ a surface superconducting state may be observed. In this state a superconducting layer remains just below the surface.

From Equation 6.13 it follows that κ must be greater than 0.42 for a superconductor to exhibit the surface superconductivity state. Thus the surface superconductivity state can be observed in type-II superconductors and some type-I superconductors (these are sometimes referred to at type 1.5 superconductors).

6.3 Models of the states

In this section I will describe the models used to represent the flux penetration in the different superconducting states.

For convenience of modelling the magnetic field inside a superconductor, I introduce the variable ζ where

$$\zeta = 1 - \frac{B}{\mu_0 H} = -\frac{M}{H}, \tag{6.1}$$

where for a superconductor $0 \leq \zeta \leq 1$ which represents the fraction of the applied field that has been excluded.

In each of the sections, I define x to be the distance into the sample, with $x = 0$ at the surface, and the positive direction into the sample. I define the width of the superconducting sample to be d.

Various different definitions of the penetration depth are used. I refer to the actual measured penetration depth as λ (also called the magnetic screening length). The London penetration depth, λ_L, is the specific theoretical limiting value of the penetration depth for a pure superconductor with local electrodynamics [19]. The Ginzburg-Landau effective penetration depth, λ_{eff}, is the temperature dependent effective penetration depth as used in the Ginzburg-Landau theory.

6.3.1 The Meissner state and the London equations

The London equations [20, 19] (See Chapter 1) are

$$\mathbf{E} = \frac{\partial}{\partial t}\left(\frac{\mathbf{J}_S}{\mu_0 {\lambda_L}^2}\right), \tag{6.2}$$

$$\mathbf{A} = -\mu_0 {\lambda_L}^2 \mathbf{J}_S, \tag{6.3}$$

where

$${\lambda_L}^2 = \frac{m}{\mu_0 n_S e^2}, \tag{6.4}$$

and $\mathbf{A}$ is the magnetic vector potential such that $\mathbf{B} = \operatorname{curl} \mathbf{A}$.

From the Maxwell equations, $\nabla^2 \mathbf{A} = -\mu_0 \mathbf{J}_S$ and Equation 6.3 leads to

$$\nabla^2 \mathbf{A} = \frac{\mathbf{A}}{{\lambda_L}^2}. \tag{6.5}$$

In a one-dimensional case, $\mathbf{A} = \mathbf{A}_0 \exp(-x/\lambda_L)$ and hence $\mathbf{B} = \mathbf{B}_0 \exp(-x/\lambda_L)$. This means that the magnetic field is screened exponentially from the bulk of the sample with a penetration depth λ_L. Taking into account the Pippard coherence length changes the penetration depth from λ_L to an effective penetration depth λ.

For a thin film sample, this leads to

$$\zeta(x) = 1 - \frac{\cosh((x - d/2)\lambda)}{\cosh(d/2\lambda)}. \tag{6.6}$$

This means that the flux decays approximately exponentially from each end. Note that as $d \to \infty$, $\zeta(d/2) \to 1$. However, unless $d \gg \lambda$ the field will not be completely expelled.

Although mathematically correct, this formula may need modification if the value of ζ is to actually be obtained. In particular, it may need to be rewritten so that the cosh evaluations do not overflow a digital representation in the case where $d \gg \lambda$.

The decay is not exactly an exponential [23] but it is close enough for the accuracy with which it is measured here. The Ginzburg-Landau equations (see Section 6.3.3) give another way of calculating the flux profile in the Meissner state.

Figure 6.1 illustrates this model for the case of $\lambda = 0.2d$. As can be seen, the exclusion

of the field is not complete.

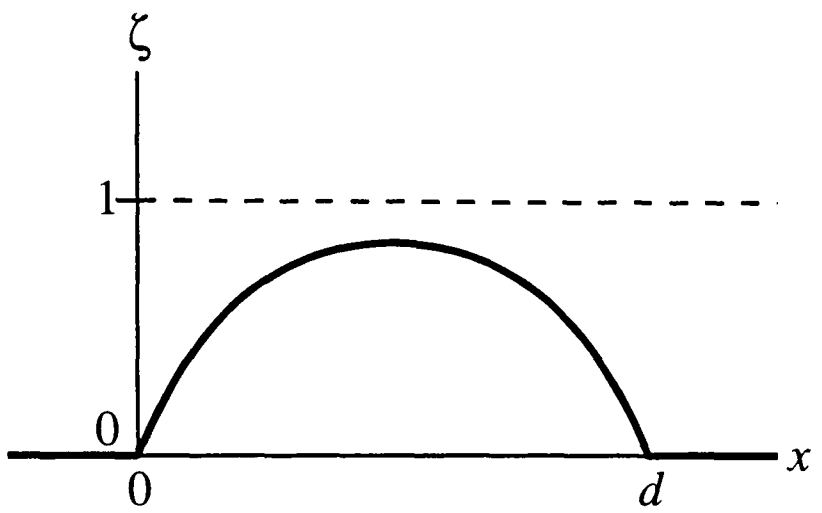

Figure 6.1: A model of the Meissner state for a film with $d = 5\lambda$

6.3.2 The mixed state

Modelling the mixed state is difficult for a thin film superconductor. In the mixed state of a bulk superconductor, flux lines should penetrate the bulk of the superconductor to form a lattice. Neutron diffraction has been observed from the flux line lattice using SANS [21, 22].

However, in these experiments on thin films, the low thickness of the sample and the granularity in the crystal mean that the flux lines are unlikely to follow a simple pattern. They are more likely to follow defect lines or grain boundaries and any variation will be significant on the scale of the sample. The flux lines may also emerge from the surface of the sample.

I have attempted to model this by considering the potential to be that of the Meissner state, with an additional uniform term representing an average flux penetration of the bulk material. At the higher fields I have also attempted to model it assuming the average flux profile is like the surface superconductivity state (see the next section).

With the limited resolution of the reflectometer and the likely distortions of the flux lattice we did not expect to detect, nor did we see any evidence for, diffraction from the lattice.

6.3.3 The surface superconductivity state and GL theory

The model of the flux penetration in the surface superconductivity state is considerably more complex than the Meissner state. I have modelled the flux penetration using a one-dimensional form of the Ginzburg-Landau equations [23, 24, 4].

Ginzburg-Landau theory describes the superconductor free energy density as a power series expansion in terms of a pseudowavefunction order parameter ψ, with powers of $|\psi|^2$ and $|\nabla\psi|^2$. Ginzburg-Landau theory is only strictly valid when the temperature is near T_c and the superconductor is local. However, there is evidence that its predictions are a good approximation over a wider range of temperature.

The Ginzburg-Landau equations define a parameter κ which is the ratio of the Ginzburg-Landau effective penetration depth $\lambda_{\text{eff}}(T)$ to the Ginzburg-Landau coherence length $\xi(T)$. Note that this is not the same as the Pippard coherence length in Equation 1.1.

As $\lambda_{\text{eff}}(T)$ and $\xi(T)$ have similar temperature dependences, κ is approximately independent of temperature.

More specifically,

$$\kappa = \frac{\lambda_{\text{eff}}(T)}{\xi(T)}, \tag{6.7}$$

$$\kappa_p = 0.96\frac{\lambda_L(0)}{\xi(0)}, \tag{6.8}$$

$$\kappa_d = 0.715\frac{\lambda_L(0)}{l}, \tag{6.9}$$

where κ_p is the limit for a pure superconductor, and κ_d is the limit for a dirty superconductor.

The values of the critical fields are related to the penetration depth, the coherence length and κ by [19]

$$H_c(T) = \frac{\phi_0}{2\sqrt{2}\,\pi\xi(T)\lambda_{\text{eff}}(T)}, \tag{6.10}$$

$$H_{c2} = \sqrt{2}\,\kappa H_c, \tag{6.11}$$

$$H_{c3} = 1.695H_{c2}, \tag{6.12}$$

$$= 2.39\kappa H_c. \tag{6.13}$$

Unfortunately, the value of H_{c1} is not simply related to the parameters, and a numerical solution would be required. However, to a rough approximation, ${H_c}^2 = H_{c1}H_{c2}$.

For the one-dimensional case, the Ginzburg-Landau equations can be written as [23, 24]

$$f'' = \kappa^2[(b')^2/f^3 + f^3 - f], \tag{6.14}$$

$$b'' = f^2 b + 2f'b'/f, \tag{6.15}$$

where $f = \psi/\psi_\infty$ is the reduced local order parameter, $b = 2\pi\xi^2\kappa B/\phi_0$ is the reduced magnetic induction, ϕ_0 is the flux quantum $(h/2e)$ and the penetration depth λ_{eff} forms the length scale of the derivatives. Note that Ref. [24] contains a typographical error in these equations.

For these to be solved, the boundary conditions must be determined. At the interface, $f'(0) = 0$, and $b(0)$ is determined by the applied field. However, the values for $f(0)$ and $b'(0)$ are not so obvious. To determine these, the differential equations can be solved with trial values until a non-physical situation occurs.

The boundary condition in the sample is set such that $b \to 0$ for the Meissner state or $b \to b(0)$ for the surface superconductivity state.

The solution is non-physical if at any point $f < 0$, $f > 1$, $b < 0$ or $b > b(0)$.

For a surface superconductivity solution, the physical solution is generally along the line (in the space of the unknown parameters) between the regions where $f < 0$ occurs and $b > b(0)$ occurs [23].

The solution is not too difficult to find along this line, but the solution can be more easily located if the Gibbs free energy is minimized. This is given by

$$\Delta G = \frac{H_c^2}{8\pi}\int_0^\infty \{2[b(0) - b]^2 - f^4\}\mathrm{d}z, \tag{6.16}$$

where H_c is the thermodynamic critical field.

It is important to note that the form of the solution to these equations is critically dependent on the exact values of the starting parameters. The form can be very different if the values of $f(0)$ and $b'(0)$ differ by a part in 10^5 from the values for the physical solution. However, if the values are close to the nominal values, the solutions are very similar, so a

numerical solution using double-precision is a useful approximation.

The equations cannot be solved analytically, so numerical solutions are required. To do this, the second order equations can be written in terms of coupled first order equations. Making the substitutions

$$y_1 = f, \tag{6.17}$$

$$y_2 = b, \tag{6.18}$$

$$y_3 = \frac{\mathrm{d}f}{\mathrm{d}x_\lambda}, \tag{6.19}$$

$$y_4 = \frac{\mathrm{d}b}{\mathrm{d}x_\lambda}, \tag{6.20}$$

where x_λ is the position in the sample scaled to the penetration depth (i.e. x/λ), we have

$$\frac{\mathrm{d}y_1}{\mathrm{d}x_\lambda} = y_3, \tag{6.21}$$

$$\frac{\mathrm{d}y_2}{\mathrm{d}x_\lambda} = y_4, \tag{6.22}$$

$$\frac{\mathrm{d}y_3}{\mathrm{d}x_\lambda} = \kappa^2[{y_4}^2/{y_1}^3 + {y_1}^3 - y_1], \tag{6.23}$$

$$\frac{\mathrm{d}y_4}{\mathrm{d}x_\lambda} = {y_1}^2 y_2 + 2y_3 y_4/y_1. \tag{6.24}$$

The Gibbs free energy can be evaluated by introducing it as a new variable in the integration, namely

$$\frac{\mathrm{d}y_5}{\mathrm{d}x_\lambda} = \left(2[b(0) - y_2]^2 - {y_1}^4\right) \tag{6.25}$$

where y_5 is proportional to the Gibb's free energy.

I have used a version of the Bulirsch-Stoer method [25] for the integration of these differential equations. A fifth order Runge-Kutta method was also used to check the results.

Both of these were modified to abort the calculation if any of the parameters took on unphysical values. They were also modified such that the magnetic potential energy was output in steps so that it could be used for the neutron reflectivity simulation.

These equations give a solution for the Meissner state that is close to an exponential falloff. For the surface state the form is that of a falloff similar to the Meissner state that is then followed by a smooth return to the maximum flux [23]

To use these equations as a model for the surface state, the characteristic parameters for the sample must be derived. Two of the three parameters, the effective penetration λ_{eff}, the critical field H_c and the Ginzburg-Landau parameter κ must be known.

The critical field is needed to provide the scale for b. From Equation 6.10, if the applied field H_a is expressed (for the Meissner state) in a reduced form $H_m = H_a/H_c$

$$b(0) = \sqrt{2}\, H_s. \tag{6.26}$$

Similarly, for the surface superconductivity state, if $H_s = H_a/H_{c2}$ then

$$b(0) = \kappa H_s. \tag{6.27}$$

From Equations 6.7 and 6.10, the value of κ is given by [19, 4]

$$\kappa = 2\sqrt{2}\,\pi \frac{\mu_0 H_c \lambda_{\text{eff}}^2}{\phi_0}. \tag{6.28}$$

Thus with two of the three variables known, the other can be derived.

6.4 Samples

To perform PNR measurements on surfaces, the quality of the samples (particularly the surfaces) is critical. Two surface characteristics that play an important role are the surface roughness and surface oxidization.

The surface roughness acts like a modulation of the scattering length density, and can be modelled like a Gaussian (see Section 7.3.3). The effect on the reflectivity curve is to change the rate of the exponential decay in the signal away from the critical edge. Ironically, this can make the magnetic signal clearer, as the reflectivity falls away more rapidly from the critical edge, increasing the depth of the flipping ratio (see Section 7.3.4). However, excessive surface roughness will make the measurements difficult.

The surface oxide layer can be modelled with a suitable layer on the top. However, as most of the oxide layers will not superconduct, the layer will move where the decay of the

magnetic field starts. Thus a large oxide layer will increase the error on the penetration depth measurements.

Reducing these effects will thus improve the measurements.

For some of the measurements here, the surfaces have been etched to try to improve the smoothness. This is to try to remove any large variations in the surface.

With the apparatus used at the moment, some oxidization of the surface is hard to avoid. However, we can avoid aggravating this by careful storage.

The surface of the sample can also be damaged by water. This is a problem if the sample needs to be warmed quickly, in which case condensation can form. This can be avoided by warming the cryostat slowly, over a period of several hours, with the sample maintained in a ^{4}He atmosphere.

Up to now, most measurements on magnetic penetration have been made on very thin films; ones where the thickness is not much larger than the penetration depth [12, 10].

This generally makes the measurement easier:

- With a thin film, less material must be deposited, so it is easier to get a smooth surface.
- Due to the small thickness (and to a lesser extent the smooth surface), interference effects can be seen in the reflectivity signal. This can make the results less ambiguous, and the magnetic signal clearer [26].

However, for such a thin sample, the properties are likely to be different to those of a bulk superconductor:

- The exclusion of the field does not come close to being total, and this will affect the penetration, particularly outside the Meissner state.
- Any strain at the substrate-superconductor interface may not completely relax, so there may be differences in the crystal.
- If the thickness d is not $\gg \xi$ then there may be size effects modifying the superconductor order parameter.

- For a thin film, the lack of total exclusion of the field will also change the value of the critical field as the overall magnetization is much lower. For a very thin film the critical field can be approximated as

$$H_{c\|} = 2\sqrt{6}\frac{h_c\lambda}{d}. \tag{6.29}$$

In these experiments we have used relatively thick samples which have a thickness at least several times that of the penetration depth. With these we hope to get characteristics similar to a bulk superconductor.

A thicker sample does lead to considerably more surface roughness, but this can largely be corrected for.

As with other applications for thin films, the lattice parameters of the substrate need to be relatively close to those of the sample material to enable the epitaxial growth of good crystals. If this is not the case then the sample will be granular.

If the grain sizes are comparable to the coherence length for the superconductor, this will change the properties of the superconductor and may also provide additional channels for flux penetration in the mixed state. It can also lead to flux pinning.

Although a thick sample does not directly cause this problem, a very thin sample may avoid this by the strain in the crystal not relaxing. However, it has been found that grain sizes often increase with sample thickness (to a limiting value), so a thick sample can help avoid small grains.

Unfortunately, PNR gives an additional constraint on the substrate choice. The substrate must be a weaker scatterer of neutrons than the sample. If this is not the case then the critical edge position will be determined by the critical edge of the substrate, and the subtle magnetic effects around the sample critical edge will be impossible to observe.

This effect prevented us from using sapphire (Al_2O_3) as a substrate for the niobium sample. Sapphire is the best known substrate for niobium and allows excellent single crystals to be grown by sputtering or MBE. Thus we were forced to use the less ideal single crystal Si substrate, which resulted in polycrystalline samples with large grains.

To improve the growth of the crystal, it is possible to use a buffer layer of another

material between the substrate and the sample, but this leads to another consideration in the modelling, and can also lead to oxidation at the substrate side of the sample.

6.5 References

[1] G.P. Felcher, *Magnetic depth profiling studies by polarized neutron reflection*, Physica B **192** 1–2 137–149 (1993).

[2] G.P. Felcher, R.T. Kampwirth, K.E. Gray and R. Felici, *Polarized-neutron reflections: A new technique used to measure the magnetic field penetration depth in superconducting niobium*, Phys. Rev. Lett. **52** 1539 (1984).

[3] K.E. Gray, G.P. Felcher, R.T. Kampwirth and R. Hilleke, *Direct investigation of the superconducting surface sheath and nonlocal electrodynamics by polarized neutron reflections*, Phys. Rev. B **42** 7Pt.A 3971–3975 (1990).

[4] M.P. Nutley, A.T. Boothroyd, C.R. Staddon, D. M^{c}K. Paul and J. Penfold, *Magnetic-induction profile in a type-I superconductor by polarized-neutron reflectometry*, Phys. Rev. B **49** 15789–15798 (1994).

[5] D.H. Kim, K.E. Gray, J.D. Hettinger, J.H. Kang and S.S. Choi, *Resistive measurement of the temperature dependence of the penetration depth of* Nb *in* $Nb/AlO_x/Nb$ *Josephson junctions*, J. Appl. Phys. **75** 12 8263–8167 (1994).

[6] H.W. Weber, E. Seidl, C. Laa, E. Schachinger, M. Prohammer, A. Junod and D. Eckert, *Anisotropy effects in superconducting niobium*, Phys. Rev. B **44** 14 7585–7600 (1991).

[7] S.M. Anlage, B.W. Langley, G. Deutscher, J. Halbritter and M.R. Beasley, *Measurements of the temperature dependence of the magnetic penetration depth in* $YBa_2Cu_3O_{7-\delta}$ *superconducting thin films*, Phys. Rev. B **44** 17 9764–9767 (1991).

[8] R.F. Broom, *Some temperature-dependent properties of niobium tunnel junctions*, J. Appl. Phys. **47** 12 5432–5439 (1976).

[9] C. Varmazis and M. Strongin, *Inductive transition of niobium and tantalum in the 10-MHz range. I. Zero-field superconducting penetration depth*, Phys. Rev. B **10** 5 1885–1895 (1974).

[10] Huai Zhang, J.W. Lynn, C.F. Majkrzak, S.K. Satija, J.H. Kang and X.D. Wu, *Measurements of magnetic screening lengths in superconducting* Nb *thin films by polarized neutron reflectometry*, Phys. Rev. B **52** 14 10395–10404 (1995).

[11] L.P. Chernenko, D.A. Korneev, A.V. Petrenko, N.I. Balalykin and A.V. Skripnik, *Measurement of magnetic field penetration depth in niobium polycrystalline films by the polarized neutron reflection method* in *Surface X-Ray and Neutron Scattering*, edited by H. Zabel and I.K. Robinson (Springer-Verlag, Berlin, 1992), p.209–217.

[12] V. Lauter-Pasyuk, H.J. Lauter, V.L. Aksenov, E.I. Kornilov, A.V. Petrenko and P. Leiderer, *Direct measurement of the magnetic field penetration depth in* $YBa_2Cu_3O_7$ *superconducing films by polarized neutron reflectometry*, Physica B **241–243** 1095–1097 (1998).

[13] V. Lauter-Pasyuk, H.J. Lauter, V.L. Aksenov, E.I. Kornilov, A.V. Petrenko and P. Leiderer, *Determination of the magnetic field penetration depth in* $YBa_2Cu_3O_7$ *superconducting films by polarized neutron reflectometry*, Physica B **248** 166–170 (1998).

[14] R. Felici, J. Penfold, R.C. Ward, E. Olsi and C. Matacotta, *Determination of the magnetic penetration depth of the high-*T_c *superconductor* $YBa_2Cu_3O_{7-x}$ *by polarized neutron reflection*, Nature **329** 523–528 (1987).

[15] A. Mansour, R.O. Hilleke, G.P. Felcher, R.B. Laibowitz, P. Chaudhari and S.S.P. Parkin, *Magnetic field penetration into the high-temperature superconductor* $YBa_2Cu_3O_{7-x}$, Physica B **156 & 157** 867–870 (1989).

[16] D.R. Harshman, G. Aeppli, E.J. Ansaldo, B. Batlogg, J.H. Brewer, J.F. Carolan, R.J. Cava and M. Celio, *Temperature dependence of the magnetic penetration depth in the high-*T_c *superconductor* $Ba_2YCu_3O_{9-\delta}$ *— evidence for conventional s-wave pairing*, Phys. Rev. B **36** 4 2386–2389 (1987).

[17] R.F. Kiefl, T.M. Riseman, G. Aeppli, E.J. Ansaldo, J.F. Carolan, R.J. Cava, W.N. Hardy, D.R. Harshman, N. Kaplan, J.R. Kempton, S.R. Kreitzman, G.M.Luke, B.X. Yang and D.Ll. Williams, *Temperature dependence of the magnetic penetration depth in* $YBa_2Cu_3O_7$ *measured by muon spin rotation*, Physica C **153** Pt1 757–758 (1988).

[18] Y.J. Uemura, V.J. Emery, A.R. Moodenbaugh, M. Suenaga, D.C. Johnston, A.J. Jacobson, J.T. Lewandowski, J.H. Brewer, R.F. Fiefl, S.R. Kreitzman, G.M. Luke, T. Riseman, C.E. Stronach, W.J. Kossler, J.R. Kempton, X.H. Yu, D. Opie and H.E. Schone, *Systematic variation of magnetic field penetration depth in high-*T_c *superconductors by muon-spin relaxation*, Phys. Rev. B **38** 1 909–912 (1988).

[19] M. Tinkham, *Introduction to Superconductivity, 2nd ed.* (McGraw Hill, 1996, ISBN 0-07-114782-9).

[20] B.I. Bleaney and B. Bleaney, *Electricity and Magnetism, 3rd ed.* (Oxford University Press, 1976, ISBN 0-19-851173-6).

[21] D. M^{c}K. Paul, E.M. Forgan, R. Cubitt, S.L. Lee, M. Wylie, H.A. Mook and M Yethiraj, *Neutron scattering from the flux-line-lattice in* $Bi_2Sr_2CaCu_2O_{8+\gamma}$, Physica B **213** 107–109 (1995)

[22] G. Brandstätter, A. Vostner, H.W. Weber, T. Chattopadhyay, R. Cubitt, H. Fischer and G.A. Emel'chenko, *Neutron diffraction by the flux line lattice in* $YBa_2Cu_3O_{7-\delta}$ *single crystals*, Physica C **282** Pt4 2089–2090 (1997).

[23] R. Felici and K.E. Gray, *Calculation of the diamagnetism of the surface sheath of superconductivity*, Phys. Rev. B **29** 11 6129–6131 (1994).

[24] K.E. Gray, *Ginzburg-Landau equations, interphase surface energy, and the intermediate state of superconductors with a paramagnetic normal state*, Phys. Rev. B **27** 7 4157-4160 (1983).

[25] W.H. Press, S.A. Teukolsky, W.T. Vetterling and B.P. Flannery, *Numerical Recipes in C* (Cambridge University Press, 1992, ISBN 0 521 43108 5).

[26] M. Mâaza, L.P. Chernenko, D. Korneev, B. Pardo, C. Sella and F. Bridou, *A way to reach high accuracy in the determination of the magnetic London penetration depth in superconductors by polarized neutron reflectometry*, Physics Letters A **218** 3–6 312–318 (1996).

Chapter 7

Neutron Reflectometry Theory

7.1 Introduction

This chapter will outline the theory of neutron reflectometry, and how we have modelled our data.

7.1.1 Practice of neutron reflectometry

Neutron reflectometry is a technique suited to investigating the structure of interfaces or thin samples [1].

In neutron reflectometry, neutrons are reflected specularly at a glancing angle from the sample. For neutrons, the refractive index of most materials is less than one, so at a critical angle θ_c, total *external* reflection may be observed.

Neutron reflectometry gives information on the structure of the sample from the way that the reflectivity of the sample changes with neutron wavevector perpendicular to the interfaces. This wavevector is usually varied in one of two ways:

- In a reflectometer connected to a pulsed source using the time-of-flight method (such as the CRISP spectrometer used in this work), the incident angle is fixed, and the wavelength of the neutrons varies during the pulse.

- In a reactor source reflectometer, the neutron beam is monochromatic, and the inci-

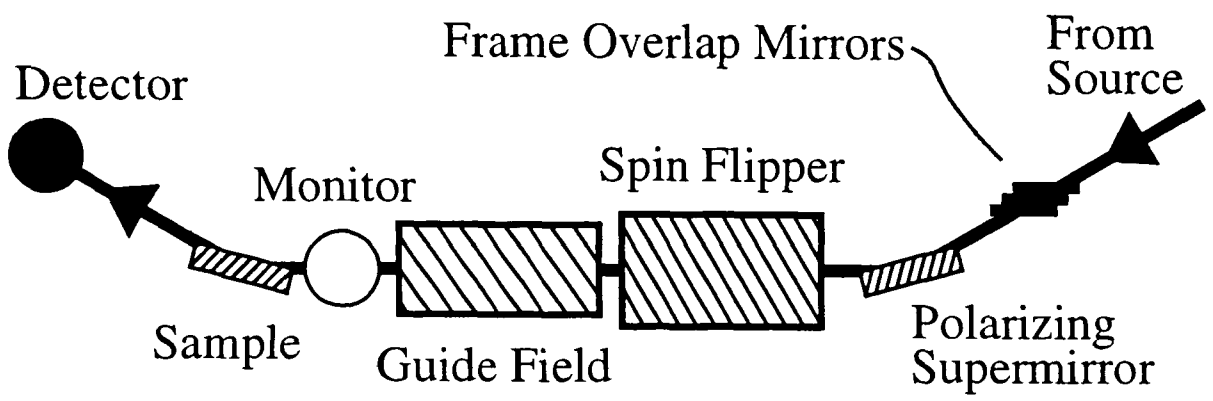

Figure 7.1: A schematic diagram of a neutron reflectometer (such as the CRISP reflectometer) in polarized mode.

dent angle is varied to change the component of the wave-vector perpendicular to the surface.

The scattering of the neutrons is dependent on the nuclear scattering length density and the absorption cross section density of the material being studied.

In the technique of polarized neutron reflectometry (PNR), the neutrons are polarized. The polarized neutrons then experience a different refractive index depending on the magnitude and relative orientation of the neutron spin to any magnetic fields present. Thus, PNR can be used to study variation in magnetic fields inside a sample, as was done in this work.

Figure 7.1 shows a schematic diagram of a time-of-flight neutron reflectometer in polarized mode.

Neutrons enter the instrument from the pulsed source. The frame overlap mirrors separate out unwanted slow neutrons from a previous pulse. The polarizing supermirror polarizes the neutrons into a single spin state. The spin flipper can change the direction of the neutron spin, and is switchable so that the two polarizations can be used. The guide field produces a remnant field which is required for the neutrons to maintain their polarization. The beam then passes through a monitor which is used to normalize the reflectivity. The neutrons are then reflected specularly from the sample and the reflected beam is measured on the detector.

In a variant of this technique, a second polarizing mirror can be placed after the sample to enable measurement of the polarization of the neutrons after they have scattered from

the sample. This polarization analysis was not used for the measurements described here.

7.2 PNR characteristics

Polarized neutron refletometry has a number of advantageous features for measuring flux penetration:

- PNR measures the penetration depth (magnetic screening length) directly, rather than its derivative with respect to temperature, as obtained by other techniques (for instance surface impedance measurements). Thus it is useful for determining absolute values of λ.

- PNR is sensitive to the shape of the flux penetration, rather than just the integrated flux, as would be obtained by a magnetization measurement. Thus in principal it can be used to investigate forms for the magnetic profile that are not exponential.

- PNR measures the magnetic screening length rather than the London penetration depth. The screening length is a more practical parameter, but it is harder to relate to fundamental theory.

- Measurements can be carried out at any temperature, not just near T_c.

- Measurements can be taken at any field, so all of the superconducting phases are in principle accessible.

- The reflectivity measurements also characterise the structure of the sample, giving information on the quality of the surface and the bulk sample. This is useful for understanding the details of a particular sample, but this dependence means care must be taken in producing suitable samples.

- The neutrons penetrate far into the sample, and so the measurement can be sensitive to changes in the flux away from the surface.

7.3 Neutron optics and reflectometry theory

7.3.1 Refractive index and the critical angle

For the purposes of refraction (and thus reflectivity), neutrons can be treated in a similar way to light, enabling the standard techniques of optics to be used. This is an approximation, but it is a good one, particularly for scattering near the critical angle, as is the case for PNR.

The neutron refractive index is

$$n = 1 - \frac{\lambda^2}{2\pi} \sum_i \rho_i b_i, \tag{7.1}$$

where λ is the neutron wavelength,

ρ_i is the scatterer density and

$\sum_i \rho_i b_i$ is the scattering length density of the material,

with the summation over the different types of scatterers in the material.

If the material is absorbing, this can be represented approximately by a complex refractive index

$$n = 1 - \frac{\lambda^2}{2\pi} \sum_i \rho_i \left[b_i + \frac{\mathrm{i}}{2\lambda} \sigma_{a_i} \right], \tag{7.2}$$

where σ_{a_i} is the absorption cross section of the absorber i.

Note that most materials have a positive scattering length density and so the refractive index is less than unity. Thus, at glancing angles total external reflection may be observed. The region of reflection close to this is the basis of neutron reflectometry.

The optical approach can be related to quantum mechanics. Considering the scattering from a quantum mechanical viewpoint makes certain parts much easier, in particular the magnetic scattering.

Taking the z direction as perpendicular to the interface, the solution of Schrödinger's equation for the z component of the neutron wave-vector gives

$$k_1^z = \sqrt{(k_0^z)^2 - \frac{2m_n V}{\hbar^2}}, \tag{7.3}$$

where $k_i^z = k_i \sin\theta_i$.

Snell's law gives

$$k_0 \cos\theta_0 = k_1 \cos\theta_1. \tag{7.4}$$

Thus

$$\begin{aligned} n &= \frac{\cos\theta_0}{\cos\theta_1} && (7.5)\\ &= \frac{\sqrt{1-(k_0^z/k_0)^2}}{\sqrt{1-\left((k_0^z)^2-\frac{2m_nV}{\hbar^2}\right)/(k_1)^2}} && (7.6)\\ &\approx 1-\frac{1}{2}(k_0^z/k_0)^2+\frac{1}{2}(k_0^z/k_1)^2-\frac{2m_nV}{2\hbar^2(k_1)^2}, && (7.7) \end{aligned}$$

where the Binomial theorem has been used to first order.

For neutrons, the refractive index is normally very close to unity, so $k_1 \approx k_0 = 2\pi/\lambda$ and thus the refractive index is related to the potential by

$$n \approx 1-\frac{m_nV\lambda^2}{4\pi^2\hbar^2}. \tag{7.8}$$

Expressing the refractive index in terms of a potential is convenient as the interaction between the neutron and magnetic field becomes simple to represent.

The magnetic flux density $\mathbf{B}$ inside the sample is given by

$$\mathbf{B} = \mu_0\mathbf{H} + \mu_0\mathbf{M}, \tag{7.9}$$

where $\mathbf{M}$ is the magnetization (the magnetic dipole moment per unit volume) and $\mathbf{H}$ is the applied field. In diamagnetic materials (such as superconductors) the magnetization is negative.

The magnetic potential V_m of the neutron is

$$V_m = -\boldsymbol{\mu}_n \cdot \mathbf{B}, \tag{7.10}$$

where

$$\mu_n = -\gamma\mu_N\sigma, \tag{7.11}$$

$$\gamma = 1.91315, \tag{7.12}$$

$$\mu_N = \frac{e\hbar}{2m_p}, \tag{7.13}$$

and $\boldsymbol{\sigma}$ is the Pauli spin operator for the neutron.

Thus, assuming that the neutron spin is either parallel or antiparallel to the applied field, and shifting the zero of energy we have

$$V_m = \pm\gamma\mu_N(B - \mu_0 H) \tag{7.14}$$

$$= \pm\gamma\mu_N\mu_0 M, \tag{7.15}$$

where the top case is for the neutron spin parallel to the applied field.

Thus, from Equation 7.8 and the refractive index in Equation 7.2 the full forms of the potential and refractive index become

$$V = \frac{2\pi\hbar^2}{m_n}\left(\sum_i \rho_i\left[b_i + \frac{\mathrm{i}}{2\lambda}\sigma_{a_i}\right]\right) \pm \gamma\mu_N\mu_0 M, \tag{7.16}$$

$$n = 1 - \frac{\lambda^2}{2\pi}\left(\sum_i \rho_i\left[b_i + \frac{\mathrm{i}}{2\lambda}\sigma_{a_i}\right]\right) \mp \frac{m_n\lambda^2}{4\pi^2\hbar^2}\gamma\mu_N\mu_0 M. \tag{7.17}$$

Thus, when the neutron spin is parallel to the applied field, and the magnetization is negative, the refractive index is increased (nearer to unity), and the potential is lower.

In terms of the variable ζ defined in Equation 6.1 ($\zeta = -M/H$), the magnetic part of the refractive index becomes

$$n_m = \pm\frac{m_n\lambda^2}{4\pi^2\hbar^2}\gamma\mu_N\mu_0 H\zeta. \tag{7.18}$$

Writing V as

$$V = D\left(\sum_i \rho_i\left[b_i + \frac{\mathrm{i}}{2\lambda}\sigma_{a_i}\right] \mp CH\zeta\right), \tag{7.19}$$

where C and D are constants then if (as in the measurements presented here) H is measured

in Oe and the scattering length density in Å^{-2} then $C = 10^{-24}(2\pi m_n \gamma \mu_N / h^2) = 2.316 \times 10^{-10}\ \text{Å}^{-2}\text{Oe}^{-1}$.

From Snell's law, $n_0 \cos(\theta_0) = n_1 \cos(\theta_1)$ (taking θ as the angle from the surface), the critical angle θ_c is given by $\cos\theta_c = n$. Thus, using the small angle approximation for cosine

$$\theta_c \approx \lambda \left(\frac{1}{\pi} \sum_i \rho_i b_i \right)^{\frac{1}{2}}, \tag{7.20}$$

for a non-absorbing material.

7.3.2 Reflection coefficient

To calculate the reflectivity from a general one dimensional potential, we consider the potential to be divided into N strips.

For certain potential forms, an analytic solution is possible [2, 3], so this is not necessary. However, analytic solutions are difficult for more complicated potentials. In this thesis where I am considering various models for flux penetration (some of which themselves must be calculated numerically), the strip division method is more suitable.

There are various different ways of calculating the reflectivity [4, 5], but the one I present here has the advantage of being flexible and conceptually simple.

The convention used here is that the positive z direction is into the sample.

Let a strip m have a width d_m and a refractive index n_m. Defining the angle of the neutron beam in the strip m and θ_m it is convenient to define the quantity $p_m = n_m \sin\theta_m$.

The Fresnel coefficient between a strip m and the previous strip is

$$r_m = \frac{p_{m-1} - p_m}{p_{m-1} + p_m}. \tag{7.21}$$

The reflectivity can be calculated by defining characteristic matrices $\mathbf{C}_m$ such that the reflectivity is given by

$$\mathbf{R} = \left| \frac{C_{21}}{C_{11}} \right|^2, \tag{7.22}$$

where

$$\mathbf{C} = \mathbf{C}_1 \mathbf{C}_2 \cdots \mathbf{C}_N \mathbf{C}_s. \tag{7.23}$$

The characteristic matrix for a strip m is [6]

$$\mathbf{C}_m = \begin{bmatrix} e^{i\delta_{m-1}} & r_m e^{i\delta_{m-1}} \\ r_m e^{-i\delta_{m-1}} & e^{-i\delta_{m-1}} \end{bmatrix}, \tag{7.24}$$

where

$$\delta_m = \frac{2\pi}{\lambda} n_m d_m \sin\theta_m, \tag{7.25}$$

which is the optical path length for the neutrons across that strip.

The first characteristic matrix is given by

$$\mathbf{C}_1 = \begin{bmatrix} 1 & r_1 \\ r_1 & 1 \end{bmatrix}, \tag{7.26}$$

and the characteristic matrix at the substrate is

$$\mathbf{C}_s = \begin{bmatrix} e^{i\delta_N} & r_s e^{i\delta_N} \\ r_s e^{-i\delta_N} & e^{-i\delta_N} \end{bmatrix}, \tag{7.27}$$

where $r_s = (p_N - p_s)/(p_N + p_s)$.

If there are no strips, the reflection coefficient becomes $|r_1|^2$ as expected.

With one strip the resultant matrix becomes

$$\mathbf{C} = \begin{bmatrix} 1 & r_1 \\ r_1 & 1 \end{bmatrix} \begin{bmatrix} e^{i\delta_1} & r_s e^{i\delta_1} \\ r_s e^{-i\delta_1} & e^{-i\delta_1} \end{bmatrix} \tag{7.28}$$

$$= \begin{bmatrix} e^{i\delta_1} + r_1 r_s e^{-i\delta_1} & r_s e^{i\delta_1} + r_1 e^{-i\delta_1} \\ r_1 e^{i\delta_1} + r_s e^{-i\delta_1} & r_s e^{i\delta_1} + r_1 r_s e^{-i\delta_1} \end{bmatrix}. \tag{7.29}$$

Thus, the reflectivity will be

$$\left| \frac{r_1 e^{2i\delta_1} + r_s}{e^{2i\delta_1} + r_1 r_s} \right|^2. \tag{7.30}$$

7.3.3 Roughness and angular divergence of the beam

To model the measured reflectivities, further corrections are needed [7, 8].

To account for roughness at the interfaces, we assume a Gaussian form for the roughness. The Fresnel coefficients become

$$r'_m = r_m \exp[\frac{1}{2}(q_m q_{m-1} \langle\sigma\rangle^2)], \tag{7.31}$$

where $\langle\sigma\rangle$ is the root mean square roughness and $q_m = 2k \sin\theta_m$.

Another way to model the roughness would be to further subdivide the strips to represent a rounded potential, but the correction in Equation 7.31 is faster to calculate.

The resolution of neutron reflectometers is limited by the angular divergence of the neutron beam. To model this, we convolve the calculated reflectivity profile with a Gaussian distribution [9].

The standard deviation σ of the Gaussian at each wave-vector is taken as

$$\sigma(k_i) = \frac{p}{100} \frac{k_i}{2\sqrt{2\log 2}}, \tag{7.32}$$

where k_i is the wave-vector and

p is the percentage deviation in the incident angle.

The $2\sqrt{2\log 2}$ factor converts from the FWHM given by the percentage deviation to the standard deviation.

For each wave-vector incident on the sample there is a Gaussian spread in the angle. As the wavelength is independent of the angle this gives a Gaussian spread in the wave-vector.

For each wave-vector k_j a summation is performed over the reflection coefficients for the wave-vectors such that

$$R'_j = \sum_{i=0}^{N} \frac{R_j \delta k}{\sqrt{2\pi}\sigma(k_j)} \exp\left[\frac{-(k_j - k_i)^2}{2\sigma(k_j)^2}\right], \tag{7.33}$$

where R_j is the uncorrected reflection coefficient,

R'_j is the and corrected reflection coefficient,

δk is the (constant) value of $k_{j+1} - k_j$ and

N is the number of wavevectors for which the reflection coefficient has been calculated.

This is an approximation which becomes inaccurate when δk is similar to or larger

that the width produced by the Gaussian spread, as then only a few points contribute to the summation. It also can become inaccurate when a large thickness is modelled, as the interference oscillations become extremely rapid and large numbers of points are needed to average them accurately.

It must also be noted that this approximation is incorrect at the edges of the wavevector range where there are no points to convolve, so a wider range than required without the convolution must be calculated.

For the beam deviations in the measurements presented here, it was found that many more points were needed for an accurate convolution than the experimental points. This is likely to be due to the effect described above of rapid interference oscillations with our relatively thick samples.

Most of the calculations were performed using 3000 points for the convolution, compared to the 138 experimental points. I chose the number of points by comparing the results for different numbers of points for a typical calculation; I chose the minimum number of points that did not show significant deviation from a calculation with a very large number of points. Choosing a minimum number of points is important, as otherwise the calculations can take a very long time to perform.

This technique for modelling the deviation is also an approximation in the case where the magnitude of the incoming wave-vector is changed (such as for a time-of-flight spectrometer), as a change in the angle does not change the neutron wavelength, but only the z component of the wave-vector. However, this only produces a small error in the complex part of the potential which itself will be small in most cases (and zero for non-absorbing materials).

7.3.4 The flipping ratio and polarization function

One convenient representation of the signal from the magnetism is the flipping ratio. This is defined as

$$F = R^+/R^-, \tag{7.34}$$

where R^+ and R^- are the reflectivities with the neutron moment parallel and antiparallel to the applied field respectively. This is the representation generally used in this thesis.

Another common representation (e.g. in Chapter 6 Ref. [12]) is the polarization function (also known as the spin asymmetry) which is defined as

$$P = \frac{R^+ - R^-}{R^+ + R^-}. \tag{7.35}$$

Thus these are simply related by $P = (F-1)/(F+1)$ and $F = (1+P)/(1-P)$.

7.3.5 Dividing the potential

To model the nuclear part of the potential, the division of the strips is usually clear; the strips should represent the physical change in the materials.

However, to model a decay of magnetic field, the way to divide the potential into strips is less obvious, as the magnetic potential generally varies continuously.

The simplest technique is to simply divide the potential into strips of equal width. This is effective, but has the disadvantage that to accurately model the potential a very large number of strips may be needed so that the calculation time becomes prohibitively long. Care must also be taken to avoid spurious interference effects.

Another solution is only to divide the potential in regions where it is significantly varying. While an improvement in speed over the original technique, this shares many of the disadvantages.

In the case of flux penetration into a superconductor, the magnetic field decays approximately exponentially. Thus I have used the technique of dividing the strips so that they follow the changes in an exponential decay.

Consider an exponential decay

$$y = \exp\left(\frac{-x}{\lambda}\right), \tag{7.36}$$

where λ controls the rate of decay.

Let the strips be divided so that each strip contains an equal value A of the integral of this decay. Thus for a strip n

$$\lambda\left[1 - \exp\left(\frac{x_n}{\lambda}\right)\right] = nA, \tag{7.37}$$

where x_n is the position of the edge of the strip furthest from the origin.

If the width of the first strip is x_1 then

$$A = \lambda \left[1 - \exp\left(\frac{-x_1}{\lambda} \right) \right]. \tag{7.38}$$

Thus

$$x_n = -\lambda \ln\left(1 - \frac{nA}{\lambda} \right). \tag{7.39}$$

Also, the number of strips n_m in a distance x_m is given by

$$n_m = \frac{\lambda}{A} \left[1 - \exp\left(\frac{-x_m}{\lambda} \right) \right]. \tag{7.40}$$

Figure 7.2 illustrates this division from one end.

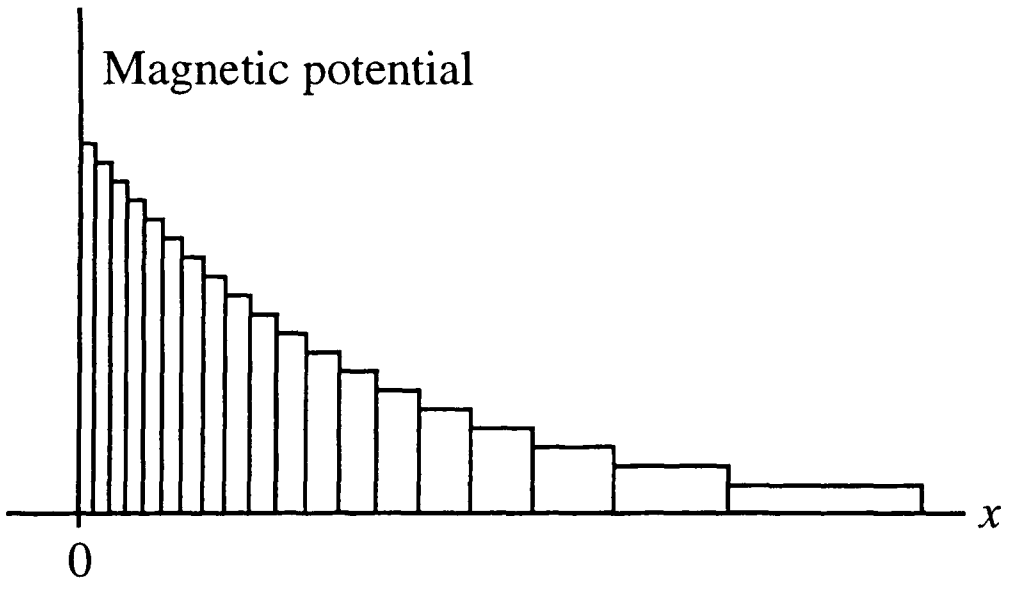

Figure 7.2: Division of the magnetic potential into strips

As the magnetic field decays from both sides of the sample, this division is used from both ends, with a filler strip in the middle.

7.4 References

[1] J. Penfold and R.K. Thomas, *The application of the specular reflection of neutrons to the study of surfaces and interfaces*, J. Phys.: Condensed matter **2** 6 1369–1412 (1990).

[2] H. Zhang and J.W. Lynn, *New exact solution of the one-dimensional Schrödinger equation and its application to polarized neutron reflectometry*, Phys. Rev. Lett. **70** 1 77–80 (1993).

[3] H. Zhang and J.W. Lynn, *Analytical calculation of polarized neutron reflectivity from superconductors*, Phys. Rev. B **48** 21 15893–15904 (1993).

[4] J. Lekner, *Reflection theory and the analysis of neutron reflection data*, Physica B **173** 1–2 99–111 (1991).

[5] I.W. Hamley and J.S. Pedersen, *Analysis of Neutron and X-ray Reflectivity Data. I. Theory*, J. Appl. Cryst. **27** 29–35 (1994).

[6] O.S. Heavens, *Optical properties of thin films*, (London: Butterworth, 1955).

[7] R.A. Cowley and T.W. Ryan, *X-ray-scattering studies of thin-films and surfaces, thermal oxides on silicon* J. Phys. D: Appl. Phys. **20** 1 61–68 (1987).

[8] S.K. Sinha, E.B. Sirota, S. Garoff and H.B. Stanley, *X-ray and neutron scattering from rough surfaces*, Phys. Rev. B **38** 4 2297–2311 (1988).

[9] J.S. Pedersen and I.W. Hamley, *Analysis of Neutron and X-ray Reflectivity Data. II. Constrained Least-Squares Methods*, Physica B **198** 1–3 16–23 (1994).

Chapter 8

Magnetic Flux Penetration Measurements

This chapter describes the measurements made on flux penetration in thin film superconductors and the analysis of the results.

8.1 Experimental techniques

8.1.1 The CRISP spectrometer at ISIS

The measurements in this part were carried out on the CRISP reflectometer at the ISIS spallation neutron source [1, 2]. The CRISP reflectometer uses the time-of-flight method in which the incident angle θ of the neutrons on the sample remains fixed. The neutron source is pulsed at 50 Hz, and the reflectivity is recorded in terms of the neutron wavelength, which is given by the flight time from the target to the detector.

See Figure 7.1 in the previous chapter for a schematic diagram of the CRISP reflectometer.

8.1.2 AC susceptometer

We used an AC susceptometer to measure the critical temperature of the niobium sample (and the oxygenated sample in Section 4.3.3).

It consists of a standard ^{4}He Orange cryostat, with a sample space equipped with primary and secondary coils. These are connected to a DSP lock-in amplifier. The lock-in amplifier provides an oscillation at 85 Hz.

Stepper motors allow the primary and secondary coils to be balanced, and the sample to be moved (including being moved entirely out of the coils).

At each temperature, the signal is measured with the sample in the coils and completely removed from the coils. Thus, the background can be removed.

This susceptometer is one that is currently in development by our group in Oxford. The $NdBa_2Cu_3O_7$ measurement was one of the earliest test measurements. The quoted error is large as many of the usual corrections (such as background removal) could not be performed at that stage. However, within the quoted error we believe the value to be accurate.

The development state of the susceptometer does lead to some difficulties. There is not currently a temperature sensor very near the sample, so there is a noticeable lag between the measured temperature and the sample temperature. For the niobium measurement, the temperature was scanned in both directions to average out this effect. It is also noticeable that the process of moving the sample in and out of the coils causes a fluctuation in the temperature which must be allowed to stabilize.

8.2 Niobium

In this section I present measurements of the magnetic penetration in a niobium thin film as a function of the applied field [3].

8.2.1 Sample

The sample was produced by R. Somekh at the Materials Science Department of Cambridge University.

The sample was a 3000 nm niobium thin film deposited by sputtering on a 5 mm Si

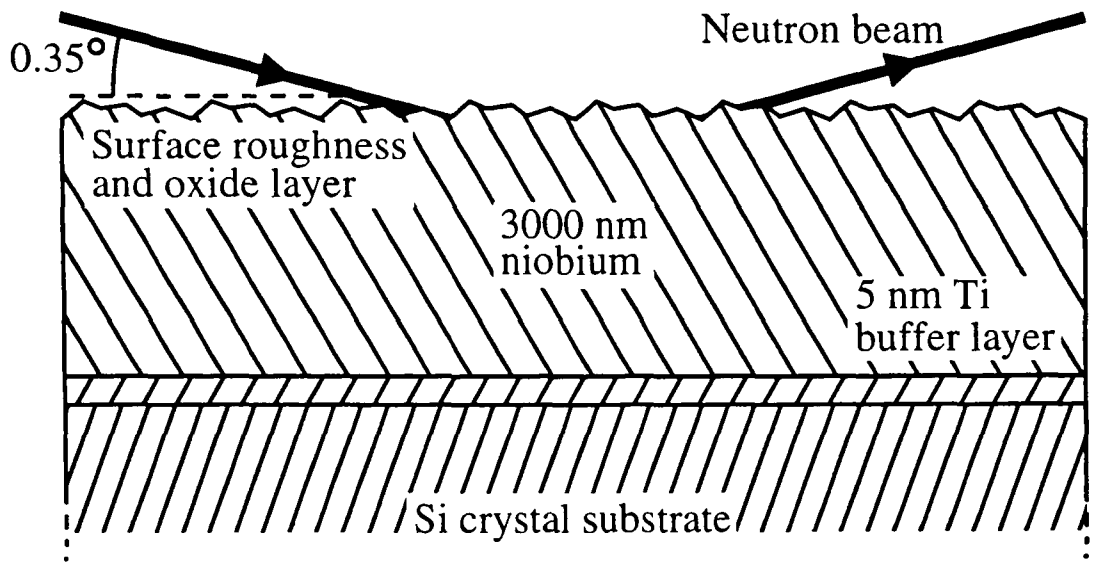

Figure 8.1: The configuration of the niobium sample

crystal substrate, with a 5 nm Ti buffer layer. The thick substrate was chosen to avoid any bending of the sample, which had proved to be a problem previously.

The thickness of the sample was chosen to be much greater than the penetration depth. The derived values of the penetration depth show that the thickness is around 50 times the penetration depth. Thus, the behaviour of the sample should be close to that of a bulk superconductor.

Parts of the sample were measured with the AC susceptometer described in Section 8.1.2. The critical temperature was found to be 9.28 ± 0.05 K.

To characterize the sample, I measured parts in a magnetometer to obtain the critical temperatures (see Section 8.2.3).

The thickness of the buffer layer is only a nominal value. The thickness was chosen to be as small as possible without risking leaving holes. The buffer layer was chosen to provide a better bond between the niobium and substrate. The lattice mismatch in a previous set of samples without the buffer layer had caused some of the films to peel off the substrate.

Figure 8.1 is a schematic diagram of the niobium sample.

8.2.2 Measurements

The reflectivity measurements were taken with the temperature kept between 3.4 K and 4.3 K (below T_c). Due to slight leaks in the cryostat, the temperature varied by a small

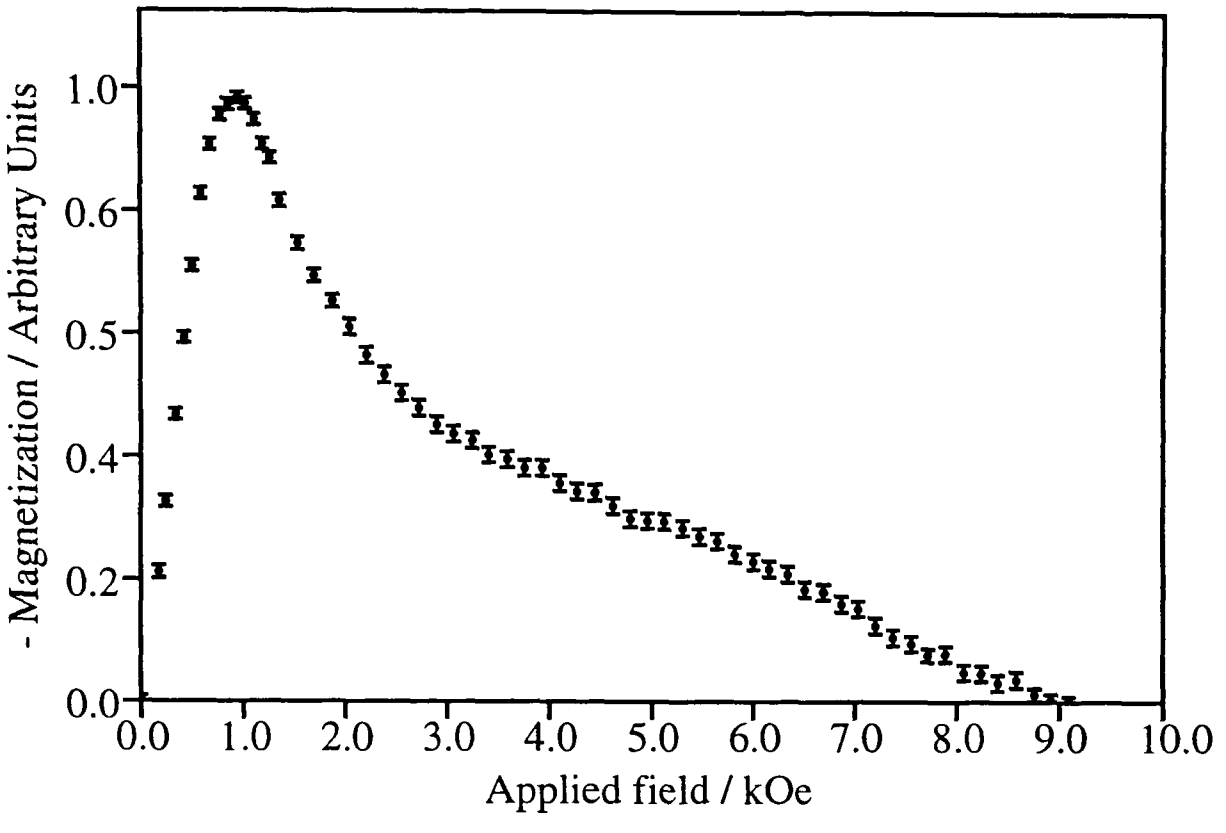

Figure 8.2: Magnetization of the niobium sample

amount. This temperature was chosen both for the ease of control (a much lower temperature is hard to obtain consistently) and so that the temperature is well away from T_c so that fluctuations in the temperature are not as problematic. A temperature closer to T_c would have the advantage that the critical fields would be depressed, allowing easier access to the non-Meissner states.

We used an electromagnet to apply a field between 400 and 4500 Oe parallel to the surface of the sample. The applied field was calibrated with a Hall probe.

Unfortunately the magnetometer measurements show that the field available was not sufficient to fully reach the surface superconductivity state at the temperature studied.

In all the measurements, the wavelength dependent reflectivity was binned into 138 data points.

8.2.3 Magnetometer measurements

Figure 8.2 the magnetization of the sample at different fields. This magnetization is negative due to the superconductor being a diamagnet. This was measured using a DC magnetometer.

The magnetometer consists of a superconducting magnet within which are two oppositely

wound coils. The sample is moved between two positions along the axis of the coil by a pneumatic piston. The integrated change in voltage gives the change in the flux, which is proportional to the magnetization.

To fit in the magnetometer, the sample had to be cut into strips. To match the conditions in the reflectometry experiment, the strips were orientated so that the long direction was along the magnetic field (and coil) axis.

It was very noticeable from the magnetization measurements that above H_{c1}, the sample traps flux, presumably at defects. Thus, the magnetization measurements are very different when the field is swept down. In fact after the field has been taken to above H_{c3} and then reduced, the sample shows large amounts of magnetization (in the opposite sense) even at zero field. This magnetization was around three quarters of the maximum diamagnetic magnetization.

The measurements presented here thus show the magnetization in one direction (that of increasing field) only.

This flux trapping effect means that for reflectivity measurements great care must be taken when applying magnetic fields to only ever increase the field. If the field needs to be decreased, the sample should be warmed above T_c, and then cooled in zero field. This will remove any trapped flux, and the field can then be increased again.

Due to the large thickness of the sample, the behaviour of the critical fields should be very similar to that of the bulk superconductor.

The transition to the mixed state is quite broad, but the measurements put H_{c1} at 950 ± 50 Oe.

From these measurements, it is not entirely clear what effect the surface state has on the magnetization. If the disappearace of magnetization is taken as H_{c3}, then H_{c3} is 9050 ± 50 Oe and H_{c2} is 5340 ± 30 Oe (derived from H_{c3} using Equation 6.12).

However, model calculations for the surface state later in this chapter indicate that the surface state magnetization is likely to be small relative to the mixed state. Thus the disapperance of magnetization is more likely to give the position of H_{c2}, which puts H_{c2} at 9050 ± 50 Oe

The critical fields are rather higher than those for pure niobium [4], again indicating a

'dirty' sample.

8.2.4 Reflectivity overview

Figure 8.3 shows the data for the flipping ratios (R^+/R^-) for the sample at the different applied fields. The dips in the flipping ratio occur around the critical edge. This shows a clear qualitative trend. In the Meissner state, the integrated area of the dip in the polarization function should increase approximately linearly with field. The signal then stops increasing as the mixed phase is entered for the applied fields of 1444 Oe and above.

As a measure of the magnetic signal, I define the integral of the polarization function (see Equation 7.35) as

$$I_P = \int_0^\infty P(Q_z)\mathrm{d}Q_z. \tag{8.1}$$

Figure 8.4 shows the values of I_P for the different applied fields.

In the Meissner state, the integral of the polarization function should increase approximately linearly.

It is notable that I_P is almost constant throughout the mixed state, despite the magnetization falling rapidly. This is further indication that PNR is particularly sensitive to the change in the magnetization near the surface.

8.2.5 Unpolarized scattering

Figure 8.5 shows the scattering from the sample in zero field. Figure 8.6 shows the same data enlarged around the critical edge.

The theoretical line is a fit based on the parameters in Table 8.1. The structure is assumed to be the nominal structure, with an additional oxide layer on the top.

It was apparent from the theoretical calculations that the shape of the reflectivity curve is highly dependent on the titanium buffer layer. This buffer layer has a similar effect on the curve as roughness at the interfaces. The fits showed little dependence on the small roughness for the surface, so the theoretical curve neglects roughness.

Thus, fixing the scattering length densities (nb) to their nominal values the only free parameters are the widths of the layers, and the angle and deviation of the beam and the

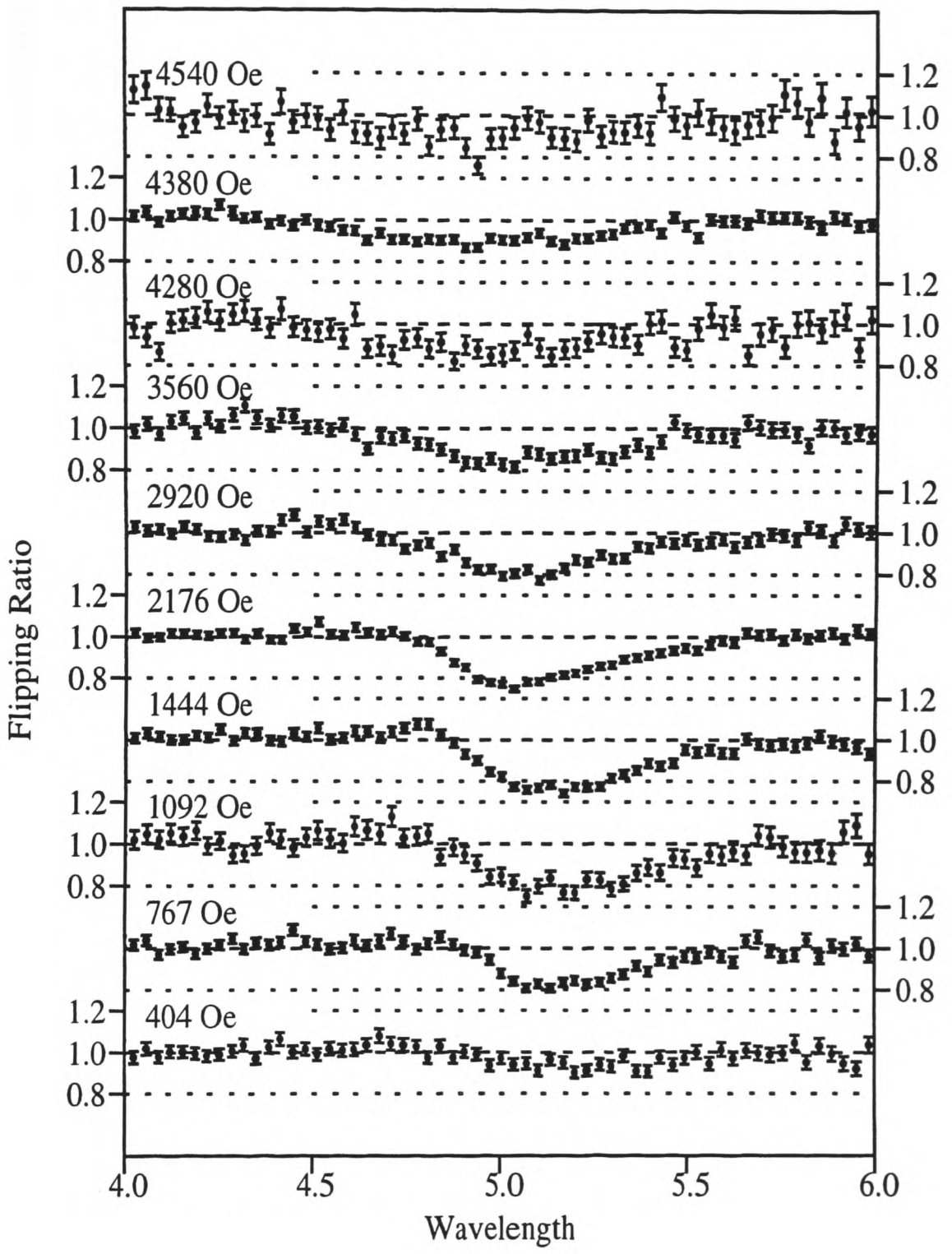

Figure 8.3: Niobium flipping ratios: The flipping ratio (R^+/R^-) is shown as a function of neutron wavelength in Å, at different applied fields.

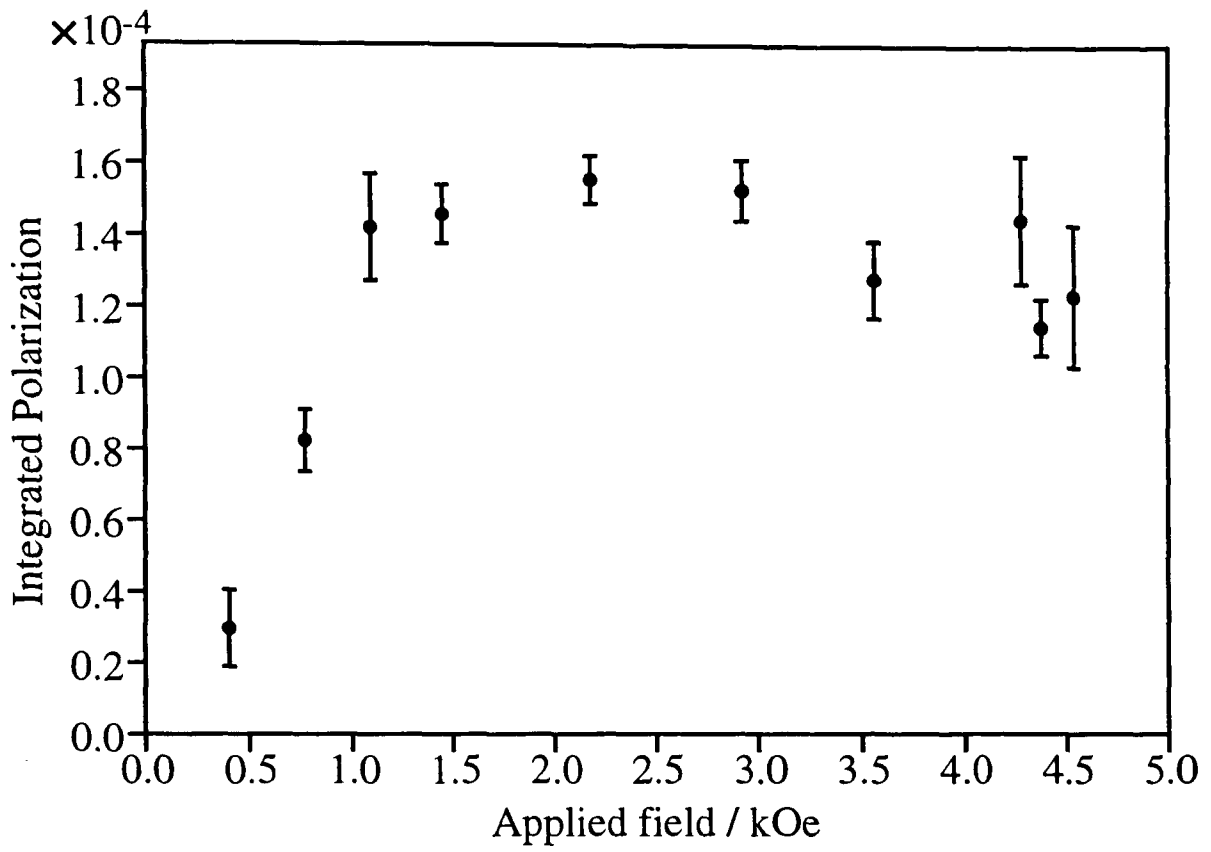

Figure 8.4: Integrated Polarization for niobium

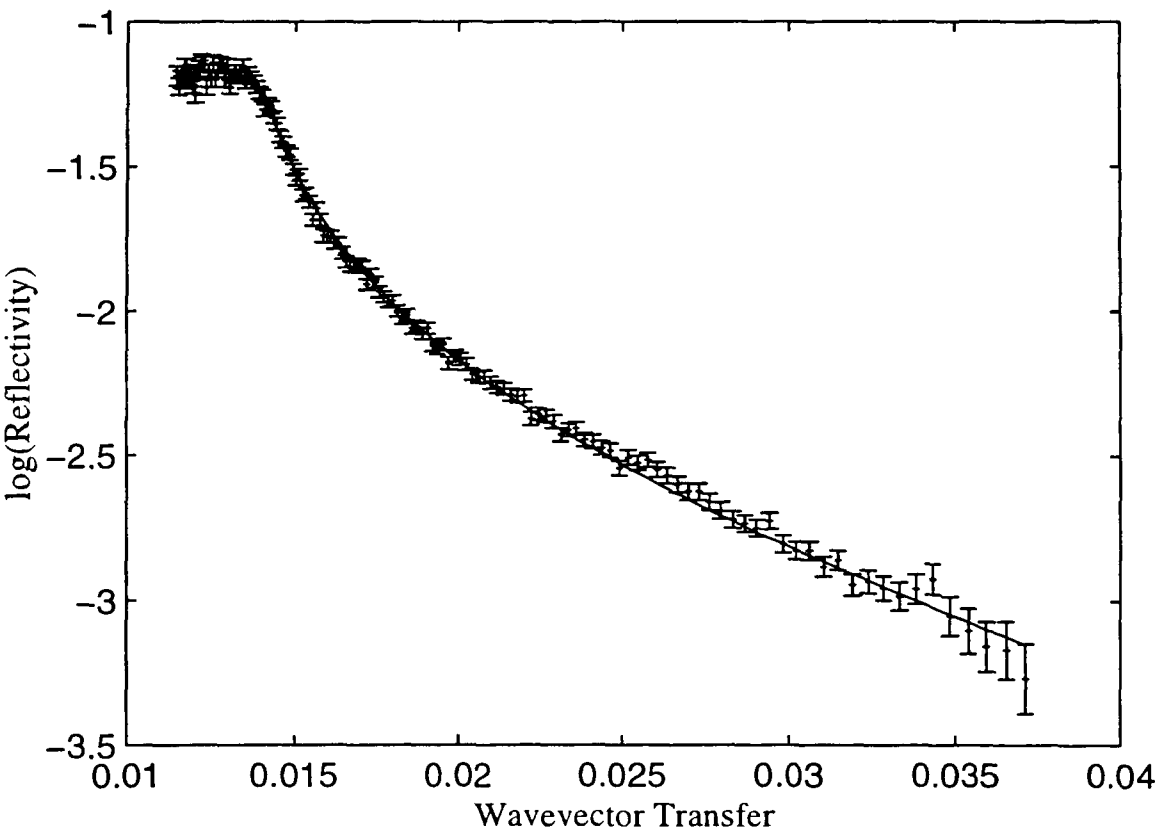

Figure 8.5: Niobium zero field reflectivity: The reflectivity of the niobium sample in zero field. The reflectivity is in arbitrary units.

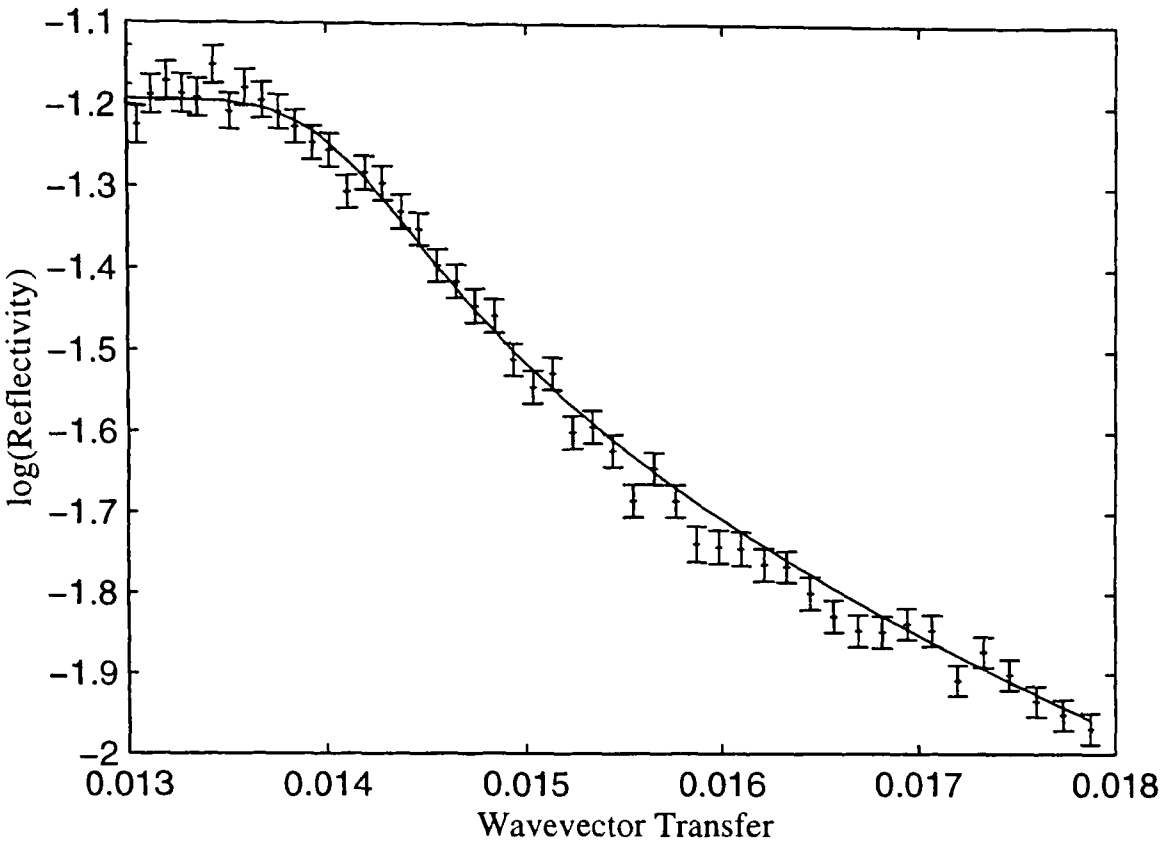

Figure 8.6: Niobium zero field reflectivity: The same data as in Figure 8.5 enlarged around the critical edge.

overall intensity.

The angle and deviation need to be variable due to the difficulties in precise alignment of the sample. The intensity needs to be variable as not all of the beam will be incident on the sample, and some will be removed by the collimators.

The low χ^2 indicates that the theoretical model is adequate, though the errors on the measurements are relatively large, so there is considerable flexibility in the model.

The widths returned by the fit are all comparable to the nominal widths.

8.2.6 Meissner state analysis

From Figures 8.4 and 8.2, the lowest two fields we measured at are in the Meissner state, and the third is just at the transition from Meissner to mixed states.

Table 8.2 shows the fitted parameters for the theoretical model of an exponential as in Equation 6.6. The strips were divided as in Equation 7.39, with an initial strip width of 8 Å and a nominal penetration depth of 600 Å.

In all of the tables of the fitted parameters for magnetic structure, intensity is given in

Parameter	Nominal	Fit	Error	Units
Reflectivity	-	6.505	0.030	10^{-2} Counts/Monitor
Incident angle	0.35	0.33860	0.00028	Degrees
Beam deviation	3.2	5.5852	0.0055	%
Top *nb*	4.495	-	-	10^{-6}Å^{-2}
Top width	-	93.9	4.2	Å
Bulk *nb*	3.93	-	-	10^{-6}Å^{-2}
Bulk width	30000	29578	458	Å
Buffer *nb*	-1.91	-	-	10^{-6}Å^{-2}
Buffer width	50	75.16	0.61	Å
Substrate *nb*	2.07	-	-	10^{-6}Å^{-2}
χ^2		1.015		

Table 8.1: Niobium zero field reflectivity parameters

Field	404 Oe	767 Oe	1092 Oe
Intensity	0.0644 ± 0.0002	0.0640 ± 0.0002	0.0656 ± 0.0002
Incident angle	0.3409 ± 0.0002	0.3391 ± 0.0001	0.3403 ± 0.0002
Beam deviation	5.584 ± 0.016	5.573 ± 0.007	5.567 ± 0.041
λ	624 ± 211	613 ± 37	633 ± 97
χ^2	3.26	5.17	2.28
FR χ^2	0.94	1.44	1.07

Table 8.2: Niobium low field reflectivity parameters: The FR χ^2 refers to the χ^2 for the model of the flipping ratio.

counts per monitor count, incident angle in degrees, beam deviation in % and penetration depth λ in Å.

Due to the differences in alignment, the intensity, incident angle and beam deviation were allowed to vary in the fit, along with the penetration depth. The applied field parameter was fixed, as were the structure parameters derived from the unpolarized measurements.

Figures 8.7,8.9 and 8.11 show the form of R^+ and R^- for the different fields, along with the model curve as described above.

Figures 8.8,8.10 and 8.12 show the flipping ratios for the applied fields, along with the same model curve.

Both of the types of figure have been scaled to show the interesting area around the critical edge. In all cases (including the later measurements not in the Meissner state) the model curve agrees well with measurement outside of this area. Above the critical edge

the reflectivity is flat, and far away from the critical edge the magnetism has negligible effect on the reflectivity, and so the simple structural model duplicates the measured values accurately.

Due to the poor statistics available for the unpolarized measurements, I also fitted the 404 Oe reflectivity curves allowing the widths of the structural strips to vary. This was to see if a better model for the structure could be obtained. However, the fit was not significantly better, and had very similar values for the widths, so the original widths were used for the rest of the fields.

An exponential decay model seems to give a good representation of the measured reflectivity.

For each of the applied fields, the derived penetration depth is around 620 Å. This is rather higher than the previously measured values for single crystal niobium, many of which are around 450 Å. This indicates that it is likely that this crystal has fairly small grains and is a 'dirty' superconductor, by the definition of Equation 6.7.

From Equation 6.28 and Equation 6.13, we have

$$\kappa^2 = \frac{H_{c3}}{2.39}\frac{2\sqrt{2}\pi\mu_0\lambda_{\text{eff}}^2}{\phi_0}. \tag{8.2}$$

Thus, if we assume that $\lambda = \lambda_{\text{eff}}$ and $H_{c3} = 9050$ Oe, then the measured values give $\kappa \approx 2.5$. This value of κ then gives a value for H_c of 1.514 kOe. If $H_{c2} = 9050$ Oe, then $\kappa \approx 3.3$.

The measurements give the value for the magnetic screening length λ, but the London penetration depth λ_L is not directly obtainable.

The deviation of the measured penetration depth from the London penetration depth is determined by how much the mean free path of the electrons is limited by defects. Away from the critical temperature, the effective penetration depth is given by (See Chapter 6 Ref. [19]):

$$\lambda_{\text{eff}}(l,T) = \lambda_L(T)\sqrt{1+\frac{\xi_0}{l}}, \tag{8.3}$$

where ξ_0 is the Pippard coherence length and l is the mean free path due to the defects.

Assuming a clean-limit coherence length of 40.9 nm and zero-temperature $\lambda_L(0)$ for the

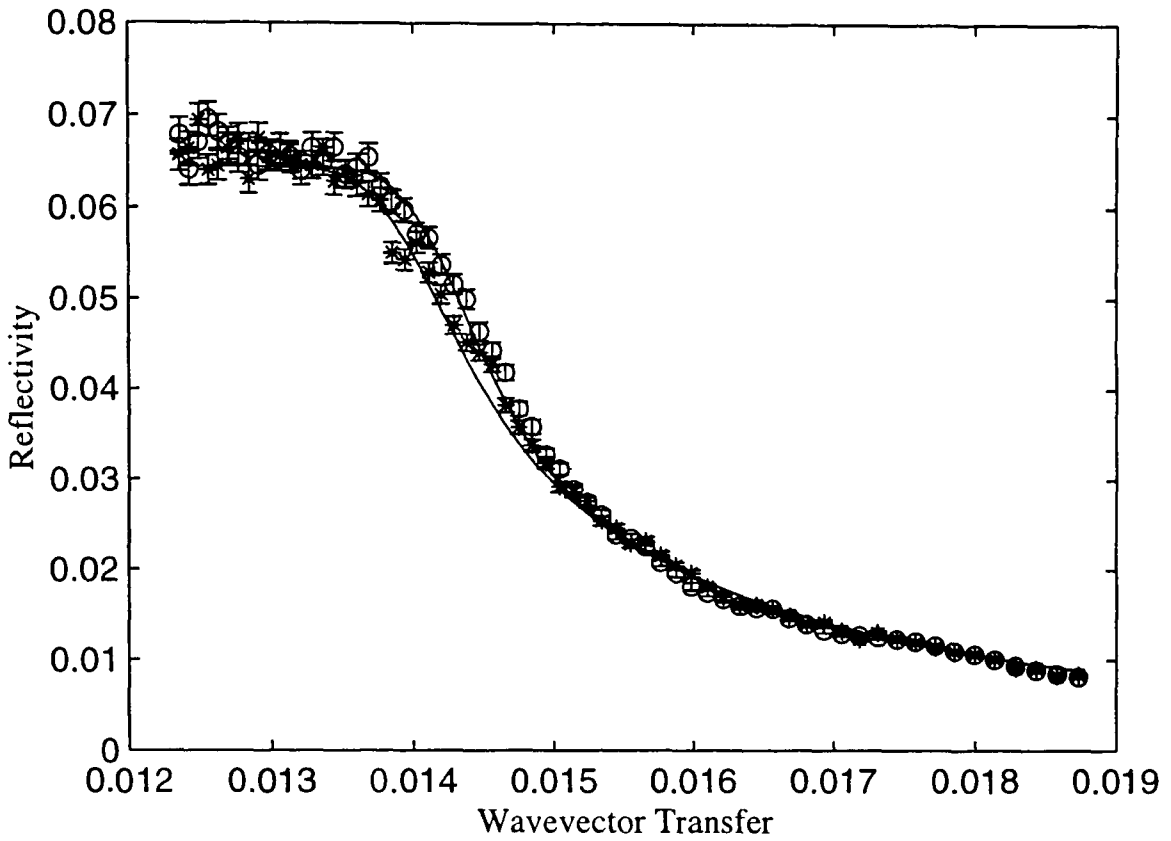

Figure 8.7: Reflectivity at 404 Oe

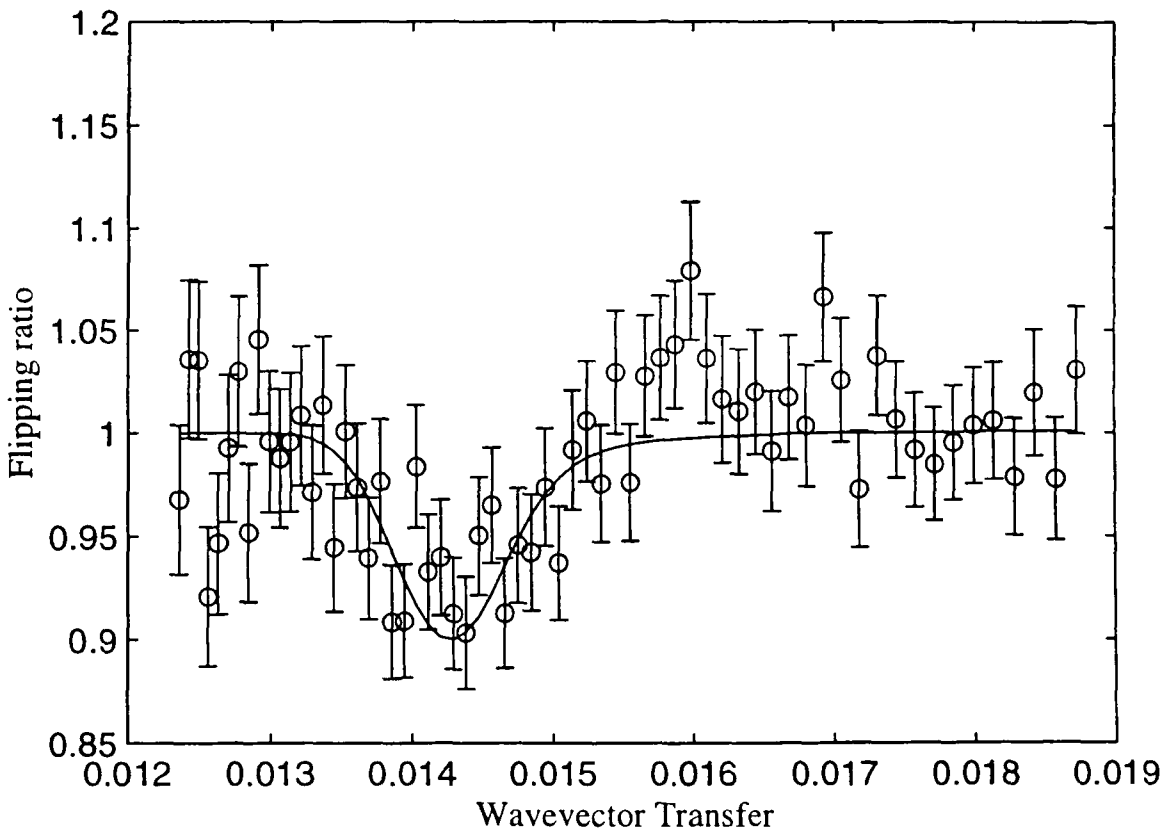

Figure 8.8: Flipping ratio at 404 Oe

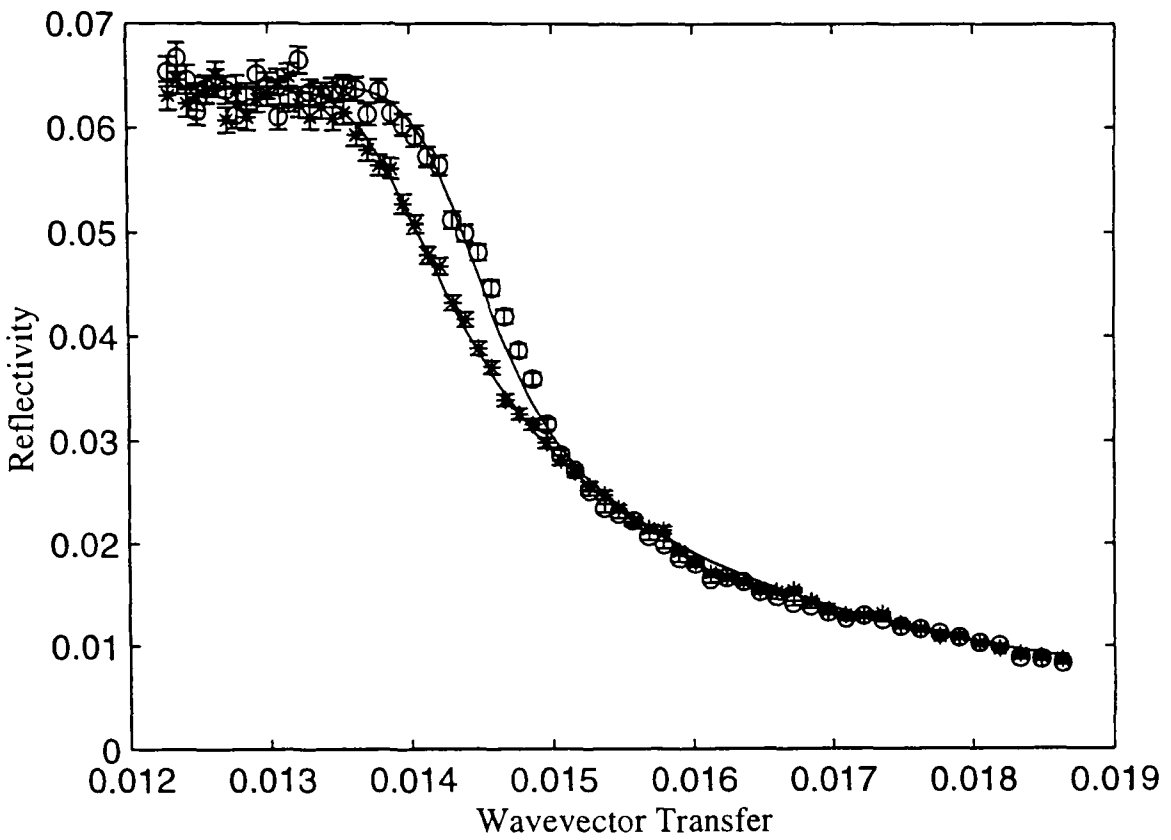

Figure 8.9: Reflectivity at 767 Oe

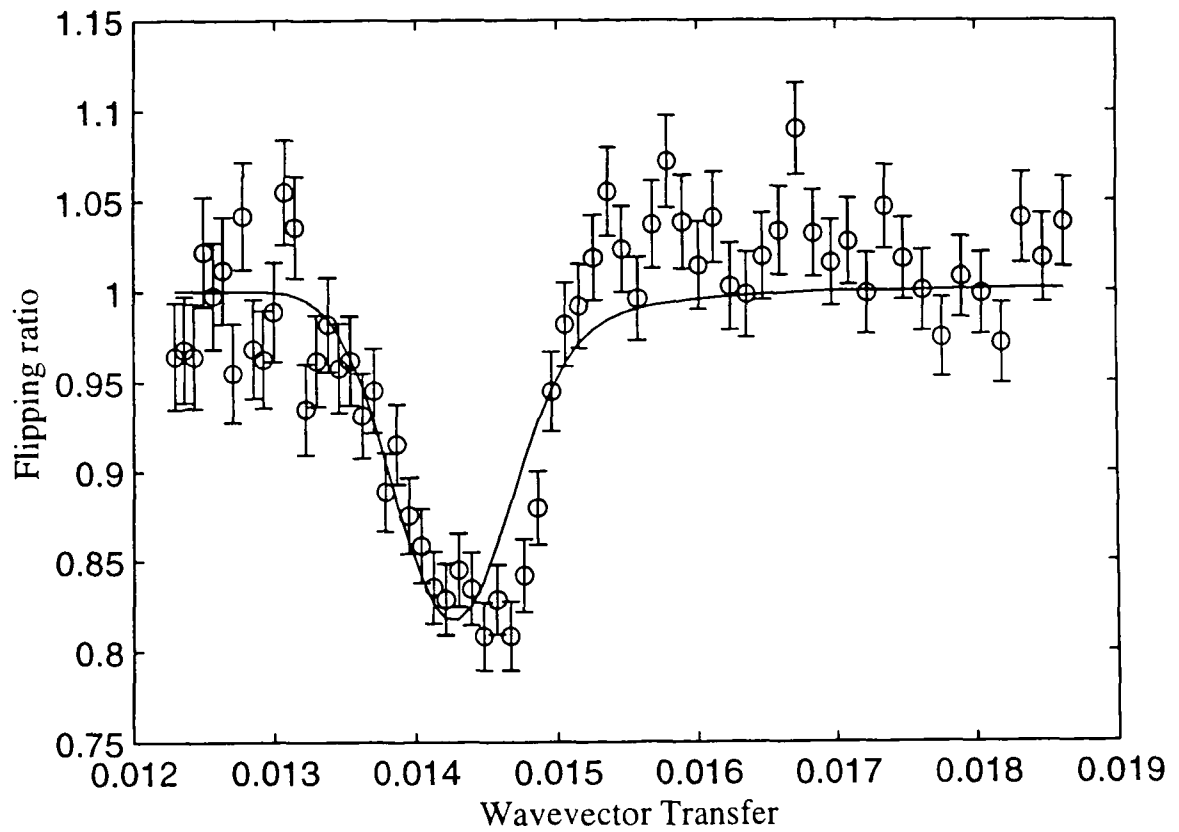

Figure 8.10: Flipping ratio at 767 Oe

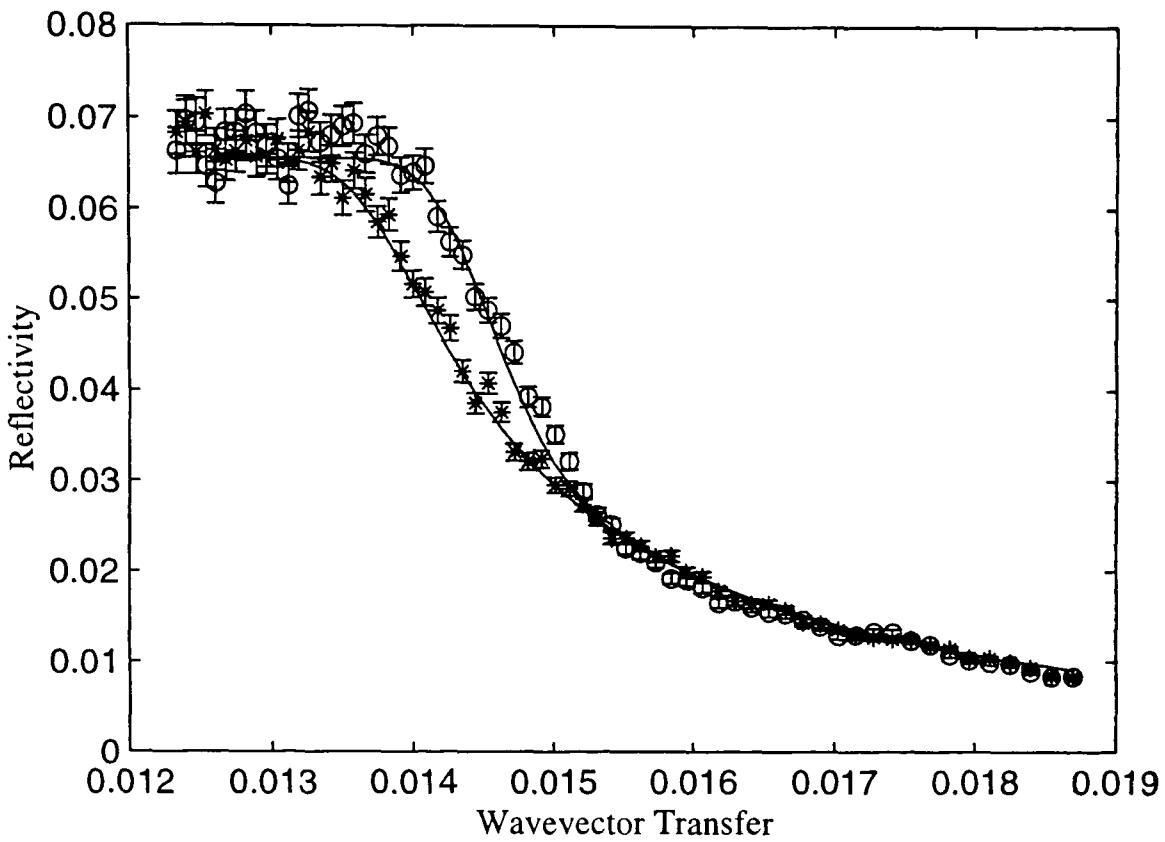

Figure 8.11: Reflectivity at 1092 Oe

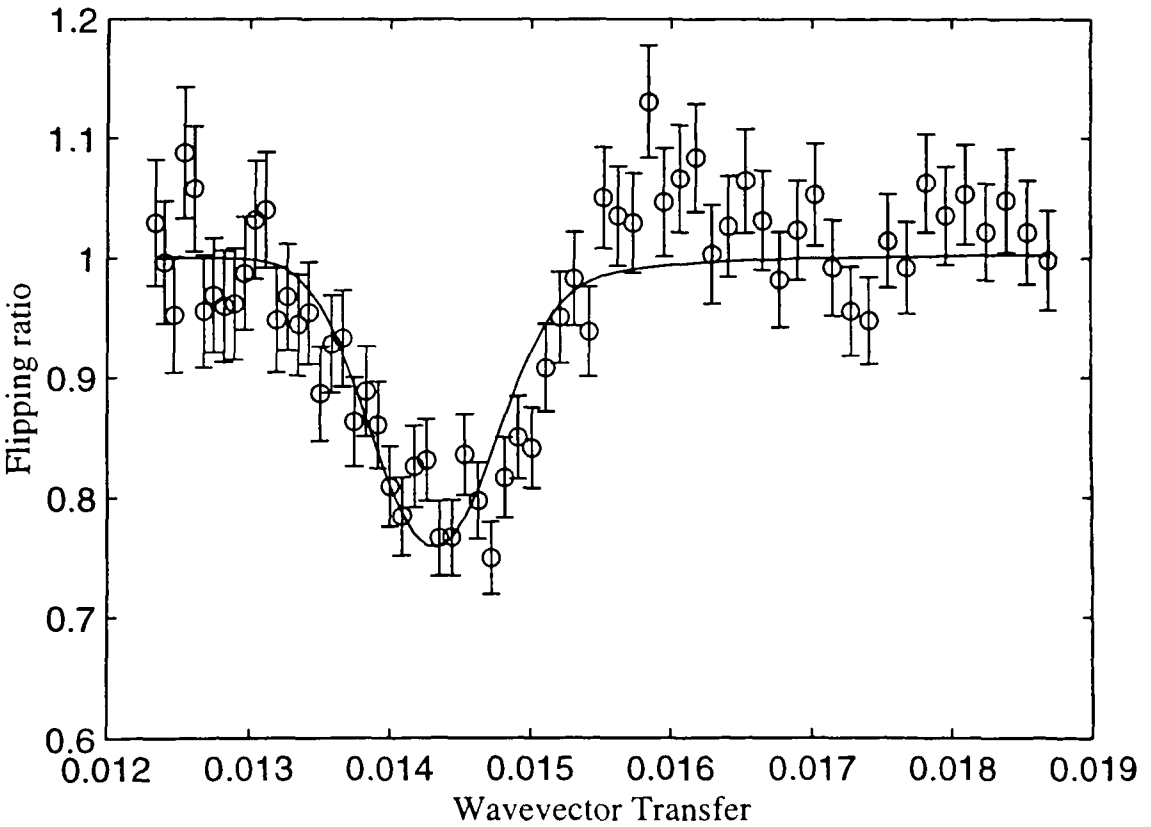

Figure 8.12: Flipping ratio at 1092 Oe

sample of 28.9 nm (See Chapter 6 Ref. [6]) gives a value of l of 11.4 nm, which is similar to sample Nb/Si − 1 in Chapter 6 Ref. [10].

The penetration depth is measured here at around 4.2 K. The zero temperature penetration depth will vary from this slightly. However, the two-fluid approximation $\lambda(T) = \lambda(0)/[1-(T/T_c)^4]^{1/2}$ suggests that in this case $\lambda(4.2\ \mathrm{K})$ is only 2% greater than $\lambda(0)$.

8.2.7 Mixed state analysis

To attempt to model the mixed state, a similar procedure was used as for the Meissner state.

However, as well as the penetration depth, the applied field was also allowed to vary. The reasoning behind this is to see if the magnetic field can be represented as if the flux tubes reduce the effective applied field.

Table 8.3 shows the fitted parameters for the different applied fields. Note that as the model becomes poor for the higher fields (see below), the actual errors on the penetration depth will be considerably larger than the random errors quoted here. This is a particular problem with this fitting technique as the effective field and the penetration depth are quite closely coupled.

Figures 8.13, 8.15, 8.17, 8.19, 8.21, 8.23 and 8.25 show the reflectivity curves for the different applied fields.

Figures 8.14, 8.16, 8.18, 8.20, 8.22, 8.24 and 8.26 show the flipping ratios.

At 1440 Oe, this is still a reasonable model for the measured reflectivity. At 2176 Oe, there is a significant deviation from the exponential decay. Above 2920 Oe, this discrepancy becomes gradually larger, and the dip in the flipping ratio becomes shallower and broader.

At the higher fields it is clear that a simple exponential decay with an effective field is no longer a realistic model.

Field	1444 Oe	2176 Oe	2920 Oe
Intensity	0.0633 ± 0.0002	0.0631 ± 0.0002	0.0652 ± 0.0002
Incident angle	0.3402 ± 0.0002	0.3380 ± 0.0002	0.3403 ± 0.0002
Beam deviation	5.563 ± 0.013	5.577 ± 0.009	5.5690.018
Effective field	1278.5 ± 6.1	1039.4 ± 9.5	1127 ± 10
λ	697 ± 49	439 ± 35	891 ± 115
χ^2	5.50	8.58	5.55
FR χ^2	1.72	3.52	3.68
Field	3560 Oe	4280 Oe	4380 Oe
Intensity	0.0645 ± 0.0002	0.0650 ± 0.0002	0.0581 ± 0.0002
Incident angle	0.3398 ± 0.0002	0.3399 ± 0.0002	0.3396 ± 0.0002
Beam deviation	5.583 ± 0.010	5.515 ± 0.070	5.652 ± 0.030
Effective field	1001 ± 5	980 ± 4	980 ± 5
λ	587 ± 57	605.267 ± 113	598 ± 47
χ^2	3.63	1.89	6.62
FR χ^2	2.32	1.69	4.58
Field	4540 Oe		
Intensity	0.0643 ± 0.0002		
Incident angle	0.3385 ± 0.0002		
Beam deviation	5.588 ± 0.013		
Effective field	761 ± 66		
λ	979 ± 7		
χ^2	1.74		
FR χ^2	1.41		

Table 8.3: Niobium high field reflectivity parameters

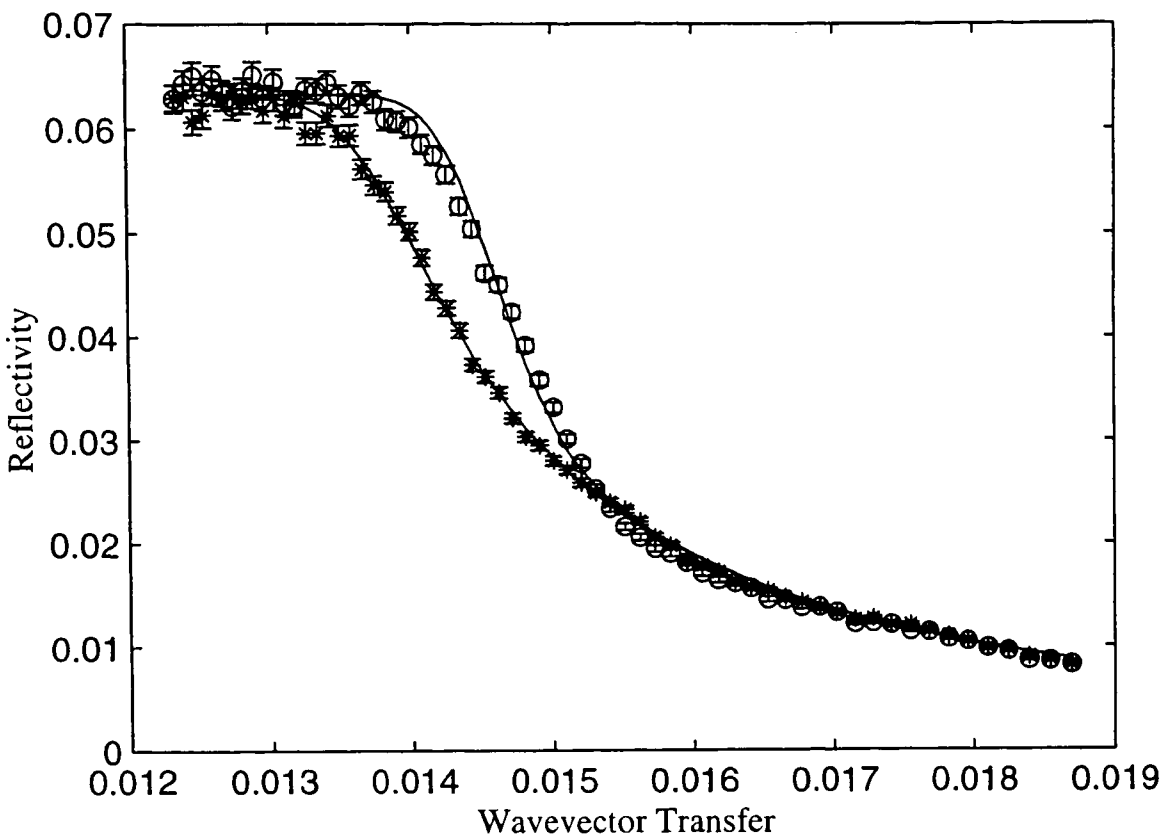

Figure 8.13: Reflectivity at 1444 Oe

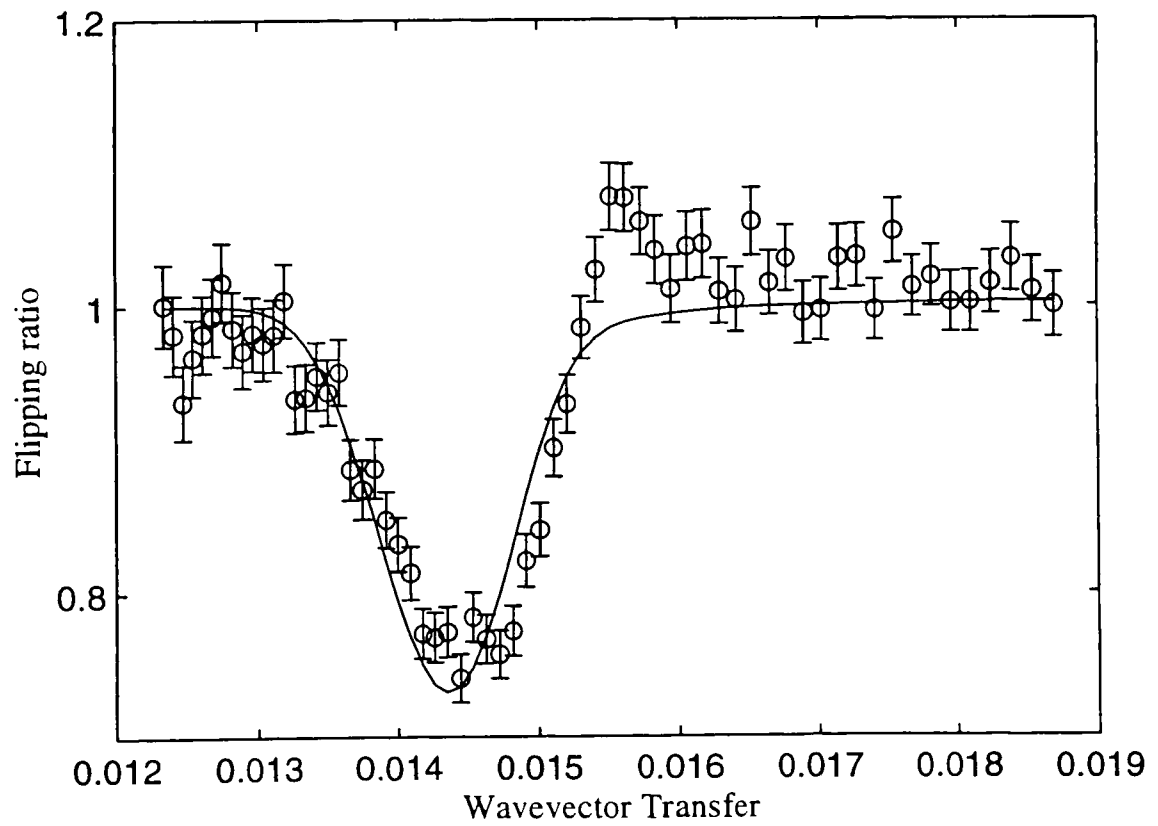

Figure 8.14: Flipping ratio at 1444 Oe

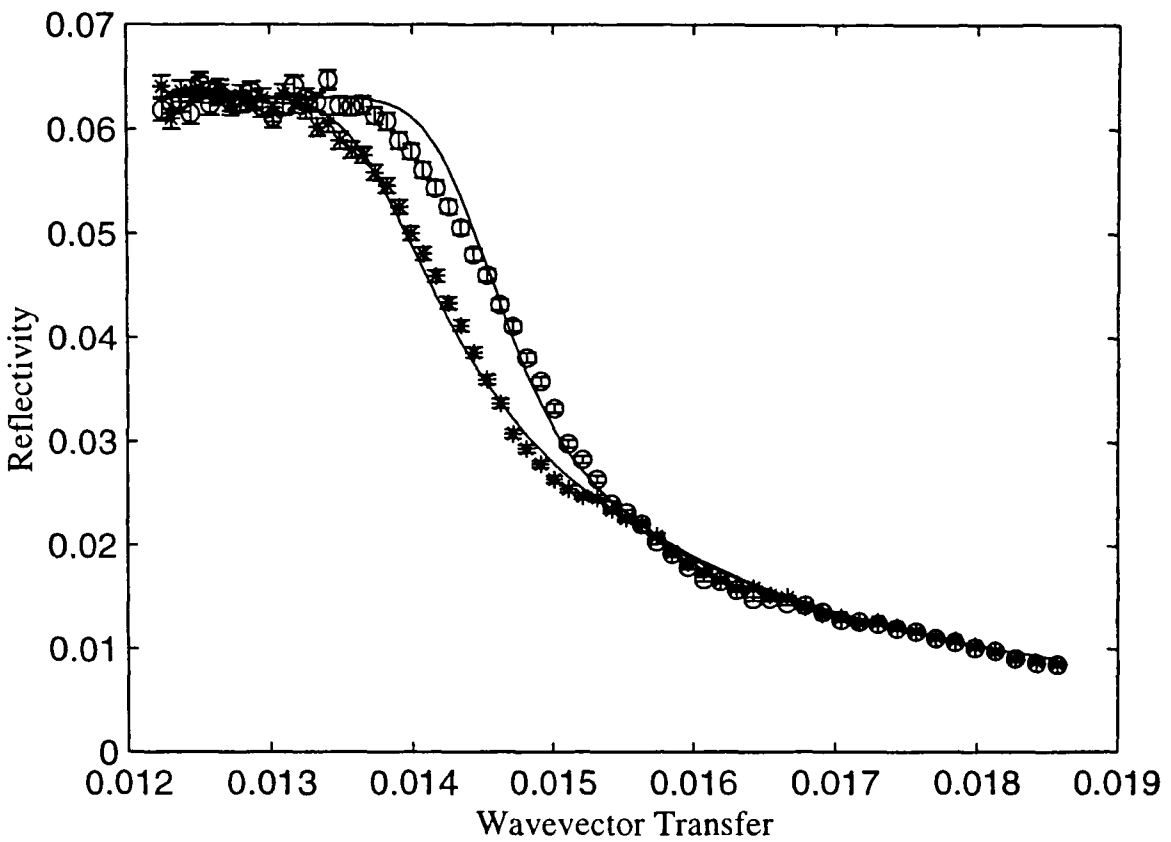

Figure 8.15: Reflectivity at 2176 Oe

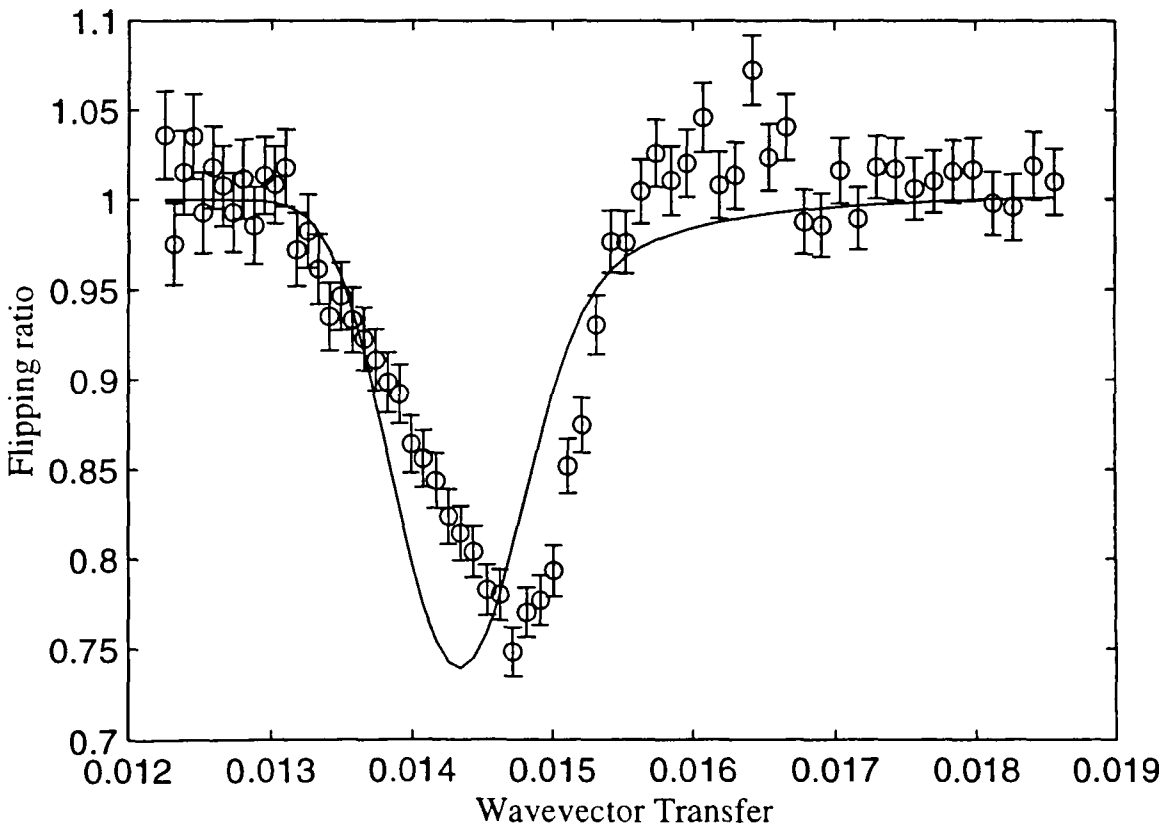

Figure 8.16: Flipping ratio at 2176 Oe

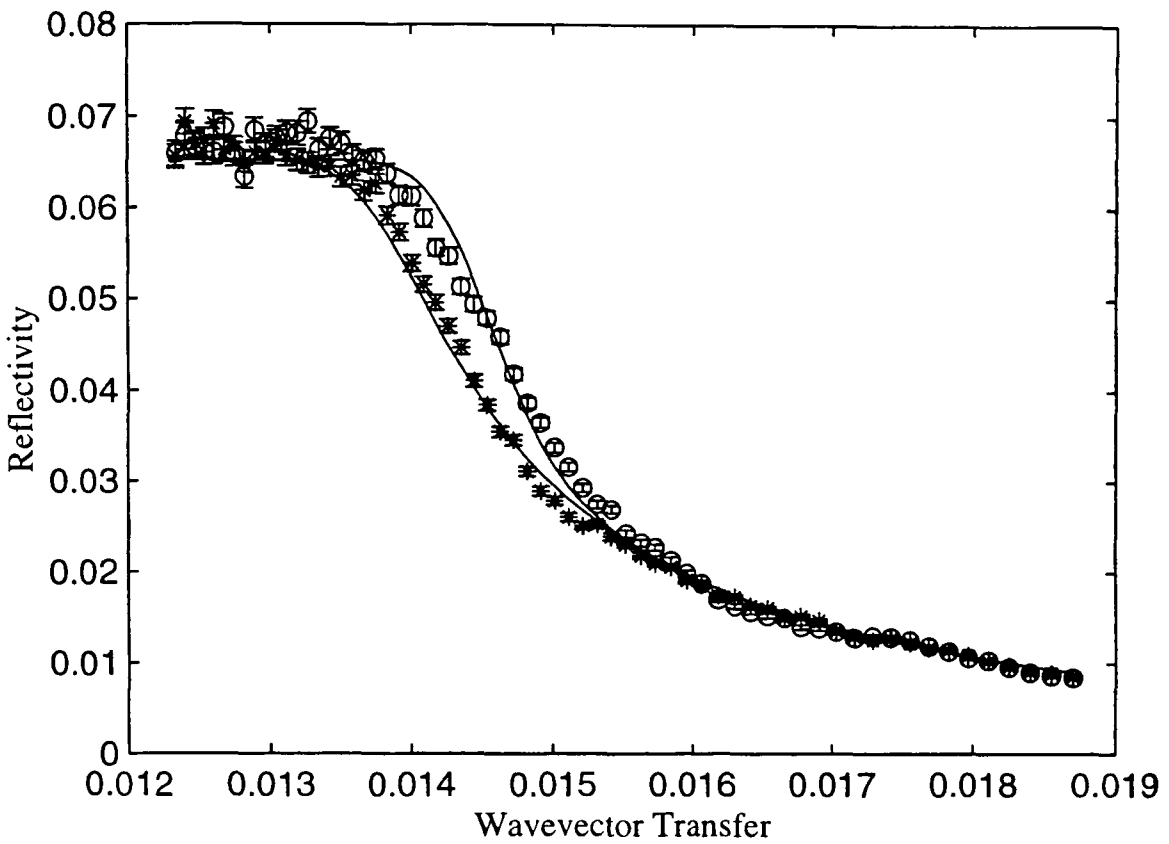

Figure 8.17: Reflectivity at 2920 Oe

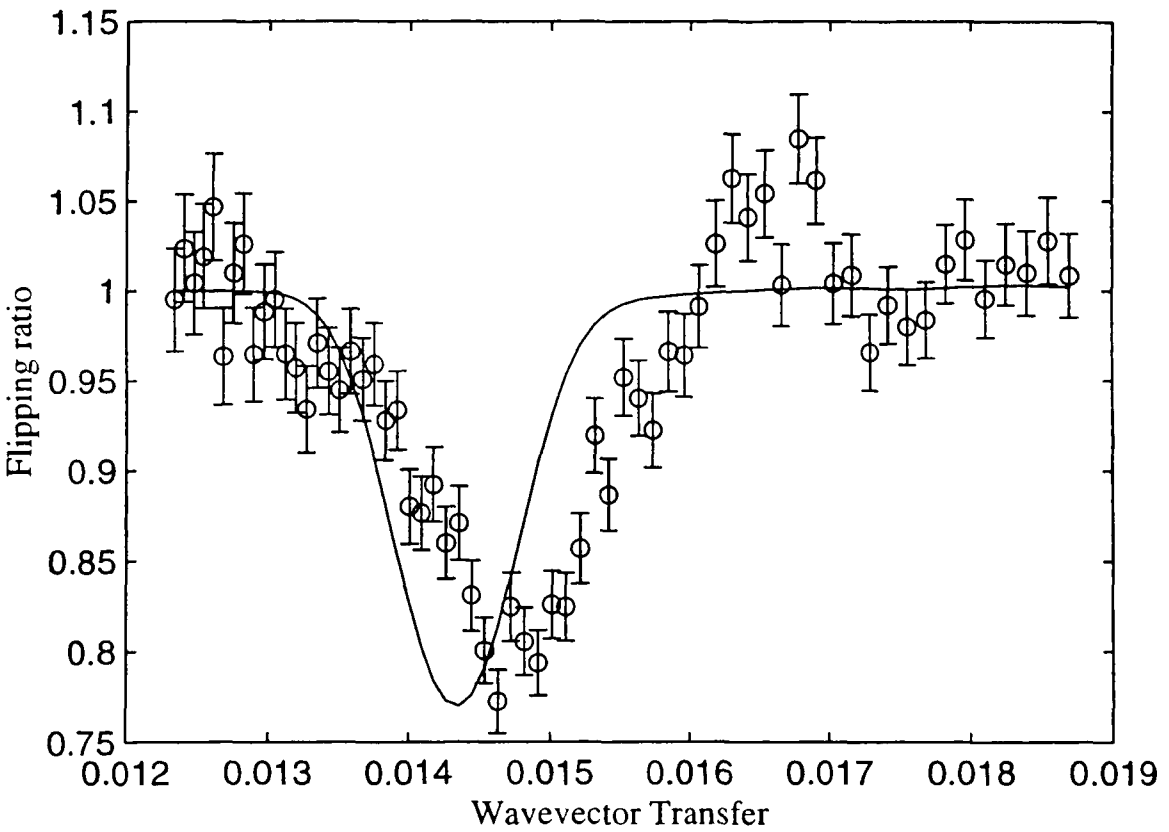

Figure 8.18: Flipping ratio at 2920 Oe

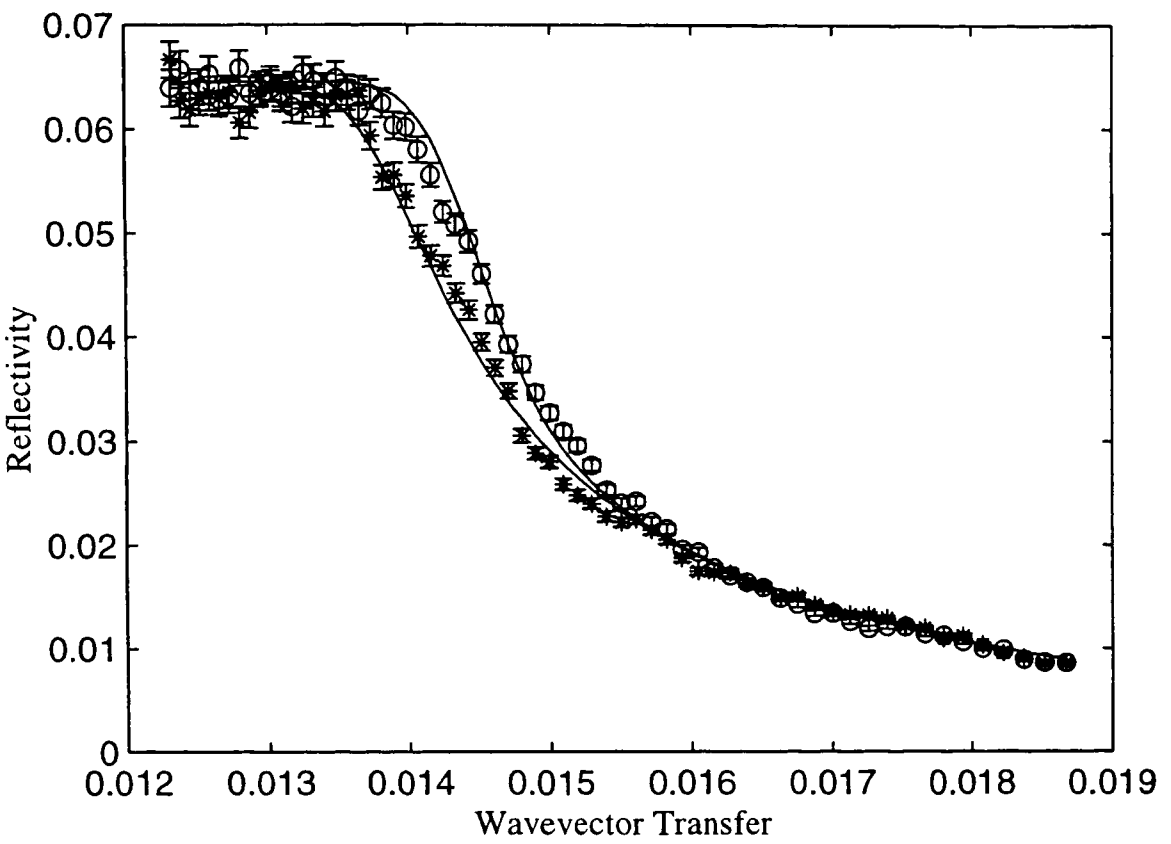

Figure 8.19: Reflectivity at 3560 Oe

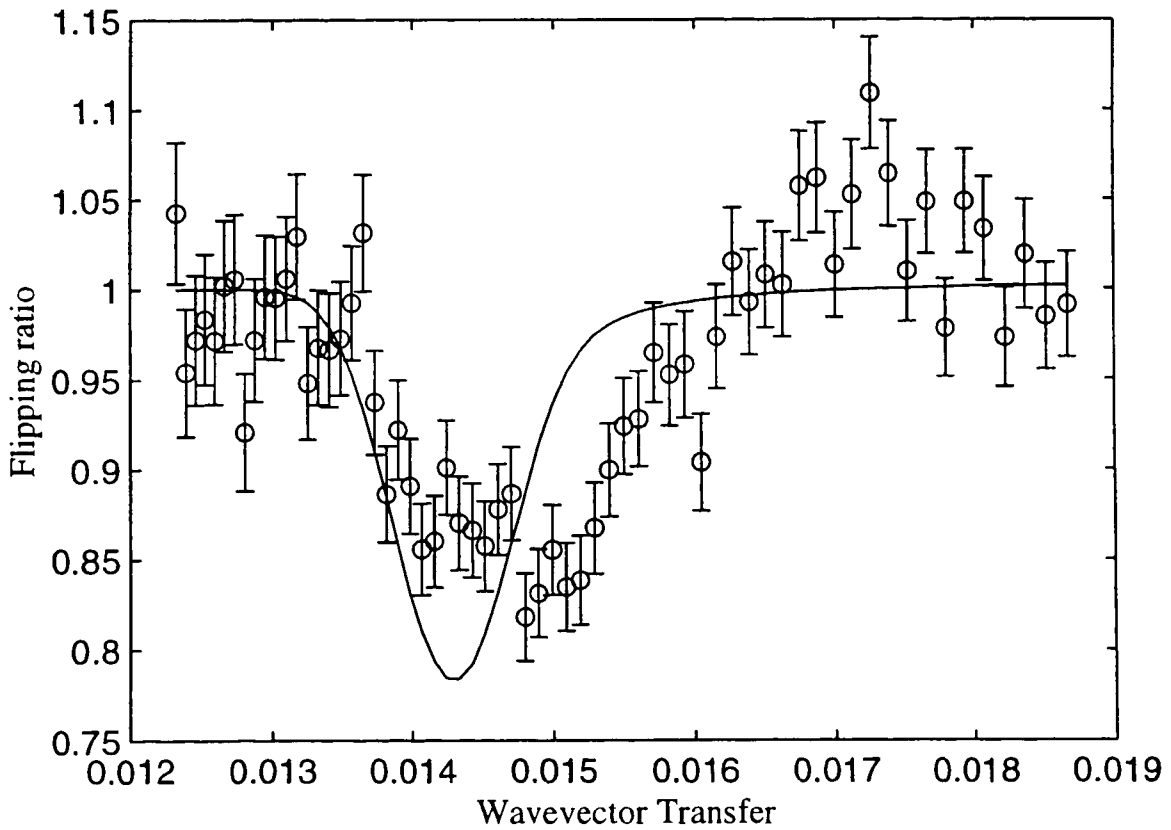

Figure 8.20: Flipping ratio at 3560 Oe

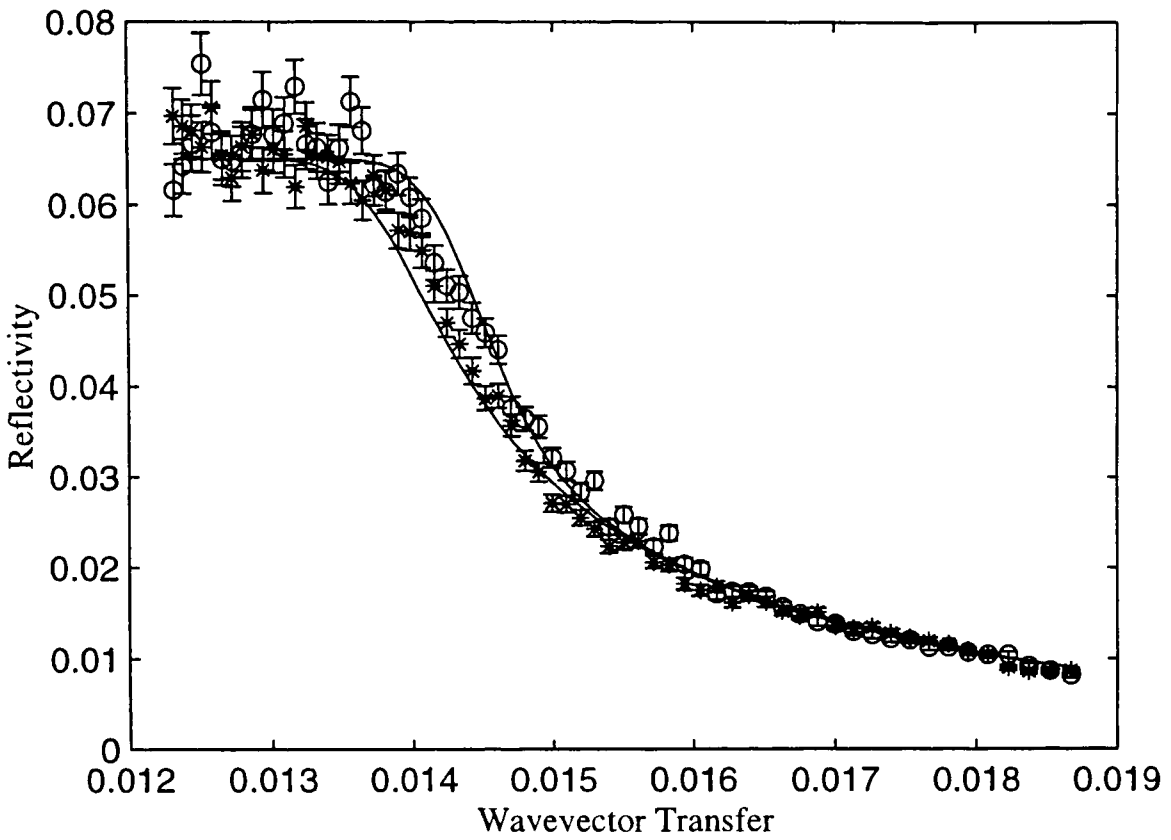

Figure 8.21: Reflectivity at 4280 Oe

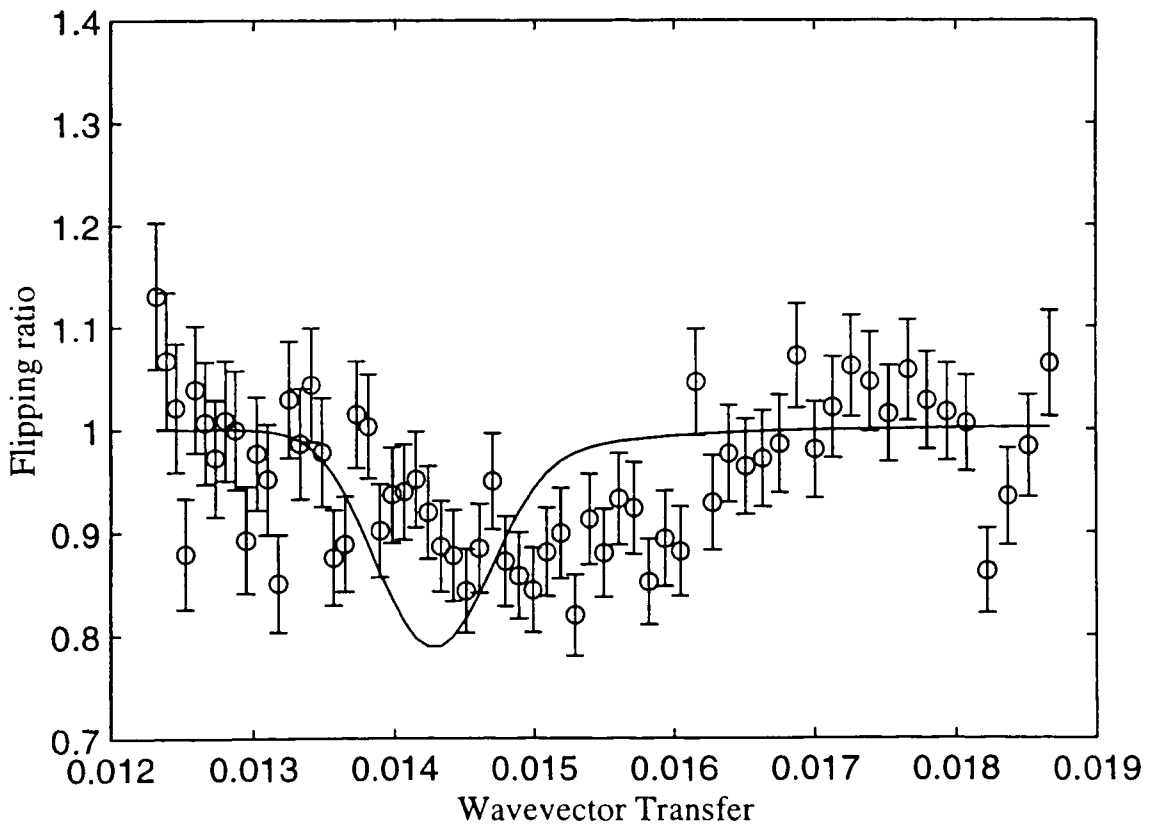

Figure 8.22: Flipping ratio at 4280 Oe

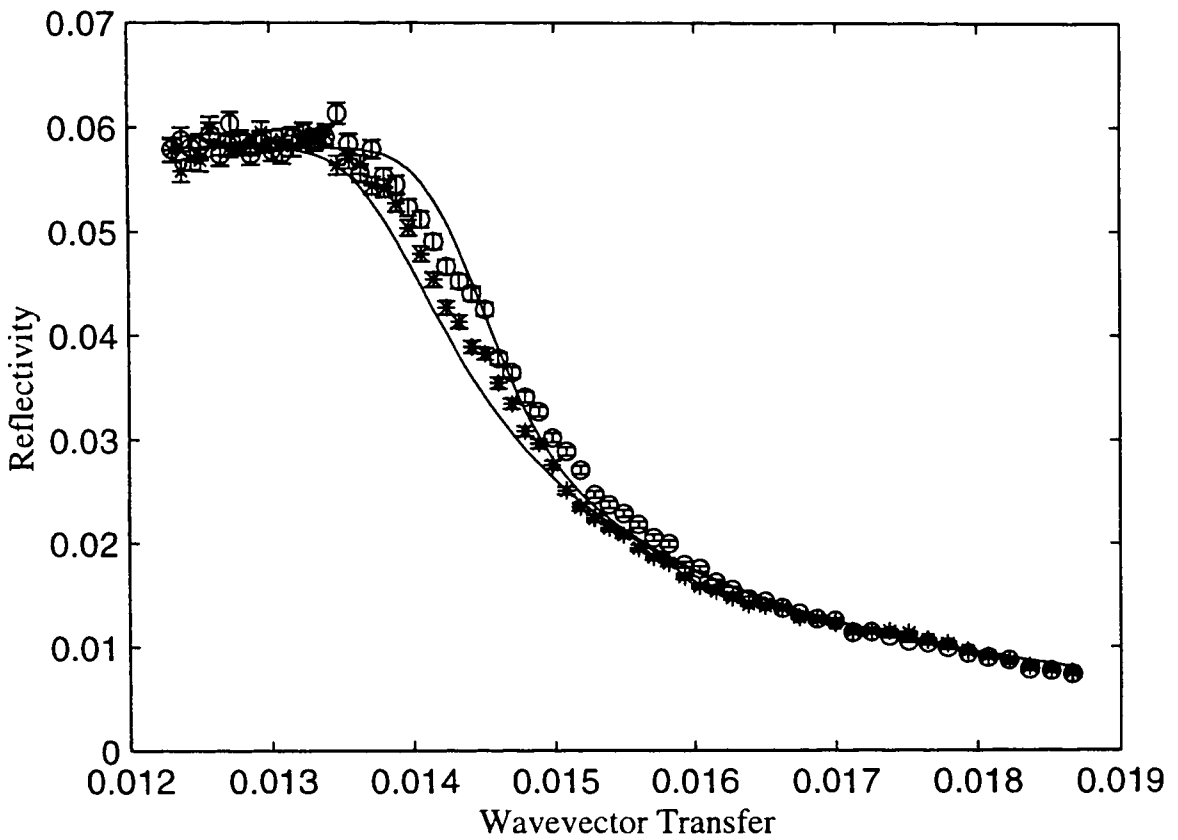

Figure 8.23: Reflectivity at 4380 Oe

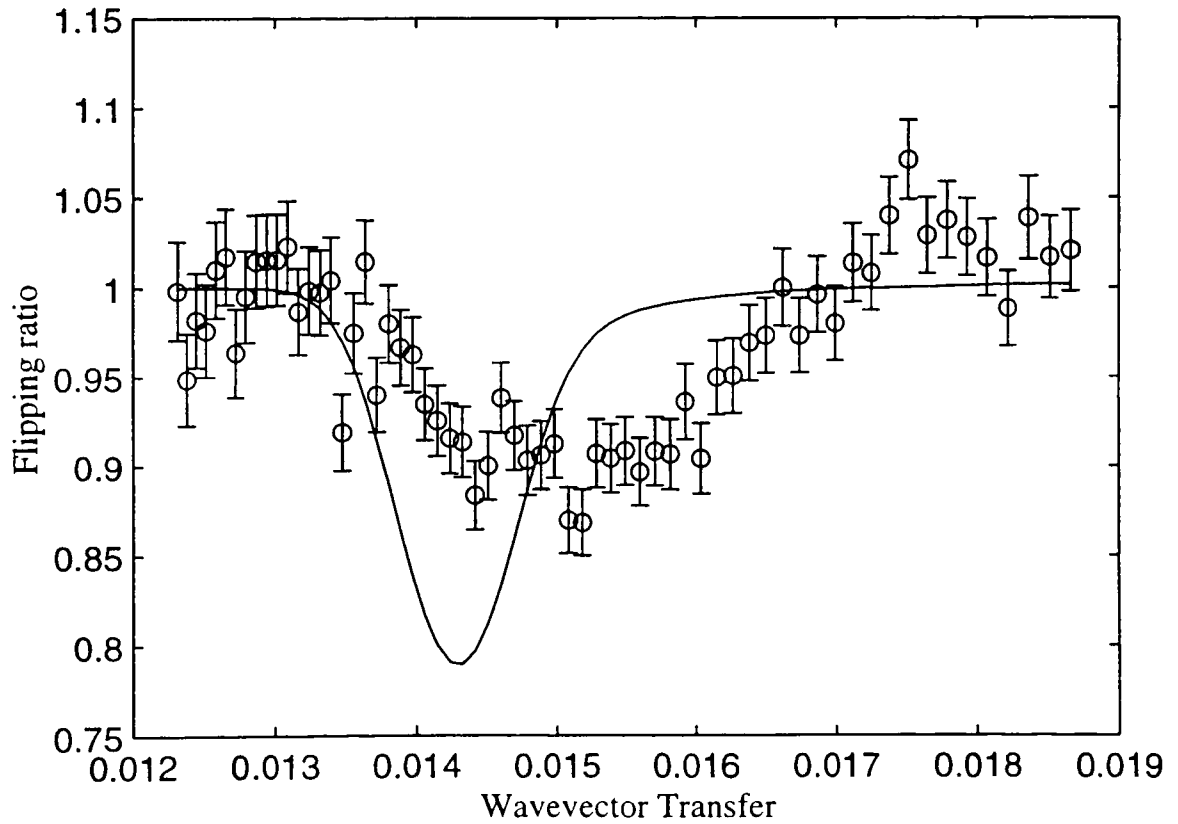

Figure 8.24: Flipping ratio at 4380 Oe

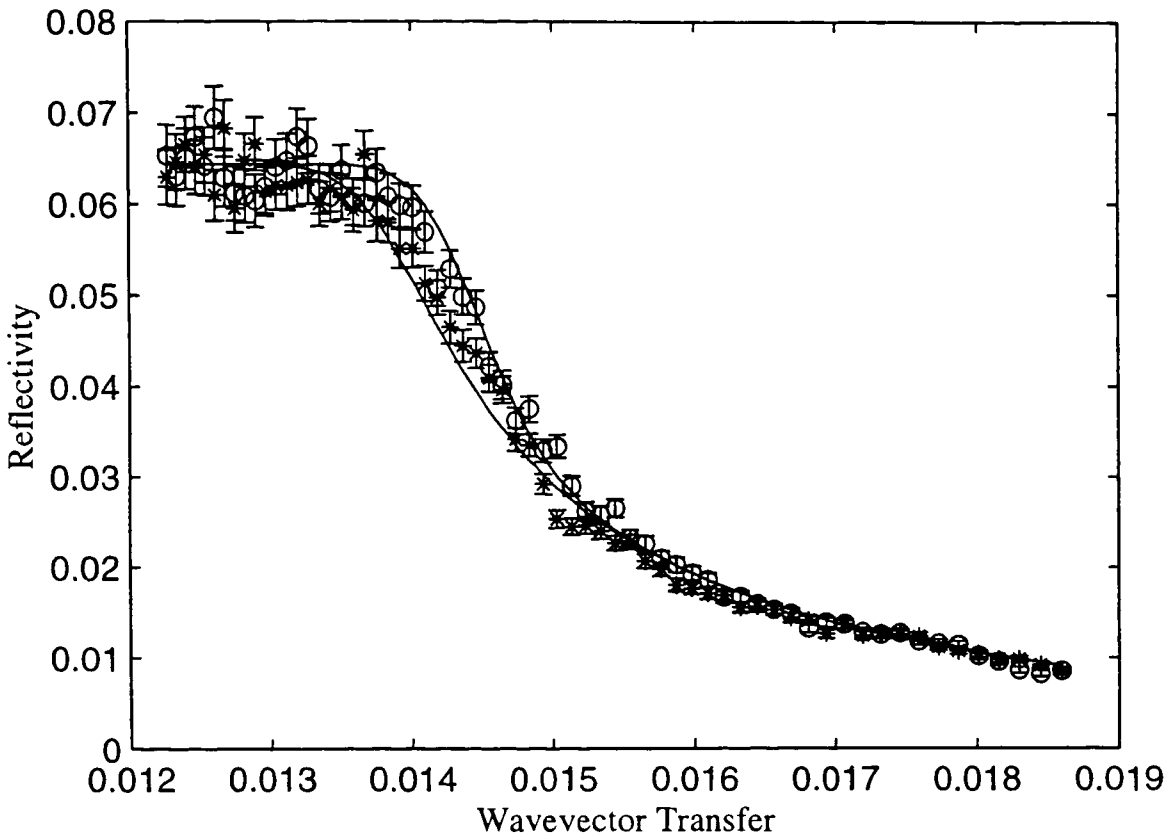

Figure 8.25: Reflectivity at 4540 Oe

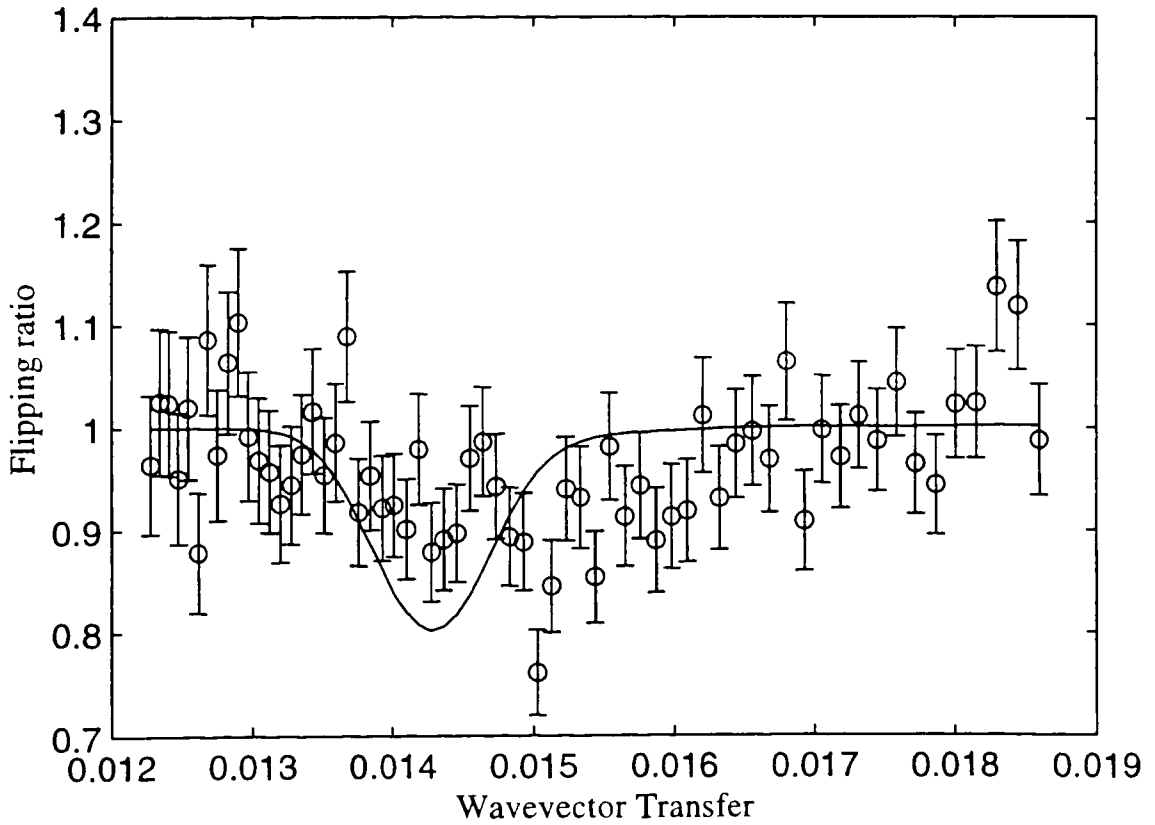

Figure 8.26: Flipping ratio at 4540 Oe

8.2.8 Surface state calculations

To model the higher field states, I also calculated the expected reflectivity for the surface state.

I used the values of κ and H_{c2} derived in Section 8.2.6. The calculated potential for the surface state at H_{c2} was then used as the basis for the magnetic potential in reflectivity fits.

The previous parameters for the mixed state were used as a basis, and the data was fitted allowing the penetration depth to vary.

Figures 8.27 and 8.28 show the reflectivity and flipping ratio at 4380 Oe overlaid with the theoretical values for the surface state. Figures 8.29 and 8.30 show the same for 4540 Oe.

At 4380 Oe, the fitted penetration depth was 820 ± 88 (with a χ^2 of 1.37 for the flipping ratio) and at 4540 Oe the fitted penetration depth was 760 ± 109 (with a χ^2 of 0.93 for the flipping ratio).

The theoretical curves are clearly a much better fit at these fields than the previous mixed state model. However, there still is a slight discrepancy with the reflectivities, with the theoretical curve being noticeably lower in some points.

If $H_{c2} = 9050$ Oe, then the change in κ makes the dip in the flipping ratio slightly smaller, but with a similar form.

8.2.9 Discussion

In the Meissner state, the exponential decay model was adequate to model the results obtained. The value of the penetration depth is consistent with that of a 'dirty' superconductor (See Chapter 6 Refs. [2, 10, 11, 13]).

At the lower field end of the mixed state, reasonable agreement with experiment is obtained for a model with a Meissner state like decay, but a reduced effective field.

Near H_{c2}, the reflectivity closely matches that expected for the surface superconductivity state. However, the magnetization measurements indicate that the sample should not be fully in the surface superconductivity state.

Thus through the mixed state there seems to be a smooth progression from the Meissner state towards the surface superconductivity state. Further measurements at fields which are in the surface superconductivity state would be required for a fully quantitative comparison.

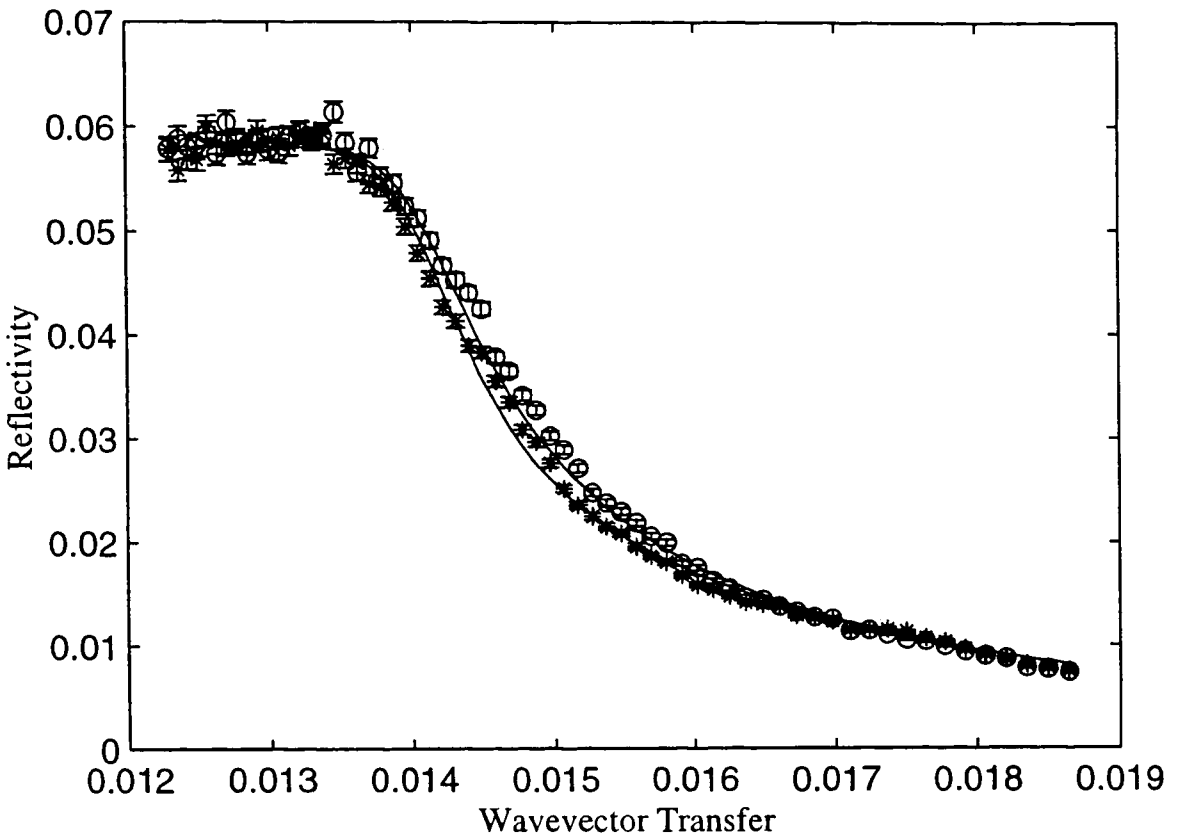

Figure 8.27: Reflectivity at 4380 Oe (surface state calculation)

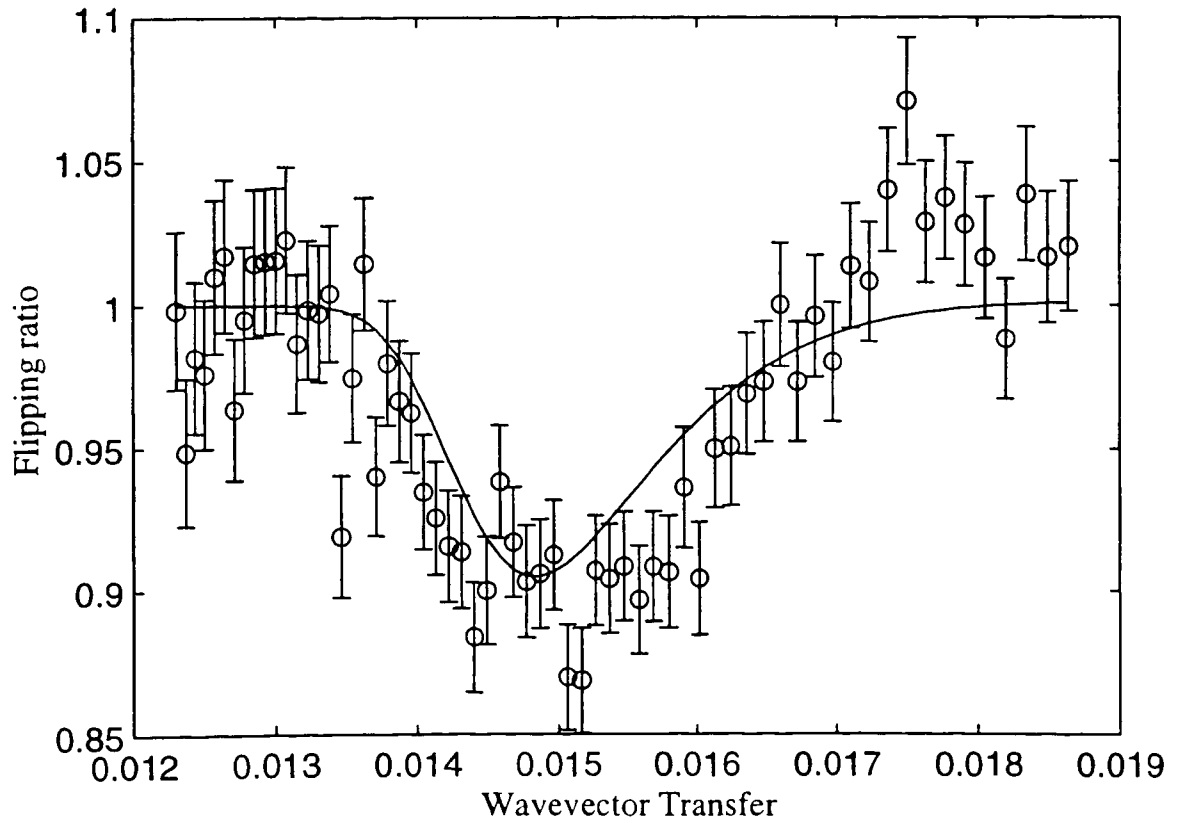

Figure 8.28: Flipping ratio at 4380 Oe (surface state calculation)

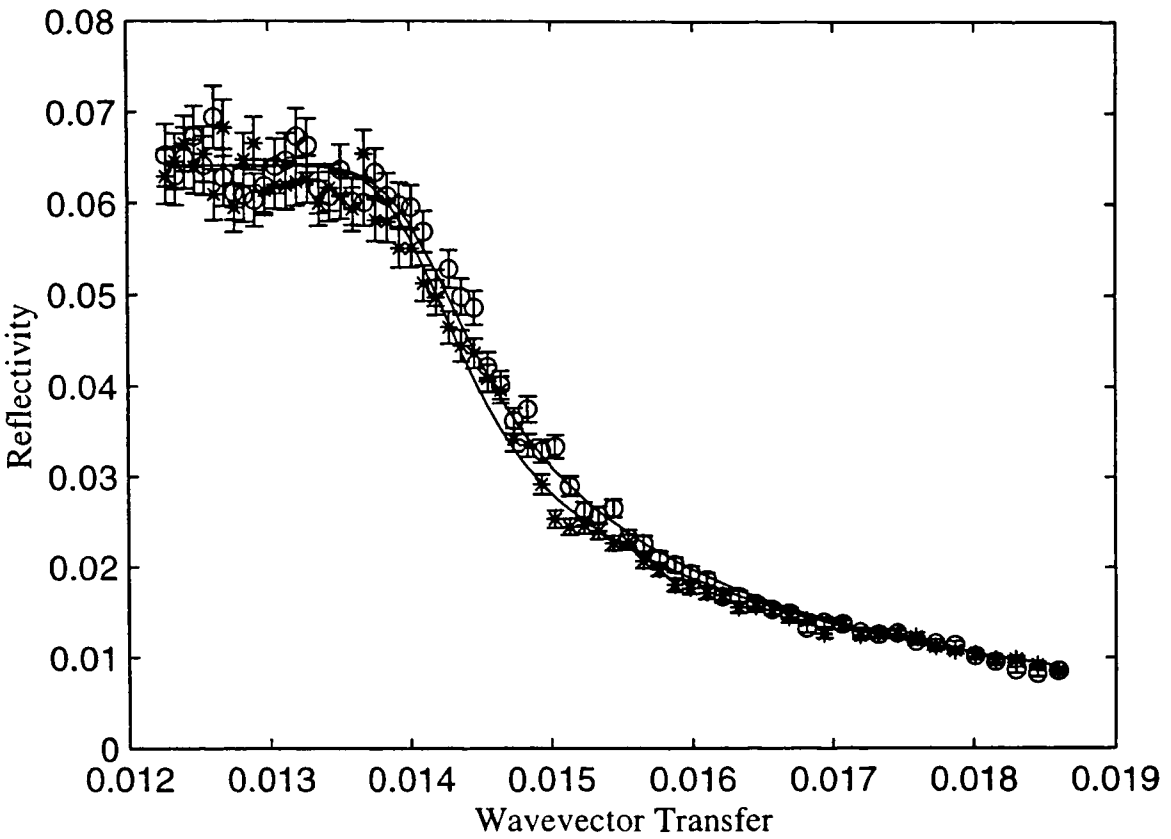

Figure 8.29: Reflectivity at 4540 Oe (surface state calculation)

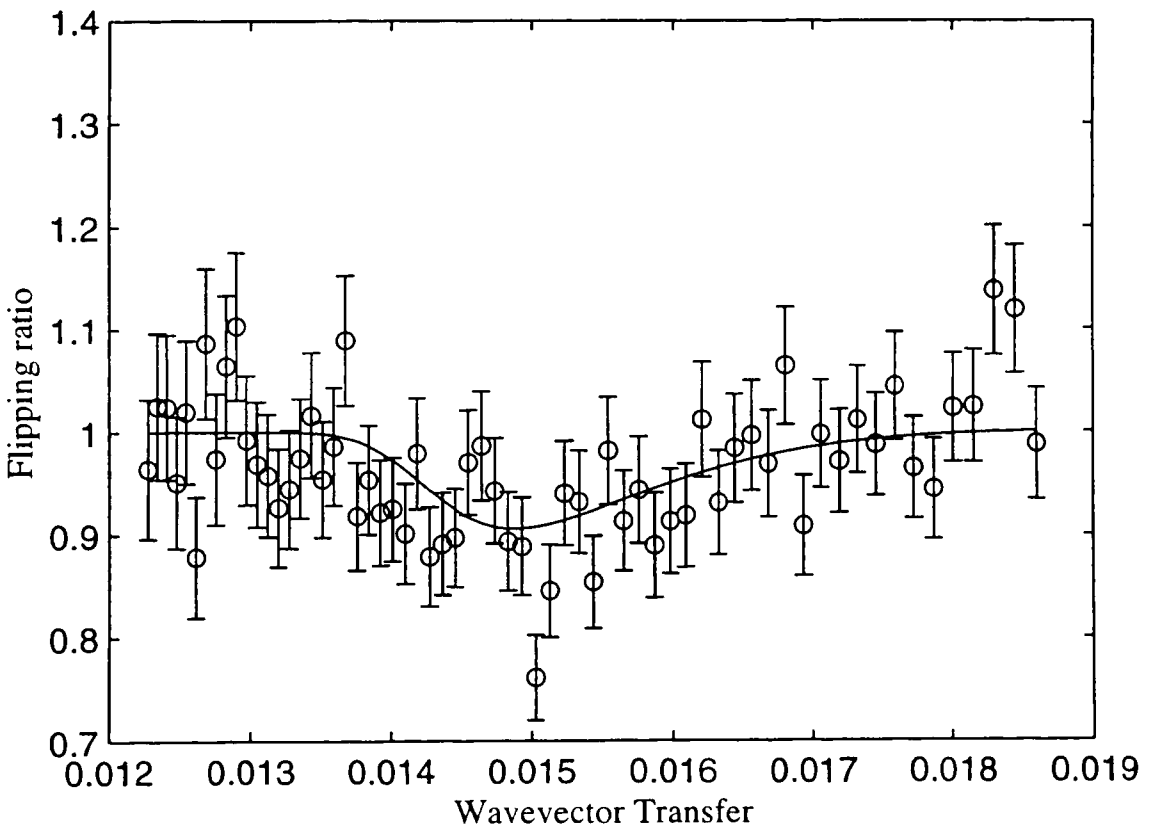

Figure 8.30: Flipping ratio at 4540 Oe (surface state calculation)

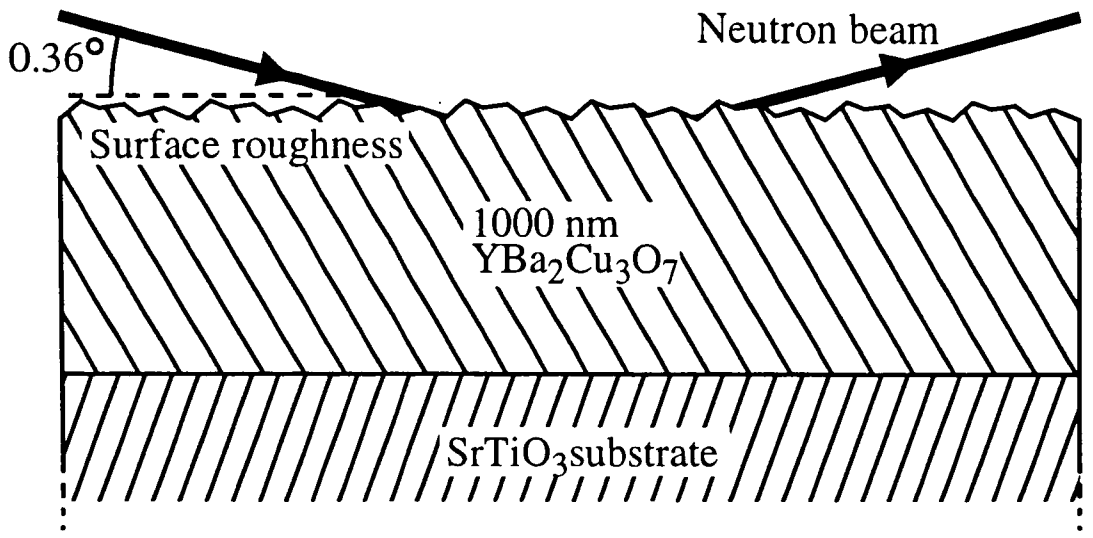

Figure 8.31: The configuration of the $YBa_2Cu_3O_7$ sample

8.3 $YBa_2Cu_3O_7$

In this section I present measurements for the magnetic penetration in a thin film sample of $YBa_2Cu_3O_7$ [5].

8.3.1 Sample

The sample measured was one of a batch from the NKT research centre, grown by T. Freltoft. These varied in thickness from 700 nm to 1400 nm.

The 1000 nm thickness sample was selected after preliminary measurements on the reflectivity.

The sample is a *c*-axis oriented, single crystalline $YBa_2Cu_3O_7$ thin film on a 20 mm × 10 mm × 1 mm (1 0 0) SrTiO3 substrate. The sample was deposited by laser ablation [6].

Figure 8.31 is a schematic diagram of the $YBa_2Cu_3O_7$ sample

8.3.2 Measurements

Unfortunately, the measurements for this sample have been contaminated due to a flaw in the instrument.

After a considerable amount of investigation over more than a year, it was determined that there was a flaw in the anti-reflection coating of the polarizer mirror. This caused an additional reflection from the polarizer, which then caused interference at the detector.

Parameter	Nominal	Fit	Error	Units
Reflectivity	-	3.39	0.02	10^{-3} Counts/Monitor
Incident angle	0.36	0.36103	0.00032	Degrees
Beam deviation	-	5.488	0.057	%
Sample *nb*	4.74	-	-	10^{-6}Å^{-2}
Sample width	10000	10019	151	Å
Sample roughness	-	103.0	1.2	Å
Substrate *nb*	3.52	-	-	10^{-6}Å^{-2}
Reduced χ^2		8.09		

Table 8.4: $YBa_2Cu_3O_7$ unpolarized reflectivity parameters

This additional beam lead to an irregular oscillation overlayed onto the reflectivity. This was particularly noticeable as a problem as there was a large oscillation above the critical edge, which should be flat once there is total reflection.

The problem was difficult to locate as it is a relatively small effect, and one that only occurs in a small fraction of the experiments run on CRISP (most of the others do not use polarization, or need as accurate statistics).

Unfortunately, the oscillations are complex and cannot be easily subtracted from the signal.

Moreover, an oscillation at the critical edge changes the slope of the critical edge, which is important for determining the penetration depth from the flipping ratio.

As with the niobium sample, the wavelength dependent reflectivity was binned into 138 data points.

8.3.3 Unpolarized reflectivity

As an approximation to the unpolarized reflectivity, the average of the low field R^+ and R^- curves was taken. Figure 8.32 shows this averaged scattering from the sample in 550 Oe field. Figure 8.33 shows the same data enlarged around the critical edge. The scale is linear in y to show the oscillations.

The theoretical line is a fit based on the parameters in Table 8.4. The structure is assumed to be the nominal structure, with a rough surface.

The only free parameters are the angle, deviation and overall reflectivity (as with the

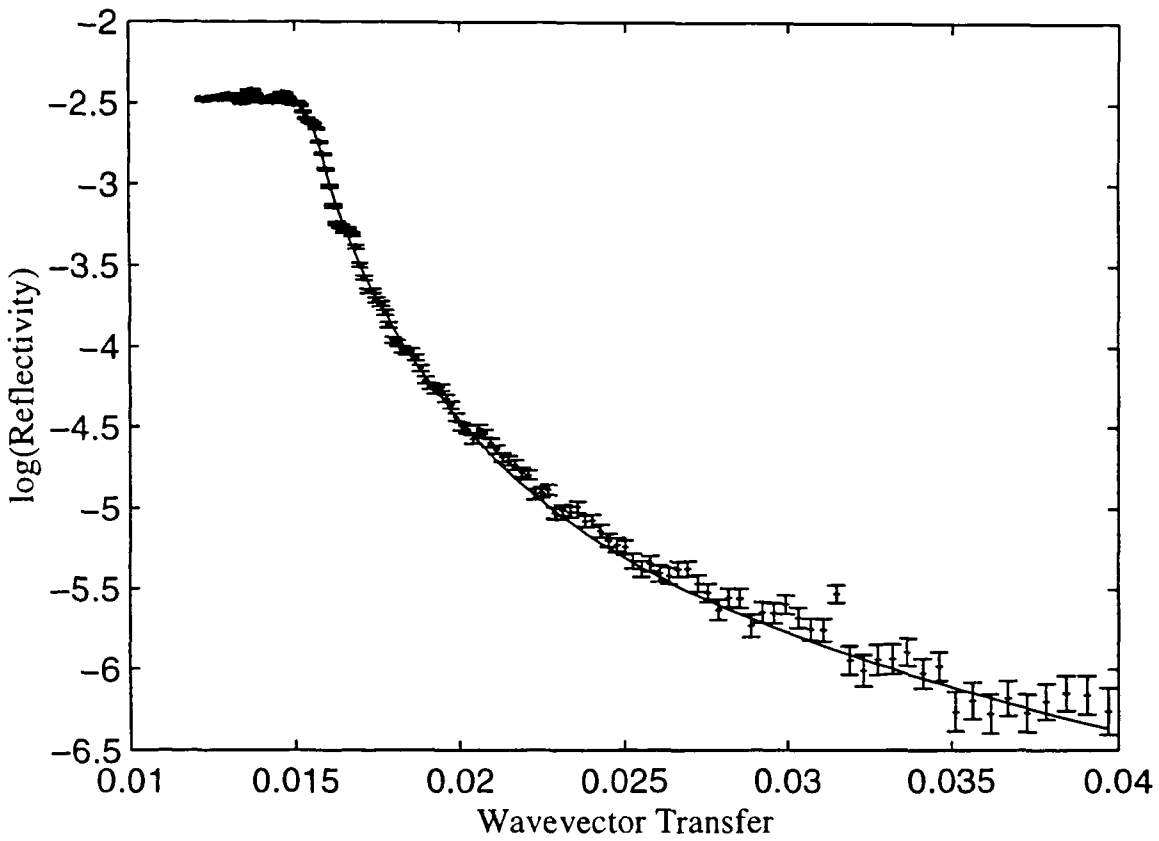

Figure 8.32: $YBa_2Cu_3O_7$ unpolarized reflectivity: The reflectivity of the $YBa_2Cu_3O_7$ sample. The reflectivity is in arbitrary units.

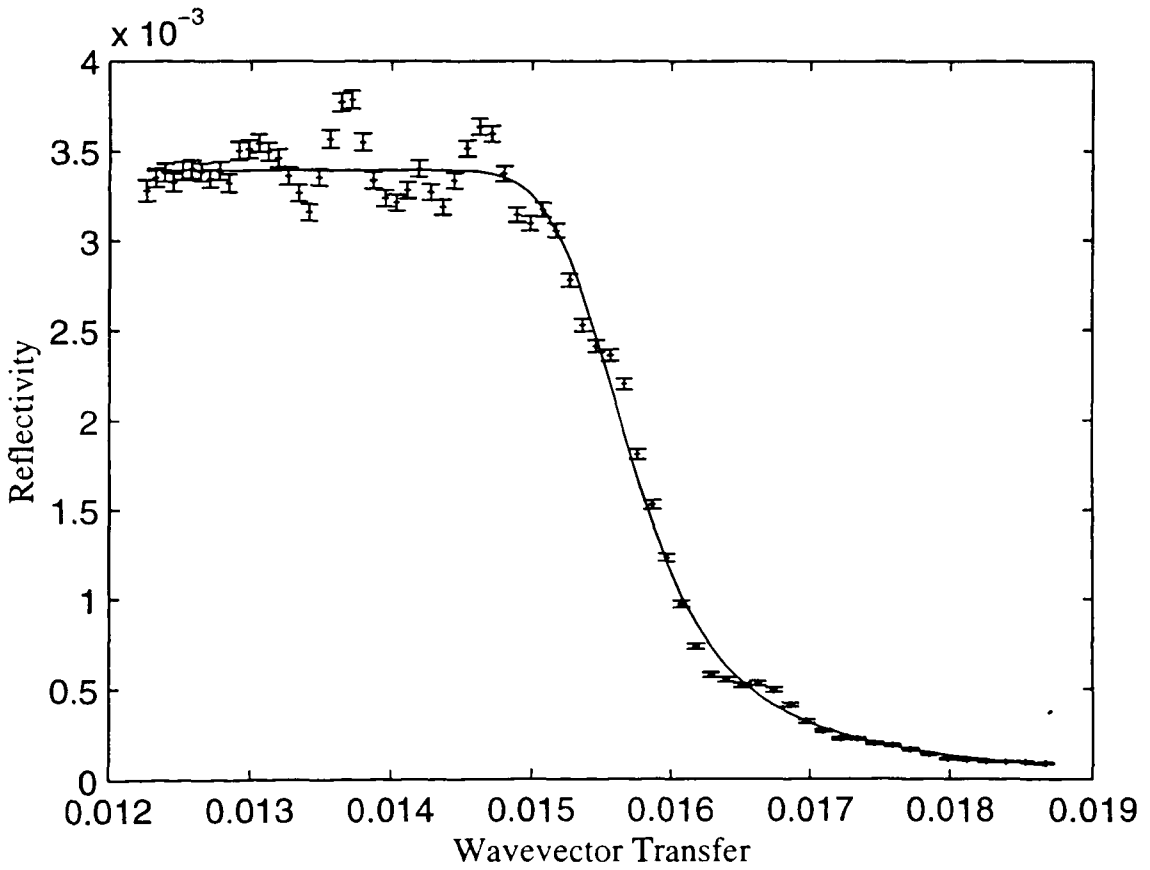

Figure 8.33: $YBa_2Cu_3O_7$ unpolarized reflectivity: The same data as in Figure 8.32 enlarged around the critical edge, on a linear scale.

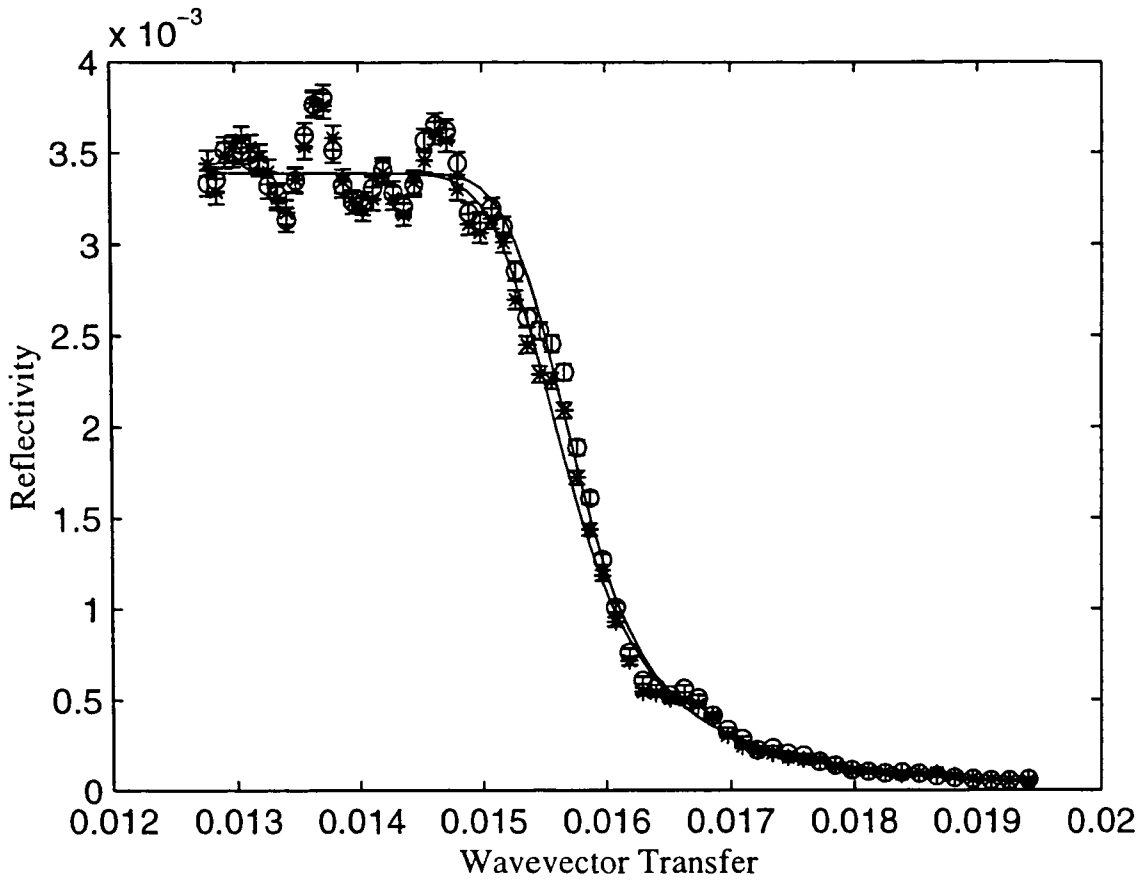

Figure 8.34: $YBa_2Cu_3O_7$ polarized reflectivity: The R^+ and R^- reflectivities in 550 Oe applied field. The asterisks mark the R^+ reflectivity and the circles mark the R^- reflectivity.

niobium sample), and the thickness and roughness of the $YBa_2Cu_3O_7$ layer.

8.3.4 Polarized reflectivity

Figure 8.34 shows the values of R^+ and R^- with the best fit model calculated lines. From this it is clear that the oscillations affect both reflectivity curves, and are larger than the size of the difference produced by the magnetic decay.

Figure 8.35 shows the flipping ratio of the two reflectivity curves, along with the ratio of the theoretical lines in Figure 8.34. This is a reasonable fit, but with a significant random error.

Table 8.5 shows the fitted values for the magnetic penetration. The χ^2 for the fit is essentially the same as in Table 8.4, as the averaged measurements had smaller errors due to the combination of the data.

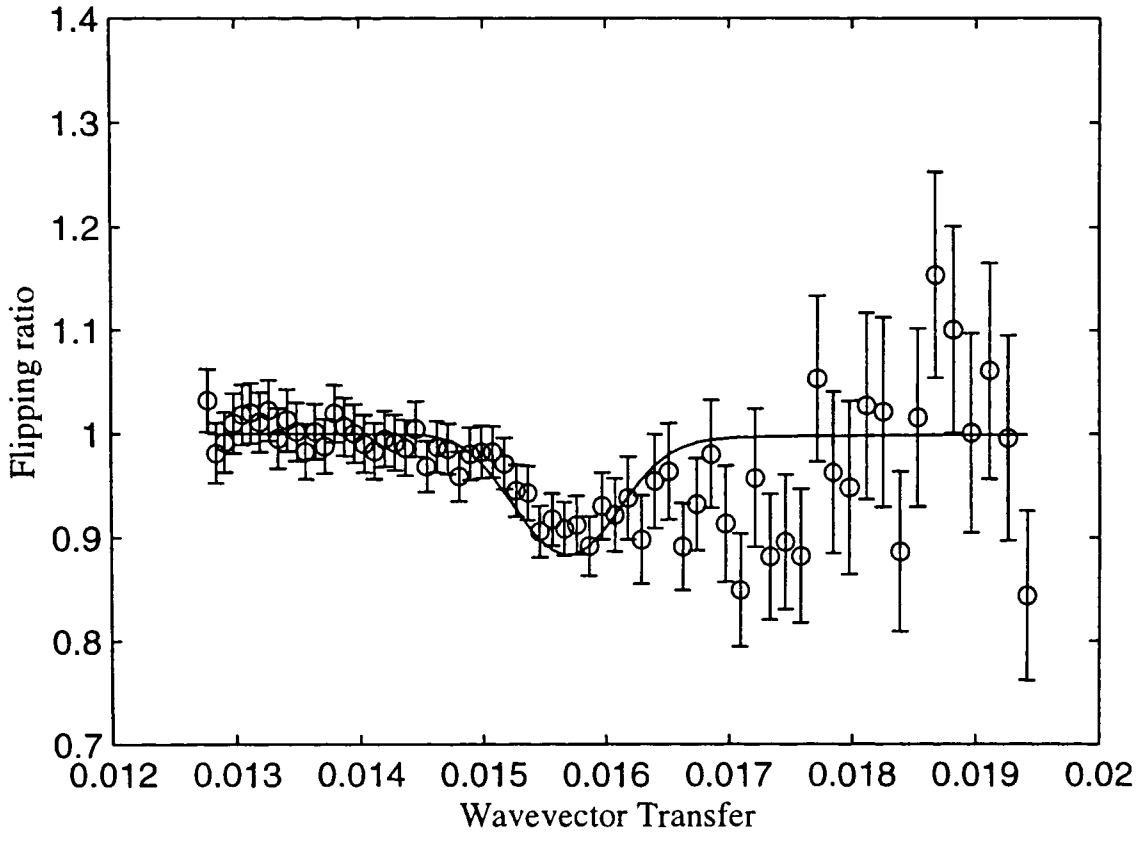

Figure 8.35: $YBa_2Cu_3O_7$ flipping ratio: The flipping ratio R^+/R^- in 550 Oe applied field.

Field	550 Oe
Intensity	$3.39 \times 10^{-3} \pm 1.4 \times 10^{-5}$
Incident angle	0.3621 ± 0.0002
Beam deviation	5.404 ± 0.014
λ	2018 ± 261
χ^2	4.44
FR χ^2	1.22

Table 8.5: $YBa_2Cu_3O_7$ magnetic penetration parameters: The FR χ^2 refers to the χ^2 for the model of the flipping ratio.

8.3.5 Discussion

The results of the measurements on $YBa_2Cu_3O_7$ are inconclusive. The oscillations introduced by the split beam have made the reflectivity impossible to analyse in a fully quantitative manner. The oscillations are most pronounced around the critical edge.

The derivation of the structure of the sample is not affected greatly (though the χ^2 is increased), as much of the information comes from the falloff at higher Q. The oscillations do not seem to have affected the overall slope too much.

Unfortunately, the model of the magnetic decay is critically dependent on the exact shape of the curve around the critical edge. Thus, there is a large error on the penetration model.

The actual error is likely to be considerably larger than the random error quoted in Table 8.5. Considering the large error, the derived value is quite close to that obtained by similar recent measurements (See Chapter 6 Refs. [12, 13]), which typically give a penetration depth around 1400 Å.

Despite the problems, these measurements do show that it is possible to study the magnetic penetration using much thicker samples than have previously been used. Certainly the signal from the magnetic decay is clearly visible.

The sample does show significant roughness at the surface, but these measurements suggest that it should be possible to account for this in the analysis.

We hope to be able to repeat these measurements in the near future with the corrected instrument. We also hope to be able to perform a more extensive study, including the mixed state and the temperature dependence of the penetration.

8.4 References

[1] J. Penfold, R.C. Ward and W.G. Williams, *A time-of-flight neutron reflectometer for surface and interfacial studies*, J. Phys. E **20** 11 1411–1417 (1987).

[2] V. Nunez, A.T. Boothroyd, J. Reynolds, J. Penfold, S. Langridge, D.G. Bucknall, P. Böni, D. Clemens and M. Senthil Kumar, *Improvements to the polarised-neutron reflectometer CRISP*, Physica B **241–243** 148–150 (1998).

[3] J.M. Reynolds, V. Nunez, A.T. Boothroyd, R. Somekh, D.G. Bucknall and S. Langridge, *Polarised neutron reflectometry studies of flux penetration in superconducting* Nb, Physica B **241–243** 1104–1106 (1998).

[4] D.K. Finnemore, T.F. Stromberg and C.A. Swenson, *Superconducting Properties of High-Purity Niobium*, Phys. Rev. **149** 1 231–243 (1966).

[5] J.M. Reynolds, V. Nunez, A.T. Boothroyd, T. Freltoft, D.G. Bucknall and J. Penfold, *Penetration depth of* $YBa_2Cu_3O_7$ *measured by polarised neutron reflectometry*, Physica B **248** 163–165 (1998).

[6] R. Kromann, J.B. Bilde-Sørensen, R. de Reus, N.H. Andersen, P. Vase and T. Freltoft, *Relation between critical current densities and epitaxy of* $YBa_2Cu_3O_7$ *thin films on* MgO *(100) and* $SrTiO_3$ *(100)*, J. Appl. Phys. **71** 7 3419–3426 (1992).

Chapter 9

Magnetic Flux Penetration Conclusions

This chapter will summarize the measurements made of the thin film superconductors and the conclusions.

9.1 Nb thin film

The measurements on niobium were made after the CRISP polarized problem had been corrected.

In the Meissner state, an exponential decay of flux models the measurements well. The penetration depth (magnetic screening length) was found to be slightly greater than 600 Å for all measurements in this state at a temperature ≈ 4 K. This combined with the magnetization measurements indicates a κ between 2.5 and 3.3 depending on the interpretation of the measurements. Comparison with other measurements indicates that the sample has a coherence length less than that of pure niobium; this is probably limited by the size of grains in the sample. The mean free path is approximately 11.4 nm.

The integrated signal of the polarization function shows a transition to the mixed state that matches closely the magnetization measurements.

The mixed state shows a gradual transition from the Meissner state towards the surface

superconductivity state, with a comparable penetration depth.

The measurements have suggested a number of improvements for future work:

- A different substrate or buffer layer would be desirable. Currently the buffer layer significantly distorts the reflectivity curve. A buffer layer is needed to provide a good bond between the substrate and sample, and the choice of substrate is limited by the scattering length requirement.
- The niobium sample probably does not need to be as thick as this one to still match the bulk properties. However, a much smaller thickness would lead to an even larger magnetization in the surface state relative to the mixed state.
- An accurate measurement of the reflectivity in zero field is desirable.
- Measurements at higher field (or closer to T_c) would enable direct measurement of the surface superconductivity state.

9.2 $YBa_2Cu_3O_7$ thin film

Due to the problems with the apparatus, our results for the $YBa_2Cu_3O_7$ thin film are inconclusive. However, we have shown that the measurement is possible to perform.

The fit of the structure is largely in agreement with the nominal structure.

The preliminary value for the penetration depth λ is 2018 ± 261 (with a considerable additional systematic error due to the experimental problems). This is rather larger that has previously been measured, but this may be expected considering the large error.

9.3 Measurement techniques

We have shown that measuring flux penetration with polarized neutron reflectometry is possible with relatively thick superconducting samples.

Using thick samples does show many of the problems which have kept people from using them in the past. In particular, with a thick sample, oscillations are not visible in the reflectivity curve, which make analysis more difficult. Also, high quality samples are harder to achieve. However, we have shown that these are not critical problems.

We have found that most of the limiting factors of the technique are properties of the sample.

In particular things that need to be considered are:

- Sample thickness: As we have shown, it is possible to perform reflectometry measurements using relatively thick samples. This has the advantage that the behaviour of the superconductor will more closely match that of the bulk superconductor. However, thick samples can make the other desirable properties harder to obtain.

- The grain size: A superconductor made of grains has somewhat different properties to a true single crystal. In particular, if the coherence length is not much smaller than the grain size then the grain size will limit the effective coherence length. The grain size is a property of the technique used to grow the crystal.

- The surface roughness: We have found that the surface roughness can have a large effect on the results obtained. However, we have found that the surface roughness can be modelled effectively. Surface roughness generally increases with sample thickness.

- Surface oxidization: Like surface roughness, surface oxidation also significantly effects the results. An oxide layer adds another uncertainty, as the oxide layer is not generally superconducting, so this offsets where the field decay will start. As the oxide layer forms over time, the storage of the samples is critical, and samples may show less oxidation if measured soon after growth.

- Water damage: We have found that the thin film samples can be vulnerable to damage from condensation. It is thus important that the samples are warmed gradually after the experiment to avoid condensation forming on them from the atmosphere.

- Sample bending: With previous niobium samples we found that the strain from a lattice mismatch was sufficient to bend the sample slightly. This is of course important for reflectometry as a bent sample will spread out the reflected beam and also reduce the resolution as the incident beam angle is effectively blurred. We solved this problem by using a very thick (5 mm) substrate for the niobium, which was extremely rigid.

- Substrate type: To be able to grow good quality samples, a suitable substrate is needed. Unfortunately, many of the substrates used to get good crystals have a high scattering length density, so the scattering from the substrate will dominate that from the sample. Thus less ideal substrates may need to be used.

- Buffer type: A way of reducing the problems of lattice mismatch is to use a buffer layer of another material. This can lead to a much better crystal, but can cause other problems. As with the substrate, the scattering length density of the buffer can be important to the form of the reflectivity. Another untried idea is to use a neutron absorbing material, so that incident neutrons will not strike the substrate. This would allow a wider choice of substrate.

Part III

Conclusions

Chapter 10

Concluding Remarks

10.1 Magnetic structure measurements

10.1.1 Results

In this thesis I have used elastic neutron scattering (using a triple-axis spectrometer) to determine the magnetic structure of $NdBa_2Cu_3O_{6+\delta}$. This is the first such study using single crystals covering the reduced and oxidized forms, and both the copper and neodymium ordering.

The main impetus of this was to compare with the previously measured $PrBa_2Cu_3O_{6+\delta}$. This is notable in that the oxygenated form does not superconduct (at least in conventionally prepared samples). The previous measurements have shown unusual magnetic structure, particularly in a coupling between the praseodymium and copper moments.

The oxygenated $NdBa_2Cu_3O_7$ crystal showed a simple structure, with the neodymium moments ordering at low temperature into a purely antiferromagnetic structure. This is different to some measurements of the praseodymium moments which have been observed to order antiferromagnetically in the *ab* plane and ferromagnetically in the *c* direction.

One reduced $NdBa_2Cu_3O_6$ crystal showed a more complex magnetic structure. This is believed to be due to the crystal having neodymium substitution on the barium sites.

At high temperatures, the copper plane moments formed a simple antiferromagnetic structure as expected (AF1). However, at low temperatures parts of this structure rotated

in different directions to form a new structure (AF2 intermediate). There was no evidence for a significant ordered moment on the Cu(1) sites, but this is not conclusive.

At very low temperatures, the neodymium moments ordered to form a two-dimensional structure, with the moments uncorrelated in the c direction.

Despite the unusual structure, there was no coupling of the neodymium and copper moments visible. No change was observed in the copper ordering when the neodymium ordered.

The other reduced crystal (which is believed to be more stoichiometric) showed a much more conventional structure. The copper plane moments ordered antiferromagnetically at high temperature (AF1), and the neodymium ions ordered antiferromagnetically at low temperature, without affecting the copper moments.

Again no coupling between the neodymium and copper moments was visible.

Thus, in conjunction with the previous measurements on $PrBa_2Cu_3O_{6+\delta}$, we have shown that $PrBa_2Cu_3O_{6+\delta}$ has an unusual ordering that does not seem to be shared by the samples measured here of $NdBa_2Cu_3O_{6+\delta}$.

As this ordering indicated a coupling between the praseodymium moments and the copper moments, then this could be relevant to the praseodymium suppression of the superconductivity.

10.1.2 Techniques

The measurements have also highlighted some of the problems of using a triple axis spectrometer for measuring magnetic structure. The alignment of the sample is critical if fully quantitative measurements are desired.

I have shown that in certain circumstances, measuring peak intensities by taking linear scans through them and correcting by the use of a Lorentz factor does not give a sufficiently accurate value to derive absolute moments reliably.

I have found that a grid procedure will give significantly better results without taking vastly more time, and is also much simpler to analyse.

10.2 Magnetic penetration measurements

In this thesis I have used polarized neutron reflectometry to study magnetic penetration in thin film superconductors that are much thicker than those commonly measured.

As expected, this has shown many of the difficulties that have limited the sample size in the past: these are the surface roughness, the grain size and the relatively ambiguous signal in the flipping ratio.

However, the relatively thick samples have enabled the penetration characteristics to be studied in a situation much closer to that of a bulk superconductor. In particular, a thick sample enables the Meissner state to have near total exclusion in the middle, the mixed state to have a significant flux penetration and the surface state magnetization at the surfaces to be genuinely separated.

10.2.1 Nb thin film

I have measured the polarized reflectivity for a niobium thin film at several applied fields through the Meissner state and almost all of the mixed state.

There is a good agreement between theory (with the model being a simple exponential decay) and experiment for the Meissner state. The penetration depth derived for this state is consistent with a sample for which defects are limiting the coherence length.

In the mixed state, the reflectivity indicates a gradual transition from a Meissner state like exponential decay towards the surface superconductivity state.

I have shown that a type-II superconductor can be measured usefully above the Meissner state by PNR. Further measurements are needed to investigate the surface superconductivity state fully.

10.2.2 $YBa_2Cu_3O_7$ thin film

Experimental difficulties have prevented us from obtaining an accurate model of the sample. However, the results are generally in line with what is expected from previous measurements.

We hope to perform a corrected and more detailed study in the future.

10.2.3 Techniques

I have found that the technique of polarized neutron reflectometry is suitable for measuring samples of these types.

However, the exact properties of the samples are critical to the measurements. High quality samples are important for PNR measurements, and these are particularly difficult to obtain with large thicknesses. As well as the sample itself, carefully chosen substrates and buffer layers are important.

Index

Index entries in **bold** represent sections and underlined entries refer to figures or tables.